JCM

Scholarly, Peer-Reviewed and Fully Refereed International Research Journal

ISSN : 2583-9152

Journal of Condensed Matter

of

Condensed Matter Research Society

Vol. 03 No. 01 (2025)

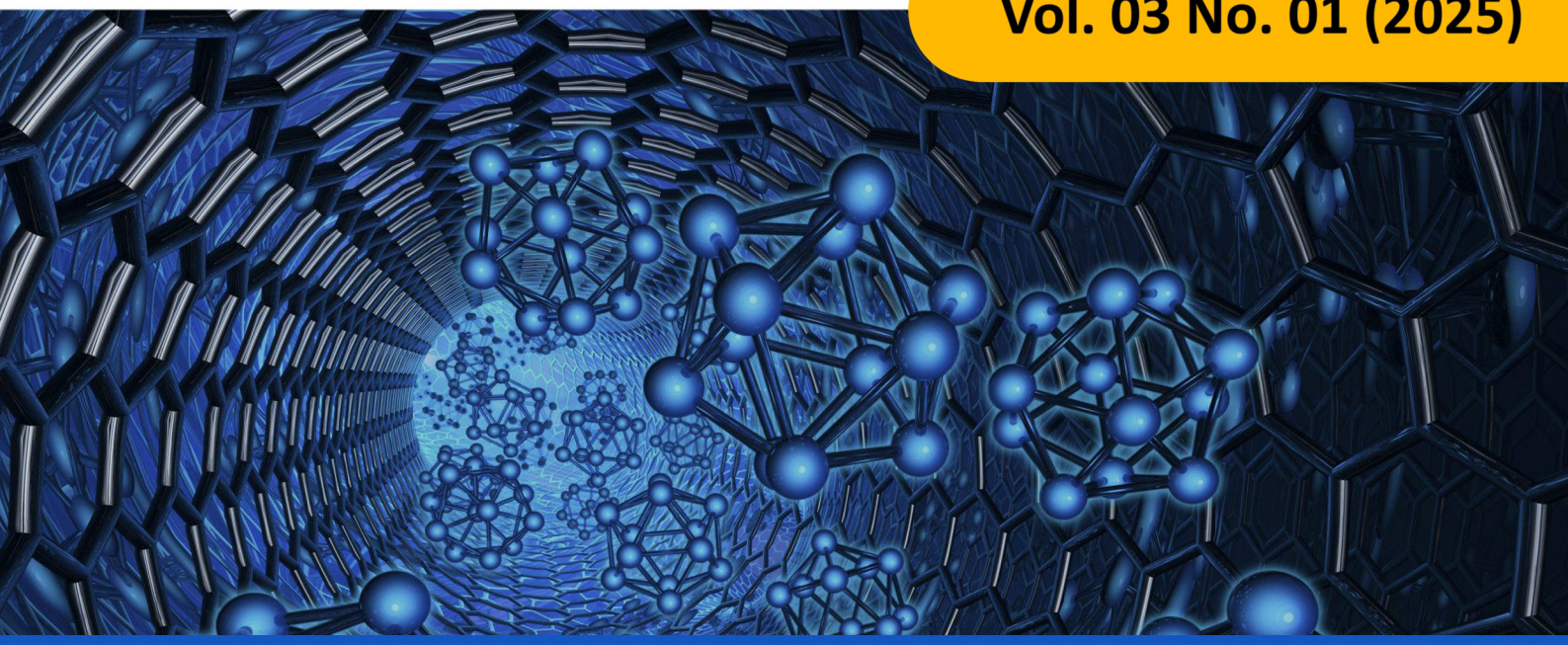

Condensed Matter Research Society

Table of Contents

Silicon and its Composites as Anode Materials in Li-ion Batteries

Ashish Kumar Mishra[a], Monika, Anjali, Balbir Singh Patial[b]

Department of Physics, Himachal Pradesh University, Summerhill, Shimla, Himachal Pradesh, 171005, INDIA

[a] mishrashish32150@gmail.com
[b] bspatial@gmail.com, bspatial@hpuniv.ac.in

Abstract

Recent technological advances need a reliable and sustainable energy storage system with a high energy density. $LiCoO_2$ and graphite are the cathode and anode materials used in current Li-ion batteries, respectively, however their capacity is restricted. The anode side of the battery plays an important function in storing Li-ions during charging and discharging cycles. Si has evolved as a unique anode material in recent decades with a theoretical capacity almost ten times that of traditional graphite. But there are various issues with Si, like massive volume expansion, electrode pulverization, decreasing cell capacity over time, etc. The electrochemical output of Si and its composites is determined by the materials utilized. Direct alloying of Si with Li yields stable phases such as $Li_{12}Si_7$, Li_7Si_3, $Li_{13}Si_4$ and $Li_{21}Si_5$ with the highest theoretical capacity. Composites of Si, which include carbon, polymer and other elements, exhibit promising outcomes. This paper summarizes and discusses current breakthroughs in Si and its composites tested as anodes in Li-ion batteries. The use of 1D, 2D and 3D carbon with various matrices for Si composite helps to accommodate volume expansion. Structural and morphological changes as well as the electrochemical performance of thus synthesized batteries have also been described.

Keywords: Li-ion battery, Anode, Silicon, Graphite, Energy storage, Cyclic stability.
Received 30 January 2025; First Review 10 February 2025; Accepted 16 February 2025

*** Address of correspondence**
Dr. Balbir Singh Patial
Department of Physics, Himachal Pradesh University, Summerhill, Shimla, Himachal Pradesh, 171005, INDIA

Email: bspatial@gmail.com

How to cite this article
Ashish Kumar Mishra, Monika, Anjali, Balbir Singh Patial, Silicon and its Composites as Anode Materials in Li-ion Batteries, J. Cond. Matt. 2025; 03 (01): 1-6

Available from:
https://doi.org/10.61343/jcm.v3i01.107

Introduction

We require a dependable energy storage system as technology advancements and energy consumption continue to rise. A system that can supply more energy in less space while being economical, portable, and with a long shelf life. There are several rechargeable energy storage options on the market with diverse chemistries such as NiCd, lead acid, NMH, Li-ion, Na-ion and K-ion. Li-ion batteries are one of the broadly used and investigated battery chemistries. It has a standard graphite anode and $LiCoO_2$ cathode with theoretical capacity of 374 $mAhg^{-1}$ and 160 $mAhg^{-1}$ respectively. Nevertheless, the demand for batteries with high energy density poses a new challenge to current technology due to its restricted capacity as the battery's capacity is solely determined by the material used.

In order to meet modern technology needs, a variety of materials have been tested to provide high energy density while remaining sustainable. Si may exhibit several advantages over the traditional anode material, graphite such as high energy density, cost effectiveness, ecologically sound and abundance. The chemistry of forming distinct phases with Li produces phases with the highest degree of lithiation. Phase diagram of Li and Si shows formation of various phases such as $Li_{12}Si_7$, Li_7Si_3, $Li_{13}Si_4$ and $Li_{21}Si_5$, where $Li_{21}Si_5$ has the highest degree of lithiation with chemistry of single Si atom forming bond with 6 Li atom giving advantage over graphite where 6 carbon makes bond with single Li atom. Figure 1 depicts the Li-Si phase diagram [1]. Si is the second most prevalent element on earth, accounting for around 27.7% of the planet's crust, making it a promising research topic [2]. Silicon does not occur in pure metallic form in nature, so we need to separate it from silica or silicates. Electronic structure of Si is $1s^2\ 2s^2\ 2p^6\ 3s^2\ 3p^2$, where two electrons (first shell), 8 electrons (second shell), and 4 electrons (outermost shell). These four electrons in the outermost shell determine Si's conductivity and structure. It has a 3D diamond like structure with a lattice constant of 5.431 angstrom having an Fd-3m space group. Before we can address Si composites, we must first understand the chemistry of Si with lithium. Li has an atomic number equal to three, making it the lightest metal on Earth. It has higher charge density, which means a lower atomic radius in comparison to its nuclear charge, making it extremely reactive and bond-forming. Because of this capacity, Li can easily polarize other molecules but not itself because of the double helium shell surrounding it. It is

also the most active metal available due to its highly negative electrode potential. Figure 1 depicts the creation of different phases. The most lithiated phase is $Li_{22}Si_5$, with one Si atom hosting 4.4 Li atoms, resulting in the largest theoretical capacity. Lithiation of Si also shows formation of $Li_{15}Si_4$ at room temperature. Lithiation of Si starts with the formation of crystalline and amorphous phases of Li_xSi. Equation 1 shows the reaction process of lithiation of Si. Figure 2 depicts the galvanostatic profile for lithiation at room temperature. But there are several problems with Si as anode such as (i) huge volume expansion, (ii) low electrical conductivity, (iii) structural deformation on every cycle, (iv) low rate of Li^+ diffusion, (v) loss of contact in middle of active material with substrate, (vi) repeated formation of SEI, (vii) continuous consumption of electrolyte and Li^+ to form SEI and (viii) puffing of battery unit. In 1976, General Motors Corporation tested Si as an anode for the first time [3], sparks research on the material. Even graphite was commercialized several years later, circa 1990-1992, as a secondary battery. Since then, several research publications on Si as anode in alkali-ion batteries have been published. Many Si composites have been tested for anode in Li-ion batteries to mitigate the problems with Si anode, such as alloying Si with other elements of lower band gap to reduce the band gap for better electronic conductivity, synthesizing carbon-based yolk and core shell structure to compensate volume change, nano-structuring to avoid cracks inside the particle of active material and surface engineering to increase Li^+ diffusion and conductivity.

$$Li_xSi \leftrightarrow xLi + Si + xe^- \qquad (1)$$

Various strategies were and are being applied to mitigate these problems with silicon being used as anode in Li-ion batteries such as pre-lithiation, alloying Si, surface modification, structural modification, nano particle synthesis etc.

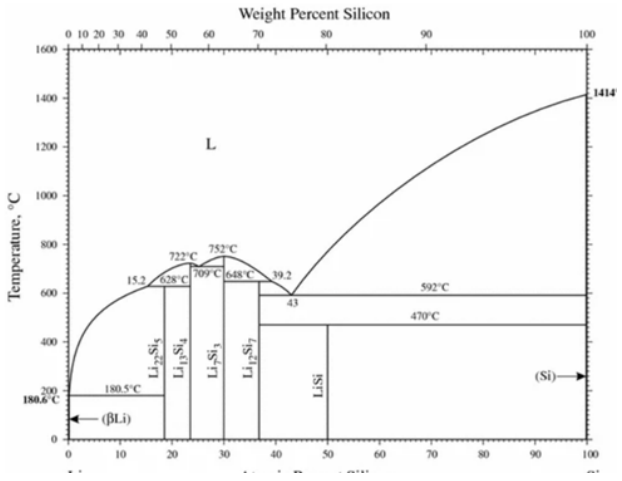

Figure 1: Phase diagram of Li-Si alloy [1]. Reprinted with permission from ACS Nano © 2013 American Chemical Society.

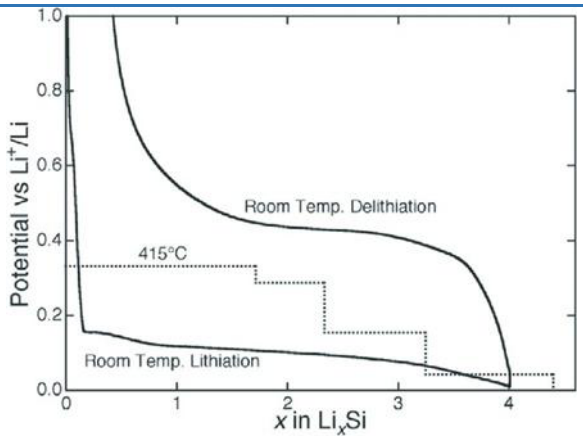

Figure 2: Graph of open circuit voltage as a function of lithium, shows formation of plateaus at elevated temperatures [4]. Reprinted with permission from Advanced Materials © 2013 John Wiley & Sons.

Silicon/Carbon (Si/C) Composites

Silicon/Carbon composite strategies were tested, including structural modification, synthesis of core and yolk shell structures, and production of nanoparticles, nanowires, and nanorods. Si/C materials demonstrate improved outcomes with increased cycling stability, longer life, and the problem of low conductivity. Si/C composite such as carbon nanotubes (CNT), synthesis of nano porous spheres helps in aiding to compensate the structural change and easing diffusivity by shortening the path of Li-ion diffusion. Si/C materials are synthesized using a variety of methods, including high-energy ball milling, pyrolysis, chemical vapour deposition, etching, and mechanofusion. Materials like conductive carbon obtained from various sources are used to synthesize Si/C to mitigate the problem of low conductivity of Si. Carbon's strong conductivity aids in obtaining a high value of charging and discharging during operation; in fact, we have traditionally used graphite, one of the allotropes of carbon, as an anode. However, despite these advantages, the continual volume expansion of Si in the composite consumes Li-ions, resulting in a paucity of active Li-ions inside the battery unit.

Table 1: Some of the Si/C materials together with synthesis roots and performance.

Composition / Material	**Synthesis roots**	**Anode Performance**	**Reference**
Si/C core shell	pyrolysis	high reversible capacity 1328.8 $mAhg^{-1}$ and high retention (97%) after 30 cycles at J=50 mAg^{-1}	[5]

Si/C core shell	electrospinning	high capacity 1384 $mAhg^{-1}$ and retention of 97% after 300 cycles	[6]
Si/C	ball milling, mixing carbon black, graphite and carboxymethyl cellulose (CMC)	reversible capacity of 1000 $mAhg^{-1}$ after 1200 cycles in ratio Si:CB:graphite:CMC= 60:15:10:50	[7]
Si/C	magnetic stirring, freeze drying and calcination	specific capacity of around 792 $mAhg^{-1}$ after 100 cycles at J = 0.1 $mAhg^{-1}$	[8]
Si/C, Si and starch	mechanical stirring pyrolyzation and mortar pestle for grinding	reversible capacity of about 781 $mAhg^{-1}$ with 91.3% capacity retention after 50 cycles at J= 100 mAg^{-1}	[9]
SiNP, SiOx as sacrificial layer and polydopamine layer for carbonization	sol-gel and self-polymerization	reversible capacity of 2833 $mAhg^{-1}$ at C/10 with 88% retention after 500 cycles	[10]

Metal-Silicide Composites

Table 2: Various metal-silicide with synthesis roots and performance.

Composition / Material	**Synthesis roots**	**Anode Performance**	**Reference**
$Li_{21}Si_5$, Li and Si powder	Prelithiation melt solidification and ball milling	1007 $mAhg^{-1}$ delithiation capacity	[11]
Si-Mg, Si and Mg powder	ball milling	discharge capacity of discharge capacity of 830 $mAhg^{-1}$ over 5-650 mV against Li	[12]
Si-Al thin films	magnetron sputtering	Li_9AlSi_3dominant phase with specific capacity 650 $mAhg^{-1}$ post 100 cycles at C/20	[13]
Si-Sn, Si and Sn powder	mechanical milling	1400 $mAhg^{-1}$ as initial capacity with 78% retention after 50 cycles	[14]
Si-Cu, Si and Cu-Zn powder	ball milling	specific capacity of 608 $mAhg^{-1}$ with 66.8% retention after 200 cycles	[15]
Si, boron nanoparticle	plasma enhanced chemical vapour deposition (PECVD)	more than 80% capacity retention after 1000 cycles	[16]

Li-Si, Ca-Si, Mg-Si, Ti-Si, Co-Si, Fe-Si, Mn-Si, Ni-Si, Cr-Si, Cu-Si, Ag-Si, Al-Si, Sn-Si, Ge-Si, and other metal silicide composites have been produced as anodes for Li-ion batteries. The integration of Li-Si alloy as an anode is viewed as a pre-lithiation process for the active anode material. Table 2 shows some metal silicide materials. This approach aims to minimize the loss of active lithium within the battery unit, which occurs during various operational stages, including the creation of the solid electrolyte interface (SEI), expansion and irreparable reactions. Si's high band gap adds to its low conductivity, which ranges between 0.7 and 1.1 eV, and alloys with other metals with low band gaps could help to alleviate the problem of low conductivity.

Silicon Oxides (SiO_x)

Comprehensive research has been published on Si oxides to construct negative electrodes by looking at its improved theoretical capacity (1950 $mAhg^{-1}$) matching to SiO_2. These are the kinds of oxides that occur naturally and in abundance, influencing the market dynamics of energy storage. SiO_x outperforms pure Si as an electrode material in terms of volume expansion. However, a number of other difficulties with SiO_x prevent its commercial usage, including its insulating properties, limited electrical

conductivity, and low initial coulombic efficiency. Table 3 shows some SiO_x based anode material with synthesis roots and performance. Several approaches are being used to synthesize SiO_x such as hydrothermal, sol-gel, chemical vapour deposition and electrospinning.

Table 3: SiO_x materials with synthesis roots and their performance.

Composition / Material	**Synthesis roots**	**Anode Performance**	**Reference**
SiO_x/Si	high energy mechanical milling	reversible capacity of 1000 $mAhg^{-1}$ with high retentivity rate	[17]
SiO/C	mechanically grinding SiO and C material	discharge capacity of 700 $mAhg^{-1}$ post 100 cycles	[18]
SiO thin film	radio frequency sputtering	Discharge capacity of 416-465 $mAhg^{-1}$ for first 100 cycles	[19]
SiO_2/C mesoporous	sol-gel, carbon coating	specific capacity at of 441 $mAhg^{-1}$ at J=500 mAg^{-1} post 500 cycles	[20]
SiO_x/C	mechanofusion	higher discharge capacity and higher initial coulombic efficiency	[21]

Various Structural Modifications

So far, various structural changes have been made to Si-based anodes to achieve the desired outcomes. Various approaches for generating nanoparticles have been shown to improve results over cracks during volume expansion. Liu *et. al.* reported that lowering the size of the produced nanoparticle below 150 nm resulted in no cracks during lithiation [22]. Nanostructures, such as Si nanowire (SiNw), aid in improving Li-ion kinetics and the rate of Li-ion diffusion in batteries. Porous Si structure also shows good results with accommodating volume expansion and increasing Li-ion diffusivity [26]. Some of the various morphological Si-based anode materials given in table 4 [22, 23, 24, 25, 27]. Nano structures like nanorods help in diffusion of Li-ion in one particular direction, helps in decrease in loss of Li-ion throughout the process. The nano size of the produced Si particles aids in enclosing them inside carbon-coated structures such as the core and yolk shell, reducing the problem of volume turn up by accommodating expansion within the shell. Despite these nano structuring qualities, there is one more feature: the high surface area of nano-synthesised Si particles, which allows for a strong contact between the substrate and the active electrode material. However, this high surface area has significant drawbacks, such as increased electrolyte consumption for the construction of a solid electrolyte interface, which splits amid cycling, resulting in the loss of more Li-ion and the formation of bunches of structure of active electrode material.

Table 4: Some of various morphological Si-based anode materials with synthesis roots and performance.

Composition/ Material	**Synthesis roots**	**Anode Performance**	**Reference**
Si nanoparticles	Si NP powder	No cracks below 150 nm	[22]
SiNW	Vapour-liquid-solid (VLS)	gives coulombic efficiency of 73% and 93% on first and second charge/discharge cycle from 4277 $mAhg^{-1}$ and 3541 $mAhg^{-1}$	[23]
Hollow Si sphere/CNT	template method	improves stability over cycles	[24]
Hollow Si (interconnected)	template method	increased rate capability with 2725 $mAhg^{-1}$ initial discharge capacity	[25]

Challenges and Future Perspective

Despite the advantage of Si's abundance on earth, it is still not recommended for usage as anode in Li-ion batteries. Several approaches showed enhanced results such as synthesizing nano structures, Si/C composite, metal alloys, etc., they still lack in providing overall performance for commercial availability in the market. Si-based anodes are a strong contender for future Li-ion battery materials.

However, Si's low conductivity, high energy band gap, and large volume expansion limit its commercial application. Although tech companies like TESLA use Si in their batteries for cars, its weightage is roughly 5% with 95% graphite, indicating that we cannot totally rely on Si-based anode materials. Si/C composites offer improved outcomes in enhancing Li-ion kinetics and diffusivity while compensating volume change. However, there is a lack of stability at high charge rates and long-term cyclic stability. Alloying and de-alloying metal silicide-based anode materials possess the ability to store more Li-ions inside the material using pre-lithiation techniques, reducing Li loss during battery operation caused by the creation of a solid electrolyte interface and trapping inside the damaged structure of the active material. Li-Si has the most powerful Li-ion storage phase ever discovered, possessing a storage capacity that is 10 times the energy than graphite. The abundance of Si in its oxide may have a significant impact on market dynamics if available with structural stability as an anode material. Various structural morphologies of Si-based anode materials including nanotubes, nanoparticles and nanowire, aid in the transport and kinetics of Li-ion within the material and provide necessary size for decreasing crack development. The advantage of Si nano morphologies is their high surface area, which also puts limitation because this surface area causes high decay of electrolyte for creation of SEI leading to side reactions.

Conclusion

This review paper provides insight into the Si as anode material by examining its characteristics and composite with other materials. To meet the aims of green energy, we need unique materials that can store energy in less space and endure the growing demand for portable energy storage devices. The tenfold capability of Si motivates researchers to develop novel Si-based anode materials to provide stability during operations. Significant progress has been recorded throughout time for Si anodes, although problems remain. The research community also need to handle the challenging process of manufacturing Si-based anode materials. This work also describes the synthesis of several Si-based composite materials. Considering the overall picture of present research, new strategies are required to accelerate the research in the appropriate path.

Acknowledgement

Ashish Kumar Mishra, the first author, is grateful to DST-INSPIRE fellowship (IF200550) from the Department of Science and Technology, Ministry of Science and Technology, Government of India.

References

1. H. Okamoto, Journal of Phase Equilibria and Diffusion 30:118-119, 2009.
2. A K Mishra, Monika and B S Patial, Material Today Electronics 7: 100089, 2024.
3. R N Seefurth and R A Sharma, Journal of The Electrochemical Society 124 (8): 1207, 1977.
4. C. J. Wen and R. A. Huggins, Journal of Solid-State Chemistry 37 (3): 271-278, 1981.
5. Y Xu, G Yin, Y Ma, P Zuo and X Cheng, Journal of Material Chemistry 20 (16): 3216-3220, 2010.
6. T H Hwang, Y M Lee, B S Kong, J S Seo and J.W. Choi, Nano Letters 12 (2): 802-807, 2012.
7. H F Anderson, C E L Foss, J Voje, R Tronstad, T Mokkelbost, P E Vullum, A Ulvestad, M Kirkengen and J P Maehlen, Scientific Reports 9 (1): 14814, 2019.
8. H Ji, X Xu, X Li, K Li, L yuan, Z Han and K Tang. Ionics 30 (5):2585-2599, 2024.
9. J Wang, C Wang, Y Zhu, N Wu and W Tian, Ionics 21: 579-585, 2015.
10. N Liu, H Wu, M T McDowell, Y Yao, C Wang and Y Cui, Nano Letters 12 (6): 3315-3321, 2012.
11. S Iwamura, H Nishihara, Y Ono, H Morito, H Yamane, H Nara, T Osaka and T Kyotani, Scientific Reports 5 (1): 8085, 2015.
12. G Roberts, E Cairns and J Reimer, Journal of Power Sources 110 (2): 424-429, 2002.
13. M H Tahmasebi, D Kramer, H Gewein, T Zheng, K C Leung, B T W Lo, R Monig and S T Boles, Journal of Material Chemistry A 8 (9): 4877-4888, 2020.
14. J Wu, Z Zhu, H Zhang, H Fu, H Li, A Wang and H Zhang, Scientific Reports 6 (1):29356, 2016.
15. H Zeng, Y He and M Chamas, Frontier in Energy Research 10: 968259, 2022.
16. G F Pach, P R Adhikari, J Quinn, C Wang, A Singh, A Verma, A Colclasure, J H Kim, G Teeter and G M Veith, ACS Energy Letters 9 (6): 2492-2499, 2024.
17. Y Hwa, C M Park and H J Sohn, Journal of Power Sources 222: 129-134, 2013.
18. M Yamda, A Ueda, K Matsumoto and T Ohzuku, Journal of Electrochemical Society 158 94): A417, 2011.
19. Q Sun, B Zhang and Z W Fu, Applied Surface Science 254 (13): 3774-3779, 2008.
20. W An, J Fu, J Su, L Wang, X Peng, K Wu, Q Chen, Y Bi, B Gao and X Zhang, Journal of Power Sources 345: 227-236, 2017.
21. S J Kim, S J Ha, J U Lee, Y P Jeon and J Y Hong, C 9 (4): 114, 2023.
22. X H Liu, L Zhong, S Huang, S X Mao, T Zhu and J Y Huang, ACS Nano 6 (2): 1522-1531, 2012.
23. C K Chan, H Peng, G Liu, K McIlwrath, X F Zhang and R A Huggins, Nature nanotechnology 3 91): 31-35, 2008.
24. H Tang, Y Xu, L Liu, D Zhao, Z Zhang, Y Wu, Y

Zhang, X Liu and Z Wang, Coatings 12 (10): 1515, 2022.

25. Y. Yao, M T McDowell, I Ryu, H Wu, N Liu, L Hu, W D Nix and Y Cui, Nano Letters 11 (7): 2949-2954, 2011.
26. A K Mishra, Monika, B S Patial. Anode materials in lithium-ion batteries, AIP Conference Proceedings, 3145:030036-1-030036-4, 2024.
27. Monika, A K Mishra and B S Patial, Journal of Condensed Matter 1 (02): 65-68, 2023.

Sustainable Future of Solid-State Electrolytes: A Review

A H Bhaina[1,a], S S Talwatkar[2], A L Sunatkari[3]

[1] *Department of Physics, Government of Maharashtra's Ismail Yusuf College of Arts, Science and Commerce, Mumbai, India.*
[2] *Department of Physics, N. G. Acharya and D. K. Marathe College of Arts, Science and Commerce, Chembur, Mumbai, India.*
[3] *Department of Physics, Siddharth College of Arts Science and Commerce, Mumbai, India.*

[a] ashish.bhaina@gmail.com

Abstract

Sustainable solid-state electrolytes (SSEs) are becoming more widely acknowledged as an essential part of the development of next-generation energy storage systems, especially for integration of renewable energy sources and electric vehicle applications. SSEs provide improved performance, stability, and safety over traditional liquid electrolytes. But as the demand for green technologies increases, there is rising concern about the sustainability of these materials, both economically and environmentally. This paper examines the state of sustainable SSEs today, with a focus on the utilization of plentiful, recyclable, and ecologically friendly materials in polymer, ceramic, and composite electrolytes. It talks about trade-offs between material sustainability and electrochemical efficiency, as well as the difficulties in scaling these technologies while keeping high performance. Furthermore, the analysis highlights significant developments and trends that will probably influence the direction of sustainable SSEs in the future.

Keywords: Sustainable solid-state electrolytes (SSEs), next-generation energy storage, renewable energy integration, electric vehicles, eco-friendly materials, polymer electrolytes, ceramic electrolytes, composite electrolytes, material sustainability, electrochemical efficiency, scalability, green technologies.
Received 30 January 2025; First Review 05 February 2025; Accepted 21 February 2025

*** Address of correspondence**
Mr. A H Bhaina
Department of Physics, Government of Maharashtra's Ismail Yusuf College of Arts, Science and Commerce, Mumbai, India

Email: ashish.bhaina@gmail.com

How to cite this article
A H Bhaina, S S Talwatkar, A L Sunatkari, Sustainable Future of Solid-State Electrolytes: A Review, J. Cond. Matt. 2025; 03 (01): 7-9

Available from:
https://doi.org/10.61343/jcm.v3i01.116

Introduction

Because of their efficiency and safety in next-generation batteries, sustainable solid-state electrolyte (SSEs) development has drawn attention. According to Bhaina et al. (2023), Na^+ ion conductors are more affordable than lithium [1]. For improved conductivity, Chen et al. (2020) examined nanostructured composite electrolytes [2]. Sodium- and potassium-ion SSEs were investigated for sustainability by Dahbi et al. (2014) and Ellis et al. (2017) [3-4]. For energy-efficient production, Fair et al. (2024) introduced cold sintering [5], whereas Chellappan et al. (2023] emphasized 3D printing [6]. SSE integration was covered by Dunn et al. (2011) about renewable energy storage [7].

Current Sustainable Approaches

Sustainable Material Selection

Sustainable solid-state electrolytes (SSEs) use available, non-toxic minerals like sodium, potassium, and magnesium to lessen the environmental impact of energy storage devices [3,8].

Table 1: Comparison between Li, Na and K [9].

Property	Sodium (Na)	Potassium (K)	Lithium (Li)
Abundance	Highly abundant	abundant	Limited availability
Cost	Low-cost alternative	More affordable than lithium	Relatively expensive
Environmental Impact	Low environmental footprint	Eco-friendly and non-toxic	High impact from mining
Performance	Moderate energy density	Promising, comparable to lithium	High energy density
Applications	Grid storage, renewable systems	EVs, sustainable solutions	EVs, portable electronics

Compared to lithium-based systems, sodium-ion SSEs are a more affordable, accessible, and environmentally friendly option. Similar to this, potassium-ion SSEs take advantage of potassium's plentiful supply and environmentally beneficial qualities to offer a cost-effective and sustainable

energy storage solution for uses such as renewable energy systems and electric cars, with promising results and a smaller environmental impact [4,10-11].

Recycling and Lifecycle Management

The circular economy in energy storage technologies is promoted by recyclable battery designs that make use of closed-loop systems, which drastically cut waste, conserve resources, and lessen their negative effects on the environment [12]. To lessen reliance on fresh resources and improve manufacturing and recycling sustainability, researchers are creating techniques to recover solid electrolytes and electrode components from spent batteries. Furthermore, dangerous fluorine-based compounds are eliminated by using non-toxic alternatives in solid-state batteries, improving recycling efficiency and providing long-term, eco-friendly solutions for renewable energy systems and electric vehicles [9].

Energy-efficient Manufacturing Processes

Low-temperature synthesis methods are the main focus of efforts to improve sustainability in the manufacturing of solid-state electrolytes (SSEs) in order to lower energy consumption and facilitate wider usage in energy storage systems. A breakthrough in environmentally friendly battery production, cold sintering makes it possible to fabricate ceramic electrolytes at lower temperatures while maintaining performance and drastically reducing energy use [5]. Furthermore, SSEs are more feasible for next-generation energy storage systems since additive manufacturing, like 3D printing, reduces energy consumption and material waste while enhancing scalability and efficiency [6].

Safety and Longevity

By increasing battery longevity and lowering hazards, solid-state electrolytes (SSEs) provide a secure and sustainable energy storage option for electric cars and grid systems. They increase safety and dependability by preventing dendritic growth, which lowers the risk of fire and short circuits [13]. They are perfect for large-scale energy storage and electric car applications because of their exceptional thermal stability, which also guarantees dependable operation under demanding circumstances [14]. The longevity and safety of energy storage technologies are combined to improve their sustainability and effectiveness.

Integration with Renewable Energy Systems

Because of their high energy density and improved safety, solid-state electrolytes (SSEs) are essential for renewable energy systems that store intermittent solar and wind energy effectively [1]. Utilizing renewable energy, SSEs contribute to electrical system stabilization by facilitating grid-scale storage [7]. Decentralized energy storage is another benefit they provide, which promotes regional energy generation and lessens dependency on centralized power networks [15]. Through increasing the effective use of renewable resources in both localized and large-scale applications, this integration improves sustainable energy infrastructure and guarantees dependable energy access.

Conclusion

Solid-state electrolytes (SSEs) are essential for tackling environmental issues, promoting sustainable energy storage, and facilitating the integration of renewable energy sources. SSEs promise safer, more durable, and scalable solutions by emphasizing environmentally friendly materials, effective recycling, and creative production. Their acceptance will be fuelled by ongoing research and development, helping to shape a more sustainable and environmentally friendly energy future.

References

1. Bhaina, A. H., Sunatkari, A. L., & Talwatkar, S. S. (2023). Journal of Physics: Conference Series, 2426(1), 012042.
2. Chen, L., Hu, C., & Shen, Y. (2020). Current Opinion in Electrochemistry, 22, 51–57.
3. Dahbi, M., Komaba, S., Kubota, K., & Yabuuchi, N. (2014). Chemical Reviews, 114(23), 11636–11682.
4. Ellis, B. L., et al. (2017). Nature Chemistry, 9(5), 513–517.
5. Fair, R. A., et al. (2024). ChemSusChem, 17, e202301920.
6. Chellappan, V., et al. (2023). Advanced Materials Technologies, 8(10), 2201832.
7. Dunn, B., Kamath, H., & Tarascon, J.-M. (2011). Science, 334(6058), 928–935.
8. Gan, X., Yan, Y., Zhang, H., and Zhou, J. (2024). *A sustainable dual cross-linked cellulose hydrogel electrolyte for high-performance zinc-metal batteries*. Nano-Micro Letters, 16, 106.
9. Balasubramanian, R., Biswal, B. K., Tran, P. T. M., Zhang, B., and Zhang, J. (2024). *Recycling of spent lithium-ion batteries for a sustainable future: Recent advancements*. Chemical Society Reviews, 53(2), 23.
10. Pramudita, J. C., et al. (2017). *Sodium-Ion Batteries: Toward Practical Applications*. Chemical Reviews, 117(19), 11372–11400.
11. Ma, Q., & Tietz, F. (2020). *Solid-State Electrolyte Materials for Sodium Batteries: Towards Practical Applications*. ChemElectroChem, 7(13), 2693–2713.
12. Gaines, L. (2018). *Lithium-ion battery recycling processes and current progress*. Journal of Materials Chemistry A, 6(37), 17722–17740.

13. Lai, M. O., Lu, L., Kotobuki, M., Song, S., Zheng, F. (2018). *Review on solid electrolytes for all-solid-state lithium-ion batteries*, Journal of Power Sources, 389, 198–213.
14. Carney, T. J., Cui, Y., Liu, W., Yang, Y., and Zheng, G. (2020). *Solid-state electrolytes for long-life lithium metal batteries*, Nature Nanotechnology, 15(6), 469–476.
15. Larcher, D., & Tarascon, J.-M. (2015). *Towards greener and more sustainable batteries for electrical energy storage*, Nature Chemistry, 7(1), 19–29.

Algae-derived Biomolecules: A Versatile Resource and Sustainable Solutions for India's Future

Abhilasha Choudhary

[1] *Department of Botany, SBRM Government College Nagaur, Rajasthan, India.*

[a] abhishiv25@gmail.com

Abstract

Over the past decade, algae have emerged as pivotal organisms, increasingly acknowledged for their profound ecological contributions and cutting-edge technological applications, particularly in the development of eco-friendly biomolecules. India's tropical climate and abundant sunlight create ideal conditions for large-scale algae cultivation, with oceans rich in microalgae, diatoms, and dinoflagellates. Of the 30,000 to 40,000 species, only a few are commercially utilized, but more can be explored for environmental, energy, and food security benefits. This review investigates algae-derived natural, carbon neutral biomolecules production and highlighting its scope and challenged in India It also outlines how algae can drive sustainability across sectors such as bio plastics, biofuels, food, cosmetics, and pharmaceuticals, along with emerging trends in the fashion industry like bio beads and bio leather. By lowering costs and reducing carbon emissions in algal biorefineries, these strategies contribute to a sustainable future. However, obstacles such as the energy-intensive production process and the need for optimized biorefinery pathways impede large-scale commercialization. Moreover, India's algae products market faces challenges, including low consumer awareness, difficulties in ensuring sustainable sourcing, and strict regulatory standards. Competition from conventional products, coupled with the need for continuous innovation to improve taste and versatility, further complicates market expansion.

Keywords: Algae-based biomolecules, Biofuels, Bioplastics, Environmental sustainability.
Received 29 January 2025; First Review 11 February 2025; Accepted 26 February 2025

*** Address of correspondence**
Abhilasha Choudhary
Department of Botany, SBRM Government College Nagaur, Rajasthan, India.

Email: abhishiv25@gmail.com

How to cite this article
Abhilasha Choudhary, Algae-derived Biomolecules; A Versatile Resource and Sustainable Solutions for India's Future, J. Cond. Matt. 2025; 03 (01): 10-15

Available from:
https://doi.org/10.61343/jcm.v3i01.91

Introduction

A sustainable innovation wave is breaking over algae, a universal and photosynthetic organism that produces a plethora of valuable biomolecules with diverse applications in modern industries. From completely freshwater to marine habitats, a wide variety of algae exist. Large forms of algae like seaweed are found in various tropical and temperate coastal environments. Small forms of algae like the microalgae used for biofuels can thrive in many different freshwater and saltwater environments. The scientists' evaluations indicate that algae hold great promise for producing biofuels [1]. Indeed, if they thrive under ideal conditions (abundant sunlight, heat, and abundant nutrients), they can double their biomass in a short duration. The proteins present in unicellular algae *Chlorella* and *Spirulina,* though not as biofuel-friendly, could help support food supply and address malnutrition [2].

In food, pharmaceuticals, and cosmetics, polysaccharides such as agar, carrageenan, and alginate-made mostly from macroalgae-serve as thickeners, stabilizers, and gelling agents, reflecting the true potential of algae as a driver for sustainable advancement and a bioeconomy [3]. Additionally, algal biomass can be used to produce animal feed, reducing reliance on conventional fodder like soybeans, often linked to resource depletion and deforestation [4].

Algae also play a significant role in environmental remediation, such as wastewater treatment, utilizing nitrogen, phosphorus, and heavy metals as nutrients while simultaneously reducing pollutants and producing biomass for further applications [5]. Algae also contribute to carbon sequestration, with their ability to absorb large amounts of CO_2 during photosynthesis, making them a viable tool in mitigating climate change [6].

Recent Trends in Algal-Based Biomolecules

1. Algal Biofuels

Recent trends in algal-based biomolecules highlight their potential in biodiesel manufacturing through high lipid

content, quick growth, and low land requirements. Studies have focused on developing lipid yield and increasing overall production efficiency through species selection (Table-I). Extensive research has been conducted on the lipid accumulation capacity of strains such as Chlorella sp., *Nannochloropsis* sp., *Scenedesmus* sp., and *Botryococcus braunii* [7]. Brazilian researchers have proven the viability of biodiesel production utilizing microalgae in open-pond systems, emphasizing its scalability. Genetic engineering advancements like CRISPR-Cas9 and metabolic engineering have allowed scientists to target critical enzymes in lipid production. biosynthesis pathway, such as acetyl-CoA carboxylase (ACC) and malic enzyme (ME), to increase lipid production [8-9]. Cultivation Optimization in which nutrient starvation (e.g., nitrogen or phosphate deficiency), high-light intensity cultivation, and two-stage systems have been used to increase lipid productivity [10-11]. Bioreactor Technology Advancements such as photo bioreactor designs, and tubular and flat-panel systems, have improved light utilization and scalability, lowering production costs [12-13].

Table 1: Algal Biofuels

Component	Biofuel Application	Co-Products
Lipids	Biodiesel (FAME production)	Lubricants, green solvents
Carbohydrates	Bioethanol, biogas	Bio-packaging, feedstock
Proteins	Residual biomass use	Animal feed, fertilizers
Pigments	-	Antioxidants, cosmetics

2. Algal Proteins and Nutraceuticals

Microalgae such as *Spirulina* and *Chlorella* are rich in essential amino acids, making them a complete protein source as cultivation requires minimal resources compared to conventional agriculture, making them particularly suitable for resource-scarce regions [14-15].furthermore these algae are integral to the production of functional foods and dietary supplements that support general health but also exhibit therapeutic benefits, enhanced immunity and reduced oxidative stress, addressing the demand for plant-based, nutrient-dense alternatives [16-17].In terms of personalized nutrition, the extensive biochemical diversity of microalgae enables the formulation of products that optimize health outcomes through targeted nutritional interventions [18].

3. Algal Polysaccharides

Algae-derived **hydrocolloids** like agar, carrageenan, and alginate are widely utilized in food, cosmetics, and pharmaceuticals for their gelling, stabilizing, thickening, and emulsifying properties, as well as in advanced applications like wound dressings and controlled-release drug formulations [19-20]. Bioactive polysaccharides from algae demonstrate immense potential in drug delivery systems due to their hydrogel-forming ability and immunomodulatory effects, making them ideal for functional foods and targeted therapeutics [21-22]. Algae-derived natural colorants such as chlorophyll, phycocyanin, and carotenoids are emerging as eco-friendly alternatives to synthetic dyes in food, textiles, and cosmetics, valued for their antioxidant, skin-health, and vision-support benefits [23-24]. Pharmaceutical applications of algae bioactive compounds include anti-inflammatory, anti-cancer, and antimicrobial effects, with chlorophyll derivatives, carotenoids, and phycocyanin demonstrating promise in drug development [25-26]. In India, algae-derived bioplastics, particularly from seaweed, are gaining momentum as sustainable alternatives to conventional plastics, with companies like Zerocircle using seaweed's regenerative and low-carbon properties to produce biodegradable materials, reducing plastic waste by up to 3,000 tons annually while supporting coastal economies in Tamil Nadu and Gujarat [27-28].

Table II: Algal Polysaccharides

Category	Component	Biochemical Component
Hydrocolloids	Agar	Polysaccharides
	Carrageenan	Polysaccharides
	Alginate	Polysaccharides
Bioactive Polysaccharides	Bioactive polysaccharides	Polysaccharides
Pigments	Chlorophyll	Pigments (chlorophyll)
	Phycocyanin	Pigments (phycobiliproteins)
	Carotenoids	Pigments (carotenoids)
Bioactive Compounds	Chlorophyll derivatives	Pigments (chlorophyll derivatives)
	Fucoxanthin	Pigments (carotenoids)
	Phycocyanin	Proteins

The Indian market for bioplastics is expanding due to government policies banning single-use plastics and promoting compostable alternatives. Despite these advancements, the sector faces challenges like reliance on imported raw materials, such as PLA and PHA. Boosting domestic production could further drive the adoption of bioplastics and strengthen the market's potential [29].

4. Environmental Applications

Wastewater Treatment

In India, algae-based wastewater treatment systems are growing more well-known for their capacity to support sustainability while effectively eliminating chemicals like nitrogen, phosphorus, and heavy metals. By effectively absorbing extra nutrients and breaking down organic contaminants, microalgae help keep water bodies from becoming eutrophic. These systems further improve their economic feasibility and environmental benefits by producing valuable by-products such as fertilizers and biofuels [30]. Research at IIT Hyderabad is driving this field's progress in India. The creation of economical bacterial-algal symbiotic systems for decentralized wastewater treatment is one of the projects. These systems concentrate on the removal of nutrients, the breakdown of organic carbon, and the removal of micropollutants. Pilot projects in gated communities have shown encouraging outcomes in terms of sustainability and usefulness. Furthermore, scaling these technologies for broader adoption is the goal of partnerships with foreign universities [31-32].

Carbon Sequestration

Algae are effective carbon sinks, which help to mitigate climate change. Large volumes of CO_2 are stored by microalgae during photosynthesis, which allows them to transform it into biomass at a rate that is far faster than that of terrestrial plants [33]. Industrial exhaust systems can be combined with algae to absorb carbon emissions and lower greenhouse gas emissions. A circular economy strategy can also be supported by using the biomass produced during this process to produce biofuel. Algae are a promising treatment for global warming due to their effectiveness and scalability in sequestering carbon [34].

Key Advancements in Algal Biotechnology

1. Genetic and Metabolic Engineering

Enhanced production of targeted biomolecules through CRISPR and synthetic biology

Algal biotechnology is being revolutionized in India by developments in synthetic biology and CRISPR-Cas9, which allow for precise genome editing improving the production of high-value chemicals, medicines, and biofuels. Research centres like the National Agri-Food Biotechnology Institute (NABI) and Jaypee University of Information Technology, together with businesses notably Reliance Industries, are spearheading initiatives to advance metabolic engineering methods for algae. These strategies, backed by government programs like the National Biopharma Mission and BIRAC incubators supporting entrepreneurs in genetic engineering and synthetic biology, involve creating artificial pathways to increase the output of molecules of commercial significance. These developments are in-line with India's emphasis on resource efficiency and sustainability, which are essential for tackling its environmental and economic issues [35].

Strain improvement for higher resilience and productivity

Strain improvement strategies, such as adaptive evolution and mutagenesis, are proving effective in enhancing algal species' resilience to environmental stressors, including temperature and salinity variations. In India, researchers are exploring these approaches to boost lipid accumulation and photosynthetic efficiency, critical for biofuel production and industrial applications. For example, the combination of adaptive laboratory evolution and mutagenesis has been employed to develop strains capable of thriving in fluctuating water conditions, often associated with industrial effluents, while maximizing lipid yields. These strategies are being paired with advanced genetic engineering to refine metabolic pathways and improve overall productivity, aligning with India's push for sustainable biofuel solutions [36-37].

2. Bioreactor Innovations

The focus of recent developments in algae cultivation methods is on expandable and economically viable solutions. Flat-panel and tubular photobioreactor designs have been adjusted to increase light penetration and nutrient consumption, which lowers operating costs and increases the efficiency of biomass production [38]. At the same time, open pond systems are being adapted for areas with lots of sunlight, such as India, where advancements in species selection, water circulation, and paddlewheel design have made large-scale production practical and profitable for uses like feedstock and biofuels [39]. These advancements are essential to overcome financial obstacles and move algae farming to industrial scales.

3. Integration with Circular Economy

By generating a single algal feedstock into several high-value products, including food additives, biofuels, and bioplastics, algae biorefineries reduce waste and improve resource efficiency-perfect examples of the circular economy [40]. Incorporating industrial waste streams, such as wastewater and CO_2 emissions, into algae culture systems is an important breakthrough in this field. In line with sustainable and environmentally friendly industrial practices, these waste products reduce pollutants and greenhouse gas emissions while providing algae with an affordable growing medium [41]. Algae's dual function in

environmental restoration and resource efficiency highlights its potential as a pillar of sustainable development.

4. Digital Technologies in Algal Research

Algal research is undergoing a revolution driven by artificial intelligence (AI) and machine learning, which make predictive modelling possible for metabolic engineering, strain selection, and cultivation optimization. By decreasing the need for trial-and-error methods, these technologies boost output and quicken the development of algae bioengineering [42]. Additionally, by guaranteeing traceability, transparency, and quality assurance, blockchain technology is revolutionizing the supply chains for algae products. Blockchain promotes consumer trust and regulatory compliance by documenting each stage of manufacturing and distribution, especially in delicate industries like drugs and nutraceuticals [43].

Opportunities for Algal-Based Biomolecules in India

Considering its abundance of natural resources, pro-biotechnology regulations, expanding biotech sector, and prospects in the international export market, India holds great promise for the advancement of algae biotechnology. Regions like Gujarat, Tamil Nadu, and Andhra Pradesh are perfect for large-scale algae production in open ponds and high-value niche applications like nutraceuticals because of their vast freshwater systems and more than 7,500 kilometres of coastline [44]. Funding and collaborations for sustainable algae projects are provided by government programs such as the National Biotechnology Development Strategy and Mission Innovation, and the industry is further supported by subsidies for aquaculture and renewable energy [45].

India is well-positioned to export high-value algae products like spirulina supplements, carotenoids, and bioactive compounds, leveraging cost advantages to meet rising international demand for bio-based products [46]. The expanding biotech ecosystem, supported by programs like Biotechnology Ignition Grant (BIG) and BioNEST, encourages innovation and entrepreneurship, with startups investigating algae-based solutions like biofuels, bioplastics, and functional foods [47].

Conclusion

Algal-based biomolecules offer transformative potential for addressing India's critical challenges in sustainable energy, environmental conservation, and public health. These renewable resources align with national goals by reducing dependence on fossil fuels, mitigating pollution, and improving health outcomes through nutraceuticals. Algae-derived bioplastics and biofuels are revolutionizing sustainable manufacturing and energy solutions. Furthermore, innovative applications in the fashion industry, such as biobeads for sustainable jewellery and bioleather as an alternative to animal leather, highlight algae's potential in reducing environmental impact [48-49]. However, the widespread adoption of algal biotechnology necessitates strategic investments in R&D to tackle challenges such as hybrid cultivation system optimization, automation, and cost reduction. Innovations in these areas can enhance scalability and make algal solutions commercially viable.

Government support through subsidies, tax incentives, and streamlined regulations is pivotal to driving private investment and building an enabling ecosystem. Public awareness campaigns emphasizing the ecological and health benefits of algae-based products can encourage consumer adoption, while partnerships among industries, academia, and global initiatives can accelerate progress through shared knowledge and innovation. By embracing algal biotechnology, India could achieve its sustainability goals and emerge as a global leader in the bioeconomy, combining economic opportunities with ecological stewardship and technological advancements. This vision underscores algae's role as a catalyst for a sustainable future.

References

1. Y. Chisti, *"Biodiesel from microalgae",* Biotechnology Advances, vol. 25, no. 3, pp. 294–306, 2007.
2. E. W. Becker, *"Micro-algae as a source of protein",* Biotechnology Advances, vol. 25, no. 2, pp. 207–210, 2007.
3. M. Rizwan, G. Mujtaba, S. A. Memon, K. Lee, N. Rashid, and M. Aziz, *"Exploring the potential of microalgae for new biotechnology applications and beyond: A review"*, Renewable and Sustainable Energy Reviews, vol. 92, pp. 394–404, 2018.
4. L. Gouveia, A. P. Batista, A. Miranda, J. Empis, and A. Raymundo, *"Chlorella vulgaris biomass used as coloring source in traditional butter cookies"*, Innovative Food Science & Emerging Technologies, vol. 8, no. 3, pp. 433–436, 2008.
5. J. K. Pittman, A. P. Dean, and O. Osundeko, *"The potential of sustainable algal biofuel production using wastewater resources"*, Bioresource Technology, vol. 102, no. 1, pp. 17–25, 2011.
6. J. Singh and S. I. Olsen, *"A critical review of life cycle assessment of microalgae-based biofuels"*, Bioresource Technology, vol. 102, no. 1, pp. 10–

19, 2011.
7. K. W. Chew, S. R. Chia, H. W. Yen, S. Nomanbhay, Y. C. Ho, and P. L. Show, *"Algae utilization and circular economy for environmental sustainability",* Biotechnology Advances, vol. 35, no. 7, pp. 1196–1205, 2017.
8. S. K. Ratha and R. Prasanna, *"Bioprospecting microalgae as potential sources of 'green energy'—Challenges and perspectives"*, Applied Biochemistry and Biotechnology, vol. 167, no. 6, pp. 1317–1331, 2012.
9. Z. Gu, Y. Liu, S. Yang, and Y. Zhang, *"Advances in metabolic engineering of microalgae to improve lipid accumulation"*, Frontiers in Bioengineering and Biotechnology, vol. 9, p. 749468, 2021.
10. S. H. Ho, W. M. Chen, and J. S. Chang, *"Scenedesmus obliquus CNW-N as a potential candidate for CO_2 mitigation and biodiesel production",* Bioresource Technology, vol. 113, pp. 22–29, 2012.
11. I. Rawat, R. R. Kumar, T. Mutanda, and F. Bux, *"Biodiesel from microalgae: A critical evaluation from laboratory to large-scale production"*, Applied Energy, vol. 103, pp. 444–467, 2013.
12. M. K. Lam and K. T. Lee, *"Microalgae biofuels: A critical review of issues, problems, and the way forward"*, Biotechnology Advances, vol. 30, no. 3, pp. 673–690, 2012.
13. S. Singh and D. W. Dhar, *"Overview of carbon capture technology using algae",* Journal of Industrial Microbiology & Biotechnology, vol. 46, no. 9–10, pp. 1263–1281, 2019.
14. E. W. Becker, *"Microalgae for human and animal nutrition"*, in Handbook of Microalgal Culture: Applied Phycology and Biotechnology, 2013, pp. 461–503.
15. M. Henriques and A. Barros, *"Microalgae: Nutritional properties and benefits for health and wellness"*, Critical Reviews in Food Science and Nutrition, vol. 60, no. 19, pp. 1–13, 2020.
16. G. Gutiérrez-Salmeán, L. Fabila-Castillo, and G. Chamorro-Cevallos, *"Nutritional and toxicological aspects of Spirulina (Arthrospira)"*, Nutrients, vol. 7, no. 4, pp. 3246–3265, 2015.
17. M. L. Wells et al., *"Algae as nutritional and functional food sources: Revisiting our understanding"*, Trends in Plant Science, vol. 22, no. 8, pp. 676–694, 2017.
18. T. Lafarga, *"Cultured microalgae and compounds derived thereof for food applications: Strain selection and cultivation, drying, and processing strategies"*, Food Reviews International, vol. 35, no. 7, pp. 1–18, 2019.
19. K. I. Draget, *"Alginates"*, in Handbook of Hydrocolloids, Woodhead Publishing, 2020, pp. 67–89.
20. C. Ramos, D. Ribeiro, and E. Pinto, *"Advances in the applications of alginate-based hydrogels in tissue engineering"*, International Journal of Biological Macromolecules, vol. 166, pp. 372–378, 2021.
21. G. Jiao, G. Yu, J. Zhang, and H. S. Ewart, *"Chemical structures and bioactivities of sulfated polysaccharides from marine algae"*, Marine Drugs, vol. 9, no. 2, pp. 196–223, 2011.
22. Z. Zhang, F. Wang, W. Wang, and J. Liang, *"Advances in bioactive marine algal polysaccharides"*, Critical Reviews in Food Science and Nutrition, vol. 60, no. 10, pp. 1857–1871, 2020.
23. J. A. del Campo, M. García-González, and M. G. Guerrero, *"Outdoor cultivation of microalgae for carotenoid production: Current state and perspectives",* Applied Microbiology and Biotechnology, vol. 74, no. 6, pp. 1163–1174, 2007.
24. A. Ranga Rao, R. Raghunath Reddy, and V. Baskaran, *"Impact of dietary carotenoids on human health—Biochemical aspects"*, Critical Reviews in Food Science and Nutrition, vol. 54, no. 12, pp. 1463–1475, 2014.
25. A. R. Ganesan, S. Ramalingam, and B. Sivasankari, *"Algal polysaccharides: An emerging therapeutic agent for biomedical applications"*, Carbohydrate Polymers, vol. 207, pp. 459–470, 2019.
26. M. Kuddus, P. Singh, G. Thomas, and A. Al-Hazimi, *"Recent developments in production and biotechnological applications of c-phycocyanin"*, BioMed Research International, vol. 2013, p. 742859, 2013.
27. The Better India, *"Indian startup is using seaweed to create bioplastics"*, 2023.
28. The Economic Times, *"Seaweed-based bioplastics: The sustainable alternative for India",* 2023.
29. Packaging 360, *"This startup is developing a low-cost, compostable alternative to single-use plastic",* https://packaging360.in.
30. L. T. Arashiro, I. Ferrer, D. P. L. Rousseau, and E. D. Van Hullebusch, *"The effect of operational parameters on microalgae-based wastewater treatment systems: A review"*, Critical Reviews in Environmental Science and Technology, vol. 50, no. 1, pp. 1–40, 2020.
31. IIT Hyderabad, *"Algal-bacterial wastewater treatment systems for nutrient removal and biofuel production: Progress and perspectives"*, [Online]. Available: IIT Hyderabad Official Portal, 2019.
32. ISTI Portal, *"IIT Hyderabad research on algal*

symbiotic systems for wastewater treatment", [Online]. Available: ISTI Portal, 2019.
33. M. A. Borowitzka, *"Algae for biofuels and energy"*, Developments in Applied Phycology, vol. 5, pp. 1–12, 2013.
34. K. Kumar, D. Ghosh, and A. Mukherjee, *"Microalgae as potential carbon sinks: Challenges and future directions"*, Journal of Cleaner Production, vol. 276, p. 124108, 2020.
35. SYNBIOBETA, *"Advances in synthetic biology for algae biotechnology: CRISPR and metabolic engineering applications"*, 2024.
36. R. Kumar Singh, R. Pandey, P. K. Gupta, and R. K. Jha, *"Adaptive laboratory evolution and mutagenesis in algal strain improvement: A review"*, Journal of Applied Phycology, vol. 33, no. 3, pp. 1583–1601, 2021.
37. N. Arora and G. P. Philippidis, *"Advances in adaptive evolution and mutagenesis for the development of robust microalgal strains"*, Frontiers in Plant Science, vol. 12, p. 789654, 2021.
38. C. U. Ugwu, H. Aoyagi, and H. Uchiyama, *"Photobioreactors for mass cultivation of algae"*, Bioresource Technology, vol. 99, no. 10, pp. 4021–4028, 2008.
39. J. Singh and A. Sharma, *"Development of suitable photobioreactor for algae production -A review"*, Renewable and Sustainable Energy Reviews, vol. 16, no. 4, pp. 2347–2353, 2012.
40. K. W. Chew et al., *"Microalgae biorefinery: High-value products perspectives"*, Bioresource Technology, vol. 229, pp. 53–62, 2017.
41. I. Rawat, R. R. Kumar, T. Mutanda, and F. Bux, *"Dual role of microalgae: Phycoremediation of domestic wastewater and biomass production for sustainable biofuels production"*, Applied Energy, vol. 88, no. 10, pp. 3411–3424, 2011.
42. R. Kumar, S. Bera, and S. Basu, *"AI-driven technologies in algal research: A comprehensive review"*, AI in Life Sciences, vol. 1, no. 2, pp. 45–60, 2022.
43. H. Hassani, E. S. Silva, and S. Unger, *"Digital technologies in algae supply chain: Blockchain and AI applications"*, Marine Drugs, vol. 18, no. 6, p. 312, 2020.
44. A. Rao, K. Patel, and R. Sharma, *"Algae cultivation and its potential in India: Opportunities and challenges"*, Journal of Sustainable Development Studies, vol. 12, no. 3, pp. 45–60, 2020.
45. Department of Biotechnology, National Biotechnology Development Strategy 2020–2030: Fostering innovation and sustainability, Government of India, 2020. [Online]. Available: https://dbtindia.gov.in.
46. V. Patil, A. Rehman, and A. Singh, *"Microalgae cultivation for value-added products: Opportunities and challenges in India"*, Journal of Environmental Management, vol. 223, pp. 425–435, 2018.
47. N. Narayanan, P. Singh, and N. Kaushik, *"Emerging trends in Indian biotechnology startups: A focus on algal bioproducts"*, Journal of Bioinnovation, vol. 15, no. 3, pp. 112–120, 2021.
48. P. Ganesan, M. Kumaravel, and S. Kalimuthu, *"Algae-derived materials in sustainable fashion: Bioleather and biobeads as eco-friendly alternatives"*, International Journal of Environmental Design, vol. 7, no. 1, pp. 34–42, 2019.
49. A. Ranga Rao, R. Sarada, and G. A. Ravishankar, *"Applications of algae-derived biopolymers in innovative industries"*, Marine Drugs, vol. 12, no. 4, pp. 2876–2892, 2014.

Negative Local Partial Density of States

Kanchan Meena[1,a], Souvik Ghosh[2,b], P Singha Deo[1,c]

[1] Department of Physics of Complex Systems, S. N. Bose National Centre for Basic Sciences, Kolkata, West Bengal, India.
[2] Department of Physics, Adamas University, Kolkata, West Bengal, India.

[a] 1996.kanchanmeena@gmail.com
[b] souvikghosh2012@gmail.com
[c] singhadeoprosenjit@gmail.com

Abstract

Real quantum systems can exhibit a local object called local partial density of states (LPDOS) that cannot be proved within the axiomatic approach of quantum mechanics. We demonstrate that real mesoscopic system that can exhibit Fano resonances will show this object and also very counterintuitively it can become negative, resulting in the enhancement of coherent currents.

Keywords: Mesoscopic systems, Coherent electrons, Hierarchy of density of states.
Received 30 January 2025; First Review 13 February 2025; Accepted 07 March 2025

*** Address of correspondence**
Kanchan Meena
Department of Physics of Complex Systems, S. N. Bose National Centre for Basic Sciences, Kolkata, West Bengal, India.

Email: 1996.kanchanmeena@gmail.com

How to cite this article
Kanchan Meena, Souvik Ghosh, P Singha Deo, Negative Local Partial Density of States, J. Cond. Matt. 2025; 03 (01): 16-21

Available from:
https://doi.org/10.61343/jcm.v3i01.113

Introduction

In recent times the subject of mesoscopic physics has attracted a lot of attention as it gives us an experimental route to probe some of the most fundamental problems in physics. As the name suggests, it is the regime that is in between the classical and quantum regimes. One such problem is that of defining a signal propagation time in quantum mechanics. This problem has been recently solved at theoretically making it completely consistent with the theory of relativity [1-5]. The puzzling feature that one has to accept as a result is that a signal can be also sent back in time, to the past. While this is counter-intuitive, a very convincing demonstration of it can be given and is presented in this work. If the signal propagation time between two points be divided by $\hbar$ then it gives the partial density of states (PDOS) which is a measure of the states through which the particle propagates between the two points. This can be shown from propagation of wave-packets in time [1, 3]. Therefore, if the PDOS become negative then the signal propagation time also becomes negative. We will demonstrate this quantity can be negative in this work which too is equally counterintuitive but consistent with all the theories of physics.

The System

For the purpose of this demonstration, we consider the three-probe set up as described below with respect to Fig. 1. The mesoscopic sample is the shaded region which is typically made of semi-conductor or metal, through which a current is passed. The leads γ or α are current leads that may be made up of the same material. Lead β is an STM tip that can attach to different points in the sample and is such that we can vary its proximity to the sample. The STM tip can thus be set up in many different ways but we will focus on one particular case. That is when the STM tip is weakly coupled to the sample at a point r through a tunnelling barrier.

Let chemical potential of left reservoir connected to lead γ be μ_γ, chemical potential of right reservoir connected to lead α is $\mu_\alpha = 0$, and the other end of the the lead β is also earthed. For incident energy E such that $0 = \mu_\alpha < E < \mu_\gamma$, only lead γ injects a current according to our classical notions. For a mesoscopic sample, this defines a quantum mechanical scattering problem. Such a set up can be obtained in the laboratory and we want to address the coherent current flowing from γ to α. It was shown [6] that in such a situation

$$\left|S'_{\alpha\gamma}\right|^2 - \left|S_{\alpha\gamma}\right|^2 = -4\pi^2|t|^2\vartheta_\beta\rho_{lpd}(E,\alpha,r,\gamma) \quad (1)$$

where

$$\rho_{lpd}(E,\alpha,r,\gamma) = \frac{-1}{2\pi}\left|S'_{\alpha\gamma}\right|^2\frac{\delta\theta_{S'\alpha\gamma}}{\delta U(r)} \quad (2)$$

is known as the local partial density of states (LPDOS), where $U(r)$ is the electrostatic potential at the point r,

$$\theta_{S'_{\alpha\gamma}} = arctan\left[\frac{\Im[S'_{\alpha\gamma}]}{\Re[S'_{\alpha\gamma}]}\right] \qquad (3)$$

and $\frac{\delta\theta_{S'\alpha\gamma}}{\delta U(r)}$ is a functional derivative. The parameter t controles coupling of states of the sample with the states at the STM tip for which ν_β is the relevant density of states (DOS). For a commercially available STM tip t and ν_β are either specified by the manufacturer or to be ingeniously determined by the user. Thus, $S'_{\alpha\gamma}$ is the scattering matrix element for scattering from γ to α. When the STM tip is removed by $t \to 0$ then this scattering amplitude will be $S'_{\alpha\gamma} = S_{\alpha\gamma}$. Coherent currents are given by $\frac{e_0}{h}\left|S'_{\alpha\gamma}\right|^2$ and $\frac{e_0}{h}\left|S_{\alpha\gamma}\right|^2$.

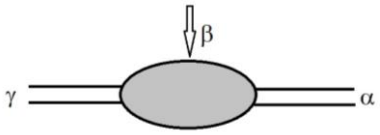

Figure 1: Here we show a simpler version of Fig. 3.2 as now there are only two fixed leads indexed γ and α apart from the STM tip β. This is a cartoon of a realistic experimental set up that help us measure some of the lower members in the hierarchy of DOS.

In earlier works, Eq. (1) could be justified in the semi-classical regime only which limits its value and applicability. The quantum regime remained unclear specially because in the quantum regime ρ_{lpd}, as calculated from Eq. (3), can become negative. We have taken the view that ρ_{lpd} is a fundamental object that cannot be found within the axiomatic framework of quantum mechanics and in this work, we will show that it can be found in nature, in the so-called mesoscopic systems, in the quantum regime. Moreover, in the quantum regime of 1D, 2D and 3D, ρ_{lpd} cannot be negative and its negativity is a speciality of the mesoscopic regime. Intuitively speaking, ρ_{lpd} is positive and the RHS is negative accounting for loss of coherent electrons to the earthed lead β. Therefore, any change of sign in ρ_{lpd} will result in a gain of coherent current due to the earthed STM tip. That can be regarded as supporting evidence for time travel because any intervention on a quantum state at an intermediate point, by an STM tip is supposed to only decohere the state. We will clarify as to why and when this can happen in real systems. Since LHS of Eq. (1) can be measured in the laboratory and so if the equality in Eq. (1) can be established then one can affirm that RHS is an objective reality that can be found in nature, although we cannot make sense of it within the axiomatic framework of quantum mechanics. The object ρ_{lpd} cannot be defined within the axiomatic framework of quantum mechanics because it is refering to only those electrons that are coming from γ and going to α. The wave-function of an electron at a point r can only be sensitive to either γor α. But the object can be defined for a mesoscopic system using the idea of a physical clock. The idea of a physical clock as envisaged by Landauer and Buttiker [7] uses the idea that the spin of an electron can be thought of as a classical magnetic dipole and if it is subject to a classical force will presess like a classical dipole in a magnetic field. The classical force can be obtained from a potential of the form $\vec{\mu} \cdot B(\vec{r})$ rather than $\vec{\mu} \cdot \vec{B}(\hat{r})$ which essentially means the dot product is not the inner product of quantum mechanics but the usual dot product for a classical precession. The magnetic moment $\vec{\mu}$ is however taken to be quantized in units of $\frac{\hbar}{2}$. For a vanishingly small magnetic field, the expectation value of angular displacement can be calculated in a spinor space using the analyticity of scattering matrix elements. The angular displacement divided by the classical Larmor frequency of a dipole of strength $\frac{\hbar}{2}$ then defines a time for which a detailed derivation can be found in [5]. The equation of motion for the electron, that is the Schrodinger equation, is not used therefore, but only the analyticity of the spinor space is used. Thus, there is no direct way to verify this object from the wave-function but if it is averaged over all coordinates of the sample (that is averaged over $r$and appropriate outgoing channels α then one arrives at an object called injectance of lead γ which is completely in agreement with what one can calculate from the wave-function. There remains the doubt whether the non-averaged object as given in Eq. (2), at all has any relevance to reality.

Our work [1-5] shows that the basic premise for defining this object ρ_{lpd} via a physical clock is that an open system is more general than a closed system. Meaning, it can only be defined if we have the leads γ and α with their open ends connected to classical electron reservoirs. In that situation it can be shown that the object defined in Eq. (3) follow directly from the topology of the complex plane that is isomorphic to the Hilbert space (or the spinor space). The exact form of the term $\vec{\mu} \cdot \vec{B}(\hat{r})$ or the exact form of the dot product does not matter. It was also shown that negativity of ρ_{lpd} is physical and corresponds to a wave-packet travelling back in time. Since a wave-packet can also carry information or signal, this raises some philosophical issues. Hence a more down to earth experimental verification will be of great help and that is what we will propound in this work.

If we start from a closed system governed by Schrodinger

equation, we cannot get an object that is γ and α dependent because in that case the idea of a physical clock does not work as they inherently need asymptotic free states that are not a linear superposition of states. The classical reservoirs destroy the linear superposition of states in the leads while linear superposition exists inside the sample (shaded region). Events in the reservoir are all classical events and quantum event can only be defined in between two classical events in the reservoirs. This will be discussed again with respect to the 1D picture given in Fig. 2. Once we know ρ_{lpd} we can use it to find other relevant quantities that we find in axiomatic framework of quantum mechanics and so we are not losing anything but only gaining some extra objects by this assertion. At any point we can go to the closed system by making the leads γ and α very weakly connected to the system and recover all that we get by solving the Schrodinger equation for the closed system.

While the general view is that quantum mechanical laws are the fundamental laws of nature and classicality emerges, we adopt the view that a quantum event can only be defined between two classical events and the quantum laws can coexist with classical laws without any contradiction. This has some obvious but significant consequences and solves some long-standing problems in physics. First is that theory of relativity and quantum mechanics can co-exist consistently and there is no immediate need to quantize gravity. That is because now in

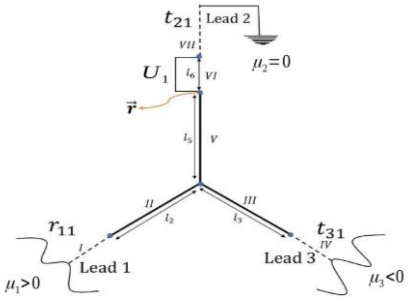

Figure 2: The sample is the three prong potential of Fig. 5.6 shown by the solid lines and the entire system consist of the sample connected to three reservoirs via three leads. Different regions of the system is marked by Roman numbers, I, IV and VII being the leads, shown by dashed lines. Lead 2 is made exactly like that in Fig. 5.6 by earthing it and the chemical potential of lead 3 is also set to zero. In that case for a small positive chemical potential will create a situation wherein only lead 1 inject a current while the two other leads carry some current away from the sample. Lead 2 connects to the sample through a tunnelling barrier shown as region VI. Lengths of different regions is shown as l_2 , l_3 etc. This system is a 1D version of the system in Fig. 1 where lead γ is renamed as lead 1, etc, and as a result $t_{31} \equiv s_{31}$, $t_{21} \equiv s_{21}$, and $r_{11} \equiv s_{11}$.

quantum mechanics, like in theory of relativity, we can relate time intervals to signal propagation time. We can clearly obtain a coordinate time and a proper time within the framework of quantum mechanics. The points inside the classical reservoirs have local clocks giving their respective local times or coordinate time that is consistent with mass distribution in synchronizing the classical local clocks. A signal can propagate from one reservoir to another reservoir according to the laws of quantum mechanics and the time delay defines a proper time that can dialate and contract and can be different from local times clocked by the classical clocks inside the reservoirs. This is a consequence of the fact that a quantum event can only be defined between two classical events. Secondly, ρ_{lpd} is a local object and removes the problem of collapse of wave-function, making it redundant, because measurements are only defined in the classical world in the reservoirs, while the time evolution of observables in the region between the reservoirs are to be determined quantum mechanically. To understand this, let us see whatρ_{lpd} means. At the point r there are electrons in a linear superposition of states. One may say that all these electrons came from lead γ (assume for the time being that ρ_{lpd} is positive definite) but some may be going to lead α (we call them dancing cats), some may be going to lead β (we call them sleeping cats) and some may be getting reflected back to lead γ (we call them beaten cats). At the point r, we have a linear superposition of dancing, sleeping and beaten cats. But we can now say something about only the dancing cats. They spend a time $\frac{-h}{2\pi}\frac{\delta\theta_{S'\alpha\gamma}}{\delta U(r)}$at the point r . At zero temperature there are $\left|S_{\alpha\gamma}\right|^2$ of these dancing cats at the point, we can average over only the dancing cats to define a local partial density of states given by $\rho_{lpd}(E,\alpha,r,\gamma) = \frac{-1}{2\pi}\left|S'_{\alpha\gamma}\right|^2\frac{\delta\theta_{S'\alpha\gamma}}{\delta U(r)}$. That means we can selectively average over the dancing cats at the point r and determine physical effects due to the dancing cats alone. In formal quantum mechanics, we cannot do this selective averaging for the dancing cats alone that are in a linear superposition with the sleeping and beaten cats. Note that$\left|S'_{\alpha\beta}\right|^2and\theta_{S'_{\alpha\gamma}}$are measured at the junction of the sink reservoir which is a classical system.

In this work we intend to justify Eq. (1) for the quantum regime, especially the situation when ρ_{lpd} becomes negative. Note that there are two DOS that feature in Eq. (1), that arev_β and an r dependent DOS that is ρ_{lpd}. There is a factor $\frac{1}{2\pi}$ for each of them that cancels the factor $4\pi^2$. This is the factor $\frac{1}{2\pi}$ that appears in Eq. (2). There can be a very simple interpretation for this factor as follows. LHS of Eq. (2) is a DOS that can accommodate electrons that are countable but $2\pi\rho_{lpd}$ is uncountable, the RHS of Eq. (2) being in terms of $\theta_{S_{\alpha\gamma}}(E)$ corresponding to a continuous rotation. Scattering probabilities $\left|S'_{\alpha\gamma}\right|^2$ and $\left|S_{\alpha\gamma}\right|^2$ are well defined in quantum mechanics and when multiplied by

a factor $\frac{e_0}{h}$ they give the measured coherent current from γ to α. One of the facts that has emerged from the study of Fano resonances in [1-5] is that $\rho_{lpd}(E,\alpha,r,\gamma)$ can be positive as well as negative, implying that $|S'_{\alpha\gamma}|^2 - |S_{\alpha\gamma}|^2$ can be also positive as well as negative in the quantum regime. Hence, according to Eq. (1), when negative then the sample will lose coherent current to the earthed STM tip, and when positive it will draw coherent current from the earth which is counter-intuitive, as any invasive STM tip is supposed to lead to collapse of wave-function. As $|S'_{\alpha\gamma}|^2$ and $|S_{\alpha\gamma}|^2$ are both measurable and so if the equality in Eq. (1) can be justified, then in relative proportions $\rho_{lpd}(E,\alpha,r,\gamma)$ is also measurable which is good enough to confirm its sign. One may always try to justify Eq. (1) from a brute force practical experiment, but we will show below that it can be justified by what we call a theoretical experiment in the sense that Eq. (1) can be established from the topology of the complex plane formed by the imaginary and real parts of a scattering matrix element and hence independent of the quantum mechanical equation of motion as well as vague ideas of spin precession.

The Model

For our theoretical experiment let us consider the system shown in Fig. 2. First of all, it is a system for which exact quantum mechanical calculations can be made and it is a system that exhibit pronounced Fano resonances. In this sense the system in Fig. 1 at Fano resonances with the modification that the upper lead is weakly coupled to earth via a strong potential can be represented by the 1D system in Fig. 2. Since it is a question of whether LPDOS is present at all in a quantum system and more importantly whether its negativity is allowed in quantum mechanics, then demonstrations in 1D quantum mechanics should suffice.

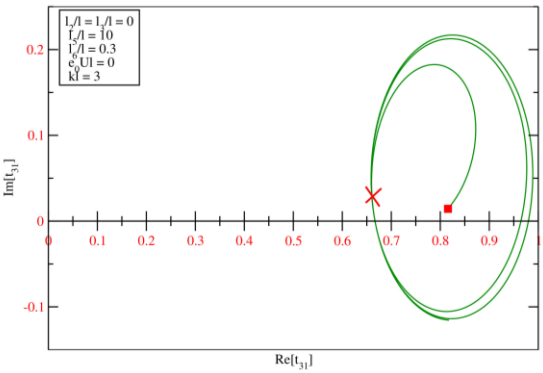

Figure 3: In this figure we plot the AD for t_{31} of the system shown in Fig. 2 for the coupling potential U_1 varying in a range that give three sub-loops, all within one Riemann surface. The starting point is marked by a small square block corresponds to $U_1 l = -1000$. The end point is unmarked and corresponds to a value $U_1 l = -10$. All the sub-loops smoothly come back to a point marked by a cross. Other parameters are mentioned inside the figure.

Let us drop the factor $|t|^2\nu_\beta$ from Eq. (1) because such factors will be only needed if we are using a commercially available STM tip, where this factor characterizes the STM tip. This requires us to drop a 2π factor in Eq. (1) for reasons mentioned in the previous paragraph. Which means for a first principle calculation for the system in Fig. 2 we expect (if the equality in Eq. (1) is correct) that

$$|S'_{\alpha\gamma}|^2 - |S_{\alpha\gamma}|^2 = -2\pi\rho_{lpd}(E,\alpha,r,\gamma) \qquad (4)$$

Now to make it correspond to Fig. 2

$$|t'_{31}|^2 - |t_{31}|^2 = -2\pi\rho_{lpd}(E,\alpha,r,\gamma) \qquad (5)$$

In Fig. 3, we plot the Argand diagram (AD) for t_{31} for the system shown in Fig. 2 by varying the potential U_1which connects the three-prong potential with lead 2 that is earthed. As U_1 is varied from $e_0U_1l = -10$ to $e_0U_1l = -1000$. We plot $\Im[t_{31}]$ versus $\Re[t_{31}]$, which is known as AD. The AD diagram make smooth sub-loops within one Riemann surface and each sub-loop is due to a Fano resonance. Any physical quantity that depends on t_{31} will go through a cycle over one particular sub-loop. For one closed sub-loop generated by monotonously varying a parameter, say $U_1(r)$, the local potential at$r$,

$$\oint_c \Delta\,\theta_{t_{31}} = \oint_c \frac{\delta\theta_{t_{31}}}{\delta U_1(r)}\Delta U_1(r) = 0$$

$$\text{where, } \theta_{t_{31}} = arctan\frac{\Im[t_{31}]}{\Re[t_{31}]}$$

Or

$$\oint_c \frac{1}{2\pi}|t_{31}|^2\frac{\delta\theta_{t_{31}}}{\delta U_1(r)}\Delta U_1(r) = \oint_c \rho_{lpd}\,(E,3,r,1)\Delta U_1(r) = 0 \qquad (6)$$

Similarly, over the same sub-loop,

$$\oint_c \frac{\delta|t_{31}|^2}{\delta U_1(r)}\Delta U_1(r) = \oint_c \Delta|t_{31}|^2 = \oint_c \Delta|\Re[t_{31}] + \Im[t_{31}]|^2 = 0 \qquad (7)$$

Therefore, from Eqs. (6) and (7) we get the equality

$$\oint_c \Delta|t_{31}|^2 = \oint_c \frac{1}{2\pi}|t_{31}|^2\frac{\delta\theta_{t_{31}}}{\delta U_1(r)}\Delta U_1(r) = 0 \qquad (8)$$

purely as a consequence of the topology of a complex plane $(\Im[t_{31}], \Re[t_{31}])$. If the Argand diagram trajectory would have enclosed the singularity, then the RHS of Eq. (6) would have been 2π instead of zero. Whatever be the terms in the Hamiltonian or the equation of motion, it is the topology of the complex plane that determines the outcome of the integration in Eq. 6. For the kind of Argand diagram in Fig. 3, that are smoothly closed within one Riemann surface, the equality in Eq. 8 is for the integrals. The integrands can well be completely different in magnitudes but the integrands will go through a positive-negative cycle over a sub-loop. Therefore, it is obvious that $\Delta|t_{31}|^2$ as well as ρ_{lpd} will go through a positive-negative cycle over a closed sub-loop as a consequence of the topology of the relevant complex plane. Given the fact that LHS is physical, the cycles of ρ_{lpd} is also physical as they are just different expressions of the same sub-loop made by the AD of t_{31}. If we want to compare the integrands in Eq. (8), then we need an extra factor of 2π as discussed before Eqs. (4) and (5). Thus,

$$\Delta|t_{31}|^2 \approx 2\pi \frac{1}{2\pi}|t_{31}|^2 \frac{\delta\theta_{t_{31}}}{\delta U_1(r)} \Delta U_1(r) \quad (9)$$

Viewing a derivative as an effect of an infinitesimal change in U_1 we get

$$|t'_{31}|^2 - |t_{31}|^2 \approx |t'_{31}|^2\left(\theta_{t_{31}} - \theta_{t'_{31}}\right) \quad (10)$$

where primed quantities and unprimed quantities are calculated for an infinitesimal difference of U_1. If we want to compare integrands then we can only write an approximate equality because we are comparing two different objects over one sub-loop. There will always be in the least a phase difference between the two quantities.

In Fig. 4, we plot LHS and RHS of Eq. (10) where the primed values and unprimed values are again for small differences in U_1 as the incident wave vector k is varied and that is the horizontal axis. It becomes clear that LHS and RHS of Eq. (10) oscillate with positive and negative values. Initially the two curves are a little different but as k increases, effects of dispersion is minimized, and magnitudes of the two curves are similar with a phase difference between them. The oscillations of both the curves are due to the smooth cyclic nature of the AD in Fig 3. In other words, the underlying principle behind the oscillation of both curves is the same. The two curves oscillate as a result of quantum interference. But the symmetric oscillation between positive and negative values and the similarity between the two curves can only be noted if there are well defined Fano resonances and signify the fact that the RHS of Eq. (1) is physical. For Breit-Wigner resonances the last two features are not seen.

Conclusions

Thus, to answer the question why and when the equality of Eq. (1) can be observed, one can say that when we have closed sub-loops within one Riemann surface for the AD of the scattering matrix element of a relevant channel like t_{31}, then the equality will be found. Such closed subloops occur if there is a Fano resonance. When other type of resonances like the Breit-Wigner resonances start interfering with the Fano resonances then two things can happen. First is that the subloops are not smoothly coming back to the point depicted by a cross mark in Fig. 3 or we do not get closed subloops at all. In that case the equality in Eq. (1) will not be strictly valid but still there can be an approximate equality. Since the smooth subloop signify analyticity of a complex quantity like t_{31}, the equality of the two curves in Fig. 4 is not a direct consequence of quantum dynamics and thus we can prove the equality of Eq. (1), in the presence of Fano resonances without invoking the axioms of quantum mechanics. In this sense it is a theoretical experiment.

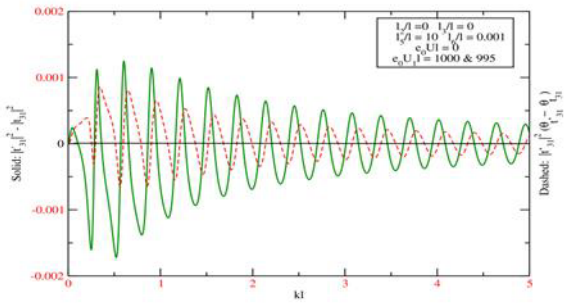

Figure 4: In this figure we are plotting the LHS and RHS of Eq. (10) to show that they both can oscillate between positive and negative values. The primed and unprimed values are for small differences in U_1 at a k value that we vary continuously. The sign change and magnitude of both the curves originate from the smooth cyclic AD of Fig. 3.

References

1. P. Singha Deo, "*Mesoscopic route to time travel*", Springer (2021).
2. U. Satpathi and P. Singha Deo, Annals of Physics, 375 491 (2016).
3. P. Singha Deo and U. Satpathi, *"Transmitting a signal in negative time"*, Results in Physics, 12 1506 (2019).
4. K. Meena and P. Singha Deo, Physica E 49, 115680 (2023).
5. P. Singha Deo and Kanchan Meena, *"Time Travel: A Reality in Mesoscopic Physics"*, Springer Nature, 2025.
6. M. Buttiker, Time in quantum mechanics, pg 279 - 303, Springer (2001).

7. T. Gramespacher, M. Buttiker: Phys. Rev. B 56, 13026 (1997); Phys. Rev. B 60, 2375 (1999); Phys. Rev. B 61, 8125 (2000).

Infrared Broadband Reflectors by Nano-Layered Periodic Cryolite/Semiconducting Media

Jyoti Sangwan[1], Deepali Sharma[1], Ram Janma[2], and Prabal P. Singh[2], Rajpal Singh[3], Narendra Kumar[1,a]

[1] *Department of Physics, SLAS, Mody University of Science and Technology, Lakshmangarh 332311, Sikar, Rajasthan, India.*
[2] *Department of Physics, UIET, Chhatrapati Shahu Ji Maharaj University, Kanpur 208024, UP, India.*
[3] *Department of Physics, Govt. M. S. College, Bikaner 334001, Rajasthan, India.*

[a] nkumar.mu.in@gmail.com

Abstract

This simulation work is based on the analysis of the dispersion characteristics of a nanolayered periodic binary PhC of cryolite and semiconducting layers by using the transfer matrix approach. The dispersion curves and reflection through layered media for optical waves are compared at oblique incidences, and some insights are drawn. It is observed that width of band gap decreases or remains same with increase in the incident angle for 1DPhC, while the bandwidth increases with the normalized frequency at fixed incidence that shows the characteristics of Bragg's gap. The results of the manuscript have promising applications in design of tunable optical filters, broadband reflectors, lasers, and modern communication industry.

Keywords: Nanolayered, Semiconducting, Cryolite, Dispersion, Bragg's gap, Band gap.
Received 10 January 2025; First Review 21 January 2025; Accepted 26 January 2025

*** Address of correspondence**
Dr. Narendra Kumar
Department of Physics, SLAS, Mody University of Science and Technology, Lakshmangarh 332311, Sikar, Rajasthan, India.

Email: nkumar.mu.in@gmail.com

How to cite this article
Jyoti Sangwan, Deepali Sharma, Ram Janma, and Prabal P. Singh, Rajpal Singh, Narendra Kumar, Infrared Broadband Reflectors by Nano-Layered Periodic Cryolite/Semiconducting Media, J. Cond. Matt. 2025; 03 (01): 22-26

Available from:
https://doi.org/10.61343/jcm.v3i01.54

Introduction

Yablonovitch [1] first introduced the photonic band gap for controlling spontaneous emission of light. Before 1987, one-dimensional photonic crystal (1D PhC) in the form of periodic multilayer dielectric stacks were studied extensively and showed that such systems have a one-dimension photonic band gap, spectral range of large reflectivity known as stop band. Leading to these studies, a detailed theoretical study of 1D optical structure was suggested by Vladimir P. Bycov, who was credited the first to investigate the photonic (PBG) on the spontaneous emission from molecule and atom embedded inside the photonic structure.

The periodic modulation of the permittivity occurs in one direction only in such 1D PhCs, where two other directions in the structure are uniform. As an example of such a PhC it can be given is similar to the Bragg grating which that is extensively used in vertical cavity surface emitting lasers as a distributed reflector. These structures are widely used as antireflecting coatings to decrease the reflectance from the surface dramatically and improve the quality of prisms, lenses, and other optical components. Further Thomas Krauss demonstrated a two-dimensional photonic crystal at optical wavelengths in 1996 [2, 3]. This opened the way to fabricate photonic crystals in semiconductor materials by borrowing methods from the semiconductor industry [3]. The two-dimensional PhCs are commercially used in PhC fiber those were first developed by Philip Russell in 1998, to enhance properties over optical fibers. By 1991, Yablonovitch had demonstrated the first 3DPBG in the microwave regime. The structure was able to produce a drilling array of holes in a transparent material, in which there are holes of each layer form an inverse diamond structure and is known as Yablonovite. Such 3D PhCs have permittivity modulation along all three directions, where the number of possible PhC configurations is much larger than those of 1D or 2D PhCs, and many works were dedicated to the design the new geometric configurations of 3D PhC, which could open new possibilities of their applications [1, 3]. Among them, the most natural 3D PhC is valuable stone opal having its unique optical properties. By turning around, it shows different colours. Although owing to such a peculiar behaviour, ancient people declared that opal had some magic powers, now it is clear that all these

peculiarities are caused by the micro-structure of opal that consists of a number of micro-spheres kept at nodes of face-centred cubic (FCC) lattice.

Although there are three types of PhC and some studies have been made on 2D- and 3D PhCs, the 1DPhC is the simplest one and has been extensively studied by using different types of materials in its binary periodic structure. The properties of metallic PBG materials with introduced defect were reported in microwave frequencies, whose experimental verifications had been made. In brief the PBG materials are composed of air, semiconductors, dielectrics, metals and polymers. By using the transfer matrix method, Kumar and Ojha [5] made an attempt to analyse the reflection properties of a PBG structure with refractive index profile. The reflected broadband in the reflection spectra were compared with the forbidden band-gaps obtained using the analogy of Kronig-Penney model [4, 5] used in the band theory of solids, and some conclusions were drawn. In recent decades, a tremendous amount of work has been devoted to 1DPhC with a variety of materials and structures [6-20]. In this simulation work, we propose a nanolayered periodic PhC of semiconducting media, whose one-layer Sodium hexafluoro aluminate and another is Germanium. We employ the transfer matrix approach for optical waves and reflection through layered media [5, 16].

Theoretical Modelling of Photonic Crystal

Figure 1 shows the binary structure of 1DPhC in which the reflectance of such a structure strongly depends on the radiation incident angle. And the optical properties of such PhC can be determined by the existence of the periodic modulation of the permittivity or the refractive index of the medium. At that, observed effects have strong analogy to the solid state, i.e., the periodically arranged structure of atoms in crystal lattice.

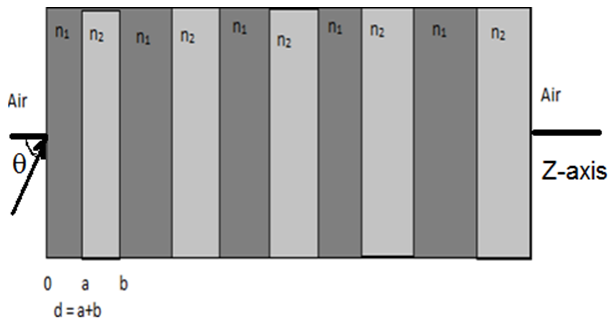

Figure 1: Periodic variation of 1DPhC structure.

We consider the EM wave propagation along x-axis through the structure, the periodic refractive is [4]

$$n(z)=\begin{cases} n_1, b<z<d \\ n_2, 0<z<b \end{cases} \quad , \quad (1)$$

with $n_1(z+d)=n_1$ and $n_2(z+d)=n_2$, and $d=a+b$ be the lattice period, with a and b as the widths of the two layers whose refractive indices are n_1 and n_2, respectively.

The 1D EM wave equation for the spatial part of the eigen mode is expressed as

$$\frac{d^2E(z)}{dz^2}+\left[\left(\frac{\omega}{c}n\right)^2-\beta^2\right]E(z)=0 \quad , \quad (2)$$

The electric field distribution $E(x)$ within each layer can be expressed as the sum of an incident and reflected plane waves, and so in the m^{th} unit cell it is written as

$$E(z)=\begin{cases} a_m e^{-ik_1(z-md)}+b_m e^{ik_1(z-md)}; & (md-a)<z<md \\ c_m e^{-ik_2(z-md+a)}+d_m e^{ik_2(z-md+a)}; & (m-1)d<z<(md-a) \end{cases} \quad , \quad (3)$$

in which a_m, b_m, c_m, and d_m are constants.

We define,

$k_i=\left[\left(\frac{\omega}{c}n_i\right)^2-\beta^2\right]^{1/2}=\frac{n_i\omega}{c}\cos\theta_i;\ i=1,2$, where θ_1 and θ_2 are the ray angles in the consecutive layers.

Assuming θ as the angle of incidence,

$\cos\theta_i=\left(1-\left(\frac{1}{n_i}\right)^2\sin^2\theta\right)^{1/2}$. With the help of TMM, we have the relation [4, 5]

$$\begin{pmatrix} a_{m-1} \\ b_{m-1} \end{pmatrix}=\frac{1}{2}\begin{pmatrix} A_{11} & A_{12} \\ A_{21} & A_{22} \end{pmatrix}\begin{pmatrix} a_m \\ b_m \end{pmatrix} \quad , \quad (4)$$

where the matrix elements are expressed as

$$A_{11}=\exp(+ik_1a)\left[\cos k_2b+\frac{1}{2}i\left(\frac{k_2}{k_1}+\frac{k_1}{k_2}\right)\sin k_2b\right],$$

$$A_{12}=\exp(-ik_1a)\left[\frac{1}{2}i\left(\frac{k_2}{k_1}-\frac{k_1}{k_2}\right)\sin k_2b\right],$$

$$A_{21}=\exp(+ik_1a)\left[-\frac{1}{2}i\left(\frac{k_2}{k_1}-\frac{k_1}{k_2}\right)\sin k_2b\right], \text{ and}$$

$$A_{22}=\exp(-ik_1a)\left[\cos k_2b-\frac{1}{2}i\left(\frac{k_2}{k_1}+\frac{k_1}{k_2}\right)\sin k_2b\right].$$

Since equation (4) above is unimodular $A_{11}A_{22}-A_{21}A_{12}=1$. By using Floquet theorem [4-6]

$$K(\beta,\omega)=\frac{1}{d}\cos^{-1}\left[\frac{1}{2}(A_{11}+A_{22})\right] \quad (5)$$

Thus, the dispersion relation (ω versus K) will be

$$cos(Kd)=cos(k_1a)\,cos(k_2b) -\frac{1}{2}\left[\frac{k_2}{k_1}+\frac{k_1}{k_2}\right]sin(k_1a)\,sin(k_2b) \quad (6a)$$

Hence,

$$cos(Kd)=cos(k_1a)\,cos(k_2b) -\frac{1}{2}\left[\frac{n_2}{n_1}+\frac{n_1}{n_2}\right]sin(k_1a)\,sin(k_2b) \quad (6b)$$

Reflectance (R_N) of the 1DPhC can be obtained by [4, 16]

$$R_N=\frac{|A_{21}|^2}{|A_{21}|^2+\left(\frac{\sin Kd}{\sin NKd}\right)^2}, \quad (7)$$

where A_{21} is matrix element and N is total number of unit cells. For a lossless media, the transmission can be obtained as $T_N=1-R_N$.

Results and Discussion

For the numerical calculations in our study, we have taken Na_3AlF_6 and Ge as $n_1=1.34$ and $n_2=4.2$ [11, 16], and their thicknesses are d1=360nm and d2=120nm, respectively [11], where d is the total stack thickness. The dispersion relation for a structure have been derived with Bloch equation as by the equation (6b) and the reflection and transmission can be obtained by the equation (7), respectively. We now plot dispersion curves and reflection spectra at incident angles 0°, 20° and 60°.

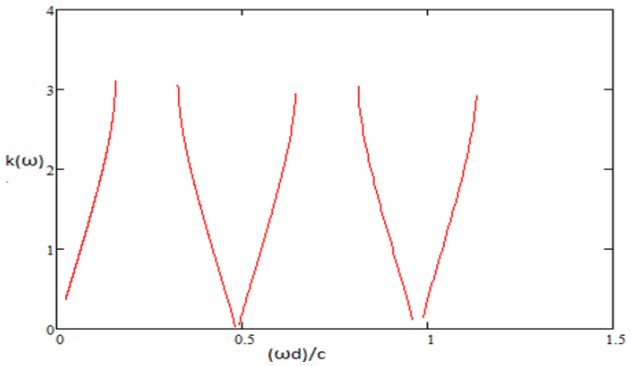

Figure 2: Plot of the dispersion relation as a function of normalized frequency for the 1DPhC at incident angle θ = 0° [16].

Figures 2, 3, and 4 represent the dispersion relation curves i.e. k(ω) versus normalized frequency, $\omega d/c$ i.e., of the structure for different oblique angle of incidences θ = 0°,

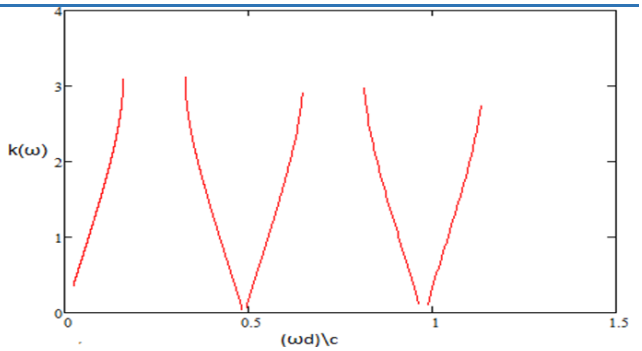

Figure 3: Plot of the dispersion relation as a function of normalized frequency for the *1DPhC* at incidentangle $\theta=20^0$ [16].

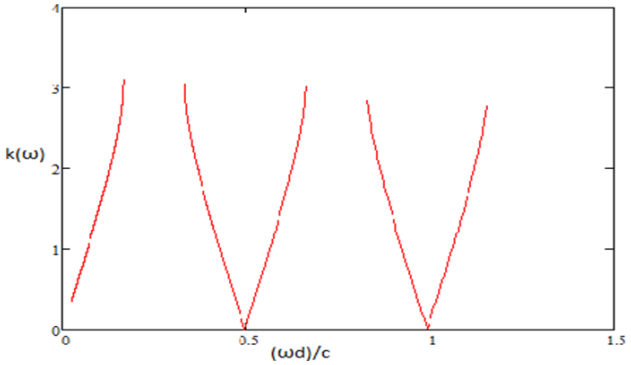

Figure 4: Plot of the dispersion relation as a function of normalized frequency for the *1DPhC* at incidentangle $\theta=60^0$.

20°, 60°. It is clear that the bandwidths of odd numbered forbidden band gaps are wide but the bandwidths of even numbered forbidden band gap are extremely narrow. It is noticeable here that the lattice constant d is arbitrary; thus, the result obtained here is only valid for arbitrary wavelengths and the existence of band gap is possible d is nearer to λ, i.e., when the normalized frequency is perpendicular.

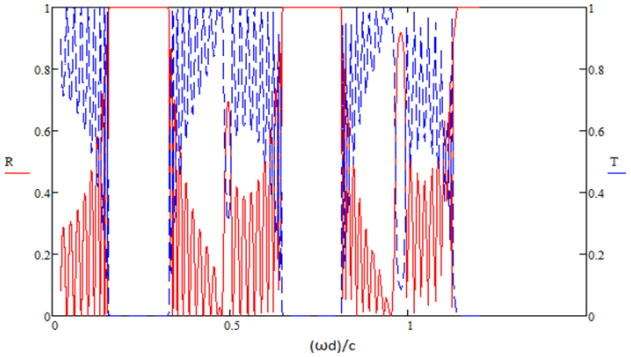

Figure 5: Plot of Reflection and Transmission as a function of normalized frequency for the *1DPhC* atincident angle $\theta=0^0$.

From Figures 5, 6, and 7, it is noted that the first and third band gap shows the hundred percent reflection therefore the transmittance is zero. i.e. at these frequencies, the waves are completely reflected and do not pass through the crystal but

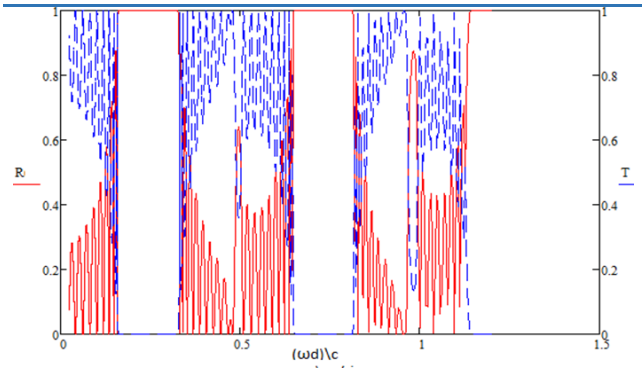

Figure 6: Plot of Reflection and Transmission as a function of normalized frequency for the *1DPhC* atincident angle $\theta = 20^0$.

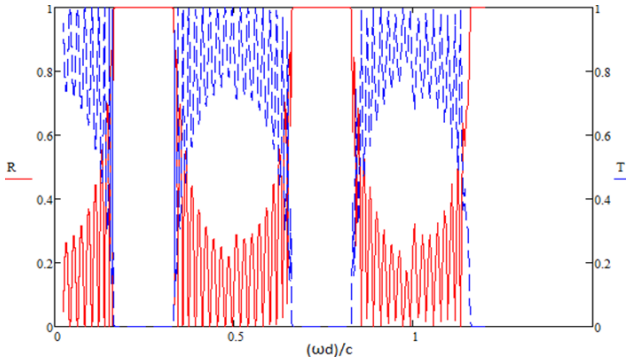

Figure 7: Plot of Reflection and Transmission as a function of normalized frequency the *1DPhC* atincident angle $\theta = 60^0$.

in second and fourth band gaps, the transmittance is not zero, which means part of the wave can pass.

Table 1: Normalized Frequency Range at Incident Angle 0^0.

S. No. of Bands	Band Gap (Dispersion Curves)	Complete Reflection Range	Bandwidth
1	1.2-1.37	1.2-1.37	0.17
2	0.808-0.65	0.808-0.65	0.158
3	0.327-0.164	0.324-0.164	0.163

Table 2: Normalized Frequency Range at Incident Angle 20^0.

S. No. of Bands	Band Gap (Dispersion Curves)	Complete Reflection Range	Bandwidth
1	1.2-1.143	1.2-1.143	0.057
2	0.811-0.652	0.811-0.652	0.159
3	0.324-0.163	0.324-0.163	0.161

From the bandwidth listed in Tables at three incident angles, it is observed that the bandgap obtained from the dispersion curves and reflection spectra are analogous and mostly same. As the incident angle increases, the width of band gap, in terms of the normalized frequency ranges for 1DPhC, decreases or remains same. However, at fixed incidence, the bandwidth increases with the normalized frequency.

Table 3: Normalized Frequency Range at Incident Angle 60^0.

S. No. of Bands	Band Gap (Dispersion Curves)	Complete Reflection Range	Bandwidth
1	1.2-1.165	1.2-1.165	0.035
2	0.822-0.667	0.822-0.667	0.155
3	0.327-0.164	0.327-0.164	0.163

Conclusion

The present work is dedicated to an analysis of a nanolayered structure, considering as a simple model of 1D semiconducting photonic crystal. From the dispersion curves, it is found that the structure with chosen refractive index profiles and lattice parameters exhibits allowed and forbidden bands. It is mentioned that with increase in the incident angle, the bandwidth for 1DPhC either decreases or remains same. However, at fixed incidence, the bandwidth increases with the normalized frequency. This study can be useful in design of tunable optical filters, nano-optics and may have promising applications in modern communication industry, lasers and optical computing.

References

1. John D. Johnno Polus, Steven G. Johnson, Joshua N. Winn, R. D. Meade, *"Photonic Crystals: Molding the Flow of Light"*, Princeton University Press, 2007.
2. N. Kumar and A. Rostami, *"Novel Features and Prospective of Photonic Crystals"*, Lambert Academic Publishing Germany (2012).
3. www.wikipedia and google search engine.
4. N. Kumar and Khem B. Thapa, B. Suthar, *"Photonic Crystals Features and Applications"*, Nova Science Publishers, USA (2013).
5. N. Kumar and S.P. Ojha, *"Photonic crystal as infrared broad band reflector with different angles of incident"*, Progress in Electromagnetics Research PIER, USA, 2008.
6. N. Kumar, B. Suthar, C. Nayak, A. Bhargava, *"Analysis of a gas sensor based on one-dimensional photonic crystal structure with a designed defect cavity"*, Phys. Scripta 98, 065506 (2023).
7. N. Kumar, G. N. Pandey, S. Kaliramna, S. S. Dhayal, *"Microwave Propagation Characteristics in Magnetized-Cold-Plasma-Based Binary Photonic Crystal with Defect of MCP Layer"*,

Macromolecular Symposia (Wiley) Volume 407, Issue 1(2023).

8. N. Kumar, G. N. Pandey, A. Lamba, B. Suthar, *"Transmission Properties of a One-Dimensional Defective Photonic Crystal Structure of Air/Magnetized-Cold-Plasma"*, Macromolecular Symposia (Wiley), Volume 407, Issue 1(2023), https://doi.org/10.1002/masy.202100520
9. G. N. Pandey, N.Kumar, P. S., K. B. Thapa, *"Transmittance Properties of Metamaterial and Dielectric Based One-Dimensional Ternary Periodic Structure"*, Macromolecular Symposia (Wiley), Volume 407, Issue 1(2023), https://doi.org/10.1002/masy.202200016
10. B. Suthar, N. Kumar, S. A. Taya, *"Design and Analysis of Tunable Multichannel Transmission Filters with a Binary Photonic Crystal of Silver/Silicon"*, The Eur. Phys. J. Plus, Springer Nature, Springer-Verlag GmbH, (Germany) 137, 1301 (2022).
11. Deepali and Jyoti, *"Anomalous Behaviour of One-Dimensional Dielectric Plasma Photonic Crystal"*, A PG dissertation submitted at Department of Physics, Mody University of Science and Technology, Lakshmangarh, India (2017).
12. G. N. Pandey, N. Kumar, P. Singh and K. B. Thapa, *"Transmission Properties in a One-Dimensional Symmetric Ternary Nanolayered Photonic Crystal Designed with Superconductor and Silicon-Based Materials"*, Springer: J Supercond Nov Magn (2022)
13. N. Kumar and J. Saraf, *"Tunable Reflectance Characteristics of Magnetized Cold Plasma Based One-Dimensional Defective Photonic Crystal",* Optik 252, 2022.
14. N. Kumar, S. Kaliramna and M. Singh, *"Design of Cold Plasma Based Ternary Photonic Crystal for Microwave Applications",* Silicon Springer Nature, (Oct 2021).
15. G. N. Pandey, B. Suthar, N. Kumar, and K. B. Thapa, *"Omnidirectional Reflectance of Superconductor-Dielectric Photonic Crystal in THz Frequency Range"*, Springer: J Supercond Nov Magn (2021).
16. V. Kumar, K. S. Singh, S. P. Ojha, *"Negative Refraction in One-Dimensional Photonic Crystal Without Negative Refraction Material"*, International Journal of Microwave and Optical Technology, Vol.5, 2010.
17. B. Suthar and A. Bhargava, *"Optical Properties of Plasma Photonic Crystal"*, International Journal of Microwave and Optical Technology, 2015.
18. S.P. Ojha, Sanjeev K. Srivastava, N. Kumar, S. K. Srivastava, *"Design of An Optical Filter Using Photonic Band Gap Material",* Optik, Germany (2003).
19. Ankit Singh, Khem B. Thapa and Narendra Kumar, *"Analysis and design of optical biosensors using one-dimensional photonic crystals",* Optik 126, 244–250(2015). http://dx.doi.org/10.1016/j.ijleo.2014.08.172
20. J. B. Pendry, *"Negative Refraction Without Negative Index in Metallic Photonic Crystal"*, OSA Publishing, 2011.

Structural and Electronic Characteristics of Cubic Half-Heusler Compound AcOF

Shivani Gaur[1,a], Madhu Sarwan[2,b], Sadhna Singh[2,c]

[1] *Department of Physics, Govt. SGS PG. College, Ganjbasoda (M.P.), India.*
[2] *Department of Physics, Barkatullah University, Bhopal (M.P.), India.*

[a] shivanigaur1470@gmail.com
[b] madhusarwan@gmail.com
[c] drsadhna100@gmail.com

Abstract

An investigation has been conducted on structural and electronic characteristics of cubic half heusler compound AcOF. The FP-LAPW approach is used in density functional theory (DFT) to conduct the investigation. GGA scheme was applied to verify the structural stability. The lattice parameter, unit cell volume, bulk modulus, and pressure derivative of bulk modulus are among the ground-state characteristics that are calculated. The calculated GGA lattice parameters correlate well with the available data. Band structure, density of state and charge density have been plotted. Electronic band structure confirms AcOF as an insulator having large Energy band gap.

Keywords: Density functional theory, Structural properties, Electronic properties and Insulator.
Received 26 January 2025; First Review 21 February 2025; Accepted 06 March 2025

*** Address of correspondence**
Shivani Gaur
Department of Physics, Govt. SGS PG. College Ganjbasoda (M.P.) India.

Email: shivanigaur1470@gmail.com

How to cite this article
Shivani Gaur Madhu Sarwan, Sadhna Singh, Structural and Electronic Characteristics of Cubic Half-Heusler Compound AcOF, J. Cond. Matt. 2025; 03 (01): 27-29

Available from:
https://doi.org/10.61343/jcm.v3i01.57

Introduction

In general, Half Heusler materials XYZ can be understood as compounds consisting of a covalent and an ionic part. The X and Y atoms have a distinct cat-ionic character, whereas X can be seen as the anionic counterpart. AcOF (XYZ) is ternary inter-metallic half heusler compound consisting Actinium, Oxygen and Fluorine. AcOF crystallizes in the MgAgAs type (FCC) cubic structure with space group F-43m (no. 216), where Ac, O and F atoms are located at 4a(0,0,0), 4b(0.5,0.5,0.5), 4c(0.25,0.25,0.25) Wyckoff positions respectively [1].

Half-Heusler compounds are interesting due to their various properties including semi-conductivity, magnetism, superconductivity, thermoelectricity and half-metallicity [2]. Half-Heusler compounds are also known as topological insulators because of their insulating properties in the interior while metallic nature at the surface [3-4]. Several compounds from this intriguing class of materials, such as LiCdP, LiCdAs, and AgMgAs, have been synthesized. However, only a few have undergone detailed characterization. Beleanu et al. [5] conducted an experimental investigation into the structural and electronic properties of LiMgZ (Z = P, As, and Sb). Their findings suggest that these alloys exhibit semiconducting behavior, with a direct band gap ranging between 1.0 and 2.3 eV. The structural, electronic, thermodynamic properties of Lithium based materials i.e. LiZnP and LiCdP have also been studied [6].

On the other hand, due to band inversion, these materials are found to exhibit topological superconductivity. No studies have been done on the structural, electronic, mechanical and optical properties of AcOF HH compound. In this paper, we have studied its structural and electronic properties and had briefly described the structural properties as well.

Method

In order to understand the physical properties of the compound, density functional theory (DFT) is the most sought and prominent tool to evaluate the compounds, predominately in material science. It is a computational quantum mechanical modelling method used to investigate the electronic structure (or nuclear structure) (principally the ground state) of many body system.

The DFT calculations under the framework of full potential linearized augmented plane wave (FP-LAPW) method available with Wien2k is used to calculate the ground state properties of the compound. The energy exchange correlation effect of energy is studied by the generalized gradient approximation (GGA) scheme. Convergence criteria were set at 0.0001 Ry for energy and 0.0001 elementary charges (e) for charge density, ensuring precise results. The electronic structure was analysed using k-point density of 2000 points to calculate the density of states (DOS). The cut-off value of $RMT*K_{max}$ = 9 (RMT is the smallest muffin-tin radius in the unit cell and K_{max} is the maximum of reciprocal lattice vector) for wave vector is picked that contributes to the plane wave expansion of the wave function in the interstitial region. Inside the atomic sphere, the maximum value of partial waves is l_{max} =10, while in the charge density, the value of G_{max} =12 $(a.u.)^{-1}$. The self-consistent simulations are repeated up to the total energies converged within 10^{-4} Ry.

Result and Discussion

Table 1: Ground state properties of AcOF HH compound.

a (Å)	V (Å) ³	B (GPa)	B’
5.851	338.04	101.84	3.92
5.950 [7]	-	-	-

The half heusler compound AcOF crystallizes in the cubic MgAgAs type structure (space group F-43m No. 216) in which Ac atoms occupy at (0, 0, 0), O atoms at (0.5, 0.5, 0.5) and F atoms at (0.25, 0.25, 0.25) symmetry as shown in Fig. 1. The optimized lattice parameter is 5.851 (Å) as shown in Table 1. In this figure the bond angle between Ac, O and F is represented by light green colour. The bond angle of AcOF is 35.097º and same for AcFO and OAcF i.e. 72.452º for the cubic structure. The bond length of Ac-F is 2.9255 Å and same bond length for the Ac-O and O-F i.e. 4.8514.

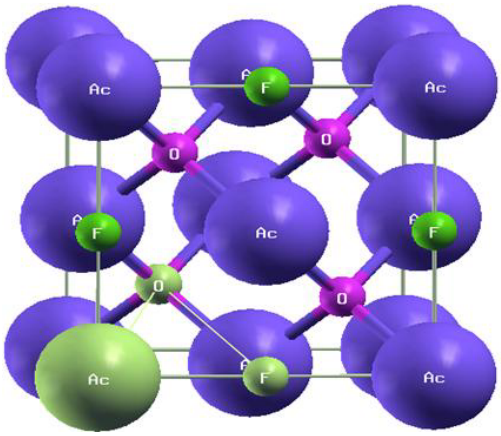

Figure 1: Structure of AcOF

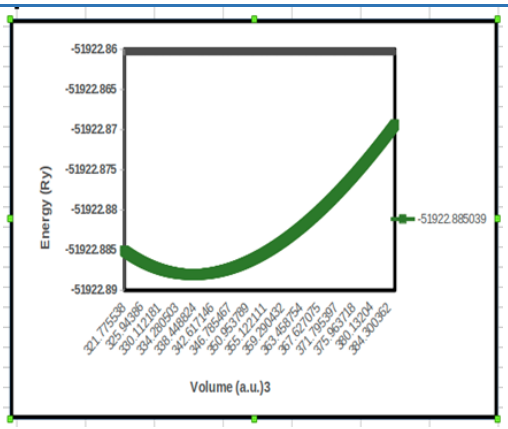

Figure 2: Energy vs volume curve of AcOF.

In Fig. 2, we have plotted energy as a function of volume and the pattern of the curve, which indicates its structural stability at the obtained Volume and Energy parameters. It is also observed from Fig. 2 that GGA calculation provides lowest possible minimum energy indicating a better stability of the compounds. We noticed that this oxide compounds stabilize in the cubic C_{1b} phase with a space group F-43m (216).

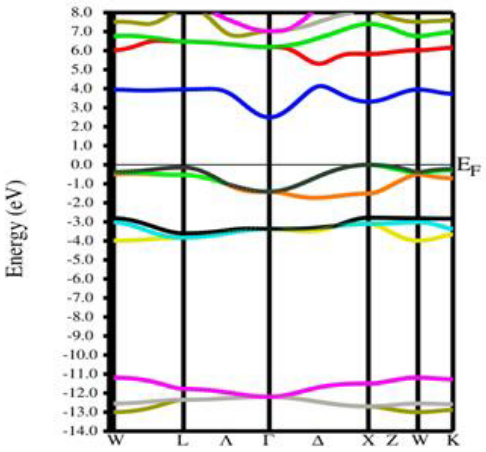

Figure 3: Band Structure of AcOF.

For the calculations of the ground state properties such as the equilibrium lattice constant (a), bulk modulus (B), and its pressure derivative (B’), we have calculated total energy as a function of unit cell volume and befitted to Birch-Murnaghan's equation of state [8] and is displayed in Table 1. The calculated value of lattice parameter is presented in Table 1 together with available theoretical results, which show very good agreement in terms of the ground state properties of the AcOF HH compound.

To achieve a comprehensive understanding of the electronic properties of AcOF a detailed analysis, including band structures and density of states (DOS), has been meticulously presented in next following Figures 3-5. The band structure analysis, shown in Figures-3 along the high-symmetry directions of the Brillouin zone, with the Fermi

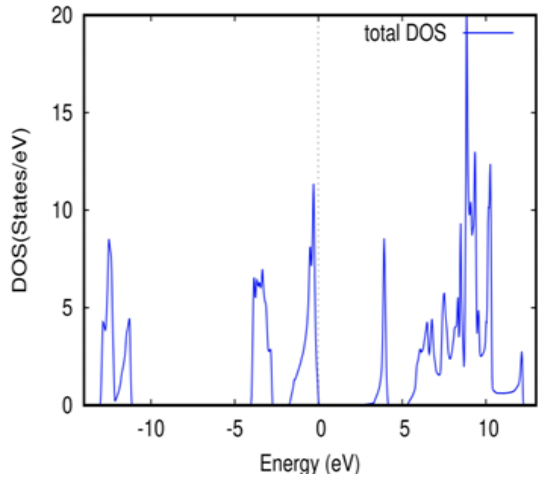

Figure 4: Total density of states (T-Doss) of AcOF.

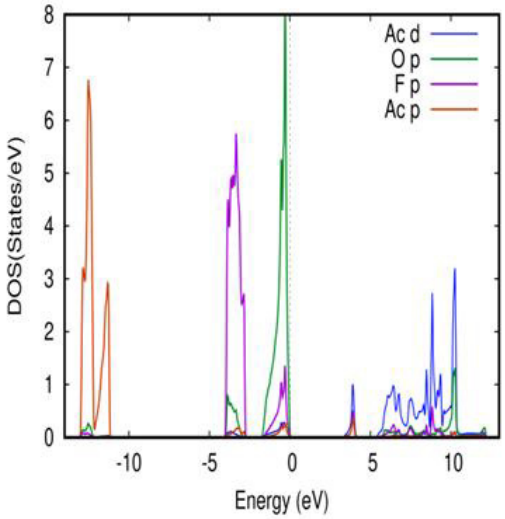

Figure 5: Partial density of states (P-Doss) of AcOF.

level set at 0 eV, confirms the insulator nature of the compound. Band diagram reveal that the lowest energy bands correspond to the Ac-p states, which extend from approximately -13.0 to -11.0 eV, while the F-p states span from approximately -4.0 to -2.9 eV. Further insights into the band structure are offered by the total density of states (TDOS), presented in Figure-4 and the partial density of states (PDOS), illustrated in this Figure-5. A highest peak is observed in O-p state in valence band which dominates near the Fermi level, suggesting an important role in bonding. After this next highest peak is due to Ac-p state showing contributions in the deep valence region (~ -10 eV). F-p state has peaks mainly in the valence band representing the dominant orbital contributions to the electronic states. These figures illustrate the small electronic interactions in AcOF near the Fermi level. A significant hybridization is observed between the O-p, F-p, Ac-p and Ac-d states. No peaks in conduction bands are observed from 0 to 4 eV, highlighting regions of pronounced band gap and density of states.

Conclusion

The structural and electronic properties of AcOF have been investigated by using FP-LAPW method within GGA. The structural stability is confirmed by the energy versus volume curve and found that it is dynamically stable in fcc cubic MgAgAs-type structure. The computed values of lattice parameters are impressively matched with other available data, though the rest of the ground-state properties are never reported before. From electronic analysis, it is seen that AcOF as a topological insulator having large band gap. In the valence band p state of O (oxygen) is near the Fermi level confirming the topological behaviour. After that large band gap is observed between valance and conduction band.

References

1. Guangqian Ding, G. Y. Gao,Li Yu, Yun Ni, and KaiLun Yao, Journal of Applied Physics 119: 025105, 2016.
2. Mohammad Sajjad Hossaina and Md. Moazzem Hossain, the European Physical Journal Plus 138: 2021.
3. S. Chadov et al., Nat. Mater. (7) 541: 2010. DOI:10.1038/nmat2770.
4. H. Lin et al., Nat. Mater. 9 (7), 546: 2010. DOI: 10.1038/nmat2771
5. A. Beleanu, M. Mondeski, Q. Juan, F. Casper, C. Felser, F. porcher, J. Phys. D: Appl. Phys. 44: 475302, 2011.
6. Madhu Sarwan, V.Abdul Shukoor and Sadhna Singh, *Distinctive Features of Semiconducting and Brittle Half-Heusler Alloys*; *LiXP (X=Zn, Cd)*, Book, Mathematics in Computational Science and Engineering. Publisher: Wiley online libiarary,2022. https://doi.org/10.1002/9781119777557.ch8.
7. https://next-en.materialsproject.org/materials/mp-36526?formula=AcOF#crystal_structure.
8. F. Birch, J. Appl. Phys. 9: 279-288 (1938).

Comparative study of Powder X-Ray Diffraction Analyses of Titanium Dioxide (TiO_2) Nanoparticles Synthesized by the Sol-Gel Method

Khyati Mody[a], I B Patel[b]

Department of Physics, Veer Narmad South Gujarat University, Surat-395007, Gujarat, India.

[a] kmody1997@gmail.com
[b] ibpatel@vnsgu.ac.in

Abstract

This study presents a comparative analysis of Powder X-ray Diffraction (XRD) data of various Titanium Dioxide (TiO_2) nanoparticle samples synthesized via the Sol-Gel method using Titanium (IV) isopropoxide as a precursor. Titanium Dioxide, known for its chemical inertness and environmental friendliness, is widely utilized in industries as a pigment and exists in three crystalline phases: anatase, rutile, and brookite. XRD analysis revealed that the synthesized nanoparticles exhibit pure anatase and anatase-rutile mixed phases. The particle sizes, ranging in nanometres, were influenced by varying precursor ratios and calcination temperatures. Additionally, this research evaluates critical characteristics such as specific surface area, dislocation density, and morphology index, providing insights into the structural and physical properties of the prepared nanoparticles.

Keywords: Titanium Dioxide (TiO_2) nanoparticles, Sol-Gel Method, X-ray Diffraction (XRD), Anatase Phase, Dislocation Density, Morphology Index, Specific Surface Area.
Received 27 January 2025; First Review 21 February 2025; Accepted 06 March 2025

*** Address of correspondence**
Khyati Mody
Department of Physics, Veer Narmad South Gujarat University, Surat-395007, Gujarat, India.

Email: kmody1997@gmail.com

How to cite this article
Khyati Mody, I B Patel, Comparative study of Powder X-Ray Diffraction Analyses of Titanium Dioxide (TiO_2) Nanoparticles Synthesized by the Sol-Gel Method, J. Cond. Matt. 2025; 03 (01): 30-35

Available from:
https://doi.org/10.61343/jcm.v3i01.71

Introduction

Titanium Dioxide (TiO_2) which is also defined as titania is one of the most versatile and widely studied materials in modern science and technology. Known for its exceptional chemical inertness, thermal stability, and environmental friendliness, TiO_2 is a naturally occurring oxide of titanium. It exists in three primary crystalline forms: anatase, rutile, and brookite, each possessing unique physical and chemical properties. Among these, the anatase and rutile phases are of particular interest due to their remarkable photocatalytic performance and optical characteristics. The anatase phase is known for its high reactivity and is often used in photocatalysis, while the rutile phase exhibits better thermal and structural stability.

Due to its non-toxic nature and strong UV light absorption, TiO_2 has found widespread applications across various industries. In the pigment industry, it serves as an essential component for paints, coatings, and plastics, providing superior opacity and brightness. In the cosmetics sector, it is used in sunscreens and skincare products to protect against harmful UV radiation. Titanium Dioxide used in the pigment industry can also be defined as titanium white or pigment white. Furthermore, TiO_2 has gained significant attention in environmental applications, such as air purification, water treatment, and self-cleaning surfaces, owing to its photocatalytic properties that enable the breakdown of organic pollutants.

In recent years, TiO_2 has emerged as a key material in renewable energy technologies. It is widely used in dye-sensitized solar cells (DSSCs) and as a photocatalyst for hydrogen production through water splitting. Its ability to function as a photocatalyst under UV light has also led to innovations in energy-efficient coatings and anti-bacterial surfaces. Moreover, its abundance in nature, low cost, and ease of synthesis have contributed to its growing importance in industrial and research domains.

Extensive studies are being conducted to further enhance the efficiency and functionality of TiO_2, particularly by tailoring its properties through methods such as doping, surface modification, and nano-structuring. These

advancements aim to optimize its performance for specific applications and explore its potential in emerging fields like biomedical devices, sensors, and advanced energy storage systems.

Overall, the versatility, affordability, and eco-friendly nature of Titanium Dioxide make it an indispensable material in both traditional industries and cutting-edge technological advancements.

The Sol-Gel method is a cost-effective and versatile chemical route for synthesizing metal oxide (MO) nanoparticles, offering precise control over particle size and morphology. X-ray diffraction (XRD) is a fundamental tool for phase identification, lattice parameter determination, and crystallite size estimation. This study aims to compare the structural properties of TiO_2 nanoparticles synthesized via the Sol-Gel method under various conditions using XRD analysis.

Experimental Methods

Materials

Table 1: Materials used in the synthesis of TiO_2

Chemical Name	Chemical Structure
Titanium tetraisopropoxide (TTIP) [the titanium precursor]	$Ti\{OCH(CH_3)_2\}_4$
Acetic acid	CH_3COOH
Distilled water	H_2O

Methodology

The Sol-Gel method is a versatile chemical process widely used for synthesizing advanced materials, such as nanoparticles, thin films, and ceramics. It involves a transformation from a liquid solution (sol) into a solid network (gel) through hydrolysis and condensation reactions of metal alkoxides or inorganic salts. This technique allows precise control over material properties, including particle size, morphology, and composition.

One of the main benefits of the Sol-Gel method is its ability to synthesize materials at relatively low temperatures, which is an advantage over traditional high-temperature techniques. The process generally starts with the preparation of a precursor solution, typically using metal alkoxides like titanium (IV) isopropoxide. This solution undergoes hydrolysis and condensation, leading to the formation of a gel. Subsequent drying and calcination convert the gel into the desired crystalline phase with specific structural characteristics.

The Sol-Gel method is highly adaptable and can produce materials in various forms, such as powders, thin films, fibers, or monolithic structures. It is widely employed in applications like optical coatings, catalysts, sensors, and bioactive materials. The technique is especially valued for producing highly pure and homogeneous materials, essential for many advanced technologies.

In recent developments, the Sol-Gel process has become increasingly popular for synthesizing metal oxide nanoparticles, including Titanium Dioxide (TiO_2). This method provides precise control over the structural and surface properties of nanoparticles, making it ideal for applications in photocatalysis, energy storage, and environmental cleanup. Its simplicity, cost-effectiveness, and scalability have made the Sol-Gel method a favored choice in both academic research and industrial manufacturing.

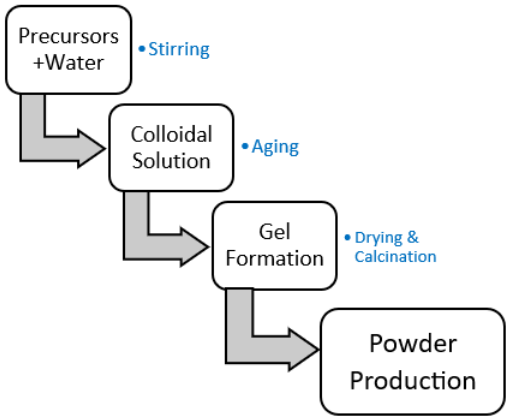

Figure1: The flowchart of Sol-gel synthesis.

The Sol-Gel process for Titanium Dioxide involved the hydrolysis and condensation of TTIP. The procedure was as follows:

1. Mix 20 ml of titanium isopropoxide with 40 ml of glacial acetic acid.
2. Stir the mixture using a magnetic stirrer until a homogeneous solution forms.
3. Gradually add 120 ml of deionized water to the solution, drop by drop, while stirring continuously for 2 hours to form the sol.
4. Place the solution in an oven set at 90°C and heat for about 12 hours to facilitate gel formation.
5. Pulverize and dry the gel at 200°C for 2 hours, resulting in the formation of a white powder.

Figure 2: Transformation of Sol to Gel.

I have carried out the experiment by changing different parameters like the precursor ratio, water amount and the calcination temperature by 200 °C, 400 °C and 500 °C which is shown in a table form as follows:

Table 2: The change in the different parameters with the different samplings.

Sample	TTIP (ml)	Acetic Acid (ml)	Dist. Water (ml)	Temperature ˚C
S1	20	40	120	200
S2	30	40	120	200
S3	20	40	200	200
S4	20	40	120	400
S5	25	45	125	500

Results and Discussion

Characterization

X-Ray diffraction is basically one of the most useful powder analysis techniques used for the detailed study of nanomaterial's structural belongings for all the types of crystal clear, limpid, transparent, and composed of crystals. X-ray diffraction analysis can be used for the following aspects:

- **Crystallinity:** Can point out whether nanoparticles are crystalline or amorphous in nature.
- **Phase:** Can pick out the phase of polycrystalline materials and compounds.
- **Crystal orientation:** Can provide detailed data on the preferred crystal orientation of a material.
- **Grain size:** Can provide details on the average grain size of a material.
- **Strain:** Can provide information on the strain in a material.
- **Crystal defects:** Can supply the data on how the crystal defects are forming inside any material.

Principle of XRD: It operates on the principle of constructive interference, where monochromatic X-rays interact with the periodic lattice planes of a crystal. When an X-ray beam strikes a crystalline material, diffraction takes place in accordance with Bragg's Law.

Steps in XRD Analysis of the Experiments-

1. **Sample Preparation**

   Five different powder samples have been prepared using the methodology, packed in glass bottles keeping stored at the room temperature and then sent to the laboratory for the analysis. ***Divergence Slit:*** A fixed divergence slit with a size of 0.3599° was used. ***Specimen Details:*** The specimen length was 10 mm, and measurement was conducted at 25°C. ***Anode Material:*** Copper (Cu) was used as the anode material with (λ)=1.5406 Å.

2. **Data Collection**

   The scan was performed in Gonio mode, covering a 2θ range from 10.0066° to 89.9956° with a step size of 0.013° and a step time of 18.87 seconds. The scan type was continuous. The XRD pattern is recorded as intensity versus the diffraction angle (2θ) for each sample.

3. **Analysis**

   The peaks in the XRD pattern are matched with reference patterns to identify phases.

4. **Calculations**

   Additional parameters have been calculated from the peak width and position. The result of which confirmed the nanosize of TiO_2.

5. **Comparison**

   Five different samples undergo the calculations and the detailed datasheet was prepared for the comparison.

Results

The comparison graph of all the TiO_2 nanoparticle samples is shown here in the below figure3. This shows the decrease in the peak intensity confirming the anatase phase.

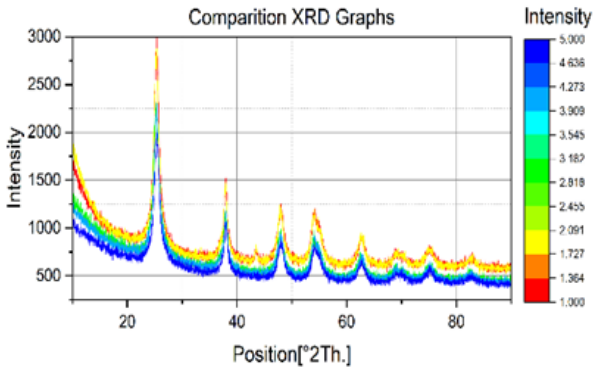

Figure 3: The peak intensity comparison of nanosized TiO_2.

X-Ray Diffraction analysis is a widely used technique for assessing the crystallinity of synthesized nanoparticles (NPs). The height of the peaks shown in the XRD graph for all the different samples indicate whether the nanoparticles are crystalline or amorphous.

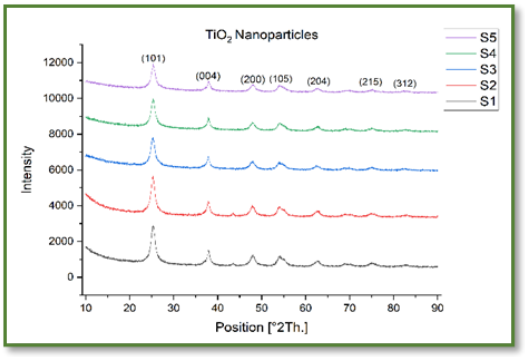

Figure 4: X-Ray Diffraction patterns of TiO_2 samples

Figure above shows the X-Ray Diffraction patterns of five different nanosized TiO_2 samples labelled as S1, S2, S3, S4 and S5 with the varying conditions given in the table2 above. The experimental XRD pattern agrees with the JCPDS card no. 21-1272 (anatase TiO_2) and the XRD pattern of TiO_2 nanoparticles other literature. High intensity peaks at around 25 ˚C and 37 ˚C strongly confirms the presence of Anatase phase of TiO_2 nanoparticles. The crystallite size of these particles can be measured using Debye–Scherrer's formula:

$$D = \frac{0.94\lambda}{\beta \cos\theta}$$

Where, 0.94 is the shape factor, λ is the wavelength of the X-ray radiation for Cu Ka, and β is the line width at half-maximum height. The position with the corresponding FWHM for all five samples is given in the below graph.

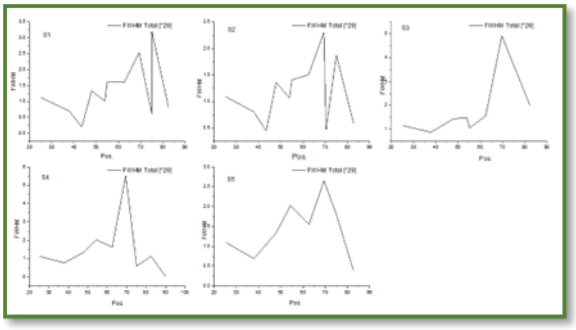

Figure 5: The FWHM versus Position graph of nanosized TiO_2.

The crystalline size with the corresponding FWHM for all five samples is given in the below table by using the equation given above:

Table 3: The change in the crystalline size by varying conditions for nanosized TiO_2.

Sample Name	FWHM (radian)	Crystalline size	Pos. [°2θ]
S1	0.01219	12.358	37.9004
S2	0.01402	10.667	37.8612
S3	0.01529	9.780	37.8327
S4	0.01330	11.245	37.9026
S5	0.01205	12.405	37.9466

The table summarizes the XRD analysis results for TiO_2 samples (S1 to S5), showing their Full Width at Half Maximum (FWHM), crystalline size, and peak positions at specific 2θ angles. The FWHM values range from 0.01205 to 0.01529 radians, corresponding to crystalline sizes between 9.780 nm and 12.405 nm. The 2θ positions of the diffraction peaks vary slightly among the samples, falling between 37.8327° and 37.9466°. This data reflects variations in the crystalline properties of the synthesized nanoparticles. This reflects that S3 with the maximum water part (200 ml) in it consists of the lowest particle size.

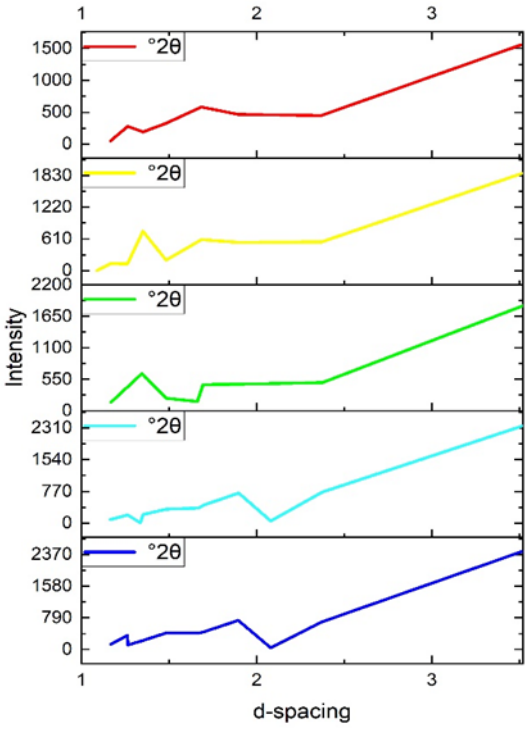

Figure 6: The comparison graph of TiO_2 nanoparticles for intensity versus d-spacing.

Significance of d-spacing

1. **Crystal Structure Identification:** The d-spacing values, combined with X-ray diffraction patterns, help identify the phases and structure of a material.
2. **Lattice Parameter Calculation:** It is used to calculate the lattice constants of a crystal system (e.g., cubic, tetragonal, hexagonal).
3. **Material Properties:** Changes in d-spacing can indicate lattice strain, defects, or distortions in the crystal structure.

Real-World Applications

Below are some emerging applications of TiO_2 nanoparticles in relation to the XRD findings:

Self-Cleaning Surfaces

TiO_2-coated surfaces exhibit superhydrophilicity and photocatalytic degradation of organic materials.

XRD analysis of crystallinity and phase composition can help optimize TiO_2 films for self-cleaning coatings used in windows, textiles, and solar panels.

Anti-Microbial and Bio-Medical Applications

TiO_2 nanoparticles show antibacterial properties under UV light, useful in hospital coatings, wound dressings, and implants.

XRD phase identification (anatase-dominant) can correlate with bioactivity and toxicity levels, ensuring safety in biomedical applications.

Hydrogen Production via Water Splitting

TiO_2 is a key material in photoelectrochemical (PEC) water splitting to generate hydrogen fuel.

XRD data on crystal phase, lattice strain, and oxygen vacancies can help optimize TiO_2 nanostructures for higher photocatalytic efficiency in hydrogen evolution.

Smart Windows and Electrochromic Devices

TiO_2 is used in smart glass technology that changes transparency based on external stimuli.

XRD studies can reveal structural stability, ensuring long-term performance in energy-efficient buildings and vehicles.

Conclusion

We have successfully synthesised TiO2 nanoparticles by using the colloidal route of methodology said to be the Sol-Gel method in very safe and environment friendly atmosphere. By changing different parameters, we have seen the changes appearing in intensity, Full width at half maximum and the crystalline size. At the end we came to know that Þ In the grown crystal the d- value is fingerprints of a specific sample which is determined by XRD. The shifting of plane d-spacing is due to the rearrangement of lattice positions. It is due to the doping of ions, atoms and impurities. Another thing which affects the d value is stress forces which is external forces.

Comparative analysis of the nanomaterials suggests:

- **Effect of Calcination Temperature:** Higher temperatures increased crystallinity but promoted the anatase-to-rutile phase transformation.
- **Effects of pH:** Alkaline conditions resulted in mixed phases, while acidic conditions favored pure anatase.
- **Effect of Hydrous solution:** More hydrous solution decreases the crystallinity and hence particle size.

This comparative XRD analysis demonstrates that synthesis parameters such as calcination temperature and pH significantly influence the structural properties of TiO_2 nanoparticles. Optimal conditions for achieving high-purity anatase with small crystallite sizes were identified, providing a foundation for tailoring TiO_2 properties for specific applications. Future studies could explore doping effects and advanced characterization techniques to further enhance TiO_2 functionality.

Acknowledgement

The authors would be happy to thank the Sophisticated Analytical Instrumentation Facility, Punjab university, Chandigarh for providing XRD instrument to analyse the samples.

References

1. A. Fujishima, K. Honda, Electrochemical photolysis of water at a semiconductor electrode, Nature 238 (1972) 37–38. https://doi.org/10.1038/238037a0.
2. C.H. Ao, S.C. Lee, Indoor air purification by photocatalyst TiO_2 immobilized on an activated carbon filter installed in an air cleaner, Chem. Eng. Sci. 60 (2005) 103–109. https://doi.org/10.1016/j.ces.2004.01.073.
3. Y. Paz, Application of TiO_2 photocatalysis for air treatment: patents' overview, Appl. Catal. B Environ. 99 (2010) 448-460. https://doi.org/10.1016/j.apcatb. 2010.05.011.
4. M. Hussain, N. Russo, G. Saracco, Photocatalytic abatement of VOCs by novel op timized TiO_2 nanoparticles, Chem. Eng. J. 166 (2011) 138–149. https://doi.org/10. 1016/j.cej.2010.10.040.
5. S. Miar Alipour, D. Friedmann, J. Scott, R. Amal, TiO2 /porous adsorbents: recent advances and novel applications, J. Hazard. Mater. 341 (2018) 404-423. https://doi.org/10.1016/j.jhazmat.2017.07.070.
6. M. Landmann, E. Rauls, W.G. Schmidt, The electronic structure and optical response of rutile, anatase and brookite TiO2, J. Phys. Condens. Matter 24 (2012) 195503. https://doi.org/10.1088/0953-8984/24/19/195503.
7. B.L. Diffey, Sources and measurement of ultraviolet radiation, Methods 28 (2002) 4-13. https://doi.org/10.1016/S1046-2023(02)00204-9.

8. W.-J. Yin, S. Chen, J.-H. Yang, X.-G. Gong, Y. Yan, S.-H. Wei, Effective band gap narrowing of anatase TiO2 by strain along a soft crystal direction, Appl. Phys. Lett. 96 (2010). https://doi.org/10.1063/1.3430005 221901.
9. R. Long, N.J. English, Band gap engineering of double- cation-impurity-doped anatase-titania for visible-light photocatalysts: a hybrid density functional theory approach, Phys. Chem. Chem. Phys. 13 (2011) 13698–13703. https://doi.org/10. 1039/C1CP21454C.
10. S.G. Kumar, L.G. Devi, Review on modified TiO2 photocatalysis under UV/Visible light: selected results and related mechanisms on interfacial charge carrier transfer dynamics, J. Phys. Chem. A 115 (2011) 13211–13241. https://doi.org/10.1021/ jp204364a.
11. J. Godnjavec, J. Zabret, B. Znoj, S. Skale, N. Veronovski, P. Venturini, Investigation of surface modification of rutile TiO_2 nanoparticles with SiO_2/Al_2O_3 on the properties of polyacrylic composite coating, Prog. Org. Coat. 77 (2014) 47-52. https://doi.org/10.1016/j.porgcoat.2013.08.001.
12. S. Ke, X. Cheng, Q. Wang, Y. Wang, Z. Pan, Preparation of a photocatalytic TiO2 / ZnTiO3 coating on glazed ceramic tiles, Ceram. Int. 40 (2014) 8891-8895. https://doi.org/10.1016/j.ceramint.2014.01.027.
13. R. Phienluphon, K. Pinkaew, G. Yang, J. Li, Q. Wei, Y. Yoneyama, T. Vitidsant, N. Tsubaki, Designing core ($Cu/ZnO/Al_2O_3$)–shell (SAPO-11) zeolite capsule cata lyst with a facile physical way for dimethyl ether direct synthesis from syngas, Chem. Eng. J. 270 (2015) 605–611. https://doi.org/10.1016/j.cej.2015.02.071.
14. Z. Li, Y. Hou, B. Ma, X. Wu, Z. Xing, K. Li, Super-hydrophilic porous TiO_2 -ZnO composite thin films without light irradiation, Environ. Prog. Sustain. Energy 35 (2016) 1121–1124. https://doi.org/10.1002/ep.12308.
15. Y. Yao, G. Li, S. Ciston, R.M. Lueptow, K.A. Gray, Photoreactive TiO_2 /carbon na notube composites: synthesis and reactivity, Environ. Sci. Technol. 42 (2008) 4952–4957. https://doi.org/10.1021/es800191n.
16. Y.-J. Xu, Y. Zhuang, X. Fu, New insight for enhanced photocatalytic activity of TiO_2 by doping carbon nanotubes: a case study on degradation of benzene and methyl orange, J. Phys. Chem. C 114 (2010) 2669–2676. https://doi.org/10.1021/jp909855p.
17. Y. Liang, H. Wang, H. Sanchez Casalongue, Z. Chen, H. Dai, TiO_2 nanocrystals grown on graphene as advanced photocatalytic hybrid materials, Nano Res. 3 (2010) 701–705, https://doi.org/10.1007/s12274-010-0033-5.
18. Y. Zhang, Z.-R. Tang, X. Fu, Y.-J. Xu, TiO2−graphene nanocomposites for gas-phase photocatalytic degradation of volatile aromatic pollutant: is TiO2 −graphene truly different from other TiO2 −carbon composite materials? ACS Nano 4 (2010) 7303–7314. https://doi.org/10.1021/nn1024219.
19. J. Liu, H. Bai, Y. Wang, Z. Liu, X. Zhang, D.D. Sun, Self-assembling TiO_2 nanorods on large graphene oxide sheets at a two-phase interface and their anti-recombina tion in photocatalytic applications, Adv. Funct. Mater. 20 (2010) 4175–4181. https://doi.org/10.1002/adfm.201001391.
20. K. Zhou, Y. Zhu, X. Yang, X. Jiang, C. Li, Preparation of graphene– TiO2 composites with enhanced photocatalytic activity, New J. Chem. 35 (2011) 353–359. https://doi.org/10.1039/C0NJ00623H.
21. J. Auvinen, L. Wirtanen, The influence of photocatalytic interior paints on indoor air quality, Atmos. Environ. 42 (2008) 4101–4112. https://doi.org/10.1016/j.atmosenv.2008.01.031.
22. M. Nuño, R.J. Ball, C.R. Bowen, Study of solid/gas phase photocatalytic reactions by electron ionization mass spectrometry: study of photoreactions by mass spec trometry, J. Mass Spectrom. 49 (2014) 716–726. https://doi.org/10.1002/jms. 3396.
23. M. Nuño, R.J. Ball, C.R. Bowen, R. Kurchania, G.D. Sharma, Photocatalytic activity of electrophoretically deposited (EPD) TiO_2 coatings, J. Mater. Sci. 50 (2015) 4822–4835. https://doi.org/10.1007/s10853-015-9022-0.
24. M. Nuño, G.L. Pesce, C.R. Bowen, P. Xenophontos, R.J. Ball, Environmental per formance of nano-structured $Ca(OH)_2$/ TiO_2 photocatalytic coatings for buildings, Build. Environ. 92 (2015) 734-742. https://doi.org/10.1016/j.buildenv.2015.05. 028.
25. P. Wolkoff, G.D. Nielsen, Organic compounds in indoor air-their relevance for perceived indoor air quality? Atmos. Environ. 35 (2001) 4407-4417. https://doi.org/10.1016/S1352-2310(01)00244-8.

Study of Gain Spectra in Optical Fiber under Modulation Instability

U Singh[1,a], Ramesh Kumar[2], A K Nagar[3] and O P Swami[3]

[1] *Department of Physics, SRRM Govt College, Jhujhunu, 333001, Rajasthan, India.*
[2] *Department of Physics, SNDB Govt PG College, Nohar, Hanumangarh, 335523, Rajasthan, India.*
[3] *Department of Physics, Govt Dungar college, Bikaner, 334001, Rajasthan, India*

[a] usnlphy@gmail.com

Abstract

In this paper, we consider the phenomenon of modulation instability. Due to nonlinear phenomenon of self-phase modulation, the propagation of continuous wave beam is essentially unstable. For modulation instability, we plot various curves for gain spectra and find the maximum gain which shows the gain dependence on power, group velocity dispersion parameter and nonlinearity parameter.

Keywords: Modulation Instability, Gain Spectra, Dispersion, Nonlinear.
Received 28 January 2025; First Review 21 February 2025; Accepted 07 March 2025

*** Address of correspondence**
U Singh
Department of Physics, SRRM Govt College, Jhujhunu, 333001, Rajasthan, India.

Email: usnlphy@gmail.com

How to cite this article
U Singh, Ramesh Kumar, A K Nagar and O P Swami, Study of Gain Spectra in Optical Fiber under Modulation Instability, J. Cond. Matt. 2025; 03 (01): 36-37.

Available from:
https://doi.org/10.61343/jcm.v3i01.75

Introduction

Modulation instability (MI) is a nonlinear phenomenon in optical fibers that results from the interaction between nonlinear Kerr effects and fiber dispersion [1]. MI leads to the growth of perturbations on a continuous wave (CW), which can result in spectral broadening. This process is crucial for applications such as supercontinuum generation, optical communication, and soliton formation in fibers [2].

The MI process is strongly influenced by parameters such as the second-order dispersion coefficient β_2, the input power level P_0, and the nonlinear parameter γ. The gain spectrum associated with MI determines the range of frequencies over which perturbations grow exponentially. This paper explores the theoretical foundations of MI, the mathematical formulation of the MI gain spectrum, and presents various curves for gain spectra under various conditions [3].

Theory

MI in optical fibers can be described by the nonlinear Schrödinger equation (NLSE) under the condition of anomalous dispersion. The NLSE is given by:

$$\iota\frac{\partial A}{\partial z}+\frac{\beta_2}{2}\frac{\partial^2 A}{\partial T^2}+\gamma|A|^2A=0$$

Where symbols have their usual meaning.

In the case of a CW input, MI occurs when perturbations are introduced on the input field. The gain spectrum associated with MI is given by:

$$g(\Omega)=|\beta_2\Omega|\sqrt{\Omega_c^2-\Omega^2}$$

Where Ω is the frequency shift from the input signal and $\Omega_c^2=\frac{4\gamma P_0}{\beta_2}$ is the cutoff frequency, beyond which there is no gain. The gain $g(\Omega)$ is real and positive for $|\Omega|<\Omega_c$, and the frequency shifts outside this range do not exhibit any growth [4].

Methodology

The parameters used for the numerical study are nonlinear coefficient γ, dispersion coefficient β_2 and input powerP_0.

The gain spectrum was calculated using the formula provided in the theoretical section. We used Scilab to compute and plot the gain spectra for different parameters.

The cutoff frequency Ω_c was calculated for each power level using the relation:

$$\Omega_c=\sqrt{\frac{4\gamma P_0}{|\beta_2|}}$$

The gain $g(\Omega)$ is computed over the range of Ω and results are plotted to compare the gain spectra for various parameters.

Results and Discussion

Gain Spectra for Different Input Powers

The MI gain spectra were computed for power levels $P_0 = 1\,W, 4\,W\ and\ 7\,W$.

The results show that as the power increases, the maximum gain and the bandwidth of the MI gain spectrum also increase. This behavior is expected because higher input power leads to stronger nonlinear interactions in the fiber, thereby enhancing the modulation instability effect.

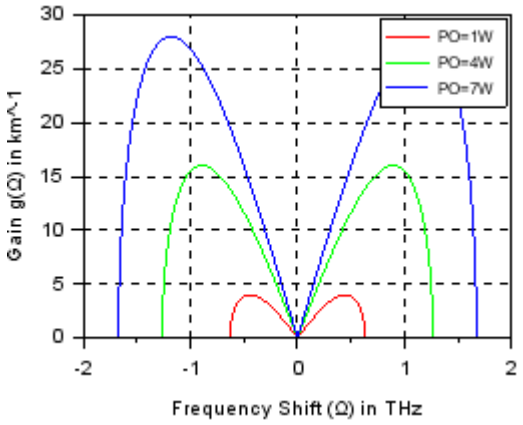

Figure 1: Gain vs Frequency Shift for different power levels

Figure 1 confirms the fact.

Impact of Dispersion Coefficient

The role of the dispersion coefficient β_2 was also analyzed. With a negative β_2 (anomalous dispersion), the MI effect is enhanced, leading to higher gains. For normal dispersion (β_2>0), MI is suppressed, and no gain is observed.

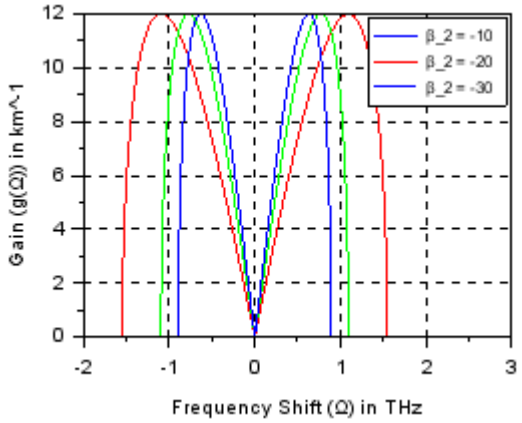

Figure 2: Gain vs Frequency Shift for different $\boldsymbol{\beta_2}$ values in ps^2.

Dependence on Nonlinearity

Here is the figure which shows the dependence of gain on nonlinearity.

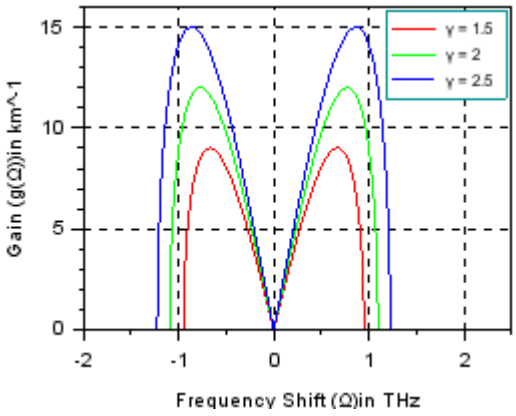

Figure 3: Gain vs Frequency Shift for different $\boldsymbol{\gamma}$ values in $W^{-1}km^{-1}$

Conclusion

The study of gain spectra under modulation instability reveals the critical role played by the nonlinear and dispersive properties. The nonlinear coefficient γ, dispersion coefficient β_2, and input power level P_0 all significantly influence the MI gain spectrum. As shown in the numerical results, higher input powers increase the gain and broaden the bandwidth of modulation instability. This has important implications for designing optical fiber systems that exploit MI for applications such as supercontinuum generation and all-optical signal processing.

These results demonstrate that the asymptotic stage of Modulation Instability is universal since the behavior of a large class of perturbations characterized by a continuous spectrum is described by the same asymptotic state. [5]

Future work may explore the interaction of MI with higher-order dispersion and Raman scattering, as well as its effects in photonic crystal fibers.

References

1. Agrawal, G. P. (2012). Nonlinear Fiber Optics (5th ed.). Academic Press.
2. Dudley, J. M., Genty, G., & Coen, S. (2006). *Supercontinuum generation in photonic crystal fiber*. Reviews of Modern Physics, *78*(4), 1135-1184.
3. Kivshar, Y. S., & Agrawal, G. P. (2003). *Optical Solitons: From Fibers to Photonic Crystals*. Academic Press.
4. Zakharov, V. E., & Shabat, A. B. (1972). *Exact theory of two-dimensional self-focusing and one-dimensional self-modulation of waves in nonlinear media*. Soviet Physics JETP, *34*(1), 62-69.
5. Biondini, G., & Mantzavinos, D. (2016). *Universal Nature of the Nonlinear Stage of Modulational Instability*. Physical Review Letters, *116* (4), 043902.

Graphene-Graphullerene Heterostructure: A Novel Material for High-Performance Capacitors

Anjna Devi[1,a], Satish Kumar[2,b], Arun Kumar[2,c]

[1] Government Degree College Baroh, Kangra-176054, Himachal Pradesh, India.
[2] Government Degree College Bilaspur, Bilaspur-174001, Himachal Pradesh, India.

[a] anjnahpu90@gmail.com
[b] 97satish02@gmail.com
[c] arun242493@yahoo.com

Abstract

This study introduces a novel graphene-graphullerene heterostructure as a promising material for high-performance capacitors. Compared to pristine graphene, this heterostructure exhibits a significantly larger surface area and porosity which enhance its energy storage capacity. Pristine graphullerene is a semiconductor with a bandgap of 0.92 eV and its integration with graphene effectively modifies its electronic properties, rendering it conductive as confirmed by band structure analysis. The unique combination of graphene's high conductivity and graphullerene's extended surface area and porosity presents a promising avenue for developing capacitors with exceptional performance characteristics.

Keywords: DFT, Graphullerene, Electronic Band Structure.
Received 28 January 2025; First Review 02 February 2025; Accepted 07 March 2025

*** Address of correspondence**
Anjna Devi
Government Degree College Baroh, Kangra-176054, Himachal Pradesh, India.

Email: anjnahpu90@gmail.com

How to cite this article
Anjna Devi, Satish Kumar, Arun Kumar, Graphene-Graphullerene Heterostructure: A Novel Material for High-Performance Capacitors, J. Cond. Matt. 2025; 03 (01): 38-40.

Available from:
https://doi.org/10.61343/jcm.v3i01.76

Introduction

Carbon's diverse bonding allows it to form a variety of structures, such as graphite, diamond, fullerenes, carbon nanotubes, and graphene [1]. These allotropes exhibit a wide range of properties; for instance, diamond is known for its hardness and thermal conductivity, while graphite displays a layered structure and electrical conductivity. Recent research has unveiled novel 2D materials like Graphullerene, a recently synthesized carbon allotrope [2-4]. Graphullerene's unique structure boasts high porosity [3-5] and a significant bandgap, making it a promising candidate for various applications. The integration of Graphullerene with graphene could yield a material with exceptional electrical and surface properties, particularly for energy storage devices such as capacitors. This study explores the Graphene-Graphullerene Heterostructuring (H-Gra/Gph) which leads to high-performance capacitor material.

Method

We conducted density functional theory (DFT) calculations using the SIESTA code [6] to investigate the electronic properties of the H-Gra/Gph. A GGA-PBE [7] functional and a DZP basis set with a confinement energy of 20 meV were applied. Geometry optimization was performed using the conjugate gradient method with a force tolerance of 0.01 eV/Å, and a 10x10x1Monkhorst-Pack k-point mesh [8] was used to sample the Brillouin zone. A 15 Å vacuum was applied along the z-axis to minimize interactions between periodic images. Norm-conserving pseudopotentials were employed for all atomic species.

Results and Discussion

The H-Gra/Gph was formed by integrating graphene sheets with graphullerene, creating a composite material with a stable, low-energy configuration. The relaxed hybrid structure of H-Gra/Gph is shown in figure 1(a). The structural optimization of H-Gra/Gph are depicted in Figure 1 (b and c).

Figure 1(b) shows the variation of total energy (E_{Total}) with respect to the lattice constant (a). The plot reveals a well-defined minimum, indicating a stable configuration for the heterostructure at an optimized lattice constant. Figure 1(c) presents the plot of total energy (E_{Total}) versus the vertical

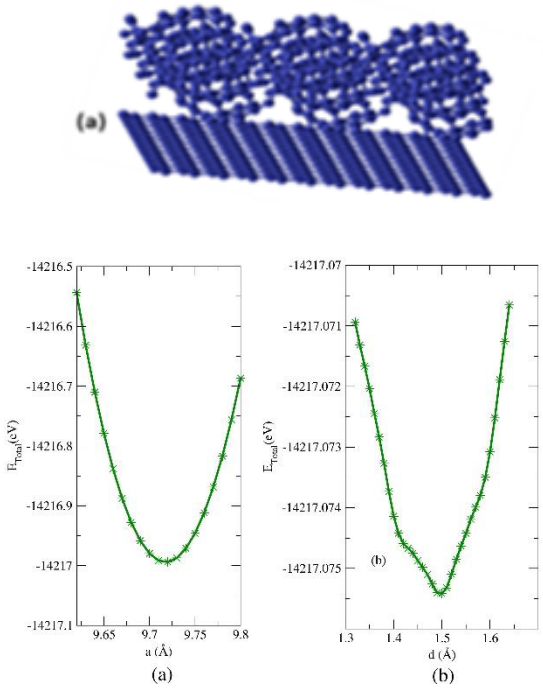

Figure 1: (a) Structure of H-Gra/Gph **(b)** Lattice constant (a) vs total energy (E_{Total}) plot and **(c)** vertical separation between Graphene and Graphullerene (d) vs total energy (E_{Total}) plot for H-Gra/Gph.

separation distance (d) between graphene and Graphullerene. This plot also exhibits a clear minimum, suggesting an energetically favourable interlayer distance for the heterostructure. These results provide valuable insights into the structural stability and optimal configuration of the H-Gra/Gph. A comparison of the structural parameters of pure Graphullerene, H-Gra/Gph. and graphene provided in table1.

Table 1: Optimized lattice constant (a), binding energy (E_b), band gap energy (E_g) of Graphene, Graphullerene and H-Gra/Gph.

Systems	a (Å)	d (Å)	E_b (eV/atom)	E_g (eV)
Graphene	2.49	----	-7.81 (-9.53)[12]	0.0
Graphullerene	9.32 (9.17)[11]	----	-7.44 (-8.564) [4]	0.92 (I) (0.7 (I))[4]
H-Gra/Gph	9.72	1.50	-7.27	----

The lattice constant of the H-Gra/Gph (9.72 Å) is slightly larger than that of pure Graphullerene (9.32 Å), while the binding energy is slightly lower (-7.27 eV/atom compared to -7.44 eV/atom). This suggests that the heterostructure is stable but has a slightly weaker interatomic bonding compared to pure Graphullerene. [4, 9-12].

Figure 2 (a) and (b) shows the electronic band structure and density of states (DOS) of pure Graphullerene and the H-Gra/Gph. Pure Graphullerene exhibits a band gap of approximately 0.92eV, confirming its semiconducting nature. The DOS plot shows a clear energy gap at the Fermi level supporting this observation. In contrast, the H-Gra/Gph exhibits a metallic behaviour with a zero-band gap. The DOS plot shows a significant overlap of the valence and conduction bands at the Fermi level, indicating the absence of an energy gap. This change in electronic properties is attributed to the interaction between Graphene and Graphullerene in the heterostructure, which modifies the band structure and leads to the formation of metallic states. Figure 2 (c) and (d) illustrates the density of states (DOS) and integrated density of states (IDOS) for the H-Gra/Gph, pure Graphullerene and Graphene. The prominent peaks in the DOS plots correspond to the electronic states available for charge conduction. The integrated DOS provides a cumulative measure of the number of states up to a given energy level. Comparing the Integrated Density of States (IDOS) plots, we observe that pure Graphullerene exhibits a higher density of states near the Fermi level compared to the H-Gra/Gph. However, it is important to note that capacitance is directly proportional to the density of states at the Fermi level (E_F). While pure Graphullerene may have a higher DOS, the conducting nature of the H-Gra/Gph, along with its porous and large surface area, make it a more promising candidate for electrode materials in supercapacitors.

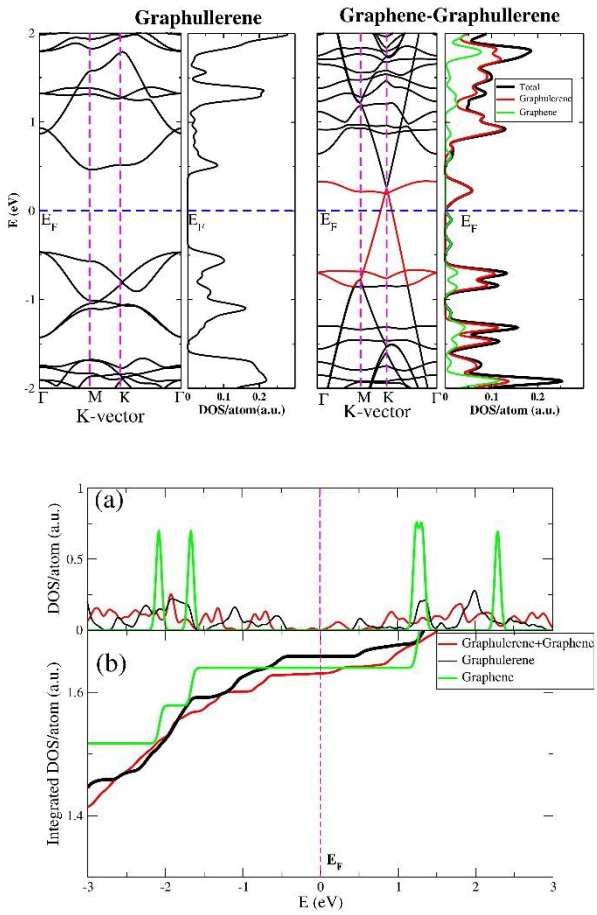

Figure 2: Electronic band structure and density of states of (a) Graphullerene and (b) H-Gra/Gph, (c) Density of states (DOS) and (d) Integrated density of states (IDOS) of H-

Conclusion and Future Prospective

In conclusion, this study has explored the potential of the H-Gra/Gph as a promising material for high-performance capacitors. DFT calculations revealed that the integration of graphene with graphullerene significantly modifies the electronic properties, transforming the semiconducting nature of pure graphullerene into a conductive material. The enhanced conductivity, coupled with the large surface area and porosity of the heterostructure can significantly offers advantages for energy storage applications and more research is needed to synthesises and fabrication processes to fully realize the potential applications of this novel material.

References

1. A. Geim and K Novoselov, Nature Mater, 6,183 (2007).
2. M. A. Khan, M. Atif, M. N. Leuenberger. arXIV 2404.16743. (2024).
3. L. Guang-Ye, M. Shi-Cong, Q. Xin-Yue, N. Jing, L. Jun-Xi, L. Pei-Yi, N. Feng, C. Shi-Zhang, ACS Applied Nano Materials 8(1), 649 (2024).
4. U. Argaman and G. Makov, npj Comp. Mat. 9, 211 (2023).
5. C. Liu, X. Yan, F. Hu, G. Gao, G. Wu, and X. Yang, Adv. Mater 30, e1705713 (2017).
6. J. M. Soler, E. Artacho, J. D. Gale, A. Garcia, J. Junquera, P. Ordejon and D. S. Portal, J. Phys.: Condes. Matter, 14 2745 (2002).
7. J. P. Perdew, K. Burke and M. Ernzerhof, Phys. Rev. Lett, 77:3865 (1996).
8. K. Chaudhary and F. Tavazza Comp. Mater. Sc. 161, 300 (2019).
9. A. Z. Zahran and G. P. Srivastava, App. Surf. Sc. 256 (19), 5783 (2010)
10. A. Devi, A. Kumar, A. Singh and P. K. Ahluwalia, AIP Conf. Proc. 2115**,** 030386 (2019).
11. S. E. Veras, E. Espada and G. Morell, Carbon Trends 15, 100360 (2024).
12. A. Devi, A. Kumar, P. K. Ahluwalia A. Singh, Materials Science and Engineering: B 271**,** 115237 (2021).

Nonlinearly Wave-Wave Interaction Leads to Solar Coronal Heating

B K Das[1,a], S K Singh[2], L K Gupta[3], R Prasad[4] and Priyank Kumar[5]

[1] *Department of Physics, COER University, Roorkee-247667, Uttrakhand, India.*
[2] *Department of Physics, Govt College Lamta, Balaghat-481551, MP, India.*
[3] *Department of Physics, Shyamlal Saraswati Mahavidyalaya, Bulandshahr-203395, UP, India*
[4] *Department of Physics, Galgotia College of Engineering and Technology, Greater Noida-201310, UP, India.*
[5] *Department of Applied Sciences & Humanities, Government Polytechnic, Dahod-389151, Gujarat, India.*

[a] drbkdas.iitd@gmail.com

Abstract

Nonlinear formulation of slow Alfvén wave in magnetized plasma which can be an essential ingredient of the solar space plasma is being studied. Various method has been adopted, mathematical formulation of the magnetohydrodynamic (MHD) waves can interpret the astrophysical phenomena happening in space plasma. The mathematical formulation of slow Alfvén wave and kinetic Alfvén wave (KAW) has been done from Maxwell equation as a make model equation. On the perturbation of slow Alfvén wave by pumped wave, the coupled wave dynamics has studied and their numerical simulation has been performed at $\theta = 50^0$. Several localized filamentary structures have observed with diverse intensities. The spectra associated with magnetic field fluctuations are also observed with Kolmogorov scaling for inertial and dispersive range spectral index which are proportional to $k^{-\frac{5}{3}}$ and k^{-3} respectively.

Keywords: Magneto Hydrodynamics (MHD), Solar Corona, Solar Space.
Received 29 January 2025; First Review 23 February 2025; Accepted 26 February 2025

*** Address of correspondence**
B K Das
Department of Physics, COER University,
Roorkee-247667, Uttrakhand, India.

Email: drbkdas.iitd@gmail.com

How to cite this article
B K Das, S K Singh, L K Gupta, R Prasad and Priyank Kumar, Nonlinearly Wave-Wave Interaction Leads to Solar Coronal Heating, J. Cond. Matt. 2025; 03 (01): 41-45.

Available from:
https://doi.org/10.61343/jcm.v3i01.85

Introduction

The general attribute of solar wind in space plasma is to eject constantly energetic particles in the space plasma. But what is actual mechanism behind the moving out of these highly energetic particles is still unanswered amid the group of investigators. Hence, it is even now an unlocked question in the area of astrophysics that how these energetic particles get accelerated [1]. The Alfvén waves (AWs) can be defined as an electromagnetic wave having low frequency travelling in magnetized plasma which take place due the equilibrium between the tension in magnetic field and ion inertia and therefore, they give the impression in the dynamics of the highly active particles in the space plasma [2]. Hence, it is assumed that AWs may be a good representative for transportation of momentum and energy in the various phenomena happening under geophysical and astrophysical scenario.

So many literatures expressed that the Alfvén waves are most imperative in laboratory plasma and space plasma. The various categories of these waves are able to explain how the transportation of energy takes place in the space plasma. It is, however, difficult to prove the detection of these waves. Recently, researchers [3-4] asserted the uncovering of these intangible Alfvén waves in various levels of solar atmosphere, for example spicules, sun umbra region and bright-points. In fact, these reports indirectly expressed about of Alfvén waves. Theoretically, considering the fully ionized plasmas they [5-6] have been thoroughly studied linear Alfvén waves. Many authors have used different methods to express damping process of moving Alfvén waves. For the damping process of linearity in the Alfvén have been studied by Leake et al. [7]. The heat released due to strongly collapsing of Alfvén waves have been explained by Song [8]. We have studied in a two-fluid model where the damping was occurred due to the collisions in the midst of electrons, ions, and neutrals, also due the collision of charged particles with EM field. Therefore, the researchers used this representation to study the chromosphere as well as the outcomes show that undamped part are closely associated with lower frequencies band

which propagate via atmosphere, at the same time as higher frequencies band are intensely damped near to low altitudes. Under the consideration of Hall - term in the uniform and non-uniform plasmas, the dampness of Alfvén waves occur within the range of ion-cyclotron frequencies, have been studied by Threlfall et al. [9]. Lastly, Lazarian [10] explained the dampness of Alfvén waves is the effect of turbulence, which may have diverse applications in the area of astronomy and astrophysics. The Alfvén waves nonlinearity is important to investigate various nonlinear phenomena occurring in the space plasmas. It has been found that the linearly polarized characteristics of Alfvén wave are amplitude dependent, therefore, larger amplitudes these waves will have more density perturbations and also their motions in line with the magnetic field owing to ponderomotive force. Particularly, the equations of Alfvén wave in linearly polarized form and is travelling parallel (||) to magnetic field in a completely conducting fluid has been solved by Hollweg [11]. He found that the velocity and density fluctuations o longitudinal wave seem to be determined by the gradients of pressure exerted by magnetic field in the low-beta plasma regime. Rankin et al. [12] examined the nonlinearity associated with shear Alfvén waves travelling in the cold magnetized plasmas. They achieved analytical approximations in the limiting case β = 0. The filamentation of nonlinear waves gives us significant evidence for the dissipation problem, which leads to transfer momentum at lower scales. Some analytical studies have been done on the Alfvén waves (AWs)collapse. With small perturbation and interaction of Alfvén waves (AWs) [13] demonstrate that the configuration and development of lower-scale filamentary structures. Marsch et al., [14-15] have mathematically formulated and studied that Alfvén waves were exhibit in the solar wind travelling slowly. Parametric instabilities illustrated and predicted the non-linearity behaviour in the Alfvén waves [16]. The kinetic properties in parametric instability may play a key role which influences the ion dynamics. Consequently, they affect the instability growth rate [17-18]. So many authors [19-20] have already examined the nonlinear interaction of inertial AW with kinetic Alfvén wave. Tam and Chang [21] explained the intrigue of heating and acceleration mechanism of solar wind in which wave-particle interaction is the prime responsible for it. Zheng [22] advocated the special outcomes of nonlinear Alfvén wave. They found that the most important effect is dampness of Alfvén waves which in turn to the heating of plasma in one-dimensional systems but Alfvén wave builds up a damped soliton, when strong dissipation takes place.

Following kinetic theory method, Hasegawa and Chen [23] deliberated various nonlinear phenomena connected with behaviour of kinetic AWs. In situ observations, it has been revealed that variations in the frequency range from 10^{-4} Hz to 10^{-2} Hz. It lies between the state in which fast streams of charged particles deriving through coronal holes and Alfvén waves going away to the sun. This constant magnetic field amplitude as well as small density fluctuations, characterizes the Alfvénic state. The turbulence of slow solar wind gives an idea about the features that the wave's propagation is not easy to categorize and their density fluctuation spectra go along with Kolmogorov power law.

In this paper nonlinear formulation of slow Alfvénic wave have been derived and discussed. With the purpose of investigation the nonlinear property of waves, proper equation of slow Alfvén wave has been derived. Its significance is to explain the particles accelerating behaviour in solar wind as well as to interpret the mechanism of solar coronal heating.

Model Equations for Slow Alfvén Wave Dynamics

(i) Equation of particles flow:

$$\frac{\partial \vec{\upsilon}_j}{\partial t} = -\frac{q_j}{m_j}\vec{\nabla}\phi + \frac{q_j}{cm_j}\left(\vec{\upsilon}\times\vec{B}_0\right) - \frac{\gamma_j k_B T_j}{m_j}\vec{\nabla}\frac{n_j}{n_0} + \frac{\vec{F}_j}{m_j} \qquad (1)$$

(ii) Navier-Stokes equation:

$$\frac{\partial n}{\partial t} + \vec{\nabla}.\left(n\vec{\upsilon}\right) = 0 \qquad (2)$$

(iii) Maxwell-Faraday equation:

$$\left(\vec{\nabla}\times\vec{E}\right) = -\frac{1}{c}\frac{\partial \vec{B}}{\partial t} \qquad (3)$$

Where υ_j, m_j, and T_j *j-type i*, *e*(ion and electron) c, n_0 and B_0 have usual meaning, velocity, masses, temperature, speed of light, density and B- field respectively and

$\vec{F}_j = \left[m_j\left(\vec{\upsilon}_j.\vec{\nabla}\right)\vec{\upsilon}_j - \left(\frac{q_j}{c}\right)\left(\vec{\upsilon}_j\times\vec{B}_0\right)\right]$ is defined for equation of the ponderomotive force. Also, Boltzmann relation expressed as $\phi = \left(\gamma_e k_B T_e/n_0 e\right)n_e - F_{ez}/eik_z$ where ω is ion acoustic and ω_{ci} is ion –cyclotron frequencies. The specific heat ratios γ_e and γ_i are for e=electron and i= ion. , k_B, T_e , n_e, ϕ and F_{ez} are defined for Boltzmann constant, electron temperature electron density, scalar potential and parallel component of electron pondermotive force respectively.

Where $C_s = \left(\frac{\gamma_e k_B T_e + \gamma_i k_B T_i}{m_i}\right)^{\frac{1}{2}}$ is the acoustic speed.

We consider that slow Alfvén wave is propagating of with frequency ω in the direction of *z*-axis, for which

$\vec{B}_0 = B_0\hat{z}$. Here, we consider *x*-*z* plane and it can be expressed as $\vec{k} = k_x\hat{x} + k_z\hat{z}$ and k is usually defined as wave number. Now, we can derive an equation for slow Alfvén wave from above well-known Maxwell's equations.

Operating with $\vec{\nabla}\times$ of Equation (3) and using Ampere's law we find

$$\nabla^2\vec{E} - \vec{\nabla}\left(\vec{\nabla}.\vec{E}\right) = \frac{4\pi}{c^2}\frac{\partial\vec{J}}{\partial t} + \frac{1}{c^2}\frac{\partial^2\vec{E}}{\partial t^2} \quad (4)$$

The nonlinear current (NL) is defined as $\sim e(n_i\vec{v}_i - n_e\vec{v}_e) + en_0\left(\vec{v}_{i,NL} + \vec{v}_{e,NL}\right)$.

We took the x-component of equation (4) and can be written as

$$\frac{\partial^2 E_x}{\partial z^2} - \frac{\partial^2 E_z}{\partial x\partial z} - \frac{1}{V_A^2}\frac{\partial^2 E_x}{\partial t^2} = \frac{4\pi n_0 e}{c^2}\frac{\partial(v_{ix}-v_{ex})}{\partial t} + \frac{4\pi n_0 e}{c^2}\frac{\partial(v_{iNL}-v_{eNL})}{\partial t} - \frac{1}{c^2}\frac{\partial^2 E_x}{\partial t^2} \quad (5)$$

We take the components *x*, *y* and *z* of $\vec{\upsilon}_j$ in equation (4), and hence the *x*-component can be written as:

$$\frac{\partial^2 E_x}{\partial z^2} - \frac{\partial^2 E_z}{\partial x\partial z} - \frac{1}{V_A^2}\frac{\partial^2 E_x}{\partial t^2} = -\beta\frac{m_e}{e}\omega^2\frac{\partial}{\partial x}\left(\frac{n_e}{n_0}\right) + \frac{4\pi ne}{c^2}\left[\frac{\omega^2 F_{ex}}{\omega_{ce}m_e} - \frac{i\omega F_{ey}}{\omega_{ce}m_e}\right] \quad (6)$$

Usually, the Alfvén wave speed is defined as $V_A = \left(B_0^2/4\pi n_0 m_i\right)^{1/2}$. Here, n_e, n_0, T_e have usual meanings. β is defined as $\beta = 8\pi N_0 T_e/B_0^2$. The approximate relationships between electric field components for each other are as follows (nonlinear terms can be neglected): $E_y = \frac{-iD}{(S-\eta^2)}E_x$, $E_z = \frac{\eta^2\cos\theta\sin\theta}{\left(P-\eta^2\sin^2\theta\right)}E_x$

where

$\eta = \frac{k^2c^2}{\omega^2}$, $S = 1 - \sum_j\frac{\omega_{pj}^2}{\left(\omega_0^2-\omega_{cj}^2\right)}$, $D = \sum_j\omega_{cj}\times\frac{\omega_{pj}^2}{\left(\omega_0^2-\omega_{cj}^2\right)}$

and $P = 1 - \sum_j\left(\frac{\omega_{pj}^2}{k_z^2V_{Tj}^2} - \frac{\omega_{pj}^2}{\omega^2}\right)$. Here, we have taken relationship derived by Stix [24]. Therefore, continuity equation expressed as

$$\frac{\partial}{\partial t}\left(\frac{n_e}{n_0}\right) = -\frac{\partial}{\partial x}(v_{ex}) - \frac{\partial}{\partial z}(v_{ez}) \quad (7)$$

From the pondermotive force we have

$$F_{jy} = \frac{q_j}{cB_0}\frac{\partial}{\partial x}\left\langle\left|E_z\right|^2\right\rangle + \frac{q_j^2}{m_j\omega^2}\left[E_z^*\frac{\partial}{\partial z}E_x\right] \quad (8)$$

and

$$F_{jy} = \frac{iq_j}{cB_0}\left[E_z^*\frac{\partial}{\partial z}E_x\right] \quad (9)$$

Now, we put the E_x, E_y in equation (4) and using pondermotive force components, one can find

$$\left[\left(\frac{\partial^2}{\partial x^2} + \frac{\partial^2}{\partial z^2} - \frac{1}{V_A^2}\frac{\partial^2}{\partial t^2}\right)\left(\frac{\partial^2}{\partial z^2} - \frac{1}{V_A^2}\frac{\partial^2}{\partial t^2}\right) + \frac{\beta}{V_A^2}\left(\frac{\omega_{pe}^2}{\omega_{ce}^2} - \frac{c^2}{V_{Te}^2}\right)\frac{\partial^4}{\partial x^2\partial t^2}\right]\left(\frac{n_e}{n_0}\right) = \frac{2\omega_{pe}^2}{\omega_{ce}^2B_0^2}\frac{\partial}{\partial x}\left[\left(\frac{\partial B_{0y}}{\partial x}\right)\left(\frac{\partial^2 B_{0y}}{\partial z^2}\right)\right] - \frac{c^2}{4\omega_{ce}^2B_0^2V_A^2}\frac{\partial^4}{\partial x^2\partial t^2}\left|\frac{\partial B_{0y}}{\partial x}\right|^2 \quad (10)$$

For $\beta = 0$, we can recover slow and fast modes of the cold plasma. After Fourier transform LHS of equation (10) and equated RHS with zero, we get,

$$\left[\left(k^2 - \frac{\omega^2}{V_A^2}\right)\left(k_\parallel^2 - \frac{\omega^2}{V_A^2}\right) + \beta k_x^2\left(\frac{\omega_{pe}^2}{\omega_{ce}^2}\frac{\omega^2}{V_A^2} - \frac{c^2}{V_{Te}^2}\frac{\omega^2}{V_A^2}\right)\right]\left(\frac{n_e}{n_0}\right) = 0 \quad (11)$$

Therefore, $k_\parallel$ (parallel component) gives the expression for slow Alfvén wave which is propagating with low frequency and in dimensionless form of slow Alfven equation is obtained as

$$\left[\frac{\partial^2 n_e}{\partial z^2} - \zeta_1\frac{\partial^2 n_e}{\partial t^2}\right] = -\left|B_{0y}\right|^2 - \zeta_2\frac{\partial^2}{\partial z^2}\left|B_{0y}\right|^2 \quad (12)$$

$$\left[\frac{\partial^2}{\partial z^2} - \zeta_1\frac{\partial^2}{\partial t^2}\right]n_e = -\left|B_{0y}\right|^2 - \zeta_2\frac{\partial^2}{\partial x^2}\left|B_{0y}\right|^2 \quad (13)$$

Where $\zeta_1 = \frac{\omega^2}{k_{0x}^2V_A^2}\frac{\left(k_{0x}\lambda_e\right)^4}{\left(1+k_{0x}^2\lambda_e^2\right)^2}$ *and* $\zeta_2 = \frac{c^2\omega^2k_{0x}^2}{2\omega_{pe}^2k_{0z}^2V_A^2}$

The equation (13) is our desired nonlinear slow Alfvén wave equation responsible for acceleration of charged particles and solar coronal heating effect. For the calculation of constants, some important parameters nearly 1AU for solar wind plasma is taken [25].

Kinetic Alfvén Wave (KAW)

The nonlinear KAW is travelling along z-axis. The magnetic field B_0 associated with it. The equation is derived by [26-28]

$$\frac{\partial^2\tilde{B}_y}{\partial t^2} = \Gamma_1\lambda_e^2\frac{\partial^4\tilde{B}_y}{\partial x^2\partial t^2} - \Gamma_2V_{Te}^2\lambda_e^2\frac{\partial^4\tilde{B}_y}{\partial x^2\partial z^2} + V_A^2\left(1-\frac{n_e}{n_0}\right)\frac{\partial^2\tilde{B}_y}{\partial z^2}, \quad (14)$$

For low-β plasmas ($\beta \ll m_e/m_i$), $\Gamma_1 = 1$ and $\Gamma_2 = 0$

For intermediate-β plasmas ($\frac{m_e}{m_i} \ll \beta \ll 1$), $\Gamma_1 = 0$ and $\Gamma_2 = 1$ Electron skin depth, $\lambda_e = \left(\sqrt{c^2m_e/4\pi n_0e^2}\right)$

Suppose a solution for (14) as

$$\tilde{B}_y = B_{0y}(x,z)e^{i(k_{0x}x+k_{0z}z-\omega t)}. \quad (15)$$

From equation (14) and (15), we get

$$-2i\omega\frac{\partial B_y}{\partial t}-\left(2ik_{0z}k_{ox}^2\lambda_e^2V_{Te}^2\right)\frac{\partial B_y}{\partial z}-\left(k_{0x}^2V_{Te}^2\lambda_e^2\right)\frac{\partial^2 B_y}{\partial z^2}-\left(V_{Te}^2\lambda_e^2k_{0z}^2\right)\frac{\partial^2 B_y}{\partial x^2}$$
$$-2ik_{0x}\lambda_e^2\left(V_{Te}^2k_{0z}^2\right)\frac{\partial B_y}{\partial x}-k_{0z}^2V_A^2\left(1-n_e/n_0\right)B_y=0. \quad (16)$$

The system of equations namely (13) and (15), we can write in the dimensionless form as:

$$\left[\frac{\partial^2 n_e}{\partial z^2}-\zeta_1\frac{\partial^2 n_e}{\partial t^2}\right]=-\left|B_{0y}\right|^2-\zeta_2\frac{\partial^2}{\partial x^2}\left|B_{0y}\right|^2 \text{ and}$$
$$+i\frac{\partial B_y}{\partial t}-i\frac{\partial B_y}{\partial x}+i\frac{\partial B_y}{\partial z}+\zeta_3\frac{\partial^2 B_y}{\partial z^2}+n_eB_y=0, \quad (17)$$

$B_0=6.2\times10^{-5}G$, $c_s=4.63\times10^6$ cms^{-1}, $n_0=8.7cm^{-3}$, $T_e=1.4\times10^5K$, $T_i=1.2\times10^5K$, $V_A=4.6\times10^6$ cms^{-1}, $V_{th,e}=1.457\times10^8$ cms^{-1}, $\omega_{ci}=0.6$ Hz, $\omega_{pe}=5.64\times10^4$ Hz and $\beta\approx2\times10^{-4}$

For $\omega=0.1$ Hz and $\lambda_e=5.32\times10^3$ cm, we find $\beta=0.857$, $k_{0x}=6.5\times10^{-8}cm^{-1}$, $k_{0z}=5.83\times10^{-8}cm^{-1}$.

From the above parameters, the value of ζ_1 is very less as compared to $\zeta_2$therefore, it can be neglected.

Simulations

The equations (13) and (15) in a $\left(\frac{2\pi}{\alpha_x}\right)\times\left(\frac{2\pi}{\alpha_z}\right)$. Suppose a spatial domain with the wave numbers α_x and α_z to be periodic. (let their perturbation $\alpha_x$and $\alpha_z$equal to 0.2, has been solved numerically. Hare, $(256)^2$grid points are taken in the spatial domain. Here we use a numerical method namely, Pseudo spectral approach for finite difference as well as Predictor-Corrector for space integration. Let there be the evolution in time with $dt=5\times10^{-5}$.

The equations involved in the numerical simulations are

$$B_y(x,z,0)=B_{y0}\left(1+0.1\cos(\alpha_x x)\right)\left(1+0.1\cos(\alpha_z z)\right) \text{ and}$$
$$n(x,z,0)=\left|B_y(x,z,0)\right|^2$$

Initially, we take B_{y0}=1 for pump slow Alfvén wave amplitude. The Fig.1, characterizes the strength of localized B- field structures. Consequently, the coupling of waves, affects the dynamics. As a result, several filamentary structures are appeared at $\theta=50^0$by maximum intensity $\left|B_y(x,z)\right|^2\approx10$, has been observed. The Figure 2, shows fluctuations power spectra in the graph of $|B_k|^2$ Vs k ,which follows Kolmogorov scaling for inertial as well as dispersive range i.e. $k^{-5/3}$ and k^{-3} respectively.

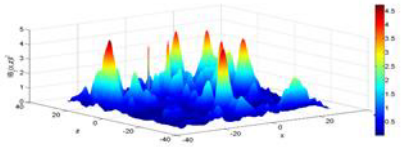

Figure 1: 3D-Filamentary structure of magnetic field strength for Slow Alfven wave at $\theta=50^0$

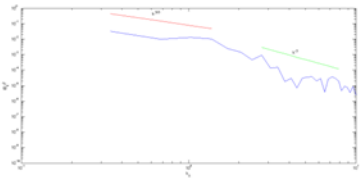

Figure 2: Evolution of magnetic strength fluctuations power spectra at $\theta=50^0$ at the end of the simulation

Discussion and Conclusion

This section of the paper summarizes formulation of the nonlinear slow of Alfvén Wave which is an important equation for the calculation of energy dissipation. On the perturbation of slow Alfvén wave by pumped wave, the coupled wave dynamics has studied and their numerical simulation has been performed at $\theta=50^0$. Several localized (x,z) filamentary structures have observed with diverse intensities. The spectra associated with magnetic field fluctuations are also observed with Kolmogorov scaling for inertial and dispersive range spectral index which are proportional to $k^{-5/3}$ and k^{-3} respectively.

References

1. Brodin, G., Stenflo L., Sol. Phys 236,285.
2. Das, B. K. et al J. Plasma Physics (2013), vol. 79, part 5, pp. 833–836
3. Srivastava, A. K., Shetye, J., Murawski, K., et al. 2017, Sci. Rep., 7, 43147
4. Kohutova, P., Verwichte, E., & Froment, C. 2020, A&A, 633, L6
5. Cramer, N. F. 2001, The Physics of Alfvén Waves (Wiley-VCH)
6. Mathioudakis, M., Jess, D. B., & Erdélyi, R. 2013, Space Sci. Rev., 175, 1
7. Leake, J. E., Arber, T. D., & Khodachenko, M. L. 2005, A&A, 442, 1091
8. Song, P., Vasyliunas, V. M. 2011, J. Geophys. Res. Space, 116
9. Threlfall, J., McClements, K. G., & De Moortel, I. 2011, A&A, 525, A155

10. Lazarian, A. 2016, ApJ, 833, 131
11. Hollweg, J. V. 1971, J. Geophys. Res., 76, 5155
12. Rankin, R., Frycz, P., Tikhonchuk, V. T., & Samson, J. C. 1994, J. Geophys. Res., 99, 21291
13. Champeaux, S., Passot, T. and Sulem, P. L.: 1997, J.Plasma Phys. 58, 665.
14. Marsch, E., Muhlhauser, K.-H., Rosenbauer, H., Schwenn, R., and Denskat, K. U.: 1981, J. Geophys. Res. 86, 9199.
15. Roberts, B., Edwin, P. M., & Benz, A. O. 1984, ApJ, 279, 857
16. Goldstein, M. L. 1978, Astrophys. J., 219, 700–704,
17. Araneda, J. A., E. Marsch, and A. F. Viñas 2007, J. Geophys. Res., 112, A04104
18. Nariyuki, Y., T. Hada, and K. Tsubouchi 2007, 14, 122110
19. [19] Wu, D. J., Wang, D. Y.and Carl G. F.: 1996, Phys Lett.13, 594.
20. Brodin, G., Stenflo,L. and Shukla,P. K. Solar Physics 2006, 236,285–291
21. Tam, S.W.Y. and Chang, T.: 1999, Geophys. Res. Lett. 26, 3189.
22. Zheng, J., Chen, Y., & Yu, M. Y. 2016, Phys. Scr., 91, 035601
23. Hasegawa, A. and Chen, L.: 1975, Phys. Rev. Lett. 35, 370.
24. Stix, T. H. 1992, Waves in Plasmas (American Institute of Physics, New York) p.33.
25. Weissman, P. R., McFadden, L. A. and Johnson, T. V.: 1999, TheEncyclopedia of the Solar
26. System (Academic Press: New York)
27. Bellan, P. M. and Stasiewicz, K. Phys. Rev. Lett. (1998),80, 3523.
28. Shukla, P. K. and Stenflo, L. Phys. Plasmas (2000), 7, 2738.
29. Shukla, P. K. and Stenflo, L.: 1999, Nonlinear MHD Waves and Turbulence Lecture Notes in Solar Phys. (1999), 536, 1.

Structural and Optical Properties of $AlAs_xSb_{1-x}$

R K Jhakal[1,a], and M D Sharma[2,b]

[1] *Department of Physics, SBD Government College, Sardar Shahr, Rajasthan, India.*
[2] *Department of Physics, Govt Dungar college, Bikaner, 334001, Rajasthan, India*

[a] jhakalraj@gmail.com
[b] mdsharma.phy@gmail.com

Abstract

We present a theoretical investigation of the structural and optical properties of $AlAs_xSb_{1-x}$ semiconducting alloys in zinc-blende structure based on the empirical pseudopotential method within the virtual crystal approximation combined with the Harrison bond-orbital model. The Elastic Constant, bulk modulus, refractive index, high frequency dielectric constant, static dielectric constant are calculated for $AlAs_xSb_{1-x}$. Our results for $AlAs_xSb_{1-x}$ ($0<x<1$) are predictions.

Keywords: Structural Properties, Optical Properties, Ternary Alloys.
Received 29 January 2025; First Review 11 February 2025; Accepted 26 February 2025

*** Address of correspondence**
R K Jhakal
Department of Physics, SBD Government College, Sardar Shahr, Rajasthan, India.

Email: jhakalraj@gmail.com

How to cite this article
R K Jhakal, and M D Sharma, Structural and Optical Properties of $AlAs_xSb_{1-x}$, J. Cond. Matt. 2025; 03 (01): 46-48.

Available from:
https://doi.org/10.61343/jcm.v3i01.90

Introduction

Semiconductor alloys based on III-V compounds have opened up new generation of device application during the last few decades [1]. Ternary alloys have the advantage that a considerably wide range of band gaps can be obtained by changing the alloy composition. Because of the wide range of its physical properties ternary alloys are an important material for many applications in microelectronics [2].

Computational Detail

The calculation of various properties of semiconductor alloys using DFT require large computational power. it is hard to model semiconductor alloys using DFT as it can only be used by means of supercells which increase the number of atoms. On contrary the EPM use the virtual crystal approximation to model the alloys which is easy to simulate. The band gap of $AlAs_xSb_{1-x}$ is calculated using empirical pseudopotential method (EPM) Considering the Zink blende structure. EPM is an approach to calculate the electronic band structure and optical properties. WE consider the disordered effects of alloys via modified virtual crystal approximation implemented in EPM [3-5]. The Value of elastic constants C_{11}, C_{12} and C_{44} are calculated using the method proposed by Baranowski [6] and Bouarissa and Kassali [7]. The Elastic Constants C_{11}, C_{12} and C_{44} for cubic Structure are Defined as:

$$C_{11} = \frac{(\sqrt{3})}{4d^5}\left[4.37\,\frac{\hbar^2}{m}\,(5+\lambda)\left(1-\alpha_p^2\right)^{\frac{3}{2}} - 0.6075\frac{\hbar^2}{m}\left(1-\alpha_p^2\right)^{\frac{1}{2}}\right] \quad (1)$$

Table 1: Various elastic constants for different alloy composition

X	Alloys	C_{11}	C_{12}	C_{44}
0.0	AlSb	97.57506	41.84139	39.52807
0.1	$AlAs_{0.1}Sb_{0.9}$	101.0197	43.32816	40.91984
0.2	$AlAs_{0.2}Sb_{0.8}$	104.3296	44.76459	42.25428
0.3	$AlAs_{0.3}Sb_{0.7}$	107.4667	46.13538	43.51549
0.4	$AlAs_{0.4}Sb_{0.6}$	110.3884	47.42344	44.68581
0.5	$AlAs_{0.5}Sb_{0.5}$	113.0475	48.60982	45.74566
0.6	$AlAs_{0.6}Sb_{0.4}$	115.3923	49.67353	46.67348
0.7	$AlAs_{0.7}Sb_{0.3}$	117.3654	50.59149	47.44562
0.8	$AlAs_{0.8}Sb_{0.2}$	118.9048	51.33841	48.03627
0.9	$AlAs_{0.9}Sb_{0.1}$	119.9428	51.88674	48.41747
1.0	AlAs	120.4065	52.20667	48.55911

$$C_{12} = \frac{(\sqrt{3})}{4d^5}\left[4.37\,\frac{\hbar^2}{m}\,(3-\lambda)\left(1-\alpha_p^2\right)^{\frac{3}{2}} + 0.6075\frac{\hbar^2}{m}\left(1-\alpha_p^2\right)^{\frac{1}{2}}\right] \quad (2)$$

$$C_{44} = \frac{3(C_{11}+2C_{12})(C_{11}-C_{12})}{(7C_{11}+2C_{12})} \quad (3)$$

Table 2: Various elastic constants for different alloy composition

X	Alloys	B_S	C_S
0.0	AlSb	60.41928	27.86684
0.1	$AlAs_{0.1}Sb_{0.9}$	62.55866	28.84575
0.2	$AlAs_{0.2}Sb_{0.8}$	64.61959	29.7825
0.3	$AlAs_{0.3}Sb_{0.7}$	66.57914	30.66564
0.4	$AlAs_{0.4}Sb_{0.6}$	68.41175	31.48246
0.5	$AlAs_{0.5}Sb_{0.5}$	70.08906	32.21886
0.6	$AlAs_{0.6}Sb_{0.4}$	71.57977	32.85936
0.7	$AlAs_{0.7}Sb_{0.3}$	72.84947	33.38697
0.8	$AlAs_{0.8}Sb_{0.2}$	73.86054	33.7832
0.9	$AlAs_{0.9}Sb_{0.1}$	74.57209	34.02803
1.0	AlAs	74.93996	34.09994

Table 3: Various refractive index values for different composition.

X	Alloys	n	ε_∞	ε_0
0.0	AlSb	2.59869765	6.7532290	6.758950997
0.1	$AlAs_{0.1}Sb_{0.9}$	2.57671772	6.6394744	6.660381224
0.2	$AlAs_{0.2}Sb_{0.8}$	2.54633767	6.4838356	6.529181622
0.3	$AlAs_{0.3}Sb_{0.7}$	2.50832385	6.2916883	6.370223121
0.4	$AlAs_{0.4}Sb_{0.6}$	2.46359120	6.0692812	6.189077591
0.5	$AlAs_{0.5}Sb_{0.5}$	2.41315494	5.8233168	5.991684468
0.6	$AlAs_{0.6}Sb_{0.4}$	2.35808168	5.5605494	5.78404425
0.7	$AlAs_{0.7}Sb_{0.3}$	2.29944394	5.2874425	5.571965674
0.8	$AlAs_{0.8}Sb_{0.2}$	2.23828074	5.0099009	5.360885644
0.9	$AlAs_{0.9}Sb_{0.1}$	2.17556613	4.7330878	5.155770962
1.0	AlAs	2.11218617	4.4613304	4.961103352

The bulk and Shear Moduli can be computed applying the following relations [8].

$$B_S = \frac{(C_{11} + 2C_{12})}{3} \quad (4)$$

$$C_S = \frac{(C_{11} - C_{12})}{2} \quad (5)$$

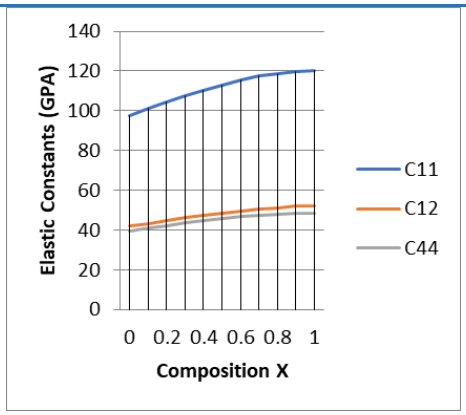

Figure 1: Elastic Constants C_{11}, C_{12}, C_{44} of $AlAs_xSb_{1-x}$ as a function of composition x.

Table 2 shows Elastic Constants Bs and Cs that are calculated by equation (4), (5) and table 3 shows refractive index values for different composition calculated by equation (6), (7), (8) using empirical pseudopotential method.

The Wavelength independent refractive index (n) is Calculated by Band gap (E_g) using Moss's Formula [9] given as

$$n^4 = \frac{E_g(E_v)}{95} \quad (6)$$

The high frequency dielectric constant ε_∞ can be obtained using the following relation:

$$\varepsilon_\infty = n^2 \quad (7)$$

According to the Harrison bond orbital model the static dielectric constant is directly related to ε_∞ as [10].

$$\varepsilon_0 = 1 + (\varepsilon_\infty - 1)\left(1 + \frac{\alpha_p^2(1+\alpha_c^2)}{2\alpha_c^2}\right) \quad (8)$$

Figure 1 Compared different Elastic Constants for composition 0<x<1 of alloy $AlAsxSb_{1-x}$.

Conclusion and Future Prospective

The structural property (Elastic Constant, bulk modulus) and optical property (refractive index, high frequency dielectric constant, static dielectric constant) are calculated for alloy ZnS_xTe_{1-x} for 10 compositions in table 1 using EPM The experimental value is given in binary numbers. It has been observed that the static and high frequency dielectric constants increase when the antimony concentration is increase. Our results are predictions.

References

1. Nadir Bouarissa, Smail Bougouffa and Ali Kamli, *"Energy gaps and optical photon frequencies in $InP_{1-x}Sb_x$"*, in Semiconductor Science and Technology 20 (2005): 265-270, 2005.

2. N Bouarissa, *"Effects of compositional disorder upon electronic and lattice properties of $Ga_xIn_{1-x}As$"*, Physics. Letter A, 245 (1998) 285-291.
3. M. L. Cohen and R. Chelikowsky, *"Electronic Structure and Optical Properties of Semiconductors"*, Springer-Verlag Berlin, 1980.
4. N. N. Patel and K B. Joshi, Eur. Phys. J. B. 59,19-23 (2007).
5. U. Paliwal, R.K. Kothari and K. B. Joshi Superlatt. Microstruct.51,635-643 (2012).
6. J. M. Baranowski, J. Phys. C: Solid State Physics 17 (1984) 6287-6302.
7. N. Bouarissa, K. Kassali, Phys. Stat. Sol. B 228(2011) 663-670.
8. M. Levinshtein, S. Rumyantsev, M. Shur. Handbook Series on Semiconductor Parameters. Vol 2 (World Scientific, 1999).
9. T. S. Moss, Proc. Phys. Soc. London B 63, 167-174 (1950).
10. Y. Oussaifi, A. B. Fredj, M. Debbichi, N. Bouarissa and M. Said, Semiconductor. Sci. Technol. 22, 641-646 (2007).

Characterization and Analysis of Europium Sulphide (EuS) Thin Films

Rekha S Bhalekar[1,a], and M M Betkar[2,b]

[1] *Dept. of Physics, SGGSIE&T, Nanded, Maharashtra, India.*
[2] *Shri Kumarswami Mahavidylaya, Ausa, Latur, Maharashtra, India.*

[a] rsbhalekar@sggs.ac.in
[b] betkarmm@rediffmail.com

Abstract

Deposition of Europium Sulphide (EuS) thin films on bare glass substrates via spray pyrolysis method in an optimized aqueous bath environment. Structural characterization was carried out to determine the optimal deposition conditions. The results indicated that the optimum temperature for depositing high-quality EuS thin films is 623 K. At this temperature, the films exhibited excellent crystallinity, as evidenced by sharp X-ray diffraction (XRD) peaks. This confirms that 623 K is ideal for forming well-crystallized EuS thin films. These findings are significant for applications requiring high-quality crystalline structures and demonstrate that the spray pyrolysis method, when operated under optimized conditions, can effectively produce EuS thin films with superior structural properties.

Keywords: Europium sulphide, spray pyrolysis, X-ray diffraction, substrate temperature, crystallinity, semiconductor devices.
Received 30 January 2025; First Review 21 February 2025; Accepted 24 February 2025

*** Address of correspondence**
Rekha S. Bhalekar
Dept. of Physics, SGGSIE&T, Nanded, Maharashtra, India.

Email: rsbhalekar@sggs.ac.in

How to cite this article
Rekha S Bhalekar, M M Betkar, Characterization and Analysis of Europium Sulphide (EuS) Thin Films, J. Cond. Matt. 2025; 03 (01): 49-51

Available from:
https://doi.org/10.61343/jcm.v3i01.114

Introduction

The europium chalcogenides EuO, EuS, EuSe, and EuTe are extensively studied materials. Glass substrates receive the deposition of Europium sulphide (EuS) thin film by adjusting precursor concentration and substrate temperature, using equal stoichiometric volumes of hydrous and anhydrous precursor solutions. Europium (III) chloride hexahydrate ($EuCl_3.6H_2O$) and thioacetamide (C_2H_5NS) serve as sources of europium and sulphur, respectively, to produce Europium sulphide (EuS) thin films. A deposited sample was then analysed for its morphology, structure, and other characteristics [1-6].

Method

Europium sulphide (EuS) thin films are deposited onto glass substrates using both hydrous and anhydrous solution baths. These baths are made from Europium (III) chloride hexahydrate ($EuCl_3{\cdot}6H_2O$) and thioacetamide (C_2H_5NS), each dissolved separately in deionized water and methanol, with equal stoichiometric volumes of 1:1. The aqueous solution of $EuCl_3$ and C_2H_5NS is thoroughly stirred using magnetic stirrer equipment at a rate of 550 rpm for 45 minutes to ensure homogeneity.

The deposition process begins with cleaning the substrates to ensure their pristine condition. Experimental substrates must be free of common contaminants such as grease, airborne dust, lint, and oil particles, as their presence can adversely affect the morphology of deposited films. Glass substrates undergo a rigorous cleaning process, which requires soaking them in a Chronic acid solution with a molarity of 0.5. for a duration of five minutes, followed by cleaning with dilute hydrochloric acid and standard laboratory detergent. Additionally, the substrates undergo ultrasonic cleaning with double-distilled water. Before deposition the substrates were meticulously dried using alcohol vapor for a duration of ten minutes [7-10].

$EuCl_3{\cdot}6H_2O$ and C_2H_5NS, used in the experiment, were sourced from Sigma Aldrich and were of analytical reagent (AR) quality grade, sourced from, Pune.

For atomization of the precursors, we employed the Spray Pyrolysis equipment using air as the gaseous medium. The nebulizer was equipped with a 'metal spray head' and a sharp needle-tip nozzle. The films produced had a subtle brownish tint.

Data related to the synthesized europium sulphide samples,

prepared under optimized conditions, can be found in Table 1 below.

Table 1: EuS thin film samples that have been synthesized

Sample	Precursor Medium	Normality Eu^{3+} + $3Cl^-$ C_2H_5 + N + S. in M	Surface Temperature range in K
A	Aqueous	0.01/0.01	(a)548, (b) 573
B		0.01/0.05	(c)598, (d) 623

The optimized preparation conditions for Europium sulphide (EuS) thin films are as follows:

• Initial Ingredients: EuCl3, C2H5NS, H2O

• Substrate Temperature: 573 K

• Precursor Concentration: 0.01 M

• Composition: 50:50

• Spray Nozzle: Metal needle.

• Spray Rate: 2 ml/min.

• Distance Between Nozzle and Substrate: 15 cm

• Carrier Gas: Air

• Gas Pressure: 3 psi

Investigating Europium Sulphide Thin Films Through X-ray Diffraction

Structural characterizations play a critical role in ensuring the reliability and efficiency of electronic components. Upcoming publications will present an analysis of the properties of materials deposited on substrate samples, with key findings emphasized.

The attribute of the deposited material is notably influenced by variations in the volumetric ratio of experimental precursors, providing an effective approach for managing these properties. To optimize the EuS volume ratio, films were prepared using different ratios: 90 to 10, 80 to 20, 70 to 30, 60 to 40, 50 to 50, 40 to 60, 30 to70, 20 to 80, and 10 to 90 respectively. By using a precursor solution concentration of 0.01 M, we coated these films at a surface temperature of 573 K, a spray rate of 2 ml/min, and a pressure of 3 psi.

Structural characterization was performed using X-ray diffraction (XRD) with a MiniFlex2 diffractometer, operating at Cu/30 kV/15 mA and utilizing kα radiation (wavelength λ = 0.1542 nm). The XRD patterns for the spray-deposited EuS films, labelled as samples A, B, C, and D, are shown in diagram 4.5 - 4.8. The diffraction peaks observed in the films correspond to 2θ values of 25.780°, 29.920°, and 42.460°, which align with the hkl planes (111), (200), and (220), respectively.

Discussion

Structural analysis: The X-ray diffraction (XRD) patterns for the spray-deposited EuS films, labelled samples A, B, C, and D, are presented in diagram. These patterns indicate that the films have a polycrystalline structure with a cubic, face-centred lattice arrangement. The diffraction peaks observed correspond to specific atomic distances within the crystal lattice.

The XRD peaks were indexed, and the inter-planar spacings (d_o) were analysed and matched against the reference values from Joint Committee on Powder Diffraction Standards card No. 75-0868.

The optimal deposition temperature for producing high-quality EuS thin films has been established at 623 K. The films display well-defined crystallinity, evidenced by sharp X-ray diffraction peaks, confirming that 623 K is ideal for producing well-crystallized thin films.

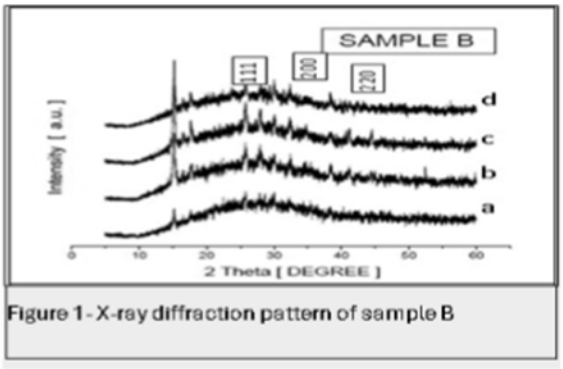

Figure 1 - X-ray diffraction pattern of sample B

Figure 1: XRD of samarium ferrite obtained after different annealing time

Conclusion and Future Prospective

In conclusion, the study demonstrates a direct correlation between substrate temperature and the crystal quality of the coated EuS thin films. As the surface temperature increases from 548 K to 623 K, there is a clear improvement in the crystal structure of the films. An enhancement in film quality is corroborated by a mean particle size of 16.18 µm, demonstrating the effective formation of well-crystallized EuS films. The crystallite sizes were largest in films coated at temperatures exceeding 623 K.

Additionally, the study found that film thickness varies with substrate temperature. Films grown under 573 K exhibited reduced thickness, likely due to insufficient decomposition process of the precursor elements. In contrast, increased thickness was observed in films formed at temperatures higher than 573 K. suggesting complete decomposition. These results underscore the importance of substrate temperature in optimizing both the crystallinity and the performance of EuS thin films in semiconductor applications is highly dependent on their thickness.

References

1. Busch, G. Journal of Physics and Chemistry of Solids 38(3), 1967.
2. Gaikwad, N. Materials Research Bulletin 38(15):2613–2626, 2001.
3. Von Molnar, S. J. Superconductivity, 16(1): 1-5, 2004.
4. Weidong, H. Synthesis and characterizations of europium chalcogenide and tellurium nanocrystals Ph.D. Thesis, Vanderbilt University, Nashville, 2011
5. Ariponnammal, S, and S K Rathiha. Int J Mod Phys B 25(27):3663,2011
6. Tanaka, K., Tatehata, N., Fujita, K., and Hirao, K. Journal of Applied Physics, 89(4): 2213,2001.
7. Sakalle, U K, P K Jha, and S P Sanyal Bulletin of Materials Science 23(3):233-235,2000.
8. Mane, R S, and C D Lokhande Materials Chemistry and Physics 78: 15-17,2002.
9. Dosev, D, B Guo, and I Kennedy Journal of Aerosol Science 37(3):402-412,2006.
10. Camenzind, Adrian, Reto Strobel, and Sotiris E Pratsinis.

Investigation of Functional Group, Optical and Structural Characteristics of Doped and Pure Glycine $LiNO_3$ Crystals

Nimisha S Agrawal[1,a], P R Vyas[1,b], I B Patel[2], D V Shah[3]

[1] *Department of Physics, Sarvajanik University, Surat-395001, India.*
[2] *Department of Physics, Veer Narmad South Gujarat University, Surat-395007, India.*
[3] *Department of Physics, Sardar Vallabhbhai National Institute of Technology, Ichchhanath, Surat-395007, India.*

[a] agrawalnimisha173@gmail.com
[b] prathmesh.vyas@scet.ac.in

Abstract

Second Harmonic Generation (SHG) from the Centro-symmetric Glycine crystals in its pure form shows a photo-type of waves on resistance from the guest molecule. Second harmonic generation may benefit from the use of such Non-Linear Optical (NLO) materials. Slow evaporation is used to form a single crystal of glycine that is excellently optically transparent and has good nonlinear optical behaviour in a solution containing fractional amounts of sodium, potassium, and lithium nitrate. A diffractometer using Cu-Kα radiation was used to record the powder X-ray diffraction spectrum, which was scanned for eight minutes in the 85-degree range. When the lattice parameter values, particle size, dislocation density, strain values, and other factors are calculated. The paper studies exhibit the powder XRD pattern of the formed crystals. According to X-ray diffraction studies, grown crystals have very good crystalline perfection and no internal structural grain boundaries. In order to investigate structural phase, presence of different chemical bonds or additional elemental group etc. within grown crystals, they were examined by the spectrum of Fourier Transform Infrared (FTIR) spectroscopy. Assigned vibration of various chemical bond groups were identified and confirmed by this investigation. Optical Characteristics of Doped and Pure Glycine $LiNO_3$ crystals were carried out by visible and ultraviolet (UV) spectra and band gap (E_g) of the synthesized sample were calculated. For a nonlinear application, it was determined that the optical transparency and cut off wavelength needed to be equals to 300 nm. For $NaNO_3$ with concentration of 20% and 60% doping, the band gap was found as 6.07 eV and 5.84 eV respectively. For KNO_3 doping with concentration of 20% and 60%, the energy band gap was found to be 6.21 eV and 5.88 eV respectively.

Keywords: Grown from solution, Slow evaporation, Glycine $LiNO_3$, XRD, FTIR, UV-Vis spectroscopy.
Received 30 January 2025; First Review 21 February 2025; Accepted 07 March 2025

*** Address of correspondence**
Nimisha S Agrawal
Sarvajanik University, R. K. Desai Marg,
Athwalines, Surat-395001, India.

Email: agrawalnimisha173@gmail.com

How to cite this article
Nimisha S Agrawal, P R Vyas, I B Patel, D V Shah, Investigation of Functional Group, Optical and Structural Characteristics of Doped and Pure Glycine $LiNO_3$ Crystals, J. Cond. Matt. 2025; 03 (01): 52-55

Available from:
https://doi.org/10.61343/jcm.v3i01.120

Introduction

Due to recent technological advancements, the optoelectronics industry has a strong need for optical single crystals and photonic fields. Such crystals are employed as devices for frequency conversion, high optical data storage etc. Glycine comes in three main types of polymers: α, β and γ. Centrosymmetric crystals of two polymorphic forms, α and β, with space groups are found as P_{21}/C and P_{21} respectively. On the other hand, γ glycine crystallizes in a non-centrosymmetric manner with a space group of P_{32}, which makes it a viable option for nonlinear applications. In the current study, a with the slow evaporation approach, a single crystal of glycine was created with the presence of $LiNO_3$ and its optical and mechanical properties were examined.

Method

At room temperature, a 4.5:1.5 ratio of glycine and $LiNO_3$ was made by dissolving it in deionized water. After stirring for around half an hour, the produced solution was filtered through filter paper. The saturation solution is maintained at room temperature in a dust-free environment in a petri dish that has been coated with perforated paper. Twenty days later, glycine lithium nitrate crystals are extracted. Following that, a solution of $NaNO_3$ and KNO_3 at concentrations of 20%, 30%, 50%, and 60% was prepared, and glycine $LiNO_3$ seeds were doped into it. Following 10 to 15 days, small and colourless crystals of Glycine $LiNO_3$ were extracted along with doped $NaNO_3$ and KNO_3 at 20%, 30%, 50%, and 60% of concentrations.

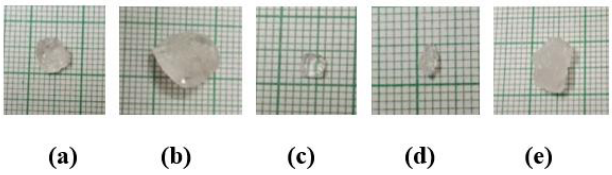

Figure 1: (a) Undoped Glycine $LiNO_3$, **(b)** to **(e)** doped with $NaNO_3$ of 20%, 30%, 50%, and 60%.

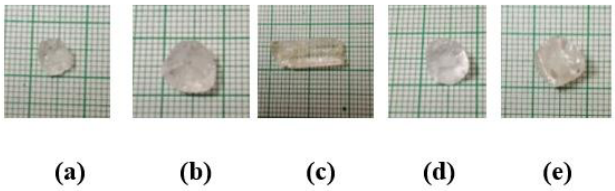

Figure 2: (a) Undoped Glycine $LiNO_3$, **(b)** to **(e)** doped with KNO_3 of 20%, 30%, 50%, and 60%.

Discussion

X-Ray Diffraction (XRD)

Using x-ray powder diffraction, the generated Glycine $LiNO_3$ pattern was obtained using a smart lab (3kw) powder x-ray diffractometer with CuKα (0.154 nm) radiation for structured analysis of the crystal. The ideal specimen was made by randomly orienting powder with crystallite size less than 10 µm concentrated with the probability distribution of crystalline orientation in polycrystalline materials. The diffraction angle (2θ), which is the angle between the incident and diffracted beams, can be altered to measure intensity and gather diffraction data by moving the tube, sample, and detector. Crushed crystal powder was scanned at a rate of 1° per minute within the 10-80° range.

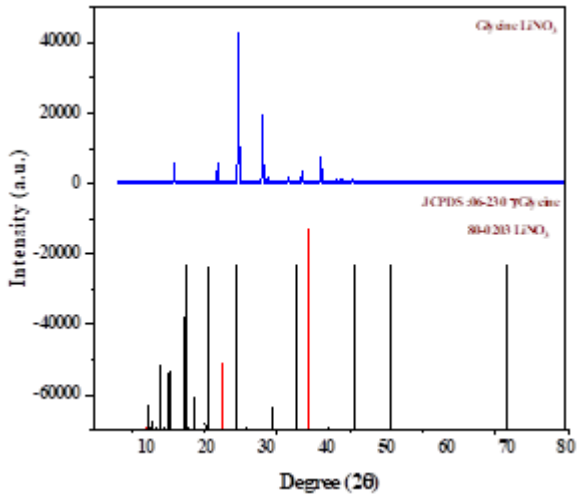

Figure 3: XRD graph of Glycine $LiNO_3$ with pure Gamma Glycine and $LiNO_3$

The JCPDS card number for Glycine and $LiNO_3$ indicates that the lattice parameter of the grown crystal is a = 7.024, b = 7.025, and c = 5.472 for Glycine. The value of α and β = 90°and γ = 120° indicates that the crystal structure is hexagonal. When the values of a, b, and c for $LiNO_3$ are 4.692, 5.034, and 15.21, and the values of α and β = 90° and 120°, respectively, the crystal structure is hexagonal which is shown in table1.

Table 1: Unit cell parameter of Glycine $LiNO_3$ Crystal

Lattice parameter	Glycine	Lithium Nitrate
a ($\dot{A}$)	7.024	4.692
b ($\dot{A}$)	7.025	5.034
c ($\dot{A}$)	5.472	15.21
α	90°	90°
β	90°	90°
γ	120°	120°
Crystal System	Hexagonal	Hexagonal
Space group	P_{31} (144)	R $\bar{3}$c (167)
Volume	233.80	290.08

Table 2: Powder XRD Data of Glycine $LiNO_3$ Crystal

2θ°		d-Spacing (Å)		hkl	References
Observed Value	Standard Value	Observed Value	Standard Value		
14.58	14.54	6.0698	6.0800	100	JCPDS Card No. 06-0230 80-0203
21.83	21.81	4.0644	4.0700	101	
25.32	25.34	3.5142	3.5100	110	
29.34	29.35	3.0078	3.0400	200	
30.18	30.25	2.9574	2.9500	111	
33.65	33.65	2.6217	2.6600	201	
35.93	35.88	2.4554	2.5000	102	
39.12	39.12	2.2554	2.3000	210	
42.51	44.58	2.0370	2.0300	300	
44.46	44.58	1.9850	2.0300	300	

Fourier Transform Infrared Spectroscopy (FTIR)

Glycine $LiNO_3$ doped with $NaNO_3$ and KNO_3 in a range of concentration-wise tests can qualitatively identify the existence of functional groups in a molecule. The FTIR spectra were obtained between range of 4000 cm^{-1} and 400 cm^{-1}. The different absorption peaks were found in FTIR

spectra for both pure glycine $LiNO_3$ and 20% doped $NaNO_3$ and KNO_3.

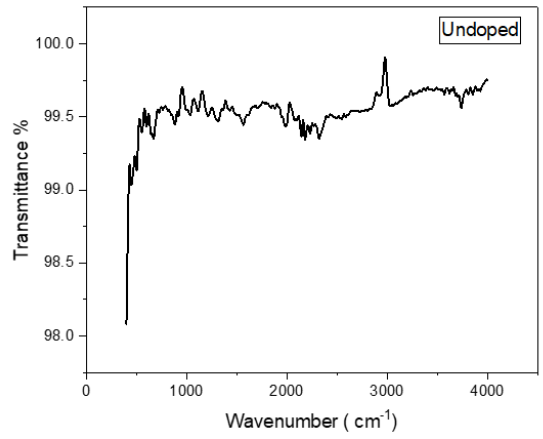

(a)

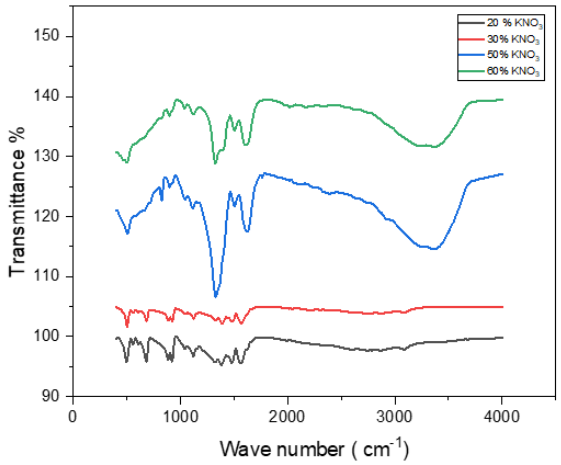

(b)

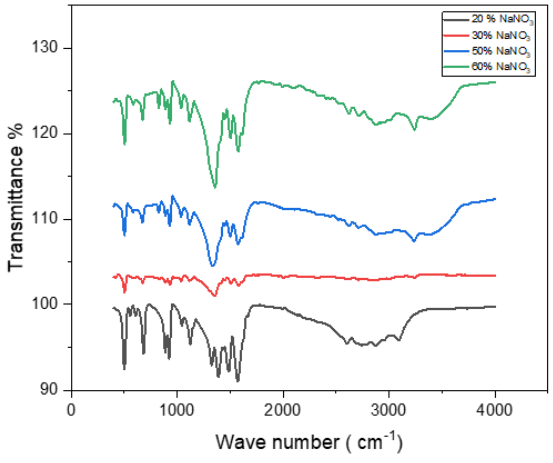

(c)

Figure 4: (a) Glycine $LiNO_3$, **(b)** doping with $NaNO_3$ and **(c)** doping with KNO_3

This work provides information on the molecular structure of the created molecule, which aids in the explanation of chemical bonding. There is a specific infrared spectrum for each chemical substance. IR detected in the range of 1340.28 cm^{-1} to 1353.78 cm^{-1}, which is consistent with the existence of the C-H group. There are observed degenerate modes of stretching vibration for N-H, C≡C, C=O, O-H.

Table 3: Wave numbers with assigned vibration of FTIR

Sr. No.	Wave number (cm^{-1})	Personalized Vibration	Wave number (cm^{-1})	Personalized Vibration
1	3382.53	N-H Group	3370.96	O-H Group
2	3241.75,3237.9	=CH-H Group	2871.49	$=CH_3$ Group
3	2715.28,2618.8	O-H Group	2601.5, 2318.02	O-H Group
4	2142.53	C≡ C Group	2181.1, 2142.53	C≡ C Group
5	1984.39	=C-H Group	1984.3, 1610.27	=C-H Group
6	1575.56,1565.9	N-H Group	1565.9, 1502.28	C=C Group
7	1353.78,1340.2	C-H Group	1328.7, 1322.93	C-N Group

UV-Vis Spectroscopy

For optical transmission of Glycine $LiNO_3$ crystal with doped sample are measured in range of 200-1100 nm using UV-Vis spectrometer. A band gap is not observable when measured in the pure Glycine $LiNO_3$ graph with a UV-vis analysis. A study of a comparable graph of Figure 5 (a) and (b) shows that band gaps arise whenever pure material is subjected to a doping concentration. At 20% and 60% doping concentrations of $NaNO_3$, the energy band gap is 6.07 eV and 5.84 eV respectively. For KNO_3, the energy band gap at 20% is 6.21 eV and at 60% of the doping concentration is 5.88 eV.

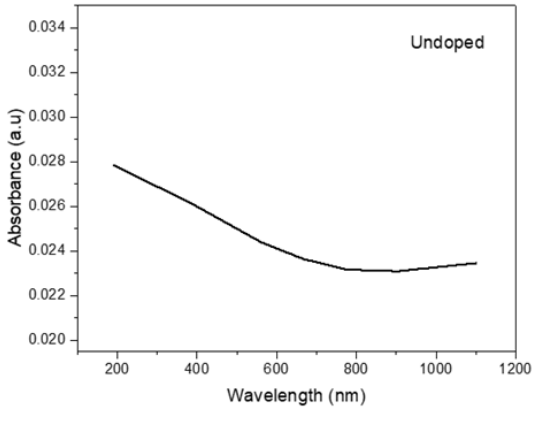

(a)

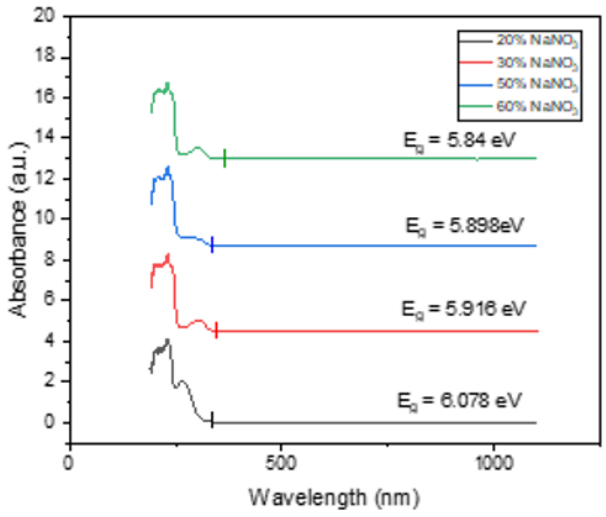

(b)

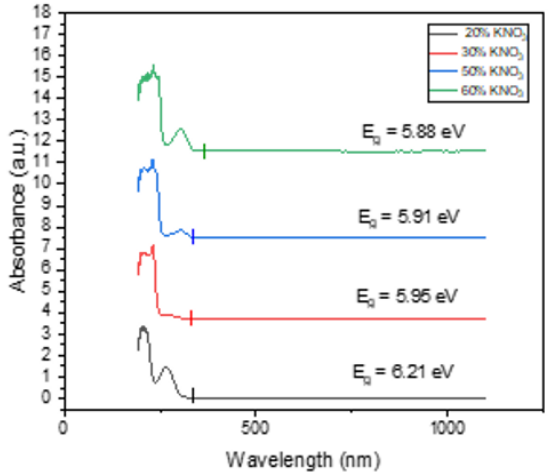

(c)

Figure 5: (a) UV-Vis spectroscopy graph of Glycine $LiNO_3$, **(b)** doped with $NaNO_3$, **(c)** doped with KNO_3

Table 4: Doping concentration of Glycine $LiNO_3$ doped with $NaNO_3$ and KNO_3

Concentration	$NaNO_3$	KNO_3
	Energy Band gap (eV)	Energy Band gap (eV)
Undoped	-	-
20%	6.07	6.21
30%	5.91	5.95
50%	5.88	5.91
60%	5.84	5.88

Conclusion and Future Prospective

Glycine $LiNO_3$ crystal structure was grown at ambient temperature via slow evaporation. Research employing UV-vis absorption spectroscopy has shown that a pure sample cannot have a band gap; however, when an impurity is added, the material starts to show a band gap, and the doping material's band gap shrinks as the concentration rises. XRD analysis confirmed that the structured type of crystal is HCP (Hexagonal Cubic Pack) and FTIR analysis confirmed the material's functional groups.

References

1. Narayan Bhat, M Dharmaprakash, S M J. Cryst. Growth, 236:376-380,2002.
2. Narayan Bhat, M Dharmaprakash, S M J. Cryst. Growth.235:511-516,2002.
3. P V Dhanaraj, T Suthan and N. P. Rajesh, Curr. Appl. Phys.10:1349-1353, 2010.
4. M E Peter and P Ramasamy, Mater. Lett.64:1-3, 2010.
5. M M Khandpekar and S P Pati, Opt. Commu. 283: 2700-2704,2010.
6. Mohd Shakir, S K Kushwaha, K K Maurya, Sumeet Kumar, M A Wahab and G Bhagavananarayan, J. Appl. Crystallogr.43:491-497,2010.
7. M E Peter and P Ramasamy, J. Cryst. Growth. 312:1952-1956,2010.
8. R Parimaladevi, C Sekar, Crystal Growth and Spectral Studies of nonlinear optical J- glycine single crystal grown from phosphoric acid, Spectrochimica Acta Part A 76: 490-495, 2010.
9. J Thomas Joseph Prakash, M Lawrence, J Felicita Vimala and M. Iyanar, Journal of Physical Science, Vol 14: 219-226, 2010.
10. C Murali, S Thomas, S Venkateshwarm and S M Sharma, Physics.364:233,2005.
11. M D Aggarwal, J Stephens, A K Batra and R B Lal, J Optoelectron. Adv. Mater,5:555,2003.
12. N Tyagi, N Sinha, B Kumar, Evidence of Sustained ferroelectricity in glycine sodium nitrate single crystal, Curr. Appl. Phy.14:156-160,2014.
13. V Ganesh, T Bhaskar Rao, K Kishan Rao,G Bhagavannarayana, Mohd Shakir,137:276-281,2012.
14. K Russelraj, P Murugakoothan, Mod.Phys.Lett. B,26, 2012.
15. M Arivazhagan, R Meenakshi, Spectrochim, Acta Part A 91:419-430,2012.

Volatile Organic Compounds as Biomarkers: Innovations in Cancer Biosensors for Early Diagnosis

Xavier T S[a], and Sumitha M S[b]

Centre for Advanced Materials Research, Department of Physics, Government College for Women, Thiruvananthapuram, University of Kerala, India.

[a] xavierkattukulam@gmail.com
[b] sumithamnair@gmail.com

Abstract

Timely cancer detection is crucial for improved survival rates and enhanced treatment efficacy. Volatile organic compounds (VOCs) have attracted much attention as potential biomarkers for cancer diagnosis because of their distinctive patterns linked to metabolic abnormalities in cancer cells. This review aims to examine advanced biosensor technologies that utilize VOCs for early cancer detection. This research seeks to elucidate the transformative potential of VOC biosensors in cancer therapy by analysing existing advancements, significant challenges, and anticipated advancement in the domain.

Keywords: Volatile Organic Compounds (VOCs), Cancer Biomarkers, Biosensors, AI Assisted Cancer Detection.
Received 30 January 2025; First Review 21 February 2025; Accepted 07 March 2025

*** Address of correspondence**
Xavier T S
Centre for Advanced Materials Research, Department of Physics, Government College for Women, Thiruvananthapuram-695014, India.

Email: xavierkattukulam@gmail.com

How to cite this article
Xavier T S, and Sumitha M S, Volatile Organic Compounds as Biomarkers: Innovations in Cancer Biosensors for Early Diagnosis, J. Cond. Matt. 2025; 03 (01): 56-63.

Available from:
https://doi.org/10.61343/jcm.v3i01.122

Introduction

Cancer profoundly affects worldwide mortality statistics [1]. Despite breakthroughs in therapeutic procedures, a delayed diagnosis diminishes the probability of successful treatment. Imaging and tissue biopsies are recognized diagnostic techniques that are challenging, invasive, and frequently exhibit sensitivity limitations. As a result, there is an increasing demand for non-invasive, quick, and accurate diagnostic methods. Cells produce low-molecular-weight substances known as volatile organic compounds as standard metabolic byproducts. Malignant cells generate distinctive profiles of volatile organic molecules due to altered metabolic activities [2]. Blood, urine, and exhaled air may include non-invasive biomarkers known as volatile organic compounds (VOCs) [3]. VOCs must be discovered and quantified to utilise advanced biosensors for improving cancer diagnosis.

The Role of VOCs in Cancer Diagnosis

1. Metabolic Basis of VOCs

The process of metabolic reprogramming is an essential one that permits cancer cells to survive apoptosis and grow at a high rate [4]. The generation of VOC is the result of a reprogramming process that involves changes in oxidative stress, lipid metabolism, and enzyme activity [5]. This mechanism produces volatile organic molecules on purpose and is essential for the creation of chemical compounds that have a high degree of volatility. It has been found that ketones, aldehydes, and alkanes can be found in breath samples that have been collected from individuals who are afflicted with gastrointestinal, lung, and breast cancers [6].

2. Sources and Sampling of VOCs

Exhaled breath is non-invasive and easy to collect, making it a diagnostic tool. Endogenous VOCs from cellular metabolism and environmental chemicals are exhaled. Thermal desorption and gas chromatography-mass spectrometry (GC-MS) detect cancer-related VOCs [6]. The speed and precision of selected ion flow tube mass spectrometry (SIFT-MS) enable real-time monitoring and early detection [7]. Metabolic reprogramming and equilibrium require blood and serum [4]. The circulation contains volatile organic molecules from systemic and local metabolism [8]. Blood is more dependable than breath. VOCs are sensitively detected by Proton-transfer-reaction mass spectrometry (PTR-MS) and GC-MS [9]. Metabolic alterations linked to cancer progression can also be shown by the local and systemic urine metabolism alterations. Both

GC-MS and Solid Phase Micro Extraction (SPME) can detect cancer-related biochemical markers in urine's volatile organic molecules [10]. Urine can be considered as a good candidate for the long-term study because to its stability.

Biosensor Technologies for VOC Detection

Using VOCs to diagnose cancer is vital in modern medicine. The reason for this is the numerous advantages that this technology provides to its consumers. Testing vapor or skin samples for volatile organic compound (VOC) concentrations is a non-invasive alternative to biopsies [11]. Recognizing cancer-associated volatile organic compound patterns simplifies the early detection. In addition, it increases the likelihood of effective treatment and patient survival. Compared to complicated and time-consuming medical examinations, screening of volatile organic molecules is more cost-effective and adaptable. VOC recognition is a major advantage which could improve cancer prognoses and transform cancer diagnosis. Table 1 and gives a brief list of endogenous VOCs identified as various cancer biomarkers and Table 2 consolidates the comparison of various aspects of currently available biosensing technologies.

Table1: Brief list of various cancer marker VOCs

Cancer types	VOCs identified	References
Lung Cancer	Benzene, Toluene, Ethylbenzene, Xylene, Naphthalene, Styrene	[1,2]
Breast Cancer	Hexanal, Heptanal, Nonanal, Benzaldehyde, Limonene	[3,4]
Colorectal Cancer	1- octane, 2-butanone, Hexanoic acid, Indole	[5,6]
Prostate Cancer	Acetone, Isoprene, 2-octanol, Hexanal, Heptanal	[7,8]
Gastric Cancer	Ethanol, 2-propanol, 2-butanone, Ethyl acetate, Dimethyl sulfide	[9,10]
Ovarian Cancer	Ethylbenzene, Benzene, Octanal, Decanal, Nonanal	[11,12]
Liver Cancer	Dimethyl disulphide, Ethylbenzene, Hexanal, Heptane	[13–15]
Esophageal Cancer	Acetone, Ethanol, 2-propanol, Benzaldehyde	[1,16]
Pancreatic Cancer	Ethyl formate, Acetone, Isoprene, Toluene	[17,18]

Table 2: Comparison table of different biosensing technologies

Biosensing Technology	Sensitivity	Specificity	Feasibility	Reference
Electronic Noses (e-Noses)	High sensitivity for detecting a wide range of VOCs, but limited by the low concentration of VOCs in complex biological samples.	Moderate specificity, prone to cross-reactivity, which may lead to false positives /negatives due to broader detection range.	Low-cost, portable, and suitable for point-of-care applications, but may lack high accuracy.	[19, 20]
Gas Chromatography-Mass Spectrometry (GC-MS)	Excellent sensitivity, considered the gold standard for precise VOC analysis with high accuracy.	High specificity, able to distinguish VOCs with very fine differences.	Low feasibility due to its complex setup, expensive instrumentation, and time-consuming procedures.	[21, 22]
Colorimetric Sensors	Moderate sensitivity, with the	Moderate specificit	High feasibility,	[23, 24]

	ability to detect VOCs through color change. May be less sensitive than other methods.	y, often lacks the ability to distinguish between closely related VOCs.	low-cost, easy-to-use, portable, and ideal for screening in low-resource settings.	
Field-Effect Transistor (FET)-based Sensors	High sensitivity, especially when functionalized with specific receptors for targeted VOCs.	Very high specificity due to selective receptor binding to specific cancer-related VOCs.	High feasibility for portable, real-time detection, but requires customization and precision in sensor design.	[25, 26]
Optical Biosensors	Moderate to high sensitivity, depending on the system design and application.	High specificity, can be designed for selective VOC detection, though some cross-reactivity may occur.	Feasible for portable use, but requires complex instrumentation, limiting its clinical accessibility.	[27]
Surface Plasmon Resonance (SPR)	Very high sensitivity due to real-time detection of refractive index changes, ideal for detecting low concentrations.	High specificity, as SPR can detect specific interactions between VOCs and receptors. However, it can be limited by receptor availability.	Moderate feasibility; requires specialized equipment and laboratory setup, limiting its widespread use.	[28, 29]

1. Biosensors Enhanced by Nanotechnology

The electrochemical biosensor is one of the most commonly employed devices for detecting volatile organic molecules. The operation of these sensors is accomplished by allowing volatile organic compounds (VOCs) to interact with a receptor, which then results in the formation of an electrical signal that can be measured. This process is repeated until the desired outcomes are achieved. It has been demonstrated that nanomaterial electrodes, which have been the focus of recent technical advancements, can improve both the sensitivity and selectivity of an electrical signal. Zhang et al. identified VOCs specific to gastric cancer cells, such as 3-octanone and butanone, using GC-MS. An electrochemical biosensor based on Au-Ag nanoparticle-coated MWCNTs demonstrated ultrasensitive detection of these biomarkers, with detection limits as low as 0.3 ppb for 3-octanone, indicating potential for early gastric cancer diagnosis [30]. The study done by Nazir et al. identified phenol 2,2 methylene bis [6-(1,1-dimethyl ethyl)-4-methyl] (MBMBP) as a significant volatile biomarker in the breath of hepatocellular carcinoma (HCC) patients, with a minimum concentration of 2100 ppm. A hexane thiol-AuNPs modified biosensor demonstrated ultrasensitive electrochemical detection of MBMBP with a limit of detection of 0.005 mol/L, confirmed its potential for early HCC diagnosis [31]. The review by Kaya etal. highlighted in the nanomaterial-based electrochemical biosensors for the sensitive and non-invasive detection of lung and colon cancer biomarkers to enable early diagnosis and treatment. Optical biosensors can detect VOC binding by observing changes in light characteristics. The detection of cancer-associated VOCs has considerable sensitivity via methods such as surface plasmon resonance (SPR) and fluorescence-based detection [32–34].

Nanotechnology has transformed biosensor design by enhancing detection limits and facilitating downsizing [35].

Figure 1 depicts Schematic representation of the SPR-based olfactory biosensor for VOC detection [36].

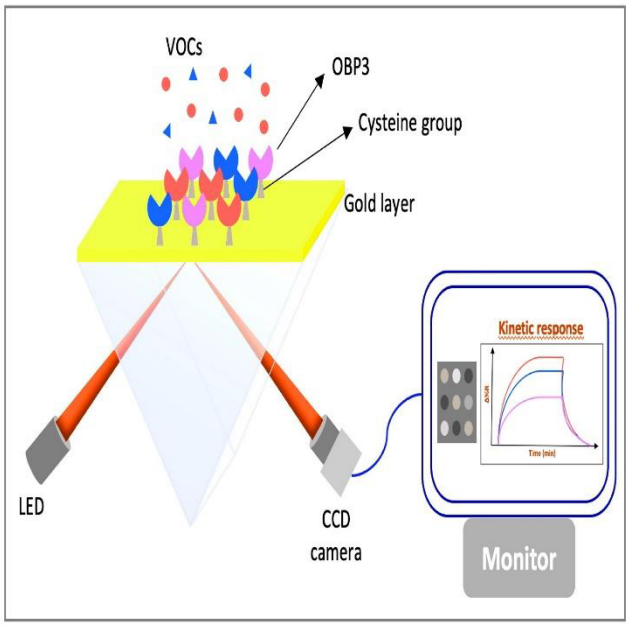

Figure 1: Schematic representation of the SPR-based olfactory biosensor for VOC detection [36].

Carbon nanotubes and quantum dots have been integrated into biosensors for the detection of VOCs at exceptionally low concentrations [37–41]. Shehada etal. developed a silicon nanowire field-effect transistor sensor capable of selectively detecting gastric cancer-related VOCs in exhaled breath while discriminating against unrelated environmental VOCs. Blind analysis of patient samples demonstrated >85% accuracy in distinguishing gastric cancer from controls, showcasing its potential for non-invasive, portable, and cost-effective cancer diagnosis [42].

2. Biosensors and Artificial Intelligence (AI)

Figure 2 schematically illustrate various medical applications of wearable biosensor design [43].

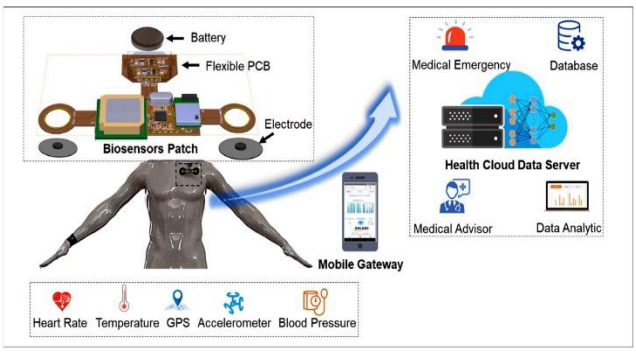

Figure 2: Schematic illustration of various medical applications of wearable biosensors [43].

The utilization of AI algorithms improves the detection of volatile organic compound patterns, hence enabling biosensors to distinguish between healthy and malignant profiles. Studies indicate that machine learning models developed using VOC datasets demonstrate considerable efficacy in precisely predicting cancer kinds. Einoch Amor etal. introduced an AI-driven nanoarray for liquid biopsy, detecting VOC patterns in blood headspace for early cancer detection and staging. The nanoarray demonstrated >84% accuracy for early detection and >97% accuracy for metastasis detection in breast, ovarian, and pancreatic cancer models, validated by mass spectrometry [44]. The study done by Johnson et al demonstrated that a DNA-decorated single-walled carbon nanotube vapor sensor array can distinguish volatile organic compound (VOC) patterns in plasma samples, achieving 95% accuracy for ovarian cancer and 90% for pancreatic cancer. The nano sensor successfully identified VOCs from early-stage cancers from the algorithm, offering a promising high-throughput diagnostic tool for these malignancies [45].

Innovations in VOC-Based Cancer Biosensors-Hybrid sensing platform, Wearable Biometric detectors, and POC devices

Many sensing modalities combined together have improved diagnostic dependability by themselves. Combining optical and electrochemical sensors has generated instruments capable of detecting a larger spectrum of VOCs [46–48]. Among popular wearable gadgets that offer continuous monitoring of VOCs can give their real-time data,and these devices are highly useful for high-risk groups specifically. Portable, user-friendly point-of- care (POC) biosensors have revolutionised cancer diagnosis [49]. Figure 3 schematically illustrates the smart phone assisted biosensors in healthcare [50].

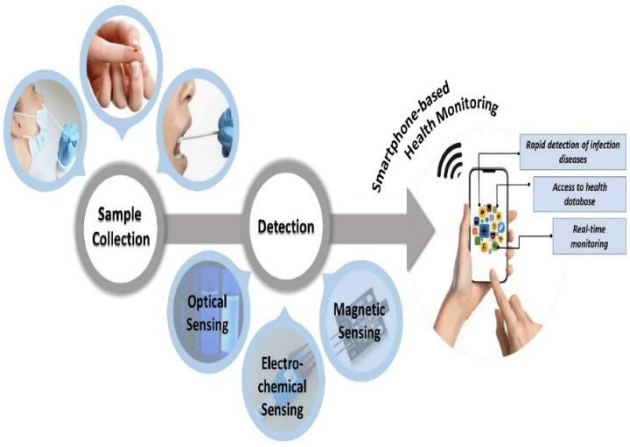

Figure 3: Schematic illustration of a POC biosensor [50]

Laboratory-level precision VOC analysis smartphone-integrated devices are among recent advances. Salimi etal. developed a smartphone-based ZnO nanosheet chemiresistive gas sensor capable of highly sensitive detection of lung cancer biomarkers such as diethyl ketone,

acetone, and isopropanol in exhaled breath [51].

Challenges and future scope

Prior to VOC detection being utilised for cancer diagnosis, certain concerns need to be addressed. Standardising VOC detection is challenging. The variability in volatile organic component profiles among cancer types, biological factors, and sampling techniques makes data collection a challenging task. The issue is resolved by standardising the collection, processing, and measurement of volatile organic compounds. By standardising procedures and merging databases for VOC profiles specific to cancer, laboratories may be able to detect VOCs in the same way.

There is a possibility of false positives due to VOC interference with cancer-related VOC signals. A combination of pre-concentration and selective filtration can improve the detection of VOCs specific to cancer by reducing background interference. Developing sensors that can distinguish between environmental pollutants and volatile organic compounds (VOCs) associated with cancer, or employing sophisticated statistical or machine learning techniques to identify VOC trends, would increase our confidence in the findings. There are limitations on the clinical usage of biosensors for volatile organic molecules. Qualitative, precise, and safe products must be approved by the FDA or EMA. Development and approval can be accelerated through pre-development coordination with government entities. Thorough clinical trials demonstrating the advantages of these devices and diagnostic biosensor guidelines are necessary to resolve these challenges.

As a result of individual and environmental factors, VOC detection findings might not be repeatable using these methods. Testing and other quality control measures aid in maintaining sensor performance. Accuracy and consistency in training are guaranteed by sensor drift monitoring and correction software. Because of their sensitivity, cancer-specific volatile organic compounds (VOCs) could go undetected in biological samples. Using signal amplification or nanomaterials, biomarkers at low concentrations can be sensitively detected. Thanks to multi-modal detection, VOCs associated with cancer may be more easily located. Combining GC-MS with SPR or electronic eyes is possible.

The high price and limited availability of GC-MS make it an impractical and unproductive tool. To put a stop to this, we urgently need portable biosensing devices for point-of-care diagnostics that are both affordable and easy to transport. In locations with limited resources, these technologies could potentially become more affordable as production ramps up utilising less expensive materials. Vapour concentration monitor data is massive and difficult to evaluate. Complex VOC trends could be explained by advanced data analysis methods such as machine learning. Through the use of straightforward software, we can assist physicians in analysing data pertaining to volatile organic compounds (VOCs) and improving diagnostics by linking VOC results to imaging or biopsies.

The accuracy, reliability, and usefulness of clinical VOC-based cancer biosensors can be enhanced by avoiding or resolving these issues. Lack of approved methods for VOC collecting, storage, and analysis results in discrepancies in sample preparation that compromise diagnostic accuracy and complicate cancer diagnosis. Ambient VOCs can interfere with cancer signals, therefore complicating the biomarker's detection. Increasing sensor sensitivity will enable one to differentiate cancer-associated VOCs from ambient interference and hence address this issue. Personal medical information revealed by VOC-based diagnostics could expose privacy concerns and genetic material exploitation questions. Well-built legal frameworks guard patient records, provide informed permission, and aid to lower diagnostic bias [52]. Future VOC-based diagnostics will classify many cancer types from a single sample, hence enhancing efficiency and screening capability. For patients residing in rural areas especially, telemedicine technology with remote analysis and at-home sample collecting could increase access. Customized metabolic profile testing can help to increase the accuracy and usefulness of the operation for several patient populations by increasing sensitivity and specificity. These technologies have enormous potential; but, for full manifestation they need research, standardizing, and ethical considerations.

Conclusion

Volatile organic compounds (VOCs) present a potential avenue for non-invasive cancer diagnostics, as biosensors facilitate rapid and precise detection. Despite ongoing challenges, continuous advancements in nanotechnology, artificial intelligence (AI), and hybrid sensing platforms contribute to overcoming current limitations. To revolutionise cancer treatment, biosensors based on volatile organic compounds (VOCs) could close the gap between lab work and real-world treatments. This would consequently save lives and enhance patient outcomes.

References

1. Bray F, Laversanne M, Sung H, Ferlay J, Siegel R L, Soerjomataram I and Jemal A 2024 Global cancer statistics 2022: *GLOBOCAN estimates of incidence and mortality worldwide for 36 cancers in 185 countries CA Cancer,* J Clin 74 229–63.
2. Hakim M, Broza Y Y, Barash O, Peled N, Phillips M, Amann A and Haick H 2012, *Volatile Organic Compounds of Lung Cancer and Possible Biochemical Pathways,* Chem Rev 112 5949–66.

3. Van Keulen K E, Jansen M E, Schrauwen R W M, Kolkman J J and Siersema P D 2020, *Volatile organic compounds in breath can serve as a non-invasive diagnostic biomarker for the detection of advanced adenomas and colorectal cancer,* Aliment Pharmacol Ther 51 334–46.
4. Schiliro C and Firestein B L 2021, *Mechanisms of Metabolic Reprogramming in Cancer Cells,* Supporting Enhanced Growth and Proliferation Cells 10.
5. Shen Q, Liu Y, Li G and An T 2024, *A review of disrupted biological response associated with volatile organic compound exposure: Insight into identification of biomarkers*, Science of The Total Environment 948 174924.
6. Lakestani S 2024, *Volatile organic compounds and cancer risk assessment in an intensive care unit*, Int J Biometeorol 68 1731–9.
7. Smith D, Španěl P, Demarais N, Langford V S and McEwan M J 2023, *Recent developments and applications of selected ion flow tube mass spectrometry (SIFT-MS),* Mass Spectrom Rev n/a e21835.
8. Dummer J, Storer M, Swanney M, McEwan M, *Scott-Thomas A, Bhandari S, Chambers S, Dweik R and Epton M 2011 Analysis of biogenic volatile organic compounds in human health and disease TrAC*, Trends in Analytical Chemistry 30 960–7.
9. Warneke C, Roberts J M, Veres P, Gilman J, Kuster W C, Burling I, Yokelson R and de Gouw J A 2011, *VOC identification and inter-comparison from laboratory biomass burning using PTR-MS and PIT-MS,* Int J Mass Spectrom 303 6–14.
10. da Costa B R B and De Martinis B S 2020, *Analysis of urinary VOCs using mass spectrometric methods to diagnose cancer: A review*, Clinical Mass Spectrometry 18 27–37.
11. Jiang R, Cudjoe E, Bojko B, Abaffy T and Pawliszyn J 2013, *A non-invasive method for in vivo skin volatile compounds sampling*, Anal Chim Acta 804 111–9.
12. Etemadi A, Poustchi H, Chang C M, Calafat A M, Blount B C, Bhandari D, Wang L, Roshandel G, Alexandridis A, Botelho J C, Xia B, Wang Y, Sosnoff C S, Feng J, Nalini M, Khoshnia M, Pourshams A, Sotoudeh M, Gail M H, Dawsey S M, Kamangar F, Boffetta P, Brennan P, Abnet C C, Malekzadeh R and Freedman N D 2024, *Exposure to polycyclic aromatic hydrocarbons, volatile organic compounds, and tobacco-specific nitrosamines and incidence of esophageal cancer*, JNCI: Journal of the National Cancer Institute 116 379–88.
13. Jia Z, Patra A, Kutty V K and Venkatesan T 2019, *Critical Review of Volatile Organic Compound Analysis in Breath and In Vitro Cell Culture for Detection of Lung Cancer*, Metabolites 9.
14. Silva C, Perestrelo R, Silva P, Capelinha F, Tomás H and Câmara J S 2019, *Volatomic pattern of breast cancer and cancer-free tissues as a powerful strategy to identify potential biomarkers*, Analyst 144 4153–61.
15. Silva C L, Passos M and Câmara J S 2012, *Solid phase microextraction, mass spectrometry and metabolomic approaches for detection of potential urinary cancer biomarkers—A powerful strategy for breast cancer diagnosis*, Talanta 89 360–8.
16. Mezmale L, Leja M, Lescinska A M, Pčolkins A, Kononova E, Bogdanova I, Polaka I, Stonans I, Kirsners A, Ager C and Mochalski P 2023, *Identification of Volatile Markers of Colorectal Cancer from Tumor Tissues Using Volatilomic* Approach Molecules 28.
17. Mezmale L, Leja M, Lescinska A M, Pčolkins A, Kononova E, Bogdanova I, Polaka I, Stonans I, Kirsners A, Ager C and Mochalski P 2023, *Identification of Volatile Markers of Colorectal Cancer from Tumor Tissues Using Volatilomic* Approach Molecules 28.
18. Janfaza S, Khorsand B, Nikkhah M and Zahiri J 2019, *Digging deeper into volatile organic compounds associated with cancer*, Biol Methods Protoc 4 bpz014.
19. Milone A, Monteduro A G, Rizzato S, Leo A, Di Natale C, Kim S S and Maruccio G 2023, *Advances in Materials and Technologies for Gas Sensing from Environmental and Food Monitoring to Breath Analysis*, Adv Sustain Syst 7 2200083.
20. Mezmale L, Ślefarska-Wolak D, Bhandari M P, Ager C, Veliks V, Patsko V, Lukashenko A, Dias-Neto E, Nunes D N, Bartelli T F, Pelosof A G, Sztokfisz C Z, Murillo R, Królicka A, Mayhew C A, Leja M, Haick H and Mochalski P 2024, *Volatilomic profiles of gastric juice in gastric cancer patients*, J Breath Res 18 026010.
21. Lubes G and Goodarzi M 2018, *GC–MS based metabolomics used for the identification of cancer volatile organic compounds as biomarkers*, J Pharm Biomed Anal 147 313–22.
22. Vassilenko V, Moura P C and Raposo M 2023, *Diagnosis of Carcinogenic Pathologies through Breath*, Biomarkers: Present and Future Trends Biomedicines 11.
23. McLane-Svoboda A K, Sanchez S W, Parnas M, Apu E H and Saha D 2024, *Use of living systems for clinical diagnostics by monitoring volatile chemicals TrAC,* Trends in Analytical Chemistry 180 117987.
24. Dima A C, Balaban D V and Dima A 2021, *Diagnostic Application of Volatile Organic*

Compounds as Potential Biomarkers for Detecting Digestive Neoplasia: A Systematic Review Diagnostics, 11.

25. Amal H, Ding L, Liu B, Tisch U, Xu Z, Shi D, Zhao Y, Chen J, Sun R, Liu H, Ye S-L, Tang Z and Haick H 2012, *The scent fingerprint of hepatocarcinoma: in-vitro metastasis prediction with volatile organic compounds (VOCs)*, Int J Nanomedicine 7 4135–46.
26. Mochalski P, Sponring A, King J, Unterkofler K, Troppmair J and Amann A 2013, *Release and uptake of volatile organic compounds by human hepatocellular carcinoma cells (HepG2) in vitro Cancer Cell*, Int 13 72.
27. Gashimova E M, Temerdashev A Z, Perunov D V, Porkhanov V A, Polyakov I S and Dmitrieva E V 2023, *Selectivity of Exhaled Breath Biomarkers of Lung Cancer in Relation to Cancer of Other Localizations*, Int J Mol Sci 24.
28. Ramírez W, Pillajo V, Ramírez E, Manzano I and Meza D 2024, *Exploring Components, Sensors, and Techniques for Cancer Detection via eNose Technology: A Systematic Review Sensors*, 24.
29. Jalal A H 2018, *Multivariate Analysis for the Quantification of Transdermal Volatile Organic Compounds in Humans by Proton Exchange Membrane Fuel Cell System Recommended Citation Jalal, Ahmed Hasnain, "Multivariate Analysis for the Quantification of Transdermal Volatile Organic Compounds in Humans by Proton Exchange Membrane Fuel Cell System*, (2018). FIU Electronic Theses and Dissertations.
30. Zhang Y, Gao G, Liu H, Fu H, Fan J, Wang K, Chen Y, Li B, Zhang C, Zhi X, He L and Cui D 2014, *Identification of volatile biomarkers of gastric cancer cells and ultrasensitive electrochemical detection based on sensing interface of Au-Ag alloy coated MWCNTs*, Theranostics 4 154–62.
31. Nazir N U A and Abbas S R 2023, *Identification of phenol 2,2-methylene bis, 6 [1,1-D] as breath biomarker of hepatocellular carcinoma (HCC) patients and its electrochemical sensing: E-nose biosensor for HCC,* Anal Chim Acta 1242 340752.
32. Usman F, Dennis J O, Aljameel A I, Ali M K M, Aldaghri O, Ibnaouf K H, Zango Z U, Beygisangchin M, Alsadig A and Meriaudeau F 2021, *Plasmonic Biosensors for the Detection of Lung Cancer Biomarkers: A Review Chemosensors*, 9.
33. Qu X, Hu Y, Xu C, Li Y, Zhang L, Huang Q, Sadat Moshirian-Farahi S, Zhang J, Xu X, Liao M and Fu Y 2024, *Optical sensors of volatile organic compounds for non-invasive diagnosis of diseases*, Chemical Engineering Journal 485 149804.
34. Kaur B, Kumar S and Kaushik B K 2022, *Recent advancements in optical biosensors for cancer detection*, Biosens Bioelectron 197 113805.
35. Onyinye O V, *The detection of cervical cancer volatile organic compounds (VOCs) biomarkers using metal oxide-polymer nanocomposite sensors*.
36. El Kazzy M, Weerakkody J S, Hurot C, Mathey R, Buhot A, Scaramozzino N and Hou Y 2021, *An Overview of Artificial Olfaction Systems with a Focus on Surface Plasmon Resonance for the Analysis of Volatile Organic Compounds*, Biosensors (Basel) 11.
37. Fernandes M P, Venkatesh S and Sudarshan B G 2015, *Early Detection of Lung Cancer Using Nano-Nose-A Review*, Open Biomed Eng J. 9 228-33.
38. Vishinkin R and Haick H 2015, *Nanoscale Sensor Technologies for Disease Detection via Volatolomics* Small, 11 6142–64.
39. Broza Y Y and Haick H 2013, *Nanomaterial-Based Sensors for Detection of Disease by Volatile Organic Compounds*, Nanomedicine 8 785–806.
40. Nath N, Kumar A, Chakroborty S, Soren S, Barik A, Pal K and de Souza F G Jr 2023, *Carbon Nanostructure Embedded Novel Sensor Implementation for Detection of Aromatic Volatile,* Organic Compounds: An Organized Review ACS Omega 8 4436–52.
41. Khatib M and Haick H 2022, *Sensors for Volatile Organic Compounds*, ACS Nano 16 7080–115.
42. Shehada N, Brönstrup G, Funka K, Christiansen S, Leja M and Haick H 2015, *Ultrasensitive Silicon Nanowire for Real-World Gas Sensing: Noninvasive Diagnosis of Cancer from Breath*, Volatolome Nano Lett 15 1288–95.
43. Phan D T, Nguyen C H, Nguyen T D P, Tran L H, Park S, Choi J, Lee B and Oh J 2022, *A Flexible, Wearable, and Wireless Biosensor Patch with Internet of Medical Things Applications Biosensors* (Basel), 12.
44. Einoch Amor R, Zinger A, Broza Y Y, Schroeder A and Haick H 2022, *Artificially Intelligent Nanoarray Detects Various Cancers by Liquid Biopsy of Volatile Markers*, Adv Healthc Mater 11 2200356.
45. Johnson A T C, Kehayias C, Carpenter E L, Piltz-Seymour J, Tanyi J L, Otto C, Lee Y E, Black T A, Yee S S and Preti G 2024, *Nanoanalysis of plasma volatile organic compounds using novel DNA-decorated carbon nanotube vapor sensors to noninvasively distinguish ovarian and pancreatic cancer from benign and control samples*, Journal of Clinical Oncology 39 5544.
46. Azzouz A, Vikrant K, Kim K-H, Ballesteros E,

Rhadfi T and Malik A K 2019, *Advances in colorimetric and optical sensing for gaseous volatile organic compounds* TrAC, 118 502–16.

47. Tripathi K M, Kim T, Losic D and Tung T T 2016, *Recent advances in engineered graphene and composites for detection of volatile organic compounds (VOCs) and non-invasive diseases diagnosis* Carbon 110 97–129.
48. Pathak A K, Swargiary K, Kongsawang N, Jitpratak P, Ajchareeyasoontorn N, Udomkittivorakul J and Viphavakit C 2023, *Recent Advances in Sensing Materials Targeting Clinical Volatile Organic Compound (VOC),* Biomarkers: A Review Biosensors (Basel) 13.
49. Rasheed S, Kanwal T, Ahmad N, Fatima B, Najam-ul-Haq M and Hussain D 2024, *Advances and challenges in portable optical biosensors for onsite detection and point-of-care diagnostics*, TrAC Trends in Analytical Chemistry 173 117640.
50. Beduk T, Beduk D, Hasan M R, Guler Celik E, Kosel J, Narang J, Salama K N and Timur S 2022, *Smartphone-Based Multiplexed Biosensing Tools for Health Monitoring Biosensors*, (Basel) 12.
51. Salimi M and Milani Hosseini S M R 2021, *Smartphone-based detection of lung cancer-related volatile organic compounds (VOCs) using rapid synthesized ZnO nanosheet*, Sens Actuators B Chem 344 130127.
52. Jalal A H, Alam F, Roychoudhury S, Umasankar Y, Pala N and Bhansali S 2018, *Prospects and Challenges of Volatile Organic Compound Sensors in Human Healthcare*, ACS Sens 3 1246–63.

An Enhanced Simulative Study on SWIRGs of $In_{0.68}Al_{0.08}Ga_{0.24}As/InP$ Lasing Nanoscale Heterostructure

Pyare Lal

Department of Physical Sciences, Banasthali Vidyapith-304022 (Rajasthan) INDIA.

drpyarephysics@gmail.com

Abstract

The foremost emphasis of this foundational research letter has been given on analytical investigation of an enhanced simulative study on shortwave infrared gains (SWIRGs) of $In_{0.68}Al_{0.08}Ga_{0.24}As/InP$ lasing nanoscale heterostructure for fiber optic cable communication applications under transverse electric and magnetic bi-modes at 300K. In the starting of this work, taking into account recent and emerging computational technology, an enhanced and improved effective mass theory for single and multi-sub-bands has been utilized to enumerate the appropriate SWIR gain parameters as well as electrons-holes (Es-Hs) levels of quasi-Fermi energies. Under advanced simulation, first of all, the salient computational performances of Es-Hs levels of quasi-Fermi sub-band energies versus injected carriers (10^{18} cm^{-3}) at 300K have been analysed simulatively. Next, electric and magnetic transverse bi-modes induced several spectral performances of SWIR-gain with wavelengths of photons have also been investigated analytically. In spite of this, the prominent performances of SWIR-differential gain ($10^{-16}cm^2$) with injected carriers (10^{18} cm^{-3}) under transverse electric and magnetic bi-modes at 300K have been analyzed dominantly. Throughout the results, the peak intensities of SWIR-gain are achieved at wavelengths 1330 nm and 1550 nm corresponding to two crests of SWIR-spectra respectively under transverse bi-modes. Consequently, this emitted SWIR light gain by $In_{0.68}Al_{0.08}Ga_{0.24}As/InP$ heterogeneous nanostructure of wavelengths ~ 1330 nm and 1550 nm can be substantially utilized in the applications of fiber optic cable communications in the transmission of SWIR-signals through the modern process of total internal reflection with minimal attenuations of SWIR-signals (in $dB \times km^{-1}$) owing to lowest fiber dispersions and fiber absorptions.

Keywords: Es-Hs quasi-Fermi sub-band energy levels, SWIR-gain, SWIR-differential gain, SWIR-loss, Transverse bi-modes.
Received 30 January 2025; First Review 21 February 2025; Accepted 07 March 2025

*** Address of correspondence**
Pyare Lal
Department of Physical Sciences, Banasthali Vidyapith-304022 (Rajasthan) INDIA.

Email: drpyarephysics@gmail.com

How to cite this article
Pyare Lal, An Enhanced Simulative Study on SWIRGs of $In_{0.68}Al_{0.08}Ga_{0.24}As/InP$ Lasing Nanoscale Heterostructure, J. Cond. Matt. 2025; 03 (01): 64-67.

Available from:
https://doi.org/10.61343/jcm.v3i01.123

Introduction

In today's advanced research, there have been observed so many differences between homogeneous and heterogeneous junctions based on nanoscale structures. As it has been known that a homogeneous structure has been formed when two materials of equal band gap interact while a heterogeneous structure has been formed when two materials of different band gap interact with each other. In taking into consideration emerging nanotechnology, for the applications of SI- telecommunication systems, an InAlGaAs heterogeneous junction nanostructure [1-9] has been investigated by researchers for emission of SI radiations. The various optoelectronic characteristics like modal confinement parameter, intensity of modal infrared gain, intensity of infrared gain [10-12] have been investigated in emerging research fields. In this research work various SWIRGs of $In_{0.68}Al_{0.08}Ga_{0.24}As$ /InP heterogeneous nanostructure at room temperature under transverse bi-modes have been simulated analytically. In order to enumerate the various SWIR-gain parameters as well as energies of Es-Hs quasi-Fermi levels an advanced effective mass theory of single and multi-sub band has been applied. Electric and magnetic transverse bi-modes induced several spectral performances of SWIR-gain with wavelengths of photons have also been investigated analytically. In spite of this, the prominent performances of SWIR-differential gain in ($10^{-16}cm^2$) with injected carriers (in 10^{18} cm^{-3}) under transverse electric and magnetic bi-modes at 300K have been analysed dominantly.

Heterostructure Details and Theoretical Method

In this simulative work, there has been proposed a heterogeneous nanostructure of five SNLs (Step-index Nanoscale Layers). This nanostructure has been simulated such that, one NQL (Nanoscale Quantum-well Layer) has

Table1: Layer-compositions and layer-parameters of $In_{0.68}Al_{0.08}Ga_{0.24}As$ /InP heterostructure.

SNLs	% x,y of ($In_{1-x-y}Al_yGa_xAs$)	Width(nm)	Wave-length (nm)	BOE (eV)
NCL (C.B.)	00%, 45%	10.00	08451	0.2574
NBL (C.B.)	34%, 27%	05.00	10472	0.1753
NQL	24%, 08%	06.00	15783	0.0734
NBL (V.B.)	34%, 27%	05.00	10472	- 0.1753
NCL (V.B.)	00%, 45%	10.00	08451	-0.2574

been sandwiched between two NBLs (Nanoscale Barrier Layers), and after that it has been covered by two NCLs (Nanoscale Cladding Layers) and after that the whole system has been grown simulatively on an InP base (substrate) layer. Layer-compositions, layer-parameters and Band offset energy (BOE) for conduction and valence bands of $In_{0.68}Al_{0.08}Ga_{0.24}As$/InP nanoscale structure have been exhibited in table 1.

An expression of Infrared gain amplification coefficient [13] as a function of photon's energies has been given by the following mathematical relationship.

$$G(\hbar\omega) = \frac{q^2\hbar 2\pi}{2n_{eff}(\hbar\omega)m_0^2\varepsilon_0 c} \times \left[1 - exp\left(\frac{\hbar\omega - \Delta f}{k_b T}\right)\right] \times \sum_{nc,nv} \frac{|M_b|^2 f_c f_v}{4\pi^2 L_W} \times \frac{(\hbar\pi\tau)dk_x dk_y}{\pi(\{\hbar\omega_{nc}+\hbar\omega_{nv}+\hbar\omega_{sg}\}-\hbar\omega)^2+(\hbar\pi\tau)^2}$$

Here- $\hbar\omega$ = Photonic energy, $\hbar$ = reduced Planck constant, ω = angular frequency, q = charge of electron, n_{eff} = effective refractive index, m_0 = mass of electron, ε_0 = permittivity of free space, c = speed of light, Δf = energy separation between quasi-Fermi levels, k_b = Boltzmann constant, M_b = bulk momentum matrix, f_c, f_v = conduction and valence band fermi functions. L_W= width of quantum well layer, k_x, k_y = wave vectors, τ = photon life time.

The differential form of infrared gain coefficient has been defined as differential gain coefficient [14-23] expressed by the following equation.

$$G'(\hbar\omega) = \frac{dG(\hbar\omega)}{dN} = \frac{8\pi^2 m_r \hbar\omega}{c\varepsilon h^3 L_W} \times \int_{E'}^{\infty} |M_b|^2 \times \left(\frac{df_c(\hbar\omega)}{dN} - \frac{df_v(\hbar\omega)}{dN}\right) \times L(\hbar\omega')d\hbar\omega'.$$

Here - $G'(\hbar\omega)$ = differential shortwave infrared gain, $\frac{dG(\hbar\omega)}{dN}$ = derivative of shortwave infrared gain with respect to carrier density, $L(\hbar\omega')$ = line shape function, $|M_b|^2$ = squared bulk momentum matrix element, m_r = reduced mass, h = Planck constant, $\frac{df_c(\hbar\omega)}{dN}$ = differential quasi fermi function for conduction band with respect to carrier density, $\frac{df_v(\hbar\omega)}{dN}$ = = differential quasi fermi function for valence band with respect to carrier density, ε = electric permittivity, c = speed of light.

Simulative Results and Discussions

An increment in infrared light per unit initial value of it at per unit length of propagating infrared light can be defined as infrared gain parameter. In fig. 1 the transverse bi-modes spectral performances of intensity of SWIR-gain with wavelengths of photons have been shown by blue right (y) and blue top (x) axes. As it has been shown in black spectra that the corresponding to two crests at lasing photon's wavelengths ~ 1330 nm and 1550 nm, the peak values of SWIR-gain have been achieved by the simulation results in transverse electric mode-TE, while in transverse magnetic mode-TM, only single peak of SWIR has been achieved at 1330 nm, it is presented by blue graph. By fig. 1, it has also been shown the energies behaviours of quasi-Fermi levels of Es and Hs with densities of injection carriers by black left (y) and black bottom (x) axes. Although the curves of Es and Hs have been shown by black and red colours respectively.

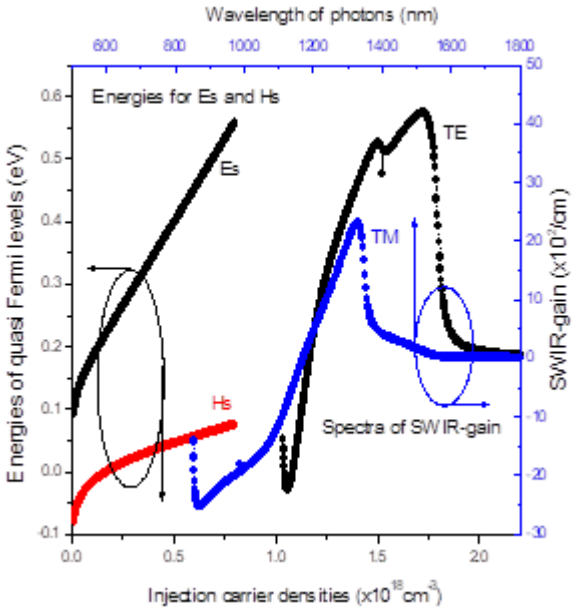

Figure 1: Transverse electric (TE) and transverse magnetic (TM) bi-modes induced spectral performances of SWIR-gain

(Shortwave infrared gain) with wavelength (nm) and levels of Es (electrons in conduction bands) and Hs (holes in valence bands) for quasi-Fermi energy sub-bands with injection carrier densities (cm^{-3}) at 300K.

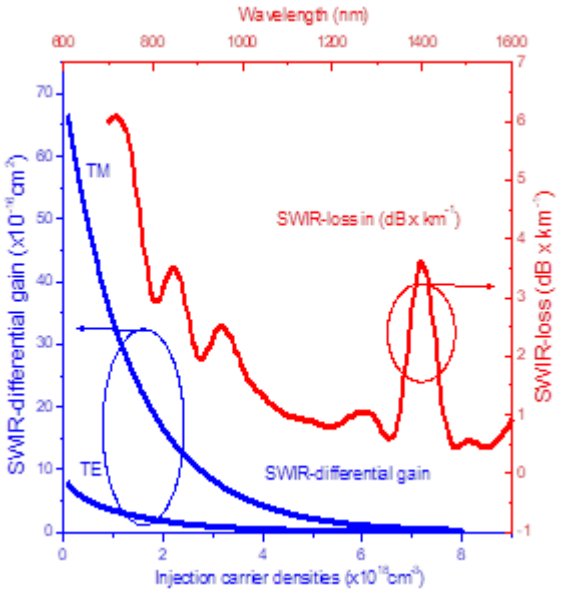

Figure 2: Simulative performances of transverse electric (TE) and transverse magnetic (TM) SWIR-differential gain (shortwave infrared differential gain in cm^2) with injected carrier concentration in cm^{-3} and SWIR-loss (shortwave infrared loss in per cm) with wavelength in nm at 300K.

As it has been observed by black and red graphs of Es and Hs that the energy separation between Es and Hs quasi-Fermi sub-bands levels enhances as an increase in injected carriers. Further, the transverse bi-modes performances of intensity of SWIR-differential gain with densities of injection carriers by left (y) and bottom (x) axes in blue colour have been graphically simulated in fig.2. Further, in fig.2 both blue curves show the inverse behaviours of differential values of SWIR-gain with densities of injection carriers. Although, in transverse mode-TM the value of SWIR-differential gain has been achieved higher than that of transverse mode-TE. Further, fig. 2 also exhibits the behaviours of SWIR-loss (in dB × km^{-1}) with wavelengths (nm) by right (y) and top (x) axes in red colour. As it has been observed by the SWIR-loss spectrum that the SWIR-loss has been found negligible at the wavelengths ~ 1330 nm and 1550 nm in the comparison of 1400 nm. Thus 1330 nm and 1550 nm wavelength's achieved SWIR-light have been largely utilized in emerging and recent applications of fiber optic cable communications in the transmission of SWIR-signals through the modern process of total internal reflection with microscopic attenuations of SWIR-signals (in dB × km^{-1}) owing to minor fiber dispersions and minor fiber absorptions.

Conclusions

At room temperature (300K), under transverse electric and magnetic bi-modes, the cardinal aim of this proposed research work has been to study of investigation on an advanced simulation of SWIRGs of $In_{0.68}Al_{0.08}Ga_{0.24}As/InP$ heterogeneous nanoscale structure. In order to enumerate the various SI-parameters as well as energies of Es-Hs quasi-Fermi levels an improved effective mass theory single and multi-sub-bands has been applied analytically. In the advanced simulations throughout the results, the peak values of SWIR-gain have been found corresponding to two crests at the photon's wavelengths ~ 1330 nm and 1550 nm. This emitted SWIR-light gain has been largely used in the applications of nanoscale fiber optic cable-based SWIR-signal communications through the process of total internal reflection with microscopic SWIR attenuation of shortwave infrared signals (in dB× km^{-1}) owing to minor fiber absorption and dispersions.

Acknowledgement

Owing to providing the enhanced research facilities by the department of physical sciences, Banasthali Vidyapith (Rajasthan), the author is very grateful.

References

1. P. A. Alvi, Pyare Lal, S. Dalela, M. J. Siddiqui, *"An Extensive Study on Simple and GRIN SCH based $In_{0.71}Ga_{0.21}Al_{0.08}As/InP$ Lasing heterostructure"*, Physica Scripta, 85, 035402 2012.
2. P. A. Alvi, Pyare Lal, Rashmi Yadav, Shobhna Dixit, S. Dalela, *"Modal gain characteristics of GRIN-InGaAlAs/InP lasing nano - heterostructures"*, Superlattices and Microstructures, Vol. 61, pp. 1-12, 2013.
3. A. Ramam and S. J. Chua, *"Features of InGaAlAs/InP heterostructures"*, Journal of Vacuum Science & Technology B: Microelectronics and Nanometer Structures Processing, Measurement, and Phenomena 16, 565, 1998.
4. D A Rybalko, I S Polukhin et al, *"Model of mode-locked quantum-well semiconductor laser based on InGaAs/InGaAlAs/InP heterostructure"*, Journal of Physics: Conference Series 741, 012079, 2016.
5. Pyare Lal, Garima Bhardwaj, Sandhya Kattayat, P.A. Alvi1, *"Tunable Anti-Guiding Factor and Optical Gain of InGaAlAs/InP Nano-Heterostructure under Internal Strain"*, Journal of Nano- and Electronic Physics, Vol. 12 No 2, 02002(3pp), 2020.
6. Pyare Lal, Sapna Gupta, PA Alvi, *"G-J study for GRIN InGaAlAs/InP lasing nano-heterostructures"*, AIP Conference Proceedings, Vol. 1536, Issue-1, pp-53-54, 2013.

7. Sandra R. Selmic, Tso-Min Chou, JiehPing Sih, Jay B. Kirk, Art Mantie, Jerome K. Butler, David Bour, and Gary A. Evans, *"Design and Characterization of 1.3-μm AlGaInAs–InP Multiple-Quantum-Well Lasers"*, IEEE Journal on Selected Topics in Quantum Electronics, Vol. 7, No. 2, March/April 2001.
8. S. Yoshitomi, K. Yamanaka, Y. Goto, Y. Yokomura, N. Nishiyama, and S. Arai, *"Continuous-wave operation of a 1.3 μm wavelength npn AlGaInAs/InP transistor laser up to 90 °C"*, Japanese Journal of Applied Physics 59, 042003, 2020.
9. Joachim Piprek, J. Kenton White, and Anthony J. SpringThorpe *"What Limits the Maximum Output Power of Long-Wavelength AlGaInAs/InP Laser Diodes?"*, IEEE Journal of Quantum Electronics, Vol. 38, No. 9, September 2002.
10. Weng W. Chow, Zeyu Zhang, Justin C. Norman, Songtao Liu, and John E. Bowers, *"On quantum-dot lasing at gain peak with linewidth enhancement factor αH = 0"*, APL Photon. 5,026101, 2020.
11. Pyare Lal and P. A. Alvi, *"Strain induced gain optimization in type-I InGaAlAs/InP nanoscale-heterostructure",* AIP Conference Proceedings 2220, 020060, 2020.
12. L. Ya. Karachinsky , I. I. Novikov , A. V. Babichev , A. G. Gladyshev , E. S. Kolodeznyi, S. S. Rochas , A. S. Kurochkin , Yu. K. Bobretsova , A. A. Klimov , D. V. Denisov , K. O. Voropaev , A. S., Ionov , V. E. Bougrov , and A. Yu. Egorov *"Optical Gain in Laser Heterostructures with anActive Area Based on an InGaAs/InGaAlAs Superlattice",* ISSN 0030-400X, Optics and Spectroscopy, 2019, Vol. 127, No. 6, pp. 1053–1056, 2019.
13. S. L. Chuang, Physics of optoelectronic devices, Wiley, New York, 1995.
14. C. Henry, *"Theory of linewidth of semiconductor lasers,"* IEEE J. Quantum Electron. 18, 259–264, 1982.
15. H. Vahala and A. Yariv, *"Semiclassical theory of noise in semiconductor lasers-Part II",* IEEE J. Quantum Electron. 19, 1102–1109, 1983.
16. Pyare Lal, Rashmi Yadav, Meha Sharma, F. Rahman, S. Dalela and P. A. Alvi, *"Qualitative analysis of gain spectra of InGaAlAs/InP lasing nano-heterostructure",* International Journal of Modern Physics B, Vol. 28, No. 29, 1450206, 2014.
17. Pyare Lal, *"An Investigation of Optical Gain of Nanomaterial AlGaAsIn/InP under CTLSs in Optical Communications",* Journal of Atomic, Molecular, Condensed Matter and Nanophysics 7(3), 189-195, 2020.
18. Pyare Lal, *"Gain Enhancement Study of Nanomaterial AlGaAs/GaAs under GRINLs",* Journal of International Academy of Physical Sciences, Vol. 24, No. 04, pp.485-491, 2020.
19. Pyare Lal, *"An Investigative Study on Growth of Light of AlGaAs/ GaAs in Nanotechnological Life Sciences",* Conference Proceeding NSCTLS-2021, ISSN: 2582-3310, Vol.2, Issue I, pp 23-32, June 2021.
20. G Bhardwaj, Pyare Lal, V Mishra, P A Alvi, *"Numerical simulation of optical properties of compressively strained GRIN- InGaAlAs/ InP type-I nano-heterostructure"*, Material Today, Proceedings, 44, 4847-4849, 2021.
21. Pyare Lal, *"An Exploratory Study on SWIRL of AlGaAs/GaAs in Advanced Bio based Nanotechnological Systems",* Journal of Advanced Materials and Nano Systems: Theory and Experiment-Part 2, Issue 2, Pages 18-33, Bentham Science Publishers, 30 Sep 2022.
22. Pyare Lal and P A Alvi, *"A Simulative Study on Electro-Optic Characteristics of InAlGaAs/InP for Fiber Optic-based Communications under Nanoscale Well Thickness Layers"*, Journal of Photonic Materials: Recent Advances and Emerging Applications, Issue 2, Pages 160, Bentham Science Publishers, 24 Jan 2023.
23. Pyare Lal, *"An Advanced Study on Temperature Influenced Electro-optic-properties of In0.73Al0.07Ga0.20As/InP in Fiber-optic Communications under Bi-modes",* Journal of Intelligent Technologies for Scientific Research and Engineering, Volume 1, Pages 45-59, Bentham Science Publishers, July 2023.

Nanoscale Wettability of Water-Alcohol Mixtures on Graphite Surface: Molecular Dynamics Study

Abdulkareem U[a] and V Madhurima[b]

Central University of Tamil Nadu, Thiruvarur, Tamil Nadu, India.

[a] akareem28@gmail.com
[b] madhurima@cutn.ac.in

Abstract

The ability to predict and control surface wettability at the nanoscale is crucial and rapidly evolving, particularly in the fields of microfluidics and nanotechnology. Typically, the contact angle is measured in simulations by creating a liquid droplet on a solid surface, fitting a curve to the droplet's interface, and determining the angle at the triple-phase contact line. However, at the molecular level, the triple-phase contact line becomes ambiguous due to the continuous motion of molecules, making conventional measurements difficult. This study reports the molecular dynamics simulations to determine the contact angle of water mixed with four primary alcohols (R_N-OH, where R = (C_NH_{2N+1}), N varies from 1 to 4) on a graphite substrate, using the Hautman and Klein method, which links the microscopic contact angle to the droplet's average centre of mass height through the concepts of equivalent contact area and volume. The water concentration is varied from 50% to 90% in the alcohol mixture. ContactAngleCalculator code is modified to calculate the contact angle of binary liquids. Results show that increasing alcohol concentration leads to greater spreading.

Keywords: Wetting, Contact Angle, Molecular Dynamics Simulation, Binary Mixtures.
Received 30 January 2025; First Review 21 February 2025; Accepted 07 March 2025

*** Address of correspondence**
Dr. V Madhurima
Central University of Tamil Nadu, Thiruvarur, Tamil Nadu, India.

Email: madhurima@cutn.ac.in

How to cite this article
Abdulkareem U and V Madhurima, Nanoscale Wettability of Water-Alcohol Mixtures on Graphite Surface: Molecular Dynamics Study, J. Cond. Matt. 2025; 03 (01): 68-70.

Available from:
https://doi.org/10.61343/jcm.v3i01.124

Introduction

Understanding the wettability of aqueous mixtures on solid surfaces is crucial for unravelling interfacial phenomena, with wide-ranging applications in material science, microfluidics, and processes like coating, adhesion, drug delivery, and fluid transport [1-3]. This paper reports the contact angle (CA) of water-alcohol binary mixture (R_N-OH, where R = (C_NH_{2N+1}), N varies from 1 to 4, R =1(methanol), R = 2(ethanol), R = 3(1-propanol) and R = 4(1-butanol) on a graphite substrate using molecular dynamics (MD) simulation. The water concentration is varied from 50% to 90% in the alcohol mixture.

Methodology

The MD simulation is carried out using large-scale atomic/molecular massively parallel simulator (LAMMPS) [4]. The alcohols are modelled using optimized potential for liquid simulation/all atom (OPLS/AA) [5, 6] force field and the water molecules using SPC/E model [7]. Two layers of graphene sheet are used to prepare the graphite. It has been found that two layers of graphene were sufficient to reproduce the CA [8]. The graphene sheets are generated using the nanotube builder plugin in VMD [9]. The graphene sheets are built with the dimension of 15 nm in both the x and y directions. The distance between the two graphene layers is 0.335 nm. The simulated water-alcohol binary mixture is centered above the graphite surface. The methodology used to simulate binary mixtures is same as our previous works [10,11]. The pair interactions are modeled using the lj/charmm/coul/long style with a cutoff of 10 Å for Lennard-Jones and 12 Å for Coulomb interactions. Long-range Coulombic interactions are handled using the particle-particle particle-mesh (PPPM) method with a precision of 1.0×10^{-4}. The simulations are performed in the NVT ensemble, maintaining a temperature of 298.15 K through the Nosé-Hoover thermostat, with a time step of 1 fs. Atomic positions are recorded every 1 ps. The simulation is run for 1 ns (i.e. 100000 time steps).

Discussion

In simulations, the CA is typically calculated by simulating a liquid droplet on a solid surface, allowing it to reach

equilibrium, and analysing its shape. The angle is measured at the triple-phase contact line by fitting a curve to the droplet's interface. However, at the molecular level, CA becomes ambiguous, as shown in Figure 1.

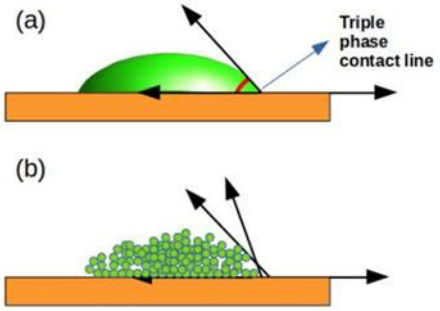

Figure 1: Schematic images of (a) macroscopic droplet, (b) microscopic droplet.

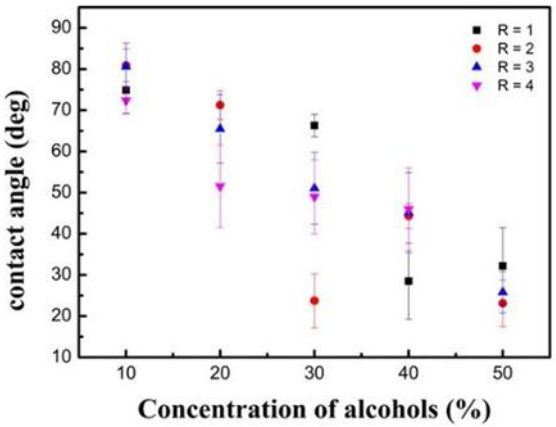

Figure 2: CA versus concentration of alcohols (%).

Hautman and Klein introduced a method for estimating the microscopic CA from the simulations, this approach uses the concepts of equivalent contact area and volume to create a quantitative link between the CA and the average height of the droplet's center of mass. The CA of the water-alcohol binary mixture on a graphite substrate is calculated using a flexible estimation tool called "ContactAngleCalculator" [12] which is specifically designed to function within VMD. The code is versatile and can be used with different MD codes. It was written only to work with a single molecular system. The code was modified to calculate the CA of the binary mixture. The modified version of the code is available at

https://github.com/akareem28/ContactAngleCalculator/blob/main/cac-cg-mult

The CA calculation using the ContactAngleCalculator code consists of four steps (i) coarse-graining the all-atom model of a molecule into a single bead and removing the evaporated molecules (ii) calculating the circular contact area from the real contact area, (iii) constructing the droplet from the real liquid volume and (iv) calculating the CA. Prior to the calculation of CA, the number density is calculated from the simulation. A detailed description of calculating CA using the Hautman and Klein method is available in reference [12, 13].

Figure 2 shows the CA versus concentration of alcohol in water-alcohol binary mixture on graphite surface. As the concentration of alcohol increases, the droplets spreads more on the graphite surface.

Conclusion and Future Prospective

The ability to predict and control surface wettability at the nanoscale is crucial and rapidly evolving, particularly in the fields of microfluidics and nanotechnology. Typically, the CA is measured in simulations by creating a liquid droplet on a solid surface, fitting a curve to the droplet's interface, and determining the angle at the triple-phase contact line. However, at the molecular level, the triple-phase contact line becomes ambiguous due to the continuous motion of molecules, making conventional measurements difficult. This study reports the MD simulations to determine the CA of water-alcohol binary mixtures on a graphite substrate. The Hautman and Klein method, which links the microscopic CA to the droplet's average center of mass height through the concepts of equivalent contact area and volume is used to calculate the CA at nanoscale. ContactAngleCalculator code is modified to calculate the contact angle of binary liquids. Results show that increasing alcohol concentration leads to greater spreading. Liquid spreads on a solid if it lowers the system's surface energy. On graphite, water-alcohol mixtures show better spreading with increasing alcohol concentration. Graphite's dispersive interactions are weak with polar water but stronger with alcohols, especially long-chain ones, reducing the contact angle at higher alcohol concentrations.

Acknowledgments

The authors express their gratitude to the Inter-University Center for Astronomy and Astrophysics (IUCAA) for providing access to their server for conducting the MD simulations. Abdulkareem U acknowledges the Council of Scientific and Industrial Research (CSIR) for awarding the Direct SRF fellowship.

References

1. S. Damiati, U. B. Kompella, S. A. Damiati, and R. Kodzius, *"Microfluidic Devices for Drug Delivery Systems and Drug Screening"*, in Genes. 9- 21-103, Feb. 2018.
2. Y Liu and X Jiang. Lab. Chip, 17(23):3960–3978, 2017.

3. K Velmurugan, M B Kulkarni, I Gupta, R Das, S Goel, and J Nirmal. Microfluidics and Multi Organs on Chip, pages 107–133, 2022.
4. A P Thompson et al. Comput. Phys. Commun., 271:108171, 2022.
5. Development and Testing of the OPLS All-Atom Force Field on Conformational Energetics and Properties of Organic Liquids. J. Am. Chem. Soc., 118(45), 1996.
6. L S Dodda, I Cabeza de Vaca, J Tirado-Rives, and W L Jorgensen. Nucleic Acids Res., 45(W1), 2017.
7. J Zielkiewicz. J. Chem. Phys., 123(10):104501, 2005.
8. F Taherian et al. Langmuir, 29(5):1457–1465, 2013.
9. W Humphrey, A Dalke, and K Schulten. J. Mol. Graph., 14(1):33–38, 1996.
10. U Abdulkareem, T R Kartha, and V Madhurima. J. Mol. Model., 28(12):382, 2022.
11. U Abdulkareem, T R Kartha, and V Madhurima. J. Mol. Model., 29(5):151, 2023.
12. Y Wang, A Kiziltas, P Blanchard, and T R Walsh. J. Chem. Inf. Model., 62(24):6302–6308, 2022.
13. C F Fan and T CaÇgin. J. Chem. Phys., 103(20):9053–9061, 1995.

Photoluminescence Properties of Eu(TTA)$_3$Phen/PS-PMMA Polymer Blend Electrospun Nanofibers

Manjusha Dandekar[1,a], Sangeeta Itankar[1,b], S. B. Kondawar[2,c]

[1] *Department of Physics, G.H. Raisoni Skill Tech University, Nagpur - 440033, India.*
[1] *Department of Physics, Suryodaya College of Engineering and Technology, Nagpur 440016, India*
[2] *Department of Physics, Rashtrasant Tukadoji Maharaj Nagpur University, Nagpur - 440033, India*

[a] manjusha.dandekar@gmail.com
[b] skawadkar18@gmail.com
[c] sbkondawar@yahoo.co.in

Abstract

Because of their 4f electrons, europium metal ions have incredibly crisp emission bands. As the overlaying 5s^2 and 5p^6 orbitals effectively protect 4f orbitals from the effects of external pressures. Complex forms of europium metal ions, such Eu(TTA)$_3$Phen, have garnered a lot of concentration for of their high fluorescence emission efficiency, which is caused by the ligands' high absorption coefficient. The Europium complex Eu(TTA)$_3$Phen doped PS-PMMA polymer mix, Eu (TTA)$_3$Phen/PS, and Eu (TTA)$_3$Phen/PMMA have been synthesized and reported here. The SEM picture, XRD and PL characterizations, and CIE chromaticity were used to characterize the synthesized nanofibers made using the electrospinning technology. The f–f electron transition of Eu^{3+} ions and the antenna effect of ligands provide this Europium β-diketon complex exceptional optical and luminous characteristics. Due to the extreme hypersensitive behaviour of the $^5D_0 \rightarrow {}^7F_2$ transition, the photoluminescence emission spectrum of nanofibers exhibits very high intense red emission. Because Eu3+ ions separate in the polymer chain of molecules, there will be more contact between the polymer and Europium complexes, which explains why polymers, polystyrene (PS), and polymethyl methacrylate (PMMA) have good optical properties. This was made possible by the polymer nanofibers' even distribution of Eu^{3+}. This is because the presence of polymer may cause the site symmetry of the Eu^{3+} ion to decrease, and the surrounding polymer media may distort it. This study demonstrates the possible use of electrospinning in a variety of polymer optoelectronic devices and emphasises its promising uses in the creation of protective textiles. Because electrospun nanofibers are strong, flexible, and have exceptional photoluminescence qualities, they are used in the newest technology for smart textiles to create smart fabrics for a variety of applications. These textiles provide as protection against a wide range of environmental threats.

Keywords: E-Textile Electrospinning method, Europium nanofibers, Photoluminescence.
Received 31 January 2025; First Review 19 February 2025; Accepted 21 February 2025.

*** Address of correspondence**
Manjusha Dandekar
Department of Physics, G.H. Raisoni Skill Tech University, Nagpur - 440033, India

Email: manjusha.dandekar@gmail.com

How to cite this article
Manjusha Dandekar, Sangeeta Itankar, S. B. Kondawar, Photoluminescence Properties of Eu(TTA)$_3$Phen/PS-PMMA Polymer Blend Electrospun Nanofibers, J. Cond. Matt. 2025; 03 (01): 71-77.

Available from:
https://doi.org/10.61343/jcm.v3i01.131

Introduction

Due to their distinctive luminescence characteristics, including extremely crisp emission bands, a long lifespan, and the possibility for high internal quantum competence, photoactive rare-earth Eu complexes in particular, europium β-diketones are of both technical and essential interest [1]. These Eu β-diketon complexes have remarkable optical and luminous properties due to the f–f electron transition of Eu^{3+} ions and the antenna effect of ligands, which opens up important possibilities [2–4]. However, the pure Eu complexes have limited practical applications and only show promise for comprehensive photophysical applications due to their poor comprehensive photophysical applications due to their poor mechanical strength, poor thermal stability, low processing ability, and poor resistance to air moisture.

Europium complexes are typically added to organic or inorganic hybrid matrices, sol–gel silica [6], or organically modified silicates and polymers, to create powders, fibres, thin solid films, etc., as a suitable way to get around these drawbacks. Eu complex-doped polymers have garnered a lot of attention due to their mechanical flexibility and ability to retain the complexes' luminescent characteristics while being processed from solution. It has been a steady increase in interest in polymer materials. There are now several ways to produce thin polymer films. Technically and financially,

polymeric materials constitute the most significant class of organic materials [7].

The polymers added RE complexes are mechanically flexible and have enhanced photoluminescence and thermal stability [8-9]. Rare earth complexes added to polymeric systems are anticipated to be used in functional devices such tiny lasers, waveguide amplifiers, and polymer fibre lasers, which are a significant component of the rapidly expanding area of photonics [10-12].

Electrospinning is a reasonably simple and efficient approach for creating fibres with a variety of compositions, long lengths, and uniform diameters when compared to other production methods [13]. With this method, a polymer solution droplet's surface is charged with a high voltage, which causes a liquid jet to be ejected via a spinneret [14]. The jet is then repeatedly stretched to create continuous, ultrafine fibres as a result of bending instability. Fibres made with this technique can have widths ranging from a few nanometres to several micrometres [15]. Nanofibers produced by the electrospinning process have several notable characteristics, such as pore sizes in the nano range, a very high surface area to volume ratio, unique physical characteristics, and the ability to be functionalised and modified chemically and physically [16–17].

Method

The optimum technique for creating Eu(TTA)$_3$Phen/Polymer nanofibers is electrospinning. Electrospinning is a somewhat simple and efficient approach for creating fibers with a variety of compositions, long lengths, and uniform diameters when compared to other fabrication methods. Fibers made with this technique can have sizes ranging from a few nanometers to several micrometers.

The solution approach was employed to create the europium complex Eu(TTA)$_3$Phen used in this investigation [1]. Figure 1 below illustrates the chemical mechanism via which Eu(TTA)$_3$Phen is created.

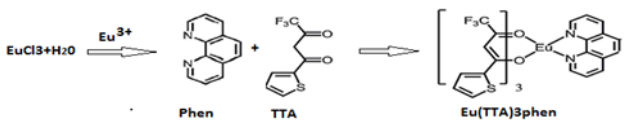

Figure 1: Chemical process of formation of Eu(TTA)$_3$Phen

Synthesis method of Eu(TTA)$_3$Phen/PMMA Composite Solutions

Following the creation of the Eu(TTA)$_3$Phen complex, several polymers, including PS (mol. wt = 350,000) and PMMA (mol. wt = 350,000), used to create Eu(TTA)$_3$Phen/Polymer composite solutions. A standard procedure for making Eu(TTA)$_3$Phen/PS involved dissolving 2g of PS in 10ml of THF (tetrahydrofuran) solvent and stirring it magnetically for 12 hours until it was homogenous. The aforesaid uniform PS polymeric solution was then magnetically agitated for 12 hours until uniform, after which 20% of Eu(TTA)$_3$Phen complex powder was added. For synthesis of Eu(TTA)$_3$Phen/PMMA and Eu(TTA)$_3$Phen/PMMA-PS polymer blend, same procedure was carried out again.

Discussion

SEM Image of Prepared Electrospun Nanofibers

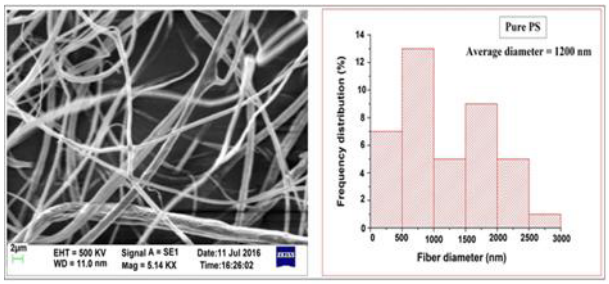

Figure 2: SEM image with histogram of PS nanofibers.

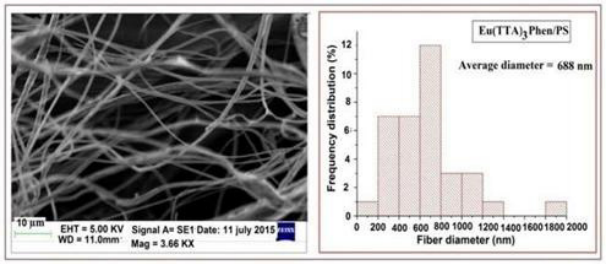

Figure 3: SEM image with histogram of Eu(TTA)$_3$Phen/PS nanofibers.

Figures 2 and 3 display the SEM image with histogram of pure Polystyrene and Eu(TTA)$_3$Phen/PS composite electrospun nanofibers, separately. Because bending instability brought on by the spinning jet and stationary collector, it exhibits morphologically nanofibrous characteristics, with a uniform diameter and variable orientation alignment. It is clear from comparing the fibre morphologies of pure Polystyrene and Eu(TTA)$_3$Phen/PS that the composite nanofibers have lower average diameters (about 688 nm) than pure Polystyrene. This might be the result of the electrospinning solution's improved conductivity brought on by the addition of Eu(TTA)$_3$Phen. Based on the Polystyrene nanofibers histogram analysis, the average fibre diameter was determined to be between 1200 and 1200 nm. However, for Eu(TTA)$_3$Phen/PS, it was 688 nm, demonstrating that the morphology of the electrospinning fibres may be effectively improved by adding the europium complex to the polymer matrix.

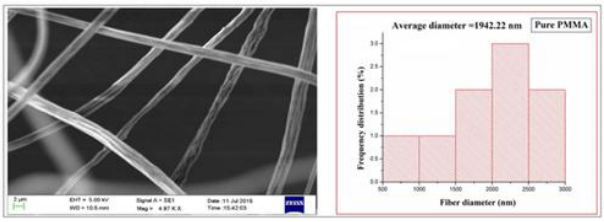

Figure 4: SEM image with histogram of PMMA nanofibers.

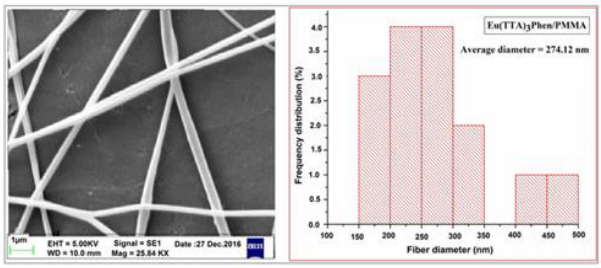

Figure 5: SEM image with histogram of Eu(TTA)$_3$Phen/PMMA nanofibers.

Figures 4 and 5 display the morphologies of uniform nanofibers of PMMA and Eu(TTA)$_3$Phen/PMMA that were generated with diameter ranging from 500 to 2000 nm. Due to the bending instability brought on by the spinning jet, all of the nanofibers have the same diameter, are aligned, and are orientated randomly. The typical diameter of the fibres was determined to be 1942.22 nm for pure PMMA and 274.12 nm for Eu(TTA)$_3$Phen/PMMA based on the analysis of the nanofiber histogram. The composite nanofibers average diameters are clearly smaller than those of the pure PMMA. This demonstrates the same cause of the electrospinning solution's improved conductivity brought on by the addition of PMMA to Eu(TTA)$_3$Phen.

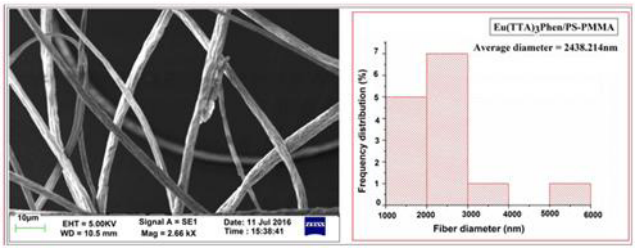

Figure 6: SEM image with histogram of Eu(TTA)$_3$Phen/PS-PMMA nanofibers.

The morphologies of the electrospun Eu(TTA)$_3$Phen/PS-PMMA composite nanofibers are displayed in Figure 6, which indicates that the bending instability linked to the spinning jet caused the nanofibers to align in a random orientation and have a uniform diameter. The nanofibers were discovered to be arbitrarily orientated on the collector because of the fixed collector and the twisting variability carried on by the electrospinning jet [16]. Based on the analysis of nanofiber historiography, the average fiber diameter was determined to be between 2438.21 nm.

XRD of Eu(TTA)$_3$Phen/PS Polymer Composite Nanofibers

Figure 7 displays the XRD result of pure PS, Eu(TTA)$_3$Phen complex, and Eu(TTA)$_3$Phen/PS composite. The range of XRD result points is 2θ = 10 to 60 degrees. The diffraction peak for pure PS nanofibers in the X-ray diffraction was at about 15.21 with plane (300), indicating that the sample was primarily amorphous. Another peak, representing the monoclinic structure of the PS unit cell, appears at 16.80 with plane (220) and 18.250 with plane (211).

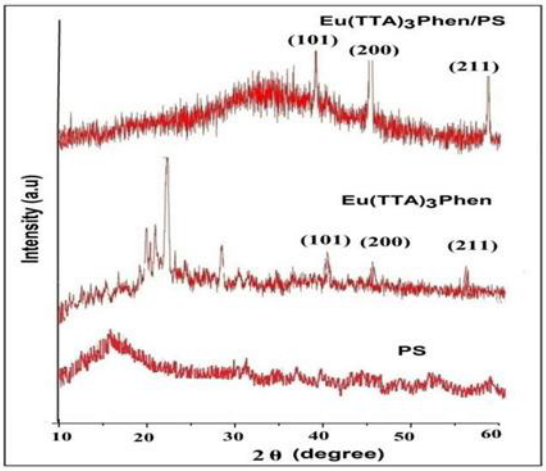

Figure 7: XRD pattern of Eu(TTA)$_3$Phen/PS.

The XRD result of the Eu(TTA)$_3$Phen complex showed well-resolved peaks at 20.26, 21.64, 21.66, 27.80. These peaks confirmed the crystalline behaviour of Eu(TTA)$_3$Phen. These strongest diffractive peaks make it abundantly evident that the Eu(TTA)$_3$Phen combination is a particular type of crystal [29]. Eu(TTA)$_3$Phen/PS X-ray diffraction almost displays a large peak of europium, indicating the presence of chemical interaction between the polymer PS and the Europium complex. PS matrices have been found to dominate the crystallinity of Eu(TTA)$_3$Phen upon the addition of polymers. It is apparent, sharp peaks of the Eu(TTA)$_3$Phen/PS have disappeared.

XRD of Eu(TTA)$_3$Phen/PMMA Fibres

Figure 8 displays the XRD result of pure PMMA, Eu(TTA)$_3$Phen, and Eu(TTA)$_3$Phen/PMMA composite. PMMA nanofibers XRD patterns display three distinctive peaks at 2θ = 29.5°, 42.5°, and 52.5°, which correspond to planes (111), (220), and (311). The non-crystalline character of pure PMMA is confirmed by the absence of any strong diffraction peaks. However, when a polymer is added to Eu(TTA)$_3$Phen/PMMA, the crystallinity of Eu(TTA)3phen is dominated by Polymer matrices. It is apparent that the distinct diffraction peaks of the Eu(TTA)$_3$Phen/PMMA pure complex have vanished. When mixing with PMMA, certain additional features appear; the

peak locations differ somewhat from pure complex. This suggests that the matrix PMMA has an impact on the complex's crystal structure, possibly as a result of the coordination with PMMA distorting the local environment of Eu^{3+} [31].

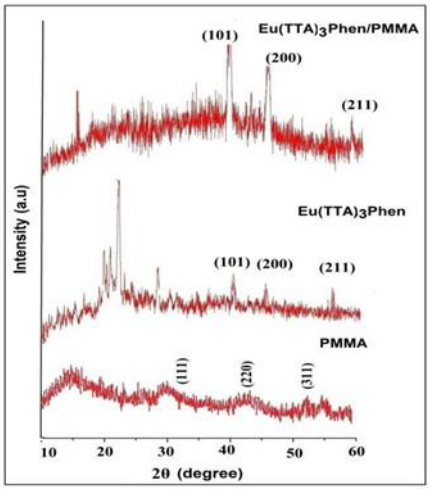

Figure 8: XRD pattern of $Eu(TTA)_3Phen$/PMMA.

Figure 9 displays the $Eu(TTA)_3Phen$/PS-PMMA composite's XRD result. It shows that the tiny matching peaks of europium have been found in the range of $2\theta = 15°$ to 58°. This finding suggests that in polymer blend matrices presence of $Eu(TTA)_3Phen$ [34].

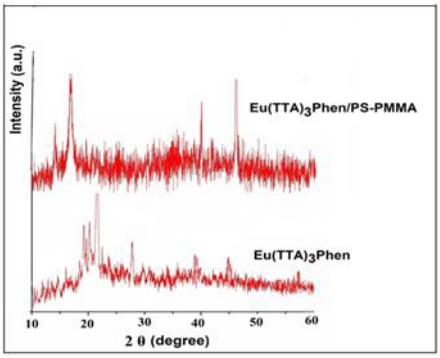

Figure 9: XRD pattern of $Eu(TTA)_3Phen$/PS-PMMA composite.

Photoluminescence in $Eu(TTA)_3Phen$

Figure 10 shows the excitation spectra of the pure $Eu(TTA)_3$phen compound at 354 nm. The ligands $\pi \rightarrow \pi^*$ electron transport results in a broad excitation band that extends from 255 to 455 nm [27–31]. Every excitation band shows blue shift and splits into two components, with peaks at roughly 271 and 346 nm, respectively.

The site symmetry of the Eu^{3+} ion may be reduced and deformed by the surrounding polymer media in the composite nanofibers. The $^7F_0 \rightarrow {}^5D_2$ and $^7F_1 \rightarrow {}^5D_1$ excitation lines are visible in the excitation spectrum of pure $Eu(TTA)_3Phen$, but they disappear in the composite fibres. This suggested that the f–f inner-shell transitions in the composite fibres would be quenched by the nonradiative energy transfer from the higher excited states to specific unknown defect levels, which took the place of the nonradiative relaxation from higher excited states to the $^5D_0$ level [28].

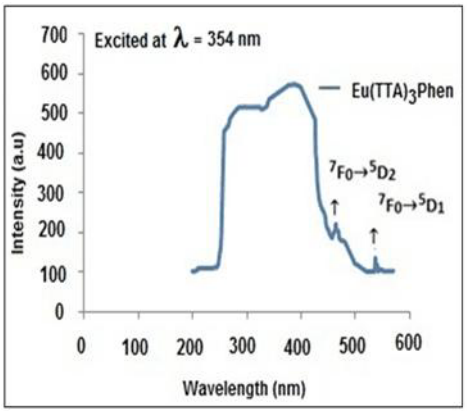

Figure 10: The excitation spectra of the $Eu(TTA)_3Phen$ complex.

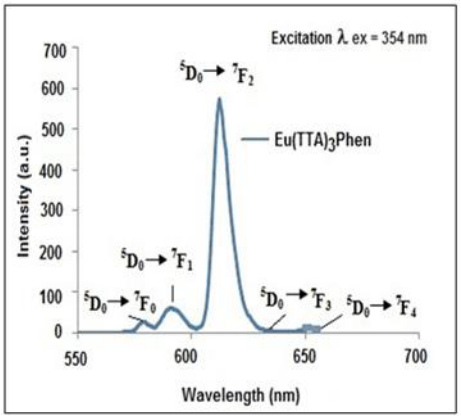

Figure 11: The emission spectra of the $Eu(TTA)_3Phen$ complex.

Figure 11 displays the $Eu(TTA)_3Phen$ complexes emission spectra. Under stimulation at 354 nm, the emission spectra of $Eu(TTA)_3Phen$ were measured between 550 and 655 nm [27–32]. The four emission peaks, at 579, 592, 612, 642, and 654 nm, are caused by the f–f transitions of Eu^{3+}. In that order, their designations are $^5D_0 \rightarrow {}^7F_0$, $^5D_0 \rightarrow {}^7F_1$, $^5D_0 \rightarrow {}^7F_2$, $^5D_0 \rightarrow {}^7F_3$, and $^5D_0 \rightarrow {}^7F_4$. The Eu^{3+} ion is found in a single chemical environment when there is just one $^5D_0 \rightarrow {}^7F_0$ line. The Eu^{3+} ion is in a single site without a centre of inversion, as evidenced by the $^5D_0 \rightarrow {}^7F_2$ transitions far higher intensity than the other transitions. The $^5D_0 \rightarrow {}^7F_1$ transition is a magnetic dipole transition among them.

The various excitation spectra of $Eu(TTA)_3Phen$/Polymers composites triggered at 354 nm are displayed in Figure 12. A wide excitation band spanning from 250 to 450 nm is produced by the ligands' $\pi \rightarrow \pi^*$ electron transfer in the case of the pure $Eu(TTA)_3Phen$ complex [33].

On the other hand, the excitation bands of Eu(TTA)$_3$Phen/Polymer composites exhibit blue shift and split in half, peaking at approximately 270 and 345 nm, respectively. This is because the presence of polymer may cause the site symmetry of the Eu^{3+} ion to be reduced and the surrounding polymer media to distort it.

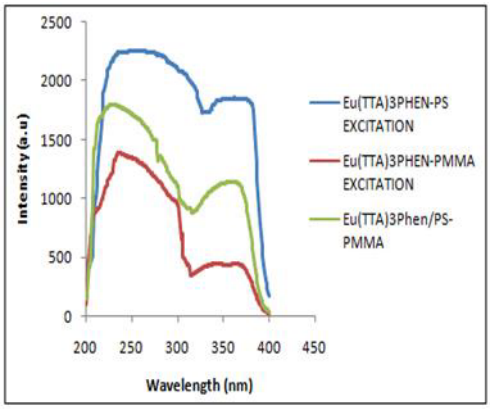

Figure 12: Excitation Spectra of Eu(TTA)$_3$Phen/Polymer composites nanofibers.

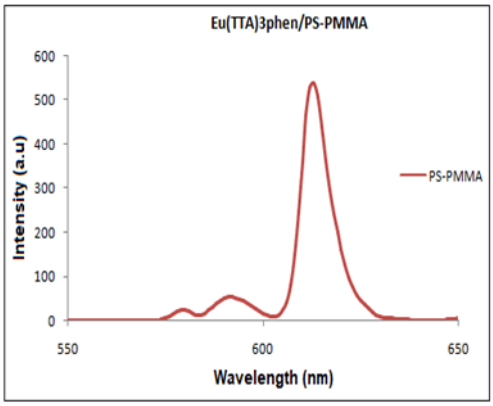

Figure 13: Emission Spectra of Eu(TTA)$_3$Phen/PS-PMMA composite nanofibers.

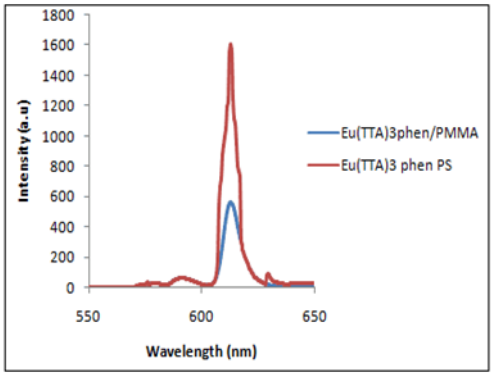

Figure 14: Emission Spectra of Eu(TTA)$_3$Phen/Polymers composite nanofibers.

Figure 13 and Figure 14 displays the Eu(TTA)$_3$Phen/Polymers composites emission spectra, which were obtained under excitation at 354 nm and ranged

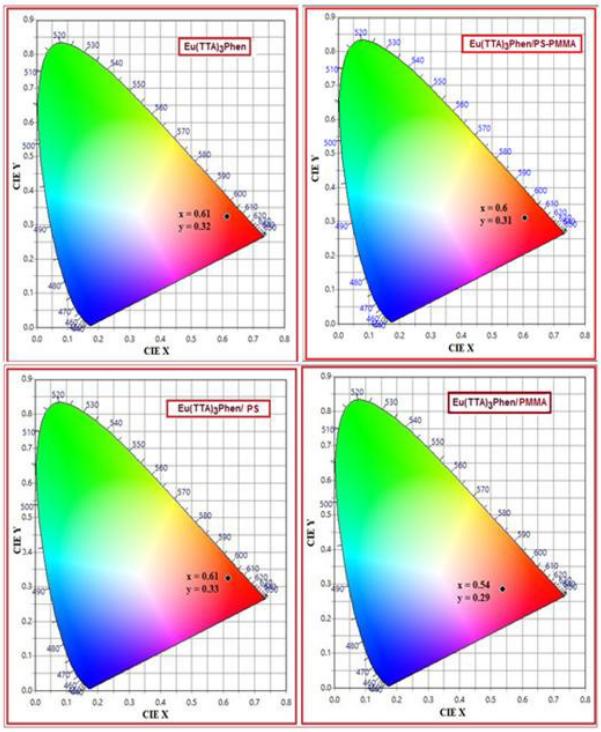

Figure 15: CIE chromaticity color coordinates for (a) Eu(TTA)$_3$Phen (b) Eu(TTA)$_3$Phen/PVDF.

from 550 to 655 nm. Four emission peaks are identified as being associated with the $^5D_0 \rightarrow {}^7F_0$, $^5D_0 \rightarrow {}^7F_1$, $^5D_0 \rightarrow {}^7F_2$, and $^5D_0 \rightarrow {}^7F_3$, respectively, and are centered at 579, 592, 612, and 652 nm. The usual red emission of the Eu^{3+} ion, attributed to the transitions between the multiplet ($^7F_{0-4}$) and the first excited state ($^5D_0$), made up the room-temperature fluorescence spectra of the composite nanofibers.

The presence of the Eu(TTA)$_3$Phen complex in polymers frequently results in a higher luminous intensity than the pure complex because the complex is equally distributed along the macromolecular chains of the polymers. Because Eu(TTA)$_3$Phen/Polymers fibers are electro spun nanofibers, their luminescent complex is distributed similarly to that of the macromolecular chain of polymers, and their luminous intensity is higher than that of bulk material [25].

Therefore, the results indicated above imply that the presence of polymers like PS and PMMA frequently increases the fluorescence intensity of the $^5D_0 \rightarrow {}^7F_2$ sensitivity transition of Eu^{3+} ions. When integrated into the microcavities of the polymer matrix, the europium complexes exhibit more disordered local surroundings due to the impact of the surrounding polymer [26]. The emission intensity increases as if the ions were excited at nearly the same wavelength when Eu^{3+} ions are implanted in a different polymer matrix.

CIE Chromaticity Coordinates

Using PL emission data, the CIE coordinates of the

$Eu(TTA)_3Phen$ complex, $Eu(TTA)_3Phen$/Polymers, and polymer blends were obtained using the Commission Internationale de l'Eclairage (CIE), Colour calculator software, shown in figure 15. The permissible CIE values for the red emission of the $Eu(TTA)_3Phen$ complex are x = 0.61 and y = 0.32 coordinates (Figure 13), which are close to the coordinates for pure red emission set by the National Television System Committee (NTSC) [14–16].

The CIE coordinates of the $Eu(TTA)_3Phen$ complex moved from their original location and showed good colour saturation upon the addition of a polymer. The calculated CIE coordinates are x = 0.61, y=0.33 for $Eu(TTA)_3Phen$/PS, x = 0.54, y = 0.29 for $Eu(TTA)_3Phen$/PMMA, and x = 0.6, y = 0.31 for $Eu(TTA)_3Phen$/Polymer-Polymer mix. The calculated CIE shows good colour saturation. As the europium complex doped polymers matrix was seen, the emission intensity increased and the CIE colour coordinates moved towards pure or saturated red emission. The complex's integrated polymer matrix emitted saturated red light, and its CIE colour coordinates were red.

Conclusion and Future Prospective

The synthesis, characterisation, and photoluminescence characteristics of $Eu(TTA)_3Phen$, $Eu(TTA)_3Phen$/Polymer composites, and $Eu(TTA)_3Phen$/Polymer-Polymer blends electrospun nanofibers made by electrospinning process are the main topics of the current study. Photoactive lanthanide complexes such as europium with β-diketones are highly interesting due to their high emission peaks in the visible and near-infrared region under UV stimulation. However, the rare-earth ions can enhance this by forming complexes with organic ligands.

The ligand $Eu(TTA)_3Phen$ may absorb far more light than the Eu^{3+} ions because the chromophores of the organic ligand have very strong absorption bands. These ligands can act as an antenna and fill the emitting excited levels by absorbing the excitation light and transferring the excitation energy to the higher energy levels of the Eu^{3+} ion. The fashion industry is becoming more interested in safety clothing as a result of the development of luminous textile materials. In addition to being beneficial in a variety of textile applications, the ability to generate light without heat without the need for an external power source is also appealing. In order to create clothing that can catch and emit light so that it is always visible, even in the dark, for a specified amount of time, the invention pertains to a photoluminescent fabric and a method of creating one.

References

1. Y. Hongquan, L. Tao, B. Chen, Y. Wua, Y. Li, *"Preparation of aligned $Eu(DBM)_3Phen$/PS fibers by electrospinning and their luminescence properties"*, Journal of Colloid and Interface Science, 2, (2013), 231-521.
2. Z. Xiaoping, W. Shipeng, H. Shui, Z. Liqun, L. Liu, *"Electrospinning preparation and luminescence properties of $Eu(TTA)_3Phen$ /polystyrene composite nanofibers"*, Journal of rare earths, 28, (2010), 332-337.
3. R. Hassey, J. Swain, N. Hammer, D. Venkataraman, M. Barnesm, *"Probing the chiroptical response of a single molecule"*, J. Science, 314, (2006), 1437-1452.
4. M. Robinson, J. Ostrowski, G. Bazan, M. Mcgehee, *"Reduced operating voltages in polymer light-emitting diodes Doped with rare-earth complexes"*, J. Adv. Mater., 15, (2003), 1547-1552.
5. M. Abdullah, T. Morimoto, K. Okuyama, *"Generating blue and red luminescence from zno/poly (ethylene glycol) nanocomposites prepared using an in-situ method"*, J. Adv. Funct. Mater, 13, (2003), 800-816.
6. B. Edison, G. Gibelli, J. Kai, E.S. Ercules, Teotonio, L. Oscar, C. Malta, *"Photoluminescent PMMA polymer films doped with Eu^{3+} diketonate crown ether complex"*, Journal of Photochemistry and Photobiology A: Chemistry, 251, (2013), 154–159.
7. K. Binnemans, Rare-earth beta-diketonates, in: K. A. Gschneidner Jr., J.-C. G. Bünzli, V. K. Pecharsky (Editors.), Handbook on the Physics and Chemistry of Rare Earths, Elsevier, Amsterdam, 35, (2004), 107–272.
8. J. C. G. Bünzli, *"Lanthanide luminescence for biomedical analyses and imaging"*, Chemical Reviews, 110, (2010), 2729–2755.
9. H. F. Brito, O. L. Malta, M. C. F. C. Felinto, E. E. S. Teotonio, *"Luminescence phenomena involving metal enolates, in: J. Zabicky (Ed.), Patai Series: The Chemistry of Metal Enolates"*, John Wiley & Sons Ltd, Chichester, England, 1, (2009), 131–184.
10. S. V. Eliseeva, J. C. G. Bünzli, *"Lanthanide luminescence for functional materials and bio-sciences"*, Chemical Society Reviews, 39, (2010), 189–227.
11. M. C. Felinto, C. S. Tomiyama, H. F. Brito, E.S. Teotonio, O. L. Malta, *"Synthesis and luminescent properties of supramolecules of b-diketonate of Eu(III) and crown ethers as ligands"*, Journal of Solid State Chemistry, 171, (2003), 189–194.
12. H. F. Brito, O.L. Malta, L. R. Souza, J. F. S. Menezes, C. A. Carvalho, *"Luminescence of the films of Europium(III) with thenoyltrifluoro acetonate and macrocyclic"*, Journal of Non-Crystalline Solids, 247, (1999), 129–133.

13. K. Sheng, B. Yan, *"Coordination bonding assembly and photophysical properties of Europium organic/inorganic/polymeric hybrid materials"*, Journal of Photochemistry and Photobiology A: Chemistry, 206, (2009), 140–147.
14. X. Ouyang, R. Yu, J. Jin, J. Li, R. Yang, W. Tan, J. Yuan, *"New strategy for label-free and time-resolved luminescent assay of protein: conjugate Eu^{3+} complex and aptamer-wrapped carbon nanotubes"*, J.Analytical Chemistry, 83, (2011), 782–789.
15. A. K. Singh, S. K. Singh, H. Mishra, R. Prakash, S. B. Rai, *"Structural, thermal, and fluorescence properties of $Eu(DBM)_3Phenx$ complex doped in PMMA"*, Journal of Physical Chemistry B, 114, (2010), 13042–13051.
16. P. Lenaerts, K. Driensen, R. V. Deun, K. Binnermans, *"Covalent coupling of luminescent tris (2-thenoyltrifluoroacetonato)lanthanide(III) complexes on a merrifield resin",* J. Chemistry of Materials, 17, (2005), 2148–2154.
17. J. Kai, M. C. F. C. Felinto, L. A. O. Nunes, O. L. Malta, H. F. Brito, *"Intermolecular energy transfer and photostability of luminescence-tuneable multicolour PMMA films doped with lanthanide"*, J. Chemistry of Materials, 11, (2011), 125-132.
18. E. Drexler, *"Engines of Creation: The Coming Era of Nanotechnology"*, Publisher Doubleday, 1, (1986), 54-85.
19. *"Nanoscience and nanotechnologies: opportunities and uncertainties"*, J. Royal Society and Royal Academy of Engineering. Published by Clyvedon press, 2, (2004), 25.
20. C. Buzea, I. Pacheco, K. Robbie, *"Nanomaterials and Nanoparticles: Sources and Toxicity"*, J. Biophysical Chemistry Biointerphase, 2, (2007), 17-71.
21. H. Singh, P. Nalwa, *"Synthesis and processing"*, Handbook of Nanostructured Materials and Nanotechnology, 21, (2004), 424-632.
22. Nanotechnology information Center: Properties, Application, Resarch and safety Guideline, American Elements, 5, (2011), 63-74.
23. Allhoff, Fritz; Lin, Patrick, Moore, Daniel, *"what is nanotechnology and why does it matter? From science to ethics"*, P.John Wiley and Sons, 1, (2009), 304-336.
24. S. K. Prasad, *"Modern Concepts in Nanotechnology"*, Discovery Publishing House. 1, (2008), 31-32.
25. Kahn, Jennifer, *"Nanotechnology"*. National Geography, 12, (2006), 98–119.
26. P. Chouhan, Dr. R. Clarkson, *"Nanotechnology: changes and challenges for world"*, international journal of Innovative Research in Engineering & Science, 2, (2016), 13-53.
27. S. Mashaghi, T. Jadidi, G. Koenderink, A. Mashaghi, *"Lipid Nanotechnology"*, Int. J. Mol. Sci. 14, (2013), 4242-4282.
28. N. Kattamuri, J. H. Shin, B. Kang, C. G. Lee, J. K. Lee, C. Sung, *"Development and surface characterization of positively charged filters"*, J. Mater Sci., 40, (2005), 4531–4539.
29. W. Margaret, Frey, Lei Li, *"Electrospinning and Porosity Measurements of Nylon-6 / Poly(ethyleneoxide) Blended Nonwovens"*, Journal of Engineered Fibers and Fabrics, 2, (2007), 63-68.
30. Kenrya, Chwee Teck Limb, *"Nanofiber technology: current status and emerging developments"*, J. Progress in Polymer Science, 2, (2017), 124–165.
31. J. M. Deitzel, J. Kleinmeyer, D. Harris, *"The effect of processing variables on the morphology of electrospun nanofibers and textiles"*, J. Polymer, 42, (2001), 261– 72.
32. A. K. Haghi, M. Akbari, *"Trends in electrospinning of natural nanofibers"*, J. Phys Status Solid, 204, (2007), 1830–1844.
33. S. Sukigara, M. Gandhi, J. Ayutsede, M. Micklus, *"Regeneration of Bombyx mori silk by electrospinning Part2. Process optimization and empirical modeling using response surface methodology"*, J. Polymer 45, (2004), 3701–3708.
34. P. K. Baumgarten, *"Electrostatic spinning of acrylic microfibers"*, J Colloid Interface Sci, 36, (1971), 71–79.

Stain Removal Efficiency of TiO_2 Nanoparticles

Meeta Saxena

Department of Physics, Sophia College for Women (Empowered Autonomous), Mumbai, Maharashtra, India.

meetasaxena31@gmail.com

Abstract

This study focuses on the synthesis of titanium dioxide (TiO_2) nanoparticles (NP) using both chemical and green synthesis methods to evaluate their effectiveness in stain removal when applied to fabrics. The research aims to compare the detergency properties of TiO_2 nanoparticles synthesized through conventional chemical techniques and eco-friendly approaches. The performance of these nanoparticles is assessed based on their ability to break down stains, highlighting their potential for textile treatment and environmental cleaning. The findings emphasize the advantages of green synthesis, contributing to sustainable and efficient fabric care solutions.

Keywords: TiO_2 Nanoparticles, Green Synthesis, Chemical Synthesis, Stain Removal, Detergency, Textile Treatment, Environmental Cleaning.
Received 31 January 2025; First Review 17 February 2025; Accepted 05 March 2025.

*** Address of correspondence**
Meeta Saxena
Department of Physics, Sophia College for Women (Empowered Autonomous), Mumbai, Maharashtra, India

Email: meetasaxena31@gmail.com

How to cite this article
Meeta Saxena, Stain Removal Efficiency of TiO_2 Nanoparticles, J. Cond. Matt. 2025; 03 (01): 78-83.

Available from:
https://doi.org/10.61343/jcm.v3i01.138

Introduction

Titanium dioxide (TiO_2) is perhaps one of the most-studied semiconducting materials and due to its excellent specific properties, which make them particularly useful in particular applications, especially on the environmental/industrial level. Its high refractive index and outstanding UV-blocking performance, making it a vital active ingredient in sunscreens and coatings [1]. Photocatalytic activity by which it catalyses to decompose the organic compounds on exposure to UV light [2]. Antibacterial activity for various applications including the medical device sector, coatings, and environmental sanitation [3]. High stability under a broad scope of applications makes them resistant for long-lasting functions [4]. Self-cleaning ability is realized due to the hydrophilicity and photocatalytic action on the decomposition of dirt and other organic stains due to light exposure and the wetting process of water [5] etc. However, one of the more promising applications of TiO_2 NPs is found in photocatalysis, where it can catalyse degradation of organic pollutants and stain removal from textiles. TiO_2 interacts with water and oxygen molecules under UV light and forms electron-hole pairs. Hydroxyl radicals and superoxide anions produced during this reaction are capable of breaking down any organic compound and can break any organic stain present. The photo reactivity of TiO_2 depends on a number of parameters like particle size, surface area, crystallinity, and presence of different crystalline phases namely anatase, rutile, and brookite [6].

Photocatalytic Properties of TiO_2

The photocatalytic activity of TiO_2 arises from the formation of electron-hole pairs by the interaction with ultraviolet light. The reactive oxygen species produced through the combination of these electron-hole pairs are highly reactive, particularly hydroxyl radicals that efficiently degrade organic compounds, which are often seen in stains found on fabrics. Therefore, although TiO_2 has been very important in purification of air and water, it is becoming a highly valued element for the treatment of fabrics. The catalytic performance of TiO_2 is highly dependent on the anatase form. Among them, the tetragonal crystal structure form exhibits high photocatalytic activity because it possesses a higher surface area and greater efficiency in producing ROS under UV irradiation, which can be used for stain removal and purification of the environment. Photocatalytic activity for the removal of stains from fabrics can be optimized if nanoparticles of NP can be synthesized in the anatase phase by tailoring the synthesis procedure of TiO_2.

Synthesis Methods

The synthesis method used for TiO_2 NP affects the

photocatalytic properties. Two synthesis methods are presented here:

Chemical Synthesis Method

The conventional chemical process for the synthesis of TiO_2 nanoparticles (NP) involves the sol gel method, in which titanium tetra iso - propoxide (TTIP) is the precursor. Generally, it requires carefully controlled environments and reactants, such as ethanol and deionized water. TiO_2 nanoparticles (NP) produced by such methods can have property control with regard to diameter, aspect ratio, and crystalline phase. The main drawback for this method, however, involves the use of hazardous chemicals along with the toxic by-products. However, its ability to make precise control in nanoparticle properties makes it the most reliable high-performance TiO_2.

Eco-Friendly (Biologically, Green) Synthesis Method

The green synthesis method, on the other hand, incorporates plant extracts as reducing agents. Such extracts include bioactive compounds like polyphenols, flavonoids, and proteins that help in the formation of nanoparticles without the use of toxic chemicals [7]. Plants like Aloe vera and neem are the most common because of their antioxidant activities.

This method is environmentally friendly, cost-effective, and reduces the overall carbon footprint of TiO_2 synthesis. It is also less hazardous and avoids the disposal problems associated with chemical waste. However, the characteristics of the TiO_2 nanoparticles (NP) produced by green synthesis are typically less controlled, resulting in more variability in particle size and crystallinity. The most popular sources for such investigations are plants, including Tulsi, Aloe vera, Neem, and green tea due to the potential availability of considerable natural resources bearing strong reducing characters. Green synthesis is a procedure that not only is environmental but also economic. This process mainly uses low cost, renewable elements. Moreover, this synthesis path is quite suitable for mass scalability and is uncomplicated due to fewer steps generally involved in synthesizing the nanomaterial. The surface properties and biocompatibility of nanoparticles (NP) produced by green synthesis might differ, indicating improved performance in areas such as environmental remediation and biomedical fields.

Applications and Future Prospects

The synthesis of TiO_2 nanoparticles (NP) using eco-friendly methods opens an exciting possibility for expanding their applications. In the field of environmental cleanup, TiO_2-based photocatalysts have demonstrated success in breaking down pollutants in water, including heavy metals, dyes, and pharmaceutical residues. The adoption of green synthesis methods could further enhance these processes by reducing the environmental impact associated with nanoparticle production. for particular applications, and mass production to cater to the growing demand for sustainable nanomaterials. In addition, TiO_2 NP is being studied for antimicrobial purposes, self-cleaning surfaces, and energy conversion systems such as dye-sensitized solar cells. Future research should emphasize efficiency gains for green synthesis methodologies, including tailored nanoparticle properties. Green synthesis combined with TiO_2 photocatalysis will possibly pave the way to new approaches to environmentally sound technologies in the coming years.

Objectives

- Synthesis of TiO_2 nanoparticles (NP) using the chemical sol-gel method.
- Green synthesis methods with plant extracts for TiO_2 nanoparticles (NP).
- Application of the synthesized TiO_2 nanoparticles (NP) to muslin fabrics.
- Testing the efficiency of TiO_2 - muslin fabrics for stain removal at sunlight exposure.
- Testing the efficiency of TiO_2 NP on muslin fabrics for stain removal.
- Comparison of chemical and green-synthesized TiO_2 nanoparticles (NP) for stain removal.

Materials and Methods

Preparation of TiO_2 Nanoparticles (NP)

1. Chemical Synthesis Method

Materials: TTIP, ethanol, deionized water.

Procedure

1 ml TTIP was dissolved in 9 ml ethanol. 5 ml of Deionized water was gradually added under constant stirring. The mixture was heated at 80°C for 2 hours to obtain a white precipitate. The precipitate was washed with ethanol and then deionized water, dried at 100°C, and then calcined at 500°C for 3 hours. Thus, TiO_2 nanoparticles (NP) from chemical synthesis (C) method was prepared [8].

2. Green Synthesis Method

Materials: TTIP, plant extracts (e.g., Tulsi powder, Aloe vera, neem), deionized water.

Procedure

Plant leaves were washed with D/w and boiled in deionized water to prepare the extract.

The prepared TTIP solution was mixed with the plant extract and heated at 80°C for 2 hours.

The resulting precipitate was washed, dried at 100°C, and calcined at 500°C for 3 hours. Thus, TiO_2 nanoparticles (NP) from green synthesis (B) method was prepared.

Characterization of TiO_2 Nanoparticles (NP)

Characterization of the synthesized TiO_2 nanoparticles (NP) is carried out using techniques like X-ray diffraction (XRD) from Pune University, Department of Physics. UV-Visible spectroscopy to confirm their phase composition, morphology, and light absorption properties. The characterized curve shows that the nanoparticles (NP) are of TiO2.

Application of TiO_2 Nanoparticles on Muslin Fabrics

Materials: Muslin fabric, synthesized TiO_2 nanoparticles (NP), polyvinyl alcohol (PVA) binder.

Procedure

The prepared TiO_2 nanoparticles (NP) were dispersed in water with a binder (1% starch solution).

Solutions for two different concentrations were prepared i) 33% TiO_2 NP solution + 67% binder & ii) 50% TiO_2 NP solution + 50% binder solution.

Muslin fabric was cut in 5 equal pieces namely, C1 [soaked in (i)], C2 [soaked in (ii)], B1[soaked in (i)], B2 [soaked in (ii) & control Co (not soaked in NP).

The muslin fabric was soaked in different concentrations of nanoparticles (NP) for 30 minutes, dried at 60°C for 1 hour to ensure proper adhesion of the nanoparticles (NP).

Stain Removal Test

Materials: Common stains (ink), TiO_2 - coated muslin fabric, sunlight, and normal water.

Procedure

Stain was applied to the cotton fabric and dried for 24 hrs. at Room temperature.

The fabric (C1, C2, B1, B2 and Co) was washed with detergent and dried. (C & B indicates chemical synthesis & green synthesis method).

Results

Preparation of TiO_2 Nanoparticles (NP) (Chemical and Biological)

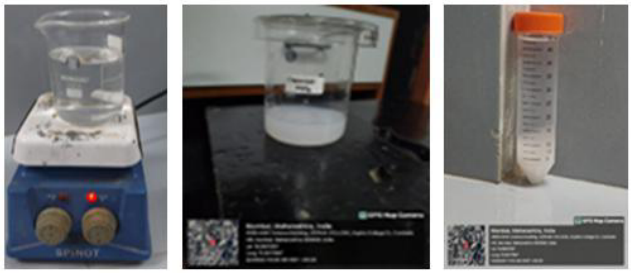

Figure 1: Preparation of chemically synthesized TiO_2 Nanoparticles (NP).

Figure 2: Preparation of biologically synthesized TiO_2 Nanoparticles (NP).

Characterization of TiO_2 Nanoparticles (NP)

X -Ray Characteristic

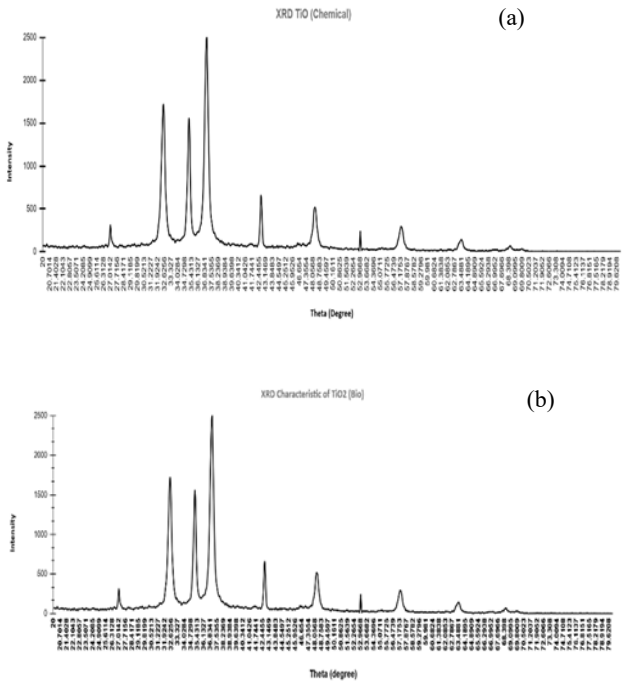

Figure 3: XRD analysis of the synthesized TiO_2 Nanoparticles. (a) XRD characterization for chemically synthesized TiO_2 nanoparticles. (b) XRD characterization for biologically synthesized TiO_2 nanoparticles

The TiO_2 Nanoparticle (NP) (Chemically synthesized and biologically synthesized) displayed nearly identical diffraction angles, suggesting that both methods produced TiO_2 with similar crystal structures. The intensity values are also closely matched, further indicating that the crystal formation and size may be consistent across both synthesis methods. There are small variations in intensity at specific angles like (36.80 & 37.140), which may indicate slight differences in crystal quality or the presence of impurities from the Aloe vera synthesis process. High-intensity peaks suggest a high degree of crystallinity in the material. The more crystalline the sample, the more coherent and sharper the diffraction patterns, leading to higher intensities at specific angles (peaks). From the X- Ray diffraction pattern figure 3 (a), (b), biologically synthesized nanoparticles are slightly more crystalline as compared to chemically synthesized nanoparticles.

UV characteristic

Figure 4. (a), (b) shows the UV characteristic of chemically synthesized and biologically synthesized nanoparticles with slight variation in the band gap energy.

(a)

(b)

Figure 4: UV characterization of synthesized TiO_2 Nanoparticles. (a) UV characterization for chemically synthesized TiO_2 nanoparticles. (b) UV characterization for biologically synthesized TiO_2 nanoparticles.

Biologically synthesized TiO_2 nanoparticles show a slight lower band gap as compared to chemically synthesized TiO_2 nanoparticles. A lower band gap indicates that the sample can absorb light in the visible range more effectively which enhances the photocatalytic activity in broader light conditions. A higher absorption peak, especially in the UV or visible range, suggests better utilization of light for photocatalysis. This translates to higher efficiency in generating reactive oxygen species (ROS), which are crucial for breaking down stain molecules.

Application of TiO_2 Nanoparticles on Muslin Fabrics

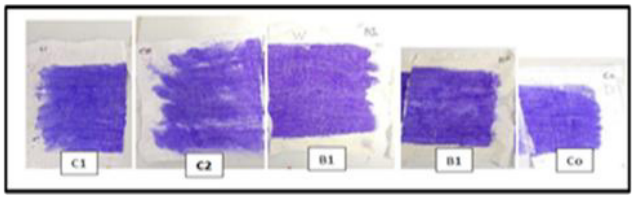

(a)

(b)

(c)

Figure 5: Application of TiO_2 on muslin fabric (a) Muslin fabric before washing. (b) Muslin fabric washed with water (c) Muslin fabric wash with detergent

Visual assessments showed that the surfaces were treated with biological TiO_2 nanoparticles appeared significantly cleaner. This enhanced stain removal capability is likely due to the unique properties of the biologically synthesized nanoparticles, suggesting their potential as a more environmentally friendly and efficient alternative for cleaning applications.

Discussion

Chemical and Biological (green synthesis) methods successfully produced TiO_2 nanoparticles. Efficient removal of the stain by the biologically synthesized TiO_2 nanoparticles can be attributed to their enhanced surface reactivity and larger effective surface area, which likely facilitate more efficient interactions with the stain molecules.

Biologically synthesized TiO_2 nanoparticles are slightly more crystalline and have a lower band gap energy as compared to chemically synthesized TiO_2 NP. A material with high crystallinity is one in which the atoms are arranged in a regular, repeating pattern, thereby forming a well-ordered crystal lattice, is a basic concept in materials science and solid-state physics. [9, 10]. For biologically synthesized TiO_2 nanoparticles, the XRD analysis shows sharper and more intense diffraction peaks than chemically synthesized TiO_2. This reflects that the structure of biologically synthesized TiO_2 crystals is more uniform, ordered, with fewer lattice distortions and defects. This indicates that a better crystallinity condition is favorable in order to be stable for good physical and chemical properties such as photocatalytic efficiency. A more crystalline material will interact better with light and make electron transition during photocatalysis more effective, which is quite crucial for their application in stain removal.

This energy difference between the valence band, where the electrons are resting, and the conduction band, where electrons are free to move, is called the band gap of the material. The amount of energy required for an electron to jump from being stationary to moving freely is the energy difference between these two bands; this is how the material will conduct electricity or facilitate chemical reactions. TiO_2 is a semiconductor, and the band gap is very important for its photocatalytic activity. The band gap of TiO_2 is typically about 3.2 eV, which means it absorbs mainly UV light. However, a lower band gap means that the material can absorb visible light in addition to UV light, making it more efficient at using sunlight or artificial light for photocatalytic reactions. Biologically synthesized TiO_2 nanoparticles, owing to their method of synthesis, inherently usually have a smaller band gap compared to chemically synthesized ones. This occurs due to organic molecules or impurities that may get incorporated within the biological synthesis process, thereby slightly changing the electronic material structure. Biologically synthesized TiO_2 has a lower band gap, which means it can absorb a larger part of the light spectrum, especially in the visible region. This improves the photocatalytic activity because more light energy can be utilized to produce reactive species that break down stains, pollutants, or organic compounds. The higher crystallinity of biologically synthesized TiO_2 provides more stable and organized structures for photocatalysis, while the lower band gap allows for more effective light absorption, particularly in the visible range. Together, these properties make biologically synthesized TiO_2 more efficient in applications like stain removal compared to chemically synthesized TiO_2.

Authors should discuss the results and how they can be interpreted from the perspective of previous studies and of the working hypotheses. The findings and their implications should be discussed in the broadest context possible. Future research directions may also be highlighted.

Conclusion

This work highlights the potential of TiO_2 nanoparticles for environmentally friendly stain removal on muslin fabrics, leveraging photocatalytic activity under sunlight. Both chemical and green (biological) synthesis methods successfully produce TiO_2 nanoparticles, but biologically synthesized TiO_2 shows superior properties in terms of crystallinity and band gap energy. The higher crystallinity in biologically synthesized TiO_2 indicates a more uniform and stable crystal structure, leading to better performance in photocatalytic applications like stain removal. Additionally, the slightly lower band gap of biologically synthesized TiO_2 enables more efficient light absorption, especially in the visible range, making it more effective at generating reactive species for breaking down stains. Therefore, biologically synthesized TiO_2 nanoparticles are more efficient for stain removal applications than chemically synthesized ones due to their enhanced structural and optical properties.

References

1. Chen, X., Ma, X., Li, P., & Zhang, Y., *"Photocatalytic Applications of Titanium Dioxide (Ti_2), In Titanium Dioxide – Advances and Applications"*, Hafiz Muhammad Ali (2021). IntechOpen Limited London United Kindom, pp 838.
2. Shraddha Jadhav, Ricardo Navarro-Mendoza, Paulina Lozano-Sotomayor, Ignacio R. Galindo-Esquivel, Oracio Serrano, Juan M Peralta-Hernandez, *"Enhanced Photocatalytic Activity of TiO2 Modified with GaI toward Environmental Application"*, Inorganic Chemistry, 59, 2, 2020, pp 1315–1322 https://doi.org/10.1021/acs.inorgchem.9b03020.
3. Zilin Guo, Hanpeng Liu, Wuzhi Wang, Zijun Hu, Xiaofang Li, Hao Chen, efeng Wang, Zhaoyang Li, Caideng Yuan, Xiang Ge, *"Recent Advances in Antibacterial Strategies Based on TiO_2 Biomimetic Micro/Nano-Structured Surfaces Fabricated Using the Hydrothermal Method"*, Biomimetics MDPI, 9(11) 2024, 656. https://doi.org/10.3390/biomimetics9110656.
4. Xiaobo Chen, *"Titanium Dioxide Nanomaterials and Their Energy Applications"*, Chinese Journal of Catalysis, 2009, 30(8):839-851 http://dx.doi.org/10.1016/S1872-2067(08)60126-6.
5. Tanu Mittal, *"Nano TiO_2- Based Smart Superhydrophilic Self – Cleaning Surfaces,*

Photocatalysts New Perspectives", Nasser Awwad, Saleh Alarfaji, Ahmed Alomary, IntechOpen, http://dx.doi.org/10.5772/intechopen.108157.

6. Maria-Anna Gatou, Athanasia Syrrakou, Nefeli Lagopati, Evangelia A Pavlatou, *"Photocatalytic TiO_2-Based Nanostructures as a Promising Material for Diverse Environmental Applications: A Review"*, Reactions MDPI, 2024, 5(1), 135 – 194 https://doi.org/10.3390/reactions5010007.
7. Rajan Dhir, Sashi Chauhan, Praddiuman Subham, Saksham Kumar, Pratham Sharma, Amrullah Shidiki, Gaurav Kumar, *"Plant-mediated synthesis of silver nanoparticles: unlocking their pharmacological potential–a comprehensive review"*, Frontiers in Bioengineering and Biotechnology, 2024, https://doi.org/10.3389/fbioe.2023.1324805.
8. Most. Mahfuza Khatun, M. Bodiul Islam, Hasnat Jahan Sumona, *"Sol-Gel Synthesis and Characterization of Titanium Dioxide Nanoparticles, In Proceedings International Conference on Mechanical"*, Industrial and Materials Engineering 2022 (ICMIME2022), RUET, Rajshahi-6204, Bangladesh (20-22 December, 2022)
9. Ashcroft W Neil; Mermin David, *"The Drude Theory of Metals"*. In Solid State Physics, Harcourt College Publishers New York, United States of America, pp 1-28
10. Kittel Charles, *"Crystal Structure, Energy Band"*, Introduction to Solid State Physics, John Wiley & Sons, Inc, 8th edition, chapter – 1 & chapter – 7pp 1-22, 161 - 182.

A First Principal investigation for Structural, Electronic and Mechanical Properties of α-Mg_3N_2

M C Rolania[a], and G Sharma

Department of Pure & Applied Physics, University of Kota, Kota-324005, India.

mangalrolania@gmail.com

Abstract

In this present work, the LCAO technique is employed to explore the structural, mechanical, as well as electronic characteristics of the α-Mg_3N_2 material. The study utilizes the GGA approach within the framework of Density Functional Theory (DFT) to optimize geometrical parameters and characterize the material's structural attributes. The findings indicate that α-Mg_3N_2 demonstrates semiconducting behaviour, as inferred from its electronic properties. With an energy band gap aligning with the optimal range of the solar spectrum, α-Mg_3N_2 is identified as a potential candidate for photovoltaic applications. A comprehensive analysis of elastic properties, including bulk modulus, shear modulus, Young's modulus, with Poisson's ratio, was discussed. Additionally, the anisotropic nature of Young's modulus, linear compressibility has been evaluated via ELATE software, revealing the predetermined elastic anisotropy of the α-Mg_3N_2 compound. Hence, the results of this investigation indicate that α-Mg_3N_2 is a good candidate for the photovoltaic sector.

Keywords: Semiconductor, Electronic structure, LCAO method, Band structure, Elastic properties.
Received 28 January 2025; First Review 11 February 2025; Accepted 19 March 2025.

*** Address of correspondence**
M C Rolania
Department of Pure & Applied Physics,
University of Kota, Kota-324005, India

Email: mangalrolania@gmail.com

How to cite this article
M C Rolania, and G Sharma, A First Principal investigation for Structural, Electronic and Mechanical Properties of α-Mg_3N_2, J. Cond. Matt. 2025; 03 (01): 84-90.

Available from:
https://doi.org/10.61343/jcm.v3i01.83

Introduction

Binary nitrides with II group elements (M_3N_2, where M = Be, Mg, Ca, Sr, Ba), have been studied for over a century [1] and are utilized across various scientific and industrial domains. These compounds serve as precursors in the synthesis of complex nitrides [2]. In industrial applications, they play diverse roles, including acting as additives in steel refinement processes [3], as additive for densification of aluminum nitride (AlN) along with silicon nitride (Si_3N_4) [4], and as catalysts facilitating the transformation of hexagonal phase of boron nitride (h-BN) in the cubic form (c-BN) [5]. Furthermore, Be_3N_2 and Mg_3N_2 have been explored in conjunction with lithium–nitrogen materials (e.g., LiN_3 and Li_2NH) for potential applications in hydrogen storage [6]. The investigation of novel semiconductors necessitates the fabrication of materials with exceptional purity to guarantee that the assessment of intrinsic physical characteristics, such as lattice constants, effective electron mass, or energy gap, is not influenced by defects. A representative case is indium nitride (InN), with energy gap is assumed to be approximately 1.9 eV for many years [7]. However, with the ease of use of premium samples in the early 2000s [8, 9], the accurate measurement of its band gap revealed a value of around 0.7 eV. A similar scenario is observed with magnesium nitride (Mg_3N_2). This is particularly intriguing, specified that its anti-bixbyite crystal arrangement and lattice components are initially determined using powder form samples and millimeter-scale single crystals at earliest [10], with further refinement carried out [11].

Ceramic magnesium nitride (Mg_3N_2) has been extensively utilized in industrial applications the same as nitriding representative to facilitate the synthesis of diverse nitride compounds [12, 13] and as a catalyst in the production of ultra-hard materials such as silicon nitride with cubic phase boron nitride [14]. In recent developments, Mg_3N_2 has also demonstrated potential in advanced applications, including high-thermal-conductivity ceramics when alloyed amid silicon [15] and as a reversible medium for hydrogen storage [16]. Notably, these uses predominantly capitalize on the material's physicochemical attributes, with little attention given to its optoelectronic characteristics. Limited theoretical studies on crystalline Mg_3N_2 suggest that it behaves as a semiconductor, exhibiting an energy band gap ranging from 1.1 to 2.26 eV, depending upon the computational approach employed [17]. Current

discussions have primarily focused on its crystal structure and the other properties of α-Mg_3N_2 through ab initio methodologies [18, 19]. Limited computational studies have analyzed its electronic properties; however, reported values for the electronic band gap (E_g) vary significantly, ranging from 1.133 to 1.19 eV [20, 21]. For a material to be viable in the PV industry, it is essential to determine its structural, electronic and mechanical properties.

Computational Details

An ab initio study of α-Mg_3N_2 is conducted using the Linear Combination of Atomic Orbitals (LCAO) methodology embodied in the CRYSTAL software package [22, 23]. After expanding atomic orbitals into linear combinations of Bloch functions using localized basis sets, the method solves self-consistent Kohn-Sham (KS) equations. The all-electron Gaussian-type basis sets for Mg and N were taken from www.tcm.cam.ac.uk, to acquire a stable system [24, 25]. The proper coupling of electron-electron and electron-nucleus interactions is crucial for controlling computation accuracy. Therefore, a precise evaluation of the contributions of the Coulomb and Hartree-Fock (HF) exchanges to the Fock matrix and total energy is crucial. If the exchange parameter and Coulomb overlap are below the threshold, the corresponding bioelectronics integral was not taken into account during computation. For the computations of geometry optimization, frequency calculations, and elastic characteristics, the convergence criteria were maintained constant.

Structural optimization was carried out starting from the initial geometry, yielding optimized lattice parameters and fractional atomic coordinates. For these calculations, the PBE [26, 27] functional was utilized. The performance of above schemes is claimed to be better than other exchange-correlation potentials as it improves the equilibrium properties of solids and surfaces. These are very strong and commonly used functional for a variety of DFT applications because these potentials are very helpful in predictions of structures, formation energies, and general characteristics [26, 27]. The Monkhorst-Pack approach is used to sample reciprocal space, using 8×8×8 k-points that correspond to 35 k-vectors in the irreducible Brillouin zone. The self-consistent field (SCF) convergence criterion (TOLDEE) was set to 10^{-8}, and the Brillouin zone (Bz) was sampled using an 8 × 8 × 8 Monkhorst-Pack k-point grid [28], corresponding to 35 k-points of the irreducible Bz. Additionally, the BROYDEN mixing algorithm [29, 30] was applied to ensure robust convergence. The structural analysis began with the use of experimental parameters [31] to calculate the equilibrium volume (V_0). A full structural optimization, encompassing both lattice constants and atomic positions, was performed to determine V_0. Subsequently, the lattice energy was computed by introducing a ±8% variation in V_0, and the resulting data were fitted via an equation of state (EOS) algorithm [32]. With the optimized structure, the electronic properties were subsequently evaluated.

Results and Discussions

Structural properties

At standard environment, magnesium nitride (Mg_3N_2) structured in a cubic lattice with the space group $Ia\bar{3}$ (No 206), adopting an anti-bixbyite-like structural arrangement. The unit cell comprises 16 formula units, amounting to a total of 80 atoms (48 magnesium and 32 nitrogen) in its typical crystallographic configuration. Nitrogen atoms occupy two distinct Wyckoff positions: 8b (N1) and 24d (N2), whereas magnesium atoms are situated at the 48e Wyckoff position. At equilibrium volume, the conventional and primitive cells of Mg_3N_2 are illustrated in Figure 1. The structural configuration reveals that nitrogen atoms form octahedral coordination with magnesium atoms, which are, in turn, tetrahedral coordinated by nitrogen atoms. Within the tetrahedral symmetry, each magnesium atom is bounded by one N1 atom along with three N2 atoms, with the bond lengths differing among them. The atomic environment of nitrogen differs due to its occupancy of two inequivalent crystallographic sites.

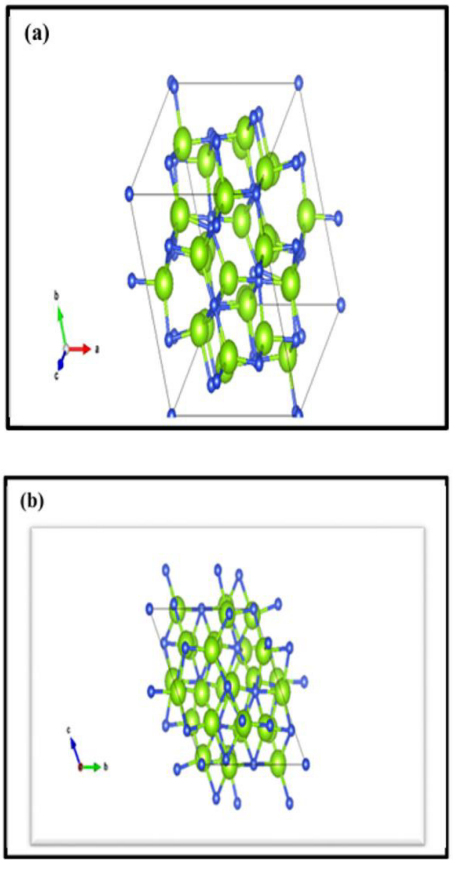

Figure 1: Structural arrangement of unit cells for α-Mg_3N_2.

To delve deeper into the analysis, the researchers aimed to simplify the structure of each material to identify its equilibrium lattice parameters corresponding to the most stable state. The energy variation as a function of volume is computed using the GGA exchange-correlation functionals. Subsequently, the data is fitted with the Birch–Murnaghan's EOS. The resulting energy-volume curve for the compounds is presented in Fig.2, with the derived parameters summarized in Table 1.

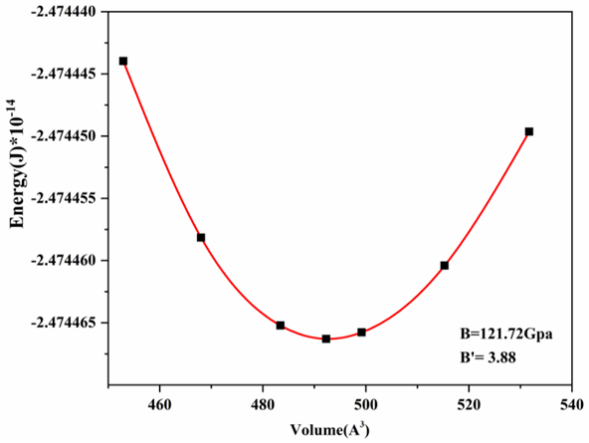

Figure 2: Volume optimization curve of α-Mg_3N_2.

Electronic properties

The appropriate assessment of electronic band gap energy is now the biggest problem because of its importance in the field of PV applications; even though the best potential for additional study has not been selected yet. The direct band gap value of Mg_3N_2 is determined to be 1.72 eV. As illustrated in Figure 3, the investigated materials display a conduction band minimum (CBM) and valence band maximum (VBM) that do not overlap, both situated at the high-symmetry Γ-point within the first Brillouin zone. Therefore, it can be concluded such compounds possess a direct band gap. Further, as we move along the directions Γ-P and Γ-H, it is observed that available energy states are decreasing and getting sharper in the second case, which shows the considerable difference. This characteristic signifies that the materials under study are categorized as direct band gap semiconductors and thus a possible candidate for PV applications. The band gap at the Γ point is near 1.72 eV in agreement with the earlier reported experimental and theoretical results. The computed band gap values correspond to approximately 62% of the experimentally determined value. It is widely recognized that DFT-GGA calculations typically underestimate the band gap in semiconductors and insulators, often predicting only 30% to 80% of the experimental value. This discrepancy arises due to the absence of integer discontinuities in the derivative of the exchange-correlation energy [34]. The results indicate the superior potential of the investigated material for optoelectronic applications, along with enhanced electron transitions from the valence band to the conduction band. The horizontal dashed line represents the reference energy level, denoting the Fermi level (EF).

The density of states (DOS), both total (TDOS) and partial (PDOS), of the investigated compound is computed to verify their semiconducting nature, as illustrated in Figure 4. The analysis discloses that the valence band (VB) is predominantly influenced by the contribution of the p-states of Mg and N atoms. The overlapping of energy bands between the energy ranges of -3 to -1 eV arises due to hybridizations between the s and p orbitals of Mg and N atoms, respectively. A lesser but still important part of the creation of this group of bands is played by the s-orbitals of two non-equivalent N atoms. The higher valence band is formed in part by the hybridized p-orbitals of the Mg and N atoms. It is believed that the band gap results from an electronic transition between the s-orbitals of Mg atoms and the s- and d-orbitals of N atoms. A secondary contribution to the VB arises from the d-orbitals of Mg atoms, with a minor input from the d-orbitals of the N2 atom, whereas the involvement of the N1 atom in the VB is negligible. Conversely, the conduction band (CB) is primarily composed of contributions from the Mg atom, while the roles of the N1 and N2 atoms in forming the conduction band are minimal.

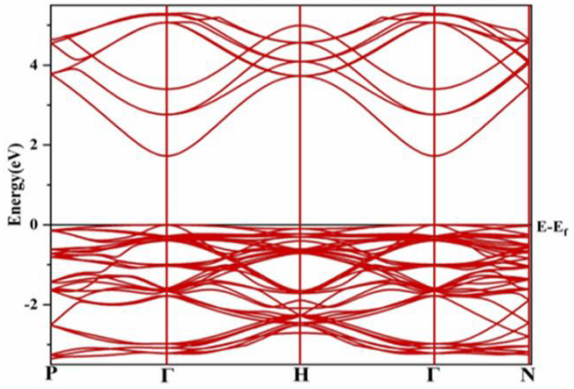

Figure 3: The band structures along the high-symmetry paths in the Brillouin zone (BZ) for α-Mg_3N_2 computed using the LCAO method. The Fermi energy, EF, represented by the horizontal line, has been aligned to the zero-energy reference level

Through a detailed examination of the PDOS for the studied materials, the orbital contributions of Mg and the N1 and N2 atoms to the TDOS near the Fermi level were identified. The findings indicate that the d-orbitals of both Mg and N atoms exhibit minimal contributions to the TDOS.

Elastic properties

The evaluation of elastic anisotropy is essential for comprehending the directional dependence of elastic

Table 1: Lattice parameter, band gap, of α-Mg3N2 following structural relaxation. Previously reported results are presented for comparison.

α-Mg_3N_2				
	Band gap	**Lattice Constant**	**Bulk Modulus (B_0)**	**Pressure derivative (B_0')**
Present work	1.728	9.9485	121.7	3.8
Reported data	2.8 [33], 1.45 [34], 1.63 [35]	9.952 [31]	110.7 [31]	4.0 [31]
Optimized atomic position				
Atom	x	y	z	
Mg	0.38	0.15	0.38	
N1	0.25	0.25	0.25	
N2	0.96	0.00	0.25	

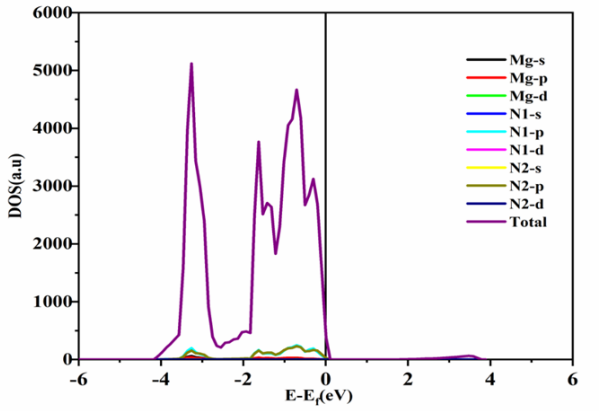

(a)

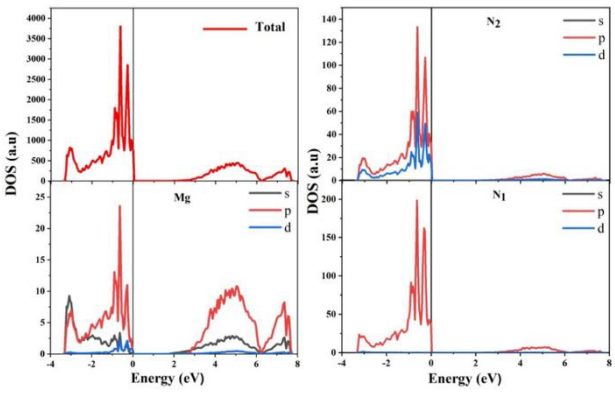

(b)

Figure 4: (a) Total and **(b)** site-specific DOS derived using the LCAO method for α-Mg_3N_2.

deformation in crystalline materials. This analysis plays a momentous role in the design and optimization of engineering devices. Assessing the elastic characteristics of Mg_3N_2 is vital for determining its structural integrity and mechanical rigidity. Table 2 presents the calculated elastic constants and moduli, providing insights into these characteristics. The determination of elastic constants that meet the Born stability criteria is essential for verifying the mechanical strength of a cubic crystal structure [36]. The Born stability requirements for the stability of a cubic structure is satisfied by the elastic constants are expressed mathematically as:

$$c_{11} + 2c_{12} > 0 \quad (1)$$

$$c_{44} > 0 \quad (2)$$

$$c_{11} - c_{12} > 0 \quad (3)$$

The resistance degree along the principal crystallographic direction is explained by the constant C_{11} .i.e., [100]. A measurement of shear deformation is provided by the elastic constant C_{44}. As Table 2 becomes evident, $C_{11} > C_{44}$ by 57.5%. There has been unidirectional distortion of the crystal structure. Moreover, when comparing the bulk's magnitude to the shear modulus, the parameter limiting mechanical stability in this combination is found to be the shear modulus. Young's modulus (E) is another parameter that determines the stiffness of the compound. The large value of E = 201.660 GPa indicates thatα-Mg_3N_2 is hard and ductile. Poisson's ratio (υ) is another way to measure a material's machinability. Poisson's ratio demonstrates how stable a compound is against shear. A value of υ = 0.225 indicates that the α-Mg_3N_2 crystal structure exhibits shear instability.

Table 2: Computed elastic components, bulk (B), Young's (E) and shear modulus (G), along with Poisson's ratio (υ) of α-Mg_3N_2 utilizing the Voigt- Reuss Hill's approach with PBE exchange-correlation functional.

Elastic Constants	**Findings (GPa)**	**Elastic Property**	**Findings (GPa)**
C_{11}	215.146	**B**	122.240
C_{12}	72.891	**G**	81.830
C_{44}	91.369	**E**	201.660
		υ	0.225 (Unit less)

Elastic Anisotropy

The level of elastic anisotropy varies across all natural materials. This study aims to comprehensively analyse the elastic anisotropy of the Mg_3N_2structure, by employing the Voigt and Reuss elastic moduli. We calculated the anisotropy indices for the bulk (A_B) and shear modulus (A_G), with the universal anisotropy index A^U, and the Zener

anisotropy factor A^Z using the respective mathematical formulations [36, 37]. The calculated values of A_B, A_G, A^U, and A^Zindicate that Mg_3N_2 exhibits pronounced shear anisotropy alongside nearly isotropic elastic compressibility.

$$A_B = \frac{B_V - B_R}{B_V + B_R} \quad (4)$$

$$A_G = \frac{G_V - G_R}{G_V + G_R} \quad (5)$$

$$A^U = \frac{B_V}{B_R} + 5\frac{G_V}{G_R} - 6 \quad (6)$$

$$A^Z = \frac{2C_{44}}{C_{11} - C_{12}} \quad (7)$$

All the nonzero values of the anisotropy parameters confirm the existence of finite anisotropy in Mg_3N_2 crystals. In contrast, for isotropic materials, the anisotropy parameters A_B, A_G, A^U are identically zero. If a solid appears, A_B, A_G, A^U, and A^Z of Mg_3N_2 0%, 0.82%, 0.05 and 1.3, respectively.

Table 3: Variations of Young's (E) and shear modulus (G)[in GPa], Poisson's ratio ν (unitless) and linear compressibilityβ[in $(TPa)^{-1}$] of Mg_3N_2.

	E_{Min}	E_{Max}	β_{min}	β_{max}	G_{Min}	G_{Max}	υ_{Min}	υ_{Max}
Present work[a]	178.250	218.730	2.771	2.771	71.128	91.369	0.133	0.294

[a]These values of G, E, β, ν have been calculated through ELATE software [32, 33].

Further, the different environmental arrangements of Mg-N_1 (N_2) atoms are taken into consideration while determining the directional characteristic of elastic moduli. Elastic moduli's angular fluctuation in three-dimensional (3D) space is seen in the fig. 5. Figure 5(b) displays a spherical model with linear compressibility in all directions, indicting zero anisotropy. (Fig. 5(a, c, and d)) show a model that is not spherical and has a significant amount of anisotropy. In the [001] direction, the shear modulus is found to reach its maximum value of 91.369 GPa, whereas Young's modulus is seen to increase in the same direction, reaching a minimum value of 178.250 GPa. The **directional dependence of Young's modulus** is a critical aspect of understanding the mechanical performance of crystalline materials, particularly anisotropic materials.

Young's modulus describes the stiffness of a material, and its directional dependence reflects how the material responds to stress differently depending on the crystallographic orientation. For example, in cubic crystals like iron or aluminium, Young's modulus is typically higher

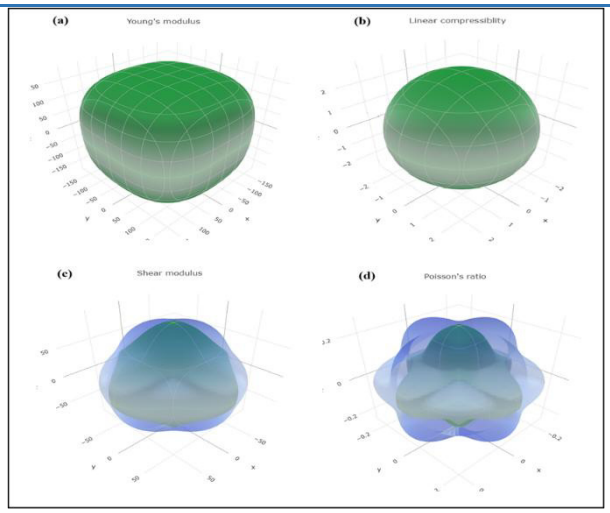

Figure 5: Angular variation of elastic modulus in 3-dimensional:(a) Young's modulus (b)linear compressibility, (c) shear modulus(d) Poisson's ratio for α-Mg_3N_2.

along the <111> direction compared to the <100> direction because atomic bonds are stronger and more densely packed along certain axes. In highly anisotropic materials like graphite or titanium alloys, this variation can be even more pronounced, with Young's modulus differing significantly between directions. This directional dependence directly impacts mechanical performance, as materials will exhibit different stiffness, deformation resistance, and stress-strain responses depending on the loading direction. For instance, in applications like aerospace components or biomedical implants, where materials are subjected to multidirectional stresses, understanding and optimizing the directional dependence of Young's modulus is crucial to prevent failure, ensure durability, and tailor materials for specific mechanical requirements. This anisotropy can significantly influence mechanical behaviour, including deformation, fracture, and load-bearing capacity. The extremes of these moduli suggest that because the material is less stiff along the [001] direction than along other directions, plastic deformation is more challenging to sustain along this direction.

Conclusion

The structural, mechanical, and electronic characteristics of the α-Mg_3N_2 material have been systematically explored using the GGA approach within the DFT framework. The optimized structural parameters were determined to characterize the material's structural attributes comprehensively. These structural data were subsequently employed to evaluate the electronic and mechanical properties of the compound. The results reveal that α-Mg_3N_2 exhibits semiconducting behaviour, exhibiting a calculated energy gap of 1.72 eV based on its electronic properties. The semiconducting nature of, α-Mg_3N_2 with a bang gap in the IR-Vis range is shown by its electronic band structure and density of states. This makes the compound

appropriate for use in both PV devices and infrared sensors. A detailed examination of the elastic attributes, like bulk, shear, Young's modulus, along with Poisson's ratio, is conducted. The analysis confirms that α-Mg_3N_2 possesses distinct elastic anisotropy. Specifically, the variation in Young's modulus ranges from a lowest amount of 178.250 GPa to a maximum value 218.730 GPa. While the shear modulus varies from a minimum of 71.128 GPa to its maximum value 91.369 GPa. The anisotropic elastic behaviour of α-Mg_3N_2 provides insights into the preferential crystallographic orientations, according to the elastic calculations, α-$Mg_3N_2$is a strong and ductile substance that can endure harsh environmental conditions while maintaining its ground state characteristics. The α-Mg_3N_2 efficiently used as a green energy source.

References

1. S. R. Römer, T. Doerfler, P. Kroll, and W. Schnick, Phys. Stat. solidi (b) 246: 1604-1613 (2009). https://doi.org/10.1002/pssb.200945011.
2. J. K. Jian, G. Wang, C. Wang, W. X. Yuan, and X. L. Chen, J. crys. Growth 291: 72-76, (2006), https://doi.org/10.1016/j.jcrysgro.2006.03.016.
3. Y. Zhuang, F. Sun, L. Zhou, C. Jiang, J. Wang, S. Li, and S. Liao, Int. J. App. Cer. Tech. 21: 2273-2287 (2024), https://doi.org/10.1111/ijac.14665.
4. L. Govindasamy, Y. J. Park, J. W. Ko, J. W. Lee, M. H. Jin, K. Kumar, and H. N. Kim, J. Korean Cer. Soc. 61: 507-536 (2024), https://doi.org/10.1007/s43207-024-00388-8.
5. A. E. Naclerio and P. R. Kidambi, Adv. Mater. 35: 2207374 (2023), https://doi.org/10.1002/adma.202207374.
6. N. Sorbie, Synthesis and structure of group I and II nitrides as potential hydrogen stores, PhD diss., University of Glasgow, 2011.
7. M. Leroux, N. Grandjean, J. Massies, B. Gil, P. Lefebvre, P. Bigenwald, and B. Gil, Phys. Rev. B 60: 1496 (1999), https://doi.org/10.1103/PhysRevB.60.1496.
8. V. Y. Davydov, A. A. Klochikhin, V. V. Emtsev, D. A. Kurdyukov, S. V. Ivanov, V. A. Vekshin, F. Bechstedt, J. Furthmüller, J. Aderhold, J. Graul, A. V. Mudryi, H. Harima, A. Hashimoto, A. Yamamoto, and E. E. Haller, Phys. Stat. Solidi (b), 234: 787-795 (2002), https://doi.org/10.1002/1521-3951(200212)234:3<787::AID-PSSB787>3.0.CO;2-H.
9. V. Y. Davydov, A. A. Klochikhin, V. V. Emtsev, A. N. Smirnov, I. N. Goncharuk, A. V. Sakharov, D. A. Kurdyukov, M. V. Baidakova, V. A. Vekshin, S. V. Ivanov, J. Aderhold, J. Graul, A. Hashimoto, and A. Yamamoto, Phys. Stat. Solidi (b), 240: 425-428 (2003), https://doi.org/10.1002/pssb.200303448.
10. D. E. Partin, D. J. Williams, and M. O'Keeffe, J. solid state chem., 132: 56-59, (1997), https://doi.org/10.1006/jssc.1997.7407.
11. O. Reckeweg and F. J. DiSalvo, Zeitschrift für anorganische und allgemeine Chemie 627, 371-377, (2001), https://doi.org/10.1002/1521-3749(200103)627:3<371::AID-ZAAC371>3.0.CO;2-A.
12. A. M. Nartowski, and I. P. Parkin, Polyhedron 21: 187-191, (2002), https://doi.org/10.1016/S0277-5387(01)00974-3.
13. H. Z. Ye, X. Y. Liu, and B. Luan, Mater. letters, 58: 2361-2364 (2004), https://doi.org/10.1016/j.matlet.2004.02.028.
14. J. Cui, D. Meng, Z. Wu, W. Qin, D. She, J. Kang, R. Zhang, C. Wang, and W. Yue, Cer. International 48: 363-372 (2022), https://doi.org/10.1016/j.ceramint.2021.09.111.
15. M. Ullah, S. Khan, A. Laref, and G. Murtaza, Philos. Mag. 100: 768-781, (2020), https://doi.org/10.1080/14786435.2019.1697835.
16. U. Paliwal, and K. B. Joshi, J. Phys. D: Appl. Phys 44: 255501(1-7), (2011). https://doi.org/10.1088/0022-3727/44/25/255501.
17. S. R. Römer, T. Dörfler, P. Kroll, and W. Schnick, Phys. Status Solidi B 246, 1604–1613, (2009). https://doi.org/10.1002/pssb.200945011.
18. S. R. Römer, W. Schnick, and P. Kroll, J. Phys. Chem. C. 113: 2943-2949, (2009), https://doi.org/10.1021/jp8077002.
19. C. Braun, S. L. Börger, T. D. Boyko, G. Miehe, H. Ehrenberg, P. Höhn, and W. Schnick, J. Am. Chem. Soc. 133: 4307-4315, (2011), https://doi.org/10.1021/ja106459e.
20. A. Mokhtari, and H. Akbarzadeh, Phys. B Cond. Mat. 337, 122-129, (2003), https://doi.org/10.1016/S0921-4526(03)00387-9.
21. E. Orhan, E. Jobic, R. Brec, R. Marchand, and J. Y Saillard, J. Mater. Chem. 12: 2475-2479, (2002). https://doi.org/10.1039/B203500F.
22. R. Dovesi, A. Erba, R. Orlando, C. M. Zicovich-Wilson, B.Civalleri, L. Maschio, M. Rérat, S. Casassa, J. Baima, S. Salustroand and B. Kirtman, WIREs Comput. Mol. Sci. 8, (2018). https://doi.org/10.1002/wcms.1360.
23. R. Dovesi, V. R. Saunders, C. Roetti, R. Orlando, C. M. Zicovich-Wilson, F. Pascale, B. Civalleri, K. Doll, N. M. Harrison, I. J. Bush, P. D'Arco, M. Llunell, M. Causà, Y. Noël, L. Maschio, A. Erba, M. Rérat and S. Casassa 2017 CRYSTAL17 User's Manual (University of Torino).
24. M. F. Peintinger, D. V. Oliveira, T. Bredow, J. Comput. Chem. 34: 451-459 (2013), https://doi.org/10.1002/jcc.23153.
25. D. V. Oliveira, M. F. Peintinger, J. Laun, T. Bredow,

J. Comput. Chem. 40: 2364-2376, (2019), https://doi.org/10.1002/jcc.26013.
26. J. P. Perdew, K. Burke, M. Ernzerhof, Phys. Rev. Lett. 77: 386, (1996), https://doi.org/10.1103/PhysRevLett.77.3865.
27. J. P. Perdew, A. Ruzsinszky, G. I. Csonka,O. A. Vydrov, G. E. Scuseria, L. A. Constantin, X. Zhouand K. Burke, Phys. Rev. Lett. 100: 136406 (2008), https://doi.org/10.1103/PhysRevLett.100.136406.
28. H. J. Monkhorst, J. D. Pack, Phys. Rev. B 13: 5188-92, (1976), https://doi.org/10.1103/PhysRevB.13.5188.
29. C. G. Broyden, Math. Comput., 19, 577-93, (1965), https://doi.org/10.2307/2003941.
30. D. D. Johnson, Phys. Rev. B 38: 12807-13, (1988), https://doi.org/10.1103/PhysRevB.38.12807.
31. J. Hao, Y. Li,Q. Zhou,D. Liu, M. Li, F. Li,X, and Li X, Inorg. Chem. 48: 9737-9740, (2009), https://doi.org/10.1021/ic901324n.
32. A. Erba, A. Mahmoud, D. Belmonte, R. Dovesi, J. Chem. Phys. 140: 124703, (2014), https://doi.org/10.1063/1.4869144.
33. K. Toyoura, T. Goto, K. Hachiya, and R. Hagiwara, Electrochimicaacta, 51: 56-60, (2005), https://doi.org/10.1016/j.electacta.2005.04.004.
34. E. Orhan, S. Jobic, R. Brec, R. Marchand, J. Y. Saillard, J. Mater. Chem. 12: 2475-2479 (2002), https://doi.org/10.1039/B203500F.
35. J. Li, C. Fan, X. Dong, Y. Jin, and J. He, J. Phys. Chem. C, 118: 10238-10247 (2014), https://doi.org/10.1021/jp411692n.
36. J. Gao, Q. J. Liu, and B. Tang, J. App. Phys., 133: 135901 (2023), https://doi.org/10.1063/5.0139232.
37. R. Gaillac, P. Pullumbi, and F. X. Coudert, J. Phys.: Condens. Matter, 28: 275201, (2016), https://doi.org/10.1088/0953-8984/28/27/275201.

Study of Optical Property of Ce^{3+} doped $Li_{15}(SO_4)_5F_4Cl$ Unique Halosulphate Phosphor

A. M. Bhake

Department of Physics, Gondwana University, Gadchiroli- 442605, India.

aparna.dhond@gmail.com

Abstract

For the first time in phosphor history, a remarkable series of Ce^{3+} ion-doped Lithium Fluoride Chloride Sulphate i.e., $Li_{15}(SO_4)_5F_4Cl$ alkaline halo sulphate phosphors are made using a wet chemical process. Using X-ray diffraction (XRD) tests, the phase creation and concentration were ascertained. Additionally, Fourier Transform Infrared (FTIR) spectroscopy was used which makes it possible to identify the chemical linkages successfully and browsing electron microscopy was tested for surface investigations (SEM). When the photoluminescence (PL) characteristics of the as-prepared phosphors were examined, it was discovered that the Ce^{3+} ions in these hosts produced a broad Ultra-Violet (UV) emission. These could be used for scintillation and as potential UV lamp phosphors.

Keywords: Halo Sulphates, Phosphor, Wet Chemical Method, Ce^{3+} ions, Photoluminescence, UV.
Received 29 January 2025; First Review 11 March 2025; Accepted 19 March 2025.

*** Address of correspondence**
A. M. Bhake
Department of Physics, Gondwana University, Gadchiroli- 442605, India

Email: aparna.dhond@gmail.com

How to cite this article
A. M. Bhake, Study of Optical Property of Ce^{3+} doped $Li_{15}(SO_4)_5F_4Cl$ Unique Halosulphate Phosphor, J. Cond. Matt. 2025; 03 (01): 91-95.

Available from:
https://doi.org/10.61343/jcm.v3i01.88

Introduction

Brilliant materials (phosphors) doped with rare earth particles assume a crucial part in current life, because of their phenomenal applications going from fluorescent lights, scintillators, variety shows, heightening screens, ionizing radiations dosimetry, etc. [1-3]. The electric and photosensitive characteristics of phosphors are significantly impacted by the substance structure, degree of underlying issue, abandonments, and the existence of dopants or debasements. Lately, there has been a lot of attention in the glowing qualities of Ce^{3+} doped structures [4-6]. Tinny film electroluminescence displays, imaging plates, luster, solid-state illumination, and thermoluminescence dosimetry are among the promising applications for the alkaline halosulphates produced with Ce^{3+} particles [7-9]. Because of its simplicity of readiness and phenomenal photoluminescence and thermoluminescence qualities, a few examinations on chloride-based halosulphate materials are likewise in the works, as countless halosulphate materials have a few fascinating optical properties [7, 10]. Because of their numerous uses, chloride-based materials have witnessed a steady increase in interest in the last two-three years. By studying optical retention, electron spin impact, photonic movement, several kinds of refractive indices, and other real features like versatile modulus, a few organizations have made significant attempts to focus on the deformities in these materials [11-14]. Ce^{3+} is an exclusive activator for scintillator applications due to its extremely fast and efficient transition as well as energy close to the sensitivity maximum of photomultiplier tubes [15, 16]. Among the uses for inorganic scintillators are dental and medical diagnostic applications. High-energy radiation detection and visualization have been made possible in large part by these mineral scintillators. The most usually employed scintillators at the moment are bismuth germanate, cesium iodide and sodium iodide fixed with thallium [17]. These have a good energy resolution, high density light production and a comparatively rapid fade time. With remarkably short decay durations of just 0.8 and 4.4 ns, BaF_2 and CsF_2 are utilized for applications that demand fast response. Their light production is relatively modest, nevertheless. There is still a great need for scintillators with better features for certain uses, and there is currently no scintillator that combines a high light yield with quick response. Since halosulphates are thought to meet these requirements, more effort is being put into creating novel materials with higher efficiency. In light of this, numerous analyses of the iridescence of Ce^{3+} in halosulphate phosphors were conducted [18]. Cerium-activated phosphors are typically regarded as expanding groups and transmit in the ultraviolet or spectral region. In any case, the Ce^{3+}-discharge is shifted to longer frequencies by the host cross section's crystal field. Because it can efficiently emit light when excited, usually in the ultraviolet (UV) or bluish range, the Ce^{+3} ion is used in this situation.

It is a useful part of specialist phototherapy equipment because of its luminous qualities [19].

In this paper, the iridescence property of Ce^{3+} particles actuated $Li_{15}(SO_4)_5F_4Cl$ halosulphate phosphors arranged by wet chemical method is being accounted for first time throughout the entire existence of phosphors.

Method

The wet chemical strategy is used to set up the series of Ce^{3+} doped $Li_{15}(SO_4)_5F_4Cl$ halosulphate phosphors. This is by far the simplest and best incorporation method when compared to the many different usual techniques [20]. Using a logical equilibrium of precision 0.0001gm, the precursors of AR grade with the highest virtue (99.99% pure) $Li_2(SO_4)$, LiCl, NH_4F, and $Ce_2(SO_4)_3$ were demonstrated up stochiometric proportion. The natural substances were broken down in twofold refined de-ionized water in an exceptionally dry climate and later, every one of the arrangements of the forerunners were merged individually. The resultant arrangement was saved for amalgamation on magnetic stirrer for 30 min. The series of Ce^{3+} doped phosphors were ready according to the various fixations going from 0.1, 0.5, 1, 2, 5, and 10 mol% in the host framework. The straightforward arrangement acquired was saved for drying in a stove for 24 hours at 80 °C. The mixture turned into a smooth white powder. It was then ground into a fine powder using a stone crusher and grinder to get it ready for a number of experiments, including electron microscopy, phosphorescence, X-ray imaging, Fourier transform spectral analysis, and more [20].

A PAN data-driven diffractometer (Cu-Kα radiation) with a miniflex 2 goniometer was implemented to test the phase perfection and crystallinity of the pre-arranged $Li_{15}(SO_4)_5F_4Cl$ phosphor using X-beam deflection test in the acute angle 2θ region with a continuous examination step of 0.011 degrees and a continuation season of 15-20 seconds. Then, at that point, for testing their optical property, the above said series of phosphors was tried for photoluminescence (PL) investigation.

Operating a 150Watt 'Xenon band illumination ' as a stimuli source and a sensitive photomultiplier tube, theRF-5301PC spectrofluoro-photometer completed the PL estimates. Using a high sensitivity spectral slit width of less than 2 nm, excitation and discharge spectra were acquired.

This spectrophotometer gives revised excitation and emanation spectra in the frequency scope of 220-400 nm and 300-700 nm separately.

Checking electron microscopy (SEM) for surface morphology and Fourier change infrared (FT-IR) spectroscopy for the distinguishing proof of chemical bonds were additionally done for the previously mentioned radiance sulphates [20].

In addition to the above material, a similar method of synthesis was being adopted here for the phosphor $Li_{15-x}R_x(SO_4)_5F_4Cl$: Ce^{3+} (R = Na, K) with only the difference of precursor of dopant/co-dopant and its concentration values in mol%.

Discussion

XRD pattern of pure Li15(SO4)5F4Cl phosphor

Fig. 1 shows the XRD pattern for lithium fluoride chloride sulphate phosphor. Accordingly, there is no standard JCPDS document to coordinate with the XRD.

Example of this phosphor thus it's exceptional because for the first time in phosphor history, it is prepared and tested.

The fact that the material was translucent makes it seen with highly intense sharp peaks. It typically indicates the presence of well-ordered repeating crystalline structure.

The interatomic spacing within the crystal lattice is dependent on peak position. Changes in peak positions can indicate variations in lattice parameters due to strain, impurities, or phase transitions.

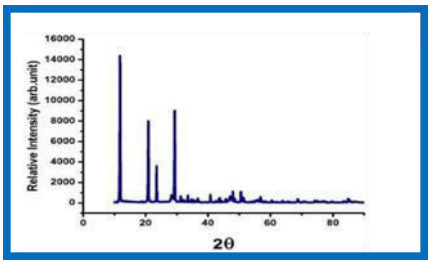

Figure 1: XRD pattern of pure $Li_{15}(SO_4)_5F_4Cl$ host material.

FT–IR study of Ce^{+3} doped Lithium fluoride chloride sulphate phosphor

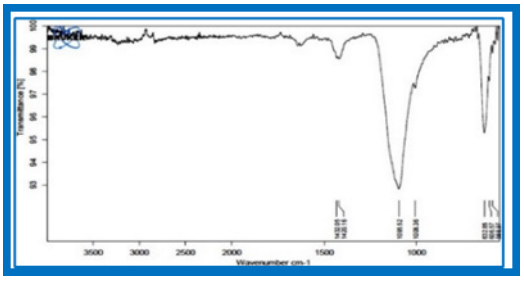

Figure 2: FT-IR ranges of Ce^{+3} doped Lithium fluoride chloride sulphate phosphor.

An IR spectrum of a chemical substance is a unique fingerprint for its identification about chemical bonds and material composition. It provides useful information about the structure of molecules quickly. FT-IR fields of $Li_{15}(SO_4)_5F_4Cl$:Ce^{3+} phosphor as shown in Fig. 2. Two

strong and extensive bands: one is due to $Li_2(SO_4)$ at 1095 cm^{-1} and another band is due to cerium at 632 cm^{-1}. Weak bands near 1432 cm^{-1} may be due to ammonium fluoride were displayed for the phosphor.

SEM analysis of $Li_{15}(SO_4)_5F_4Cl:Ce^{3+}$ phosphor

The $Li_{15}(SO_4)_5F_4Cl$ phosphor's crystallite size is visible in the SEM micrograph, which shows highly detailed magnified image as shown in Fig. 3a, 3b, 3c. Typically, crystallites are between two to five micrometres in size.

The crystallites have a crisp surface shape. The particles are composed of lengthy structure, it means tend to cluster together, forming larger structures. Fig 3 (a). Also, it shows remarkably agglomerated crystallites and have a strongly constructed particles appear robust and well-formed. Its layers-like appearance shows the structure seems to have multiple layers, possibly resembling a sheet-like or stacked formation Fig. 3 (b), 3 (c).

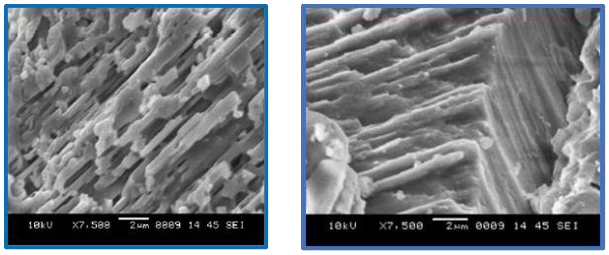

(a) (b)

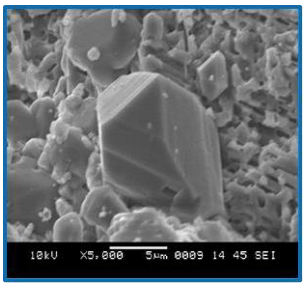

(c)

Figure 3 (a), (b), and (c): Surface Morphology of $Li_{15}(SO_4)_5F_4Cl$ phosphor

Photoluminescence (PL) in Ce^{3+} doped $Li_{15}(SO_4)_5F_4Cl$ Phosphor

In the Ce^{3+} doped lithium fluoride chloride sulphate host lattice, the PL excitation spectrum of Ce^{3+} ions reveals wideband fluorescence with a highest intensity at 254 nm and an inclined peaking at 236 nm when stimulated at 340 nm. Fig. 4 illustrates an electron from the $4f^1$ orbital is moved to the $5d^1$ orbital when Ce^{3+} absorbs energy. Due to its stronger interactions with the surrounding ions and greater spatial extension, the $5d^1$ orbital undergoes considerable crystal potential splitting.

The wavelengths of emission of lithium fluoride chloride sulphate phosphors series at various doping ratios are presented in Figs. 5(i) and 5(ii) when exposed at 254 nm of wavelength. When activated by 254 nm UV light, the phosphors show broadband emission that stretches from 260 to 406 nm with a maximum of roughly 325 nm. Other than intensity variations, the phosphors remain unchanged with changing dopant concentrations. Because of the splitting of its 4f ground state, Ce^{3+} emission should consist of a double band. However, in this instance, it is not possible to immediately discern between the emission spectrum's doublet bands.

Consequently, it splitted into two separate Gaussian components, as shown in Fig. 6(iii), with peak centres on the energy scale at 31152.64 cm^{-1}(321 nm) and 28248cm^{-1} (354 nm). The energy difference between these two bands is 2904 cm^{-1}. The Stoke's shift is found to be 8600 cm^{-1}. The shift in PL intensity of Lithium fluoride chloride sulphate phosphors with Ce^{3+}- doping level is depicted in Fig. 6(i). It is discovered that as the doping concentration rises, the emission intensity of the Ce^{3+} ions first increase before peaking at x = 0.01. The concentration quenching effect then causes the intensity to drop as the concentration rises further [21]. When the dopant concentration is sufficiently high, the following equation connects the luminous intensity I to the dopant concentration x,

$$\frac{I}{x} = k\,[1 + \beta.x^3]^{\theta-1} \qquad (1)$$

This equation can be loosely written as follows for a specific host matrix as

$$log\frac{I}{x} = c - \frac{\theta}{3}\log x \qquad (2)$$

where k, β, and c are constants for the same excitation state [21].

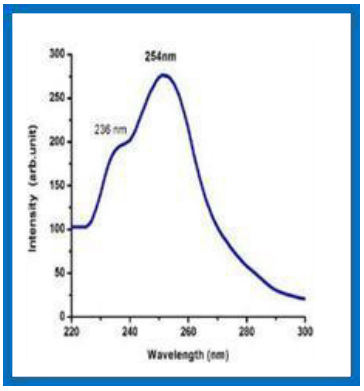

Figure 4: Pattern of Ce^{3+} doped $Li_{15}(SO_4)_5F_4Cl$ phosphor excitation

The electric multipole index, θ, illustrates collaborations between electric dipoles, dipoles-quadrupoles and electric quadrupoles when its values are 6, 8, and 10. Fig. 6(ii) shows the association between log (I/x) and log (x) for

lithium fluoride chloride sulphate (x > 0.01) phosphor based on its emission spectra acquired at 325 nm. The plotted data's gradient, $(-\theta/3)$ = -3.3859, was found to be appropriate for a straight line. As a result, θ is 10.1577, which is rather near to 10. In addition to making the materials stable and potentially useful for high-resolution displays, electroluminescent devices, vacuum discharge lamp phosphor screens, etc., This implies that the concentration quenching of Ce^{3+} luminous intensity is mostly caused by the electric quadrupole–electric quadrupole interaction mechanism.

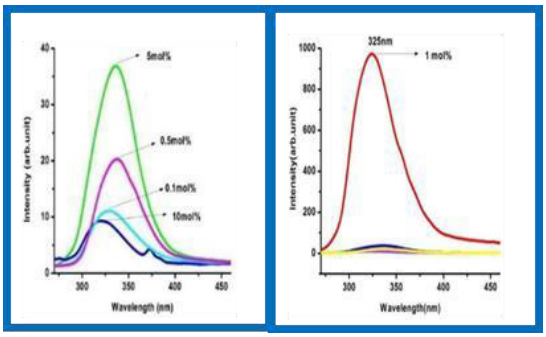

Figure 5: (i) $Li_{15}(SO_4)_5F_4Cl:Ce^{3+}$ phosphor emission spectrum, with the exception of 1 mol%. **(ii)** $Li_{15}(SO_4)_5F_4Cl:Ce^{3+}$ emission spectrum at 1 mol%.

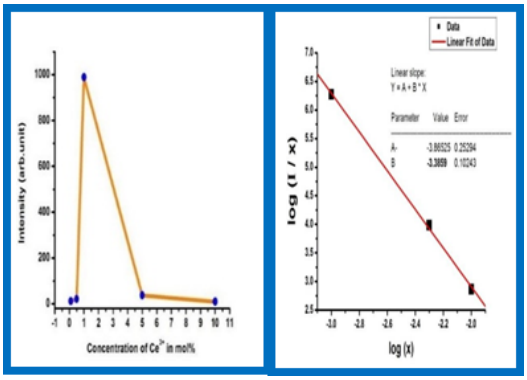

Figure 6: (i) The PL influence verses doping concentration in mol%, **(ii)** The plot of log(I/x) versus log(x) for $Li_{15}(SO_4)_5F_4Cl:Ce^{3+}$phosphors is linear.

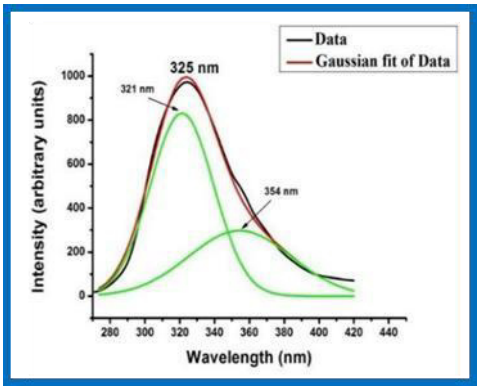

Figure 6 (iii): Gaussian functions (λ_{exc} = 254 nm) were used to fit the PL spectra of $Li_{15}(SO_4)_5F_4Cl:Ce^{3+}$ phosphors, which has an emission peak at 325 nm.

Photoluminescence in Ce^{3+} doped $Li_{15-x}Na_x(SO_4)_5F_4Cl$ Phosphor

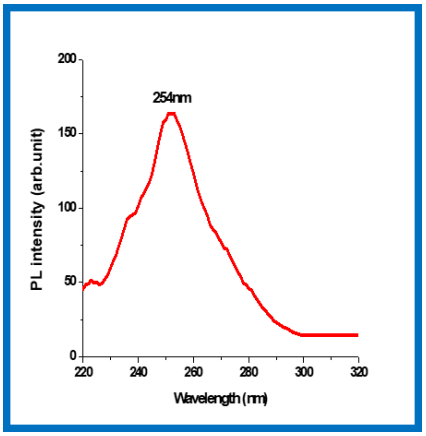

Figure 7: Excitation spectra of $Li_{15-x}Na_x(SO_4)_5F_4Cl:Ce^{3+}$ 1 mol% (R=Na, K) as x= 1, 3, 5, 10 mol%.

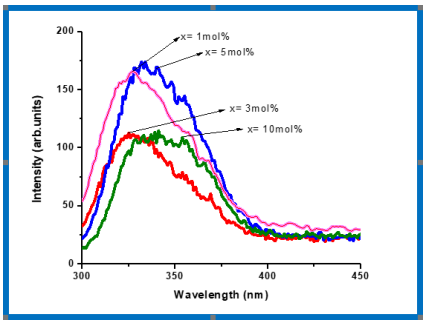

Figure 8: Emission patterns of $Li_{15-x}Na_x(SO_4)_5F_4Cl:Ce^{3+}$ 1 mol%.

An attempt is made to study the $Li_{15}(SO_4)_5F_4Cl$: Ce^{3+} phosphor by co-doping it with sodium (Na^+) ions in the host crystal lattice. It is monitored that in the case of $Li_{15}(SO_4)_5F_4Cl$: Ce^{3+} phosphor, the PL intensity was exceptional for 1 mol% of Ce^{3+} [Fig. 5 b]. For $Li_{15-x}Na_x(SO_4)_5F_4Cl:Ce$:1 mol%, Fig. 7 and 8 display the excitation and emission spectra, respectively for x = 1, 3, 5, 10 mol% of sodium (Na^+) ions. In this case, the prominent excitation is peaking at 254 nm which overlaps very well with Hg emission (253.7 nm) and we obtained the broadband emission at around 327 nm for different concentrations of Na^+ as x =1, 3, 5, and 10 mol%. It is evident from Fig. 8 that the PL intensity is lowest at 10 mol% of Na^+ ions and highest at 5 mol%. Co-doping Na+ ions in the host matrix is thought to cause concentration quenching, which significantly reduces the total PL intensity. On the other hand, weak spin-orbit coupling of the ground state of Ce^{3+} ions are indicated by the single peaking at about 327 nm [22].

Photoluminescence in Ce^{3+} doped $Li_{15-x}K_x(SO_4)_5F_4Cl$ Phosphor

Similarly by keeping Ce^{3+} constant at 1 mol%, the new host $Li_{15-x}K_x(SO_4)_5F_4Cl$: Ce^{3+} 1 mol% phosphor was synthesized

by the wet chemical method in which lithium-ion is being replaced by potassium ion. Figure 7 and Figure 9 display the excitation and emission pattern of $Li_{15-x}K_x(SO_4)_5F_4Cl$: Ce^{3+}:1 mol%, respectively for x = 1, 3, 5, 10 mol% of potassium (K^+) particles. The excitation spectra have prominent maxima at 254 nm which well matched with Hg emission (253.7 nm) and monitored the broadband emission at around 325 nm-355 nm for different concentrations of K+ as x =1, 3, 5, and 10 mol%. From Fig. 9, The PL intensity is seen to be lowest at 3 mol% of K^+ ions and highest at 1 mol%. Once more, it is claimed that co-doping K^+ ions in the host matrix causes concentration quenching, which significantly reduces the overall PL intensity. On the other hand, the single peaking at about 325–355 nm suggests that the ground state of Ce^{3+} ions have a modest spin-orbit/loop coupling. The strong crystal field at the Ce^{3+}site, which predominates over the spin-orbit/loop coupling, could be the cause of the minor shift towards a longer wavelength [22].

However, the fact that the PL emission intensity is higher (Fig. 9, 700 A.U.) when K^+ ions are doped in the host matrix as opposed to when Na^+ ions are doped (Fig. 8, 175 A.U.) suggests that K^+ ions are predominating in the replacement of lithium ions.

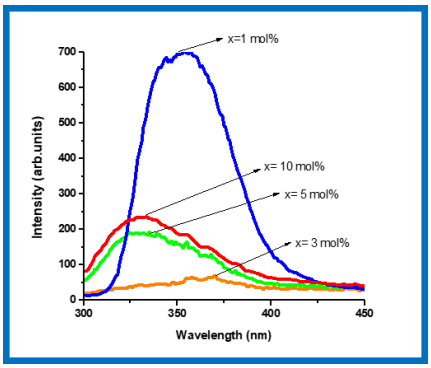

Figure 9: Shows the host $Li_{15-x}K_x(SO_4)_5F_4Cl$: Ce^{3+}:1 mol% emission pattern.

Conclusion and Future Prospective

The luminous characteristics of $Li_{15}(SO_4)_5F_4Cl$ halosulphate phosphor doped with polycrystalline Ce^{3+} ions were successfully synthesized using wet chemical synthesis and are being reported for the first time in phosphor history. These phosphors' morphological, spectroscopic, and structural characteristics were examined using SEM, FTIR and XRD, respectively. The PL emission spectra of the three phosphors listed above were all found to be in the near-UV range. When exposed to 254 nm UV illumination, a 1 mol% concentration of $Li_{15}(SO_4)_5F_4Cl$: Ce^{3+} phosphor showed a remarkable PL emission intensity at 325 nm wavelength.

Because of their effective broad-band emission in the ultraviolet spectrum, all of the Ce^{3+} doped phosphors discussed in this paper may find use in scintillation applications. These phosphors' optical features suggest that they could be useful materials for luminous phosphors in the ultraviolet (UV) band, which spans from 300 nm to 450 nm and be used for glimmer. A thorough examination of these phosphors' additional features will undoubtedly demonstrate their merit for a wide range of future uses.

References

1. M. Mohapatra, B. Rajeswari, N. S. Hon, R. M. Kadam, V. Natarajan, J. Lumin., 166: 1, 2015.
2. A. Pandey, V. K. Sharma, D. Mohan, R. K. Kale, P. D. Sahare, J. Phys. D: Appl. Phys. 35: 1330, 2002.
3. G. N. Nikhare, S. C. Gedam, S. J. Dhoble, Lumin. 30: 163, 2015.
4. V. C. Kongre, S. C. Gedam, S. J. Dhoble, Luminescence, 2015. DOI 10.1002/bio.2875.
5. A. Poddar, S. C. Gedam, S. J. Dhoble, Luminescence, 2014. DOI 10.1002/bio.2755.
6. B. P. Kore, N. S. Dhoble, S. P. Lochab, S. J. Dhoble, J. Lumin. 145: 299, 2014.
7. E. V. D. van Loef1, P. Dorenbos1, C. W. E. van Eijk1, K. W. Kramer, and H. U. Gudel Phys. Rev. B 68: 045108, 2003.
8. V. C. Kongre, S. C. Gedam, S. J. Dhoble, J. Lumin. 135:55, 2013.
9. A. Poddar, S. C. Gedam, S. J. Dhoble, J. Lumin. 149:245, 2014.
10. S. C. Gedam, S. J. Dhoble, J. Lumin. 142:139, 2013.
11. H. Meeks, A. Janner, Phys Rev B. 38 :8075, 1988.
12. G. Wahlstrom, K. Chao, Phys Rev B. 36: 9573, 1987.
13. S. Y. Jeong, M. S. Jang, S. K. Han, S. Haussuhl, Cryst Res Tech. 27:883,1992.
14. K. Annapurna, R. N. Dwivedi, S. Buddhudu, Mater Lett. 53: 359, 2002.
15. K. W. Kramer, P. Dorenbos, H. U. Gudela and C. W. E. van Eijk, J. Mater. Chem. 16: 2773, 2006.
16. Growth and Evaluation of Improved CsI:Tl and NaI:Tl Scintillators. Crystals 12: 151,2022. https://doi.org/10.3390/cryst12111517.
17. P. Dorenbos, J. Lumin. 91: 155, 2000.
18. S. C. Gedam, S. J. Dhoble, S. V. Moharil, J. Lumin. 126 :121, 2007.
19. G. B. Nair, S. J. Dhoble, Luminescence, 2015. DOI 10.1002/Bio.2919.
20. A. M. Bhake, G. Nair, G. D. Zade, S. J. Dhoble, J. BC Lumin., 2016. DOI 10.1002/bio.3131.
21. Sandra Barysaite, Jevgenij Chmeliov, Leonas Valkunas, and Andrius Gelzinis*Cite This: J. Phys. Chem. B, 128: 4887−4897, 2024.
22. A. Nag. T. R. N. Kutty, Mat. Che. and Phy., 91: 524-531, 2005.

Investigating the Mass Spectra of Di-Hadronic Molecule by Potential Model

Dipesh Yadav[a], Chetan Lodha[b], and Ajay Kumar Rai[c]

Department of Physics, Sardar Vallabhbhai National Institute, of Technology (SVNIT), Surat, Gujarat-395007, India.

[a] dipesh1729@gmail.com
[b] iamchetanlodha@gmail.com
[c] raiajayk@gmail.com

Abstract

In the present paper we address the enthralling problem of discovering and comprehending the hadronic-like molecular interactions. We use a Yukawa-like screening potential in s-wave state in conjunction with the One Boson Exchange potential to calculate the mass spectra. We suggest interaction between two hadrons, a dipole-like in colour-neutral state that results in the production of a hadronic molecule along with application of the compositeness theorem of Weinberg, which is used to differentiate these molecules from other hadronic states. We compute the mass spectra for various di-mesonic states, using the proposed interaction potential.

Keywords: Exotic; Hadronic-Molecule; Meson.
Received 29 January 2025; First Review 11 March 2025; Accepted 19 March 2025.

*** Address of correspondence**
Dipesh Yadav
Department of Physics, Sardar Vallabhbhai National Institute, of Technology (SVNIT), Surat, Gujarat-395007, India

Email: dipesh1729@gmail.com

How to cite this article
Dipesh Yadav, Chetan Lodha, and Ajay Kumar Rai, Investigating the Mass Spectra of Di-Hadronic Molecule by Potential Model, J. Cond. Matt. 2025; 03 (01): 96-102.

Available from:
https://doi.org/10.61343/jcm.v3i01.89

Introduction

In recent decades, significant efforts have been directed toward the search for hadronic molecules, both theoretically and experimentally [1-7]. These molecules, akin to the deuteron which are strong candidates within the model of Quantum Chromodynamics (QCD).

QCD can comprehended as the fundamental theory describing strong interactions. Alongside the well-established conventional baryons (three-quark systems) and mesons (quark-antiquark pairs), hadronic molecules present an intriguing extension of QCD's predictive power.

Conventional baryons, such as protons and neutrons, serve as the important part of atomic nuclei, and their properties, including masses, magnetic moments, and decay modes, have been extensively studied using potential models, lattice QCD, and experimental data [8-16]. Similarly, mesons like Pions, kaons, and charmonium states (e.g., J/ψ and ψ(2S)) play critical roles in understanding hadronic interactions and mediating nuclear forces [17-18]. However, the discovery of exotic hadrons has extended the particle physics frontier beyond these conventional states. In recent years, several narrow exotic resonances have been observed, such as X(6900) [1]P_c(4450)[2], Z_b(10610)-/(10650) [4] X (3872) [5], Z $(4430)^+$ [6], Y (4260) [7], , and. These states, which defy straightforward classification within the conventional baryon-meson framework, have sparked intense interest in their underlying substructures.

Various theoretical explanation has been proposed for these exotic states, including:

- **Conventional heavy baryons**, [14-16] where exotic states are attributed to excited or unconventional configurations of three quark pairs with one or more heavy quarks.
- **Conventional heavy meson** [17-18]: where states are attributed to excited or unconventional configurations of quark-antiquark pairs with one or more heavy quarks.
- **Hadronic molecules** [19-20], which describe these states as loosely bound systems of two or more hadrons
- **Conventional light meson** [21]: where states are attributed to excited or unconventional configure-ions of quark-antiquark pairs with light quarks.
- **Conventional light baryons** [22-23]: where exotic states are attributed to excited or unconventional configurations of three light quark pairs.

- **Compact tetraquarks** [24-29], **Compact penta-quarks** [30] representing a tightly bound state of diquarks and antidiquarks.

The decay width (Gamma) in hadron spectroscopy signifies the stability of a particle, where a larger (Gamma) corresponds to a shorter lifetime. This classification aids in distinguishing decays into three categories: strong (rapid), electromagnetic (intermediate), and weak (gradual). Measuring (Gamma) plays a crucial role in the identification of exotic hadrons. Theoretical approaches to these models include effective field theory [31], QCD sum rules [3], lattice QCD [32], and potential models [33-34]. Comprehensive reviews, such as, consolidate these findings and provide an overview of their experimental and theoretical progress.

This study narrows its focus to the di-hadronic molecular model in a potential framework. primary questions drive this investigation are: (i) understanding how interactions between two colour-neutral hadrons lead to bound states, and (ii) differentiating hadronic molecular states from conventional hadrons or compact exotic states [27]. A key theoretical insight is that the One-Pion Exchange (OPE) potential provides sufficient long-range attraction to support molecular binding [28]. However, OPE alone fails to account for the very close-range interactions, necessitating inclusion for One Boson Exchange (OBE) potentials and Yukawa-like screening potentials [29]. Hadronic molecules provide good path to probe the strong force at quantum level. These systems, formed through delicate interactions between colour-neutral hadrons, highlight the intricate dynamics of QCD. Despite substantia l progress, many questions remain, particularly regarding the binding mechanisms, stability, and mass spectra of these states.

This study employs theoretical tools such as Weinberg's theorem to distinguish hadronic molecules from loosely coupled systems, providing a systematic approach to classification. Special emphasis is placed on calculating the mass spectra of di-hadronic states, which are significant for both theoretical exploration and experimental validation. By analysing their binding energies and stability, this work aims to uncover patterns inherent to hadronic molecular states. These findings not only deepen our understanding of strong interactions and QCD but also provide valuable insights for experimentalists working at facilities like PANDA, J-PARC, Belle, and LHCb [30]. As hadronic molecules bridge the gap between conventional baryons/mesons and exotic hadrons, further theoretical and experimental advancements are crucial for unravelling the full complexity of the strong force and its manifestations in nature. The current work is organized as follows: after the introduction in Section 1 theoretical, Section 2 describes the mass spectra generated by this formalism for hadronic molecule. Section 3 summarizes the results and Section 4 draws the final conclusion.

Theoretical Framework

Interhadronic Interaction

The deuteron, which is formed by the bound states of a P and N, is widely recognized as a molecule. To analyse and predict other hadronic compounds similar to the deuteron, it is helpful to use the deuteron itself as a model. Understanding such bound states involves addressing two fundamental questions: (i) why two color-neutral hadrons are attracted to one another and (ii) how 2 hadrons form a bound state. Regard to the definition of a molecule, a bound state requires a sufficiently strong attractive potential, which can be quantified by an effective coupling constant. Several realistic potentials, such as the Paris Group potential, the Nijmegen Group potential, and the full-Bonn (CD-Bonn) potential, have been developed to address the first question.

The potentials in question are derived from particle exchange, referred to as (OBE-P) Potentials, which extend Yukawa's pion exchange potential utilized to elucidate the nuclear force. The OBE-P encompasses long, medium, and short-range interactions via meson exchange, with the mass of the exchanged mesons dictating the force's range. Addressing the second inquiry why it is difficult for two color-neutral hadrons to establish a bound state—demands a nuanced comprehension of fundamental interactions at exceedingly short distances, where OBE-P exhibits limitations.

In order to distinguish the hadronic molecular states from other hadronic states, the Compositeness Theorem becomes essential. The challenge lies in identifying these molecular states accurately. To address this, we employ Weinberg's compositeness theorem, which provides a systematic framework for identifying molecular states by differentiating them from other hadronic configurations. This approach is critical for resolving the challenges faced in the hadronic molecular model and distinguishing these states from other potential forms of matter.

Effective Potential (One Boson Exchange + Yukawa - Screen like)

The di-hadronic molecule's Hamiltonian:

$$H = \sqrt{P^2 + m_{h_1}^2} + \sqrt{P^2 + m_{h_2}^2} + V_{hh} \quad (1)$$

Where H stands for the Hamiltonian or total energy of the system, P represents the momentum of the particles, and m_{h1} and m_{h2} are the masses of the first and second particles,

respectively. V_{hh} is the potential term that describes interactions or external forces affecting the system.

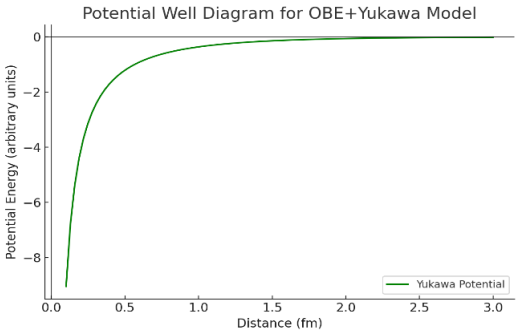

Figure 1: One Boson Exchange + Yukawa -Screen like potential

Through the utilization of the hydrogen-like trial wave function, we are able to ascertain the expected value of the Hamiltonian within the framework of the variational technique. We are able to determine the masses of low-lying di-mesonic states by using the expectation value of the Hamiltonian mathematical model.

$$H\psi = E\psi \quad \text{and} \tag{2}$$

$$\langle \text{Kinetic Energy} \rangle = \frac{1}{2}\left\langle r_{ij}\frac{dV_{hh}}{dr_{ij}}\right\rangle \tag{3}$$

and wave-function parameter can be obtain using virial theorem for each state.

The interaction potential, articulated by the One Boson Exchange potential (OBE-P) and a phenomenological attractive screened Yukawa-like potential [35] in the s-wave state, is elucidated in greater detail in the reference. The light mesons relevant to the One Boson Exchange potential (OBE-P) include π, η, σ, a0 (or δ), ω, and ρ. The OBE potential, which is the aggregate of all one-meson exchanges, namely

$$V_{OBE}=V_{ps}+V_s+V_v \tag{5}$$

Thus, Vps, Vs, and Vv represent the distinct s-wave one-meson exchange interaction potentials for pseudoscalar, scalar, and vector mesons, respectively. These potentials are articulated as

$$V_{ps} = \frac{1}{12}\left(\frac{g_{\pi qq}^2}{4\pi}\left(\frac{m_\pi}{m}\right)^2\frac{e^{-m_\pi r_{ij}}}{r_{ij}}\right)\left[(\tau_i\cdot\tau_j) + \frac{g_{\eta qq}^2}{4\pi}\left(\frac{m_\eta}{m}\right)^2\frac{e^{-m_\eta r_{ij}}}{r_{ij}}\right](\sigma_i\cdot\sigma_j) \tag{6}$$

Where Vps: Potential energy due to the pion and eta meson exchange interactions, $g_{\pi qq}$: Coupling constant for the pion-quark-quark interaction, m_π: Mass of the pion, m: Reference mass (e.g., the mass of the quark), r_{ij}: Distance between particles i and j, τi: Isospin operator for particles i and j, $g_{\eta qq}$: Coupling constant for the eta-quark-quark interaction. m_η: Mass of the eta meson, σi: Spin operator for particles i and j.

$$V_s = \frac{g_{\sigma qq}^2}{4\pi}m_\sigma\left[1-\frac{1}{4}\left(\frac{m_\sigma}{m}\right)^2\right]\frac{e^{-m_\sigma r_{ij}}}{m_\sigma r_{ij}} + \frac{g_{\delta qq}^2}{4\pi}m_\delta\left[1-\frac{1}{4}\left(\frac{m_\delta}{m}\right)^2\right]\frac{e^{-m_\delta r_{ij}}}{m_\delta r_{ij}}(\tau_i\cdot\tau_j) \tag{7}$$

Vs: Scalar potential energy due to the sigma and delta meson exchange interactions., $g_{\sigma qq}$: Coupling constant for the sigma-quark-quark interaction., m_σ: Mass of the sigma meson., $g_{\delta qq}$: Coupling constant for the delta-quark-quark interaction., m_δ: Mass of the delta meson., τ_{ij}: Isospin operator for particles i and j.

$$V_v = \frac{g_{\omega qq}^2}{4\pi}\left(\frac{e^{-m_\omega r_{ij}}}{r_{ij}}\right) + \frac{1}{6}\frac{g_{\rho qq}^2}{4\pi}\frac{1}{m^2}(\tau_i\cdot\tau_j)(\sigma_i\cdot\sigma_j)\left(\frac{e^{-m_\rho r_{ij}}}{r_{ij}}\right) \tag{8}$$

Vv: Vector potential energy due to the omega and rho meson exchange interactions, $g_{\omega qq}$: Coupling constant for the omega-quark-quark interaction, m_ω: Mass of the omega meson., $g_{\rho qq}$: Coupling constant for the rho-quark-quark interaction., m_ρ: Mass of the rho meson, τ·: Isospin operator for particles i and j, σi·σj: Spin operator for particles i and j.

The One Boson Exchange potential (OBE-P), incorporating finite size effects attributable to the extended structure of hadrons, can be articulated as

$$V_\alpha(r_{db}) = V_\alpha(m_\alpha, r_{db}) - F_{\alpha 2}V_\alpha(\Lambda_{\alpha 1}, r_{db}) + F_{\alpha 1}V_\alpha(\Lambda_{\alpha 2}, r_{db}) \tag{9}$$

Where Vα: Potential energy due to the interaction at distance r_{db}, Vα (mα, rdb): Potential energy term dependent on the parameter m_α and distance r_{db}, $F_{\alpha 2}$: Scaling factor for the term involving Λα1, Vα(Λα1,r_{db}):Potential energy term dependent on the parameter Λα1and distance r_{db}, Fα1:Scaling factor for the term involving Λα2., Vα(Λα2,r_{db}): Potential energy term dependent on the parameter Λα2 and distance r_{db}

Where α represents the η, σ, π, δ, ω, and ρ mesons, while

$$\Lambda\alpha 1=\Lambda\alpha+\epsilon \quad \text{and} \quad \Lambda\alpha 2=\Lambda\alpha-\epsilon$$

$$F_{\alpha 1} = \frac{\Lambda_{\alpha 1}^2 - m_\alpha^2}{\Lambda_{\alpha 2}^2 - \Lambda_{\alpha 1}^2} \quad \text{and}$$

$$F_{\alpha 2} = \frac{\Lambda_{\alpha 2}^2 - m_\alpha^2}{\Lambda_{\alpha 2}^2 - \Lambda_{\alpha 1}^2} \tag{10}$$

The subscript α refers to mesons such as ω, η, σ, π, δ, and ρ, where $(\epsilon/\Lambda_\alpha \ll 1)$, which suggests that a value of 10 MeV is a reasonable choice for the mass scale. To enhance the strength of the total effective dihadronic potential, a Yukawa screening potential is introduced [36]. This is necessary because the effective s-wave One Boson Exchange potential (OBE-P) is weak due to the highly sensitive cancellation between individual meson exchanges.

The residual running coupling constant, denoted as k_{mol}, and the screening fitting parameter (c) are introduced through the Yukawa-like potential. The intensity of the interaction can be modified using these parameters. A specific formula can estimate the residual running coupling constant (k_{mol}), incorporating the masses of the exchange mesons, the regularization parameter (Λ_α), and the coupling constants.

The estimation of the coupling constant is based on realistic potentials, which are modified to explain the properties of the deuteron using NN-phase shift data. For consistency, the same coupling constants used in the works of Machleidt (2001) and Weinberg (1965) for the deuteron are applied to other hadronic molecular systems. In this context, the meson-hadron coupling constants are approximated similarly to those used for nucleon-nucleon systems.

$$g_{\alpha hh} \cong g_{\alpha NN} \quad (11)$$

$g_{\alpha hh}$ and $g_{\alpha NN}$ represent the coupling constants for meson-hadron and meson-nucleon interactions, respectively.

The meson exchange's effective coupling constant exhibits scaling behaviour and has the ability to alter the interaction potential's strength. Knowing the coupling constant's effective strength allows us to obtain precise information about the degree of the hadron-meson-hadron interaction's individual meson exchange potential. In order to fix our model parameter, the meson-hadron coupling constant has been approximated.

The Yukawa-like screening potential was introduced to enhance the strength of the effective dihadronic interaction potential, as the efficacy of the effective s-wave one-boson exchange is constrained by the cancellation of individual meson exchanges. The Yukawa-type potential displayed is integrated.

$$V_Y = -\frac{k_{mol}}{r_{ij}} e^{-\frac{c^2 r_{ij}^2}{2}} \quad (12)$$

- The coupling constants are taken from realistic nucleon-nucleon potential models (Machleidt, 2001).
- Screening parameters are adjusted to fit deuteron binding energy for consistency.
- The meson masses are adopted from Particle Data Group (PDG) 2022.

V_Y: Potential energy due to the interaction, k_{mol}: A constant related to the molecular interaction strength, rij: Distance between particles i and j, c: A parameter related to the spread or range of the interaction.

In this context, k_{mol} signifies the running coupling constant, whereas c represents the screening fitting parameter. The value of k_{mol} can be calculated using the subsequent equation:

$$k_{mol}(M^2) = \frac{4\pi}{\left(11-\frac{2}{3}n_f\right)\ln\frac{M^2+M_B^2}{\Lambda_Q^2}} \quad (13)$$

Where $M = \frac{2md\ mb}{(md+mb)}$, md and mb are masses of constituent hadron which form di-hadronic molecule system. M_B = 950 MeV, Λ_Q is taken 399 MeV and 225 MeV for light and heavy meson, respectively. n_f is flavour number. The net inner hadronic potential V_{hh} is given below as

$$V_{hh} = V_{OBE} + V_Y \quad (14)$$

V_{OBE}: The overall binding energy is denoted by this term. It takes into consideration the energy needed to hold the components (such as quarks) of the hadron or molecule together. Understanding the stability and structure of the system depends on this binding energy.

V_Y: The interaction between particles mediated by mesons (such Pions or other mesons) is referred to as the Yukawa potential. Particularly in nuclear and particle physics, the Yukawa potential is crucial for comprehending the interaction between particles at a specific range.

The parameters that remain invariant in the current model encompass the masses, the exchange meson coupling constant, and Λ_Q, as referenced in sources. The computation of the residual running coupling constant, k_{mol}, is executed utilizing Equation (13). This model is adjusted to estimate the experimental binding energy of the deuteron by altering the color screening parameter, c, which acts as the sole free parameter.

It is important to note that three pseudoscalars at a single vertex do not conserve parity. Consequently, pseudoscalar exchanges between two pseudoscalar systems are not allowed by parity conservation. In the strong interaction, however, parity is a well-conserved quantum number. Hence σ, ω and a_0 exchanges donate to the One Boson Exchange (OBE) potential in the case $D^0\overline{K^\pm}$ and of $K\bar{K}$ and di-mesonic states. When calculating di-mesonic states, the σ -meson mass is taken as m_σ = 725 MeV for total isospin I_T=0, and m_σ= 500 MeV for I_T=1. For pseudoscalar-pseudoscalar states, such as f0(980) and a0(980), only σ, a_0 and ω exchanges are considered, as these exchanges are the sole contributors to the OBE potential of S-wave.

Results and Discussion

In the present study, the mass spectra of various dihadronic molecules have been calculated and analysed in compare-son with their corresponding threshold masses and experimental predictions. These results are summarized in Table 1, where the molecular states are categorized in accordance to their quantum numbers [37] JP and their

natural energy scale. Calculated masses are benchmarked against meson thresholds to ensure accuracy. For this analysis, the parameters were adopted from the latest (Particle Data Group and PANDA) [38-44], ensuring consistency with current experimental and theoretical standards.

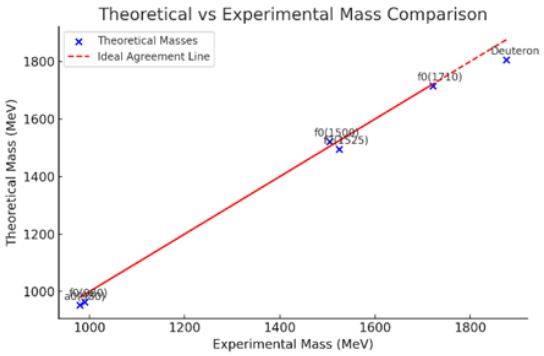

Figure 2: Theoretical vs Experimental Mass Comparison.

Conclusion and Future Prospective

In conclusion, the mass spectra of various di-hadronic molecules have been calculated within a non-relativistic framework. The methodology developed in this study lays the groundwork for future research aimed at exploring molecular hadrons composed of multiple hadrons. The findings from this work offer valuable insights and serve as a reference for experimental investigations conducted by future facilities such as PANDA, J-PARC, Belle, LHCb, PDG and others. This study adds to our growing understanding of unusual hadrons and their involvement in QCD. Further research in this subject will provide further insight into the underlying forces that regulate subatomic particles. The interaction of theory and experiment will remain critical in unravelling the riddles of hadronic molecules.

Table 1: The mass spectra of diverse molecular states, accompanied by their respective threshold masses in MeV.

Candidate	Molecular elucidation	S-Wave I(JP)	Threshold mass MeV	Exp.-mass MeV	This-Work mass MeV	Natural energy scale ($m_\pi^2/2\mu$) MeV	Uncertainty (MeV)
Deuteron	P n	0 (1+)	1877.84	1875.6	1805.5	19.91	±1.2
f0 (980)	K $\bar{K}$	0 (0+)	995.228	990 ± 2	964.07	37.02	±1.8
a0 (980)	K $\bar{K}$	1 (0+)	995.228	980 ± 20	953.17	37.03	±2.3
f0 (1500)	ρ ρ	0 (0+)	1550.98	1505 ± 6	1521.35	23.93	±3.1
f2(1525)	ρ ρ	0 (2+)	1550.98	1525 ± 5	1495.03	23.93	±3.5
f0(1710)	K* K*	0 (0+)	1791.8	1722±5	1715.22	22.21	±4.0

References

1. LHCb Collaboration, *"Observation of structure in the J/ψ-pair mass spectrum"*, Sci. Bull. 65, 1983–1993 (2020). DOI: 10.1016/j.scib.2020.08.032.
2. Aaij R, Adeva B, Adinolfi M, Ajaltouni Z, et al. (LHCb Collaboration), *"Observation of the Doubly Charmed Baryon Ξ_cc⁺⁺"*, Phys. Rev. Lett. 119, 112001 (2017). DOI: 10.1103/PhysRevLett.119.112001.
3. Agaev S. S., Azizi K., Sundu H., *"Heavy four-quark mesons [bC̄][b̄c]: Scalar particle"*, Phys. Lett. B 858, 139042 (2024). DOI: 10.1016/j.physletb.2024.139042.
4. K.-F. Chen, W.-S. Hou, M. Shapkin et al. (Belle Collaboration), *"Observation of Anomalous γ(1S)π+ π− and γ(2S)π+π−(2S) production near the γ(5S) Resonance"*, Phys. Rev. Lett .100 112001 (2008). DOI:10.1103/PhysRevL ett.100.112001.
5. Choi S-K, Olsen SL, Abe K, Abe T, et al. (Belle Collaboration), *"Observation of a Narrow Charmon -unlike State in Exclusive $B^\pm \to K^\pm \pi^+ \pi - J/\psi$ Decay"*, Phys. Rev. Lett. 91, 262001 (2003). DOI: 10.1103/PhysRevLett.91.262001.
6. Choi S-K, Olsen SL, Adachi I, Aihara H, Aulchenko V, et al. (Belle Collaboration), *"Observation of a Resonance-like Structure in the $\pi^+\pi^-\psi'$ Mass Distribution in Exclusive $B \to K\pi^+\pi^-\psi'$ Decays"*, Phys. Rev. Lett. 100, 142001 (2008). DOI: 10.1103/PhysRevLett.100.14200.
7. Coan TE, Gao YS, Liu F, Artuso M, Blusk S, Butt J, et al. (CLEO Collaboration), *"Charmonium Decays of Y (4260), ψ (4160), and ψ (4040)"*, Phys. Rev. Lett. 96, 162003 (2006). DOI: 10.1103/PhysRevLett.96.162003.
8. Ansari A., Menapara C., Rai A. K., *"Singly charm baryons with higher-order\ (O(1\/m^2) \) corrections in hCQM: Revisited"*, Int. J. Mod. Phys. A 38, 2350108 (2023). DOI: 10.1142/S0217751X23501087.
9. Ansari, A., Menapara, C., and Rai, A. K., Int. J. Mod. Phys. A 39, 2499001 (2024). DOI:

10.1142/S0217751X2499001X.
10. Jakhad P, Oudichhya J, and Rai A.K, *"Masses of higher excited states of Ξc′ and Ωc baryons"*, Int. J. Mod. Phys. A 39, 2443005 (2024). DOI: 10.1142/S0217751X2443005X.
11. Jakhad P, Oudichhya J, AK Rai, *"Masses of higher excited states of Ξc′ and Ωc baryons"*, Int. J. Mod. Phys. A 39, 28, 2443005 (2024). DOI: 10.1142/S0217751X2443005X.
12. Kakadiya A., Menapara C., and Rai A.K, *"Mass spectroscopy and decay properties of Ξcb, Ξbb baryons"*, Int. J. Mod. Phys. A 38, 2341003 (2023). DOI: 10.1142/S0217751X23410038.
13. Kakadiya A., Shah Z., and Rai A. K., *"Mass spectra and decay properties of singly heavy bottom-strange baryons"*, Int. J. Mod. Phys. A 37, 2250053 (2022). DOI: 10.1142/S0217751X22500531.
14. Menapara C. and Rai A. K., *"Spectroscopy of light baryons: Δ resonances"*, Int. J. Mod. Phys. A 37, 2250177 (2022). DOI: 10.1142/S0217751X22501779.
15. Menapara C. and Rai A. K., *"Mass spectra of singly, doubly, triply light-strange baryons in light of $\mathcal{O}(1m^2)$ relativistic correction"*, Int. J. Mod. Phys. A 38, 2350053 (2023). DOI: 10.1142/S0217751X23500537.
16. Menapara C. and Rai A.K., *"Hadron Spectroscopy : Light, Strange Baryons"*, Few Body Syst. 65, 63 (2024). DOI: 10.1007/s00601-024-01933-1.
17. Kher V., Devlani N., and Rai A.K., *"Spectroscopy, Decay properties and Regge trajectories of the \(B \) and \(B_s \) mesons"*, Chin. Phys. C 41, 093101 (2017). DOI: 10.1088/1674-1137/41/9/093101.
18. Kher V., Devlani N., and Rai A. K. , *"Excited state mass spectra, Decay properties and Regge trajectories of charm and charm-strange mesons"*, Chin. Phys. C 41, 073101 (2017). DOI: 10.1088/1674-1137/41/7/073101.
19. Rai A. K , P. C. V., and Pandya J. N., *"Decay rates of quarkonia and potential models"*, J. Phys. G 31, 1453-1464 (2005). DOI: 10.1088/0954-3899/31/12/007.
20. Rai A. K., Pandya J. N., and P. C. V. *"Multiquark states as di-hadronic molecules"*, Nucl. Phys. A 782, 406-409 (2007). DOI: 10.1016/j.nuclphysa.2006.10.023.
21. Oudichhya J., Gandhi K., Rai A.K, *"Kaon and strangeonium spectrum in Regge phenomenology"*, Phys. Rev. D 108, 1, 014034 (2023). DOI: 10.1103/PhysRevD.108.014034.
22. Shah Z., Kakadiya A., and Rai A. K, *"Spectra of Triply $(\Omega_c cb)$ and $(\Omega_b bc)$ Baryons"*, Few Body Syst. 64, 40 (2023). DOI: 10.1007/s00601-023-01817-w.
23. Shah Z. and Rai A. K., *"Masses and Regge trajectories of triply heavy \(Ω_ccc \) and \(Ω_bbb \) baryons"*, Eur. Phys. J. A 53, 195 (2017). DOI: 10.1140/epja/i2017-12386-2.
24. Lodha C., Oudichhya J., Tiwari R., and Rai A. K. , *"All Charm Tetraquark Spectra in Coulombic Plus Quadratic Potential"*, J. Condens. Matter 1, 105-109 (2023). DOI: 10.61343/jcm.v1i02.23.
25. Lodha C., Rai A.K., *"Exploring strangeonium meson and all strange tetraquark candidates through mass spectra and decay properties"*, Eur. Phys. J. Plus 139, 7, 663 (2024). DOI: 10.1140/epjp/s13360-024-05461-z.
26. Lodha C. and Rai A. K., *"Investigation of Mass and Decay Characteristics of the All-light Tetraquark"*, Few Body Syst. 65, 99 (2024). DOI: 10.1007/s00601-024-01968-4.
27. Lodha, C., Rai, A.K., "Investigation of Mass and Decay Characteristics of the Light-Strange Tetraquark", *Indian J Phys* (2025). DOI: 10.1007/s12648-024-03524-6.
28. Tiwari R, Rai AK, *"Mass-Spectroscopy of Hidden Charm and Hidden Strange Tetraquarks in Diquark-Antidiquark Approach"*, Few Body Syst. 64, no.2, 20 (2023). DOI: 10.1007/s00601-023-01805-0.
29. Tiwari R, Oudichhya J, Rai A K, *"Mass-spectra of light-heavy tetraquarks"*, Int. J. Mod. Phys. A 38, no.33n34, 2341007 (2023). DOI: 10.1142/S0217751X23410075.
30. Yang, G., Ping, J., and Segovia, J., *"Fully charm and bottom pentaquarks in a lattice-QCD inspired quark model"*, Phys. Rev. D 106, 014005 (2022). DOI: 10.1103/PhysRevD.106.014005.
31. Wang B, Meng L, Zhu SL, *"Molecular tetraquarks and pentaquarks in chiral effective field theory"*, Nucl. Part. Phys. Proc. 324-329, 45-48 (2023). DOI: 10.1016/j.nuclphysbps.2023.01.0 10.
32. Radhakrishnan A, Padmanath M, Mathur N, *"Isoscalar axial-vector bottom-charm tetraquarks from QCD"*, Nuovo Cim. C 47, no.4, 168 (2024). DOI: 10.1393/ncc/i2024-24168-x.
33. Huang H, Deng C, Liu X, Tan Y, Ping J, *"Tetraquarks and Pentaquarks from Quark Model Perspective"*, Symmetry 15, no.7, 1298 (2023). DOI: 10.3390/sym15071298.
34. Entem DR, Machleidt R, Nosyk Y, *"High-quality two-nucleon potentials up to fifth order of the chiral expansion"*, Phys. Rev. C 96, no.2, 024004 (2017). DOI: 10.1103/PhysRevC.96.024004.
35. Weinberg S, *"Evidence That the Deuteron Is Not an Elementary Particle"*, Phys. Rev. 137, no.3B, B672-B678 (1965). DOI: 10.1103/PhysRev.137.B672.

36. Machleidt R, *"High-Precision, Charge-Dependent Bonn Nucleon-Nucleon Potential"*, Phys. Rev. C 63, 024001 (2001). DOI: 10.1103/PhysRevC.63.024001.
37. Workman RL et al. (Particle Data Group), *"Review of Particle Physics"*, PTEP 2022, 083C01 (2022). DOI: 10.1093/ptep/ptac097.
38. Workman, R. L., and Particle Data Group, *"Review of Particle Physics"*, Prog. Theor. Exp. Phys. 2022, 083C01 (2022). DOI: 10.109 3/ptep /pt ac097.
39. Singh, B., et al. [PANDA], *"Feasibility studies of time-like proton electromagnetic form factors at PANDA at FAIR"*, Eur. Phys. J. A 52, no. 10, 325 (2016). DOI: 10.1140/epja/i2016-16325-5.
40. PANDA Collaboration, *"Physics Performance Report for PANDA: Strong Interaction Studies with Antiprotons"*, arXiv:0903.3905 [hep-ex] (2009). DOI: 10.48550/arXiv.0903.3905.
41. Singh, B., et al. [PANDA], *"Experimental access to Transition Distribution Amplitudes with the PANDA experiment at FAIR"*, Eur. Phys. J. A 51, 107 (2015). DOI: 10.1140/epja/i2015-15107-y.
42. Lange, S., Galuska, M., Reiter, S., Prencipe, E., and Spataro, S. *"New Studies of XYZ States at PANDA"*, arXiv preprint arXiv:1311.7597 (2013). DOI: 10.48550/arXiv.1311.7597.
43. PANDA Collaboration, *"Physics Performance Report for PANDA: Strong Interaction Studies with Antiprotons"*, arXiv:0903.3905 [hep-ex] (2009). DOI: 10.48550/arXiv.0903.3905.
44. PANDA Collaboration. *"Hyperon Signatures in the PANDA Experiment at FAIR",* arXiv preprint arXiv:2304.11977 (2023). DOI: 10.48550/arXiv.2304.11977.

Structural Characterization, Raman Spectroscopy and FTIR Spectroscopy Studies of Pr^{3+} Doped Tellurium Bismuth Borate Glasses

Pawan Kumar[a], S S Meena[b], Menka Meena, Nitiksha Sharma, Beena Bhatia

Department of Physics, Jai Narain Vyas University, Jodhpur, Rajasthan, India.

[a] pawankumar26174@gmail.com
[b] ssmeenaphy12@gmail.com

Abstract

A set of composition-based undoped and Pr^{3+}-doped Tellurium Bismuth Borate glasses $20TeO_2$: (30-X)Bi_2O_3: $50B_2O_3$: XPr_2O_3 (where X= 0, 0.1, 0.3, 0.5, 0.7 mol%) have been fabricated via standard melt quenching technique. All of the manufactured glasses were made of completely amorphous material, according to X-ray diffraction (XRD) patterns. The refractive index, density, optical absorption, FTIR and Raman spectroscopy have been applied to investigate the structural and optical properties. FTIR spectral measurements have been utilized to identify the network vibration of Pr_2O_3 doped Tellurium glasses. FTIR reveals symmetrical stretching vibrations of Te-O in TeO_4 as well as B-O stretching (BO_3) units. Signals in the FTIR mainly observed around 1032 cm^{-1},1180 cm^{-1}, 1349 cm^{-1}, 1395 cm^{-1} and 1501 cm^{-1} while Raman scattering peaks are located at 436 cm^{-1}, 542 cm^{-1}, 770 cm^{-1}, 940 cm^{-1}, 1028 cm^{-1}, 1232 cm^{-1} and 1361 cm^{-1}. Both reflective index and density increases with increasing rare earth ion concentration.

Keywords: Tellurium Glasses, FTIR Spectroscopy, Raman Scattering and Optical Absorption.
Received 29 January 2025; First Review 07 February 2025; Accepted 19 March 2025.

*** Address of correspondence**
Pawan Kumar
Research Scholar: Department of Physics, Jai Narain Vyas University, Jodhpur, Rajasthan, India.

Email: pawankumar26174@gmail.com

How to cite this article
Pawan Kumar, S S Meena, Menka Meena, Nitiksha Sharma, Beena Bhatia, Structural Characterization, Raman Spectroscopy and FTIR Spectroscopy Studies of Pr^{3+} Doped Tellurium Bismuth Borate Glasses, J. Cond. Matt. 2025; 03 (01): 103-105.
Available from:
https://doi.org/10.61343/jcm.v3i01.93

Introduction

Since they are optical glasses containing Pr^{3+} ions, they are useful as photonic materials in various technologies due to their broad absorption in the visible-near infrared region [1]. Commercially available GaN diode lasers provide good utilization due to their broadness and absorption at 443 nm, which corresponds to the energy of the Pr^{3+} ion $^3H_4$ - $^3P_2$ [3]. Telluride networks consist mainly of TeO_3 trigonal pyramidal (Tp) units with long electron pairs and TeO_4 trigonal bipyramidal (Tbp) units. Add iron oxides, alkali metals and alkaline earth metals to convert Tbp units to Tp units. Raman spectroscopy and infrared (IR) spectroscopy are the two most important vibrational non-invasive tools in many fields such as biology, geology, materials science and recently space exploration [4]. Combined Raman-infrared spectroscopy can be used to analyze various important properties including phonons, aggregation state and energy of functional groups of the crystal lattice. Therefore, the properties of the material have a direct effect on the Raman spectroscopy parameters (band frequency, intensity, band shape and full width at half maximum or FWHM). These constraints are: (1) Orientation of the crystal lattice or molecules; (5) Inconsistencies and stresses in the material (due to mechanical, thermal or acoustic effects) [5].

FTIR spectra recorded in the 1000–1600 cm^{-1} region for Pr^{3+}-doped alkali and mixed-alkali heavy metal borate glass matrices. In general, the vibrational modes of the borate glass network consist of three important band regions. The first group of bands, which occur at 1200–1600 cm^{-1} is due to the asymmetric stretching vibration of B -O bonds in BO_3 units. Therefore, the aim of this study is the spectral and fluorescence analysis of Pr^{3+} telluride bismuth borate glass for optical devices.

Method

In the tellurite bismuth borate glass system $20TeO_2$ was doped with Pr^{3+} ions as follows: (30-x) Using the solution quenching process, $20TeO_2$: (30-x)Bi_2O_3: $50B_2O_3$: XPr_2O_3 (where x = 0, 0.1, 0.3, 0.5 and 0.7 Mol%) was prepared. Chemical reagents, particularly TeO_2, Bi_2O_3, B_2O_3 and Pr_2O_3 were used in this study. Mix well using an agate mortar and pestle. After the lamb is melted in an electric

muffle furnace at 950 °C for two hours and completely melted, it is quickly poured into a preheated stainless-steel mold. The mold is placed at 350 °C for two hours to eliminate thermal stress and tension. These models are always polished with a fine cerium oxide powder.

Table 1: Chemical Composition of Pr^{3+} doped TEBIB Glasses.

Glass System	Glass Composition
TEBIB (Pr0)	20TeO2:30Bi2O3:50B2O3
TEBIB (Pr0.1)	20TeO2:29.9Bi2O3:50B2O3:0.1Pr2O3
TEBIB (Pr0.3)	20TeO2:29.7Bi2O3:50B2O3:0.3Pr2O3
TEBIB (Pr0.5)	20TeO2:29.5Bi2O3:50B2O3:0.5Pr2O3
TEBIB (Pr0.7)	20TeO2:29.3Bi2O3:50B2O3:0.7Pr2O3

Result and Discussion

All of the manufactured glasses were made of completely amorphous in nature, according to X-ray diffraction (XRD) patterns. From the figure 2 and 3 it is clear that reflective index and Density of the samples increase with increases in rare earth ion concentration respectively. From the FTIR spectra peaks are available in the range from 1000 cm^{-1} to 1600 cm^{-1} that reveals symmetrical stretching vibrations of Te-O in TeO_4 as well as B-O stretching (BO_3) units. The prominent feature in most synthetic tellurium borate glasses Raman spectra are intensive bands in the 400 – 1400 cm- region due to symmetric stretching motions of Te-O in TeO_4 as well as B-O stretching (BO_3) units.

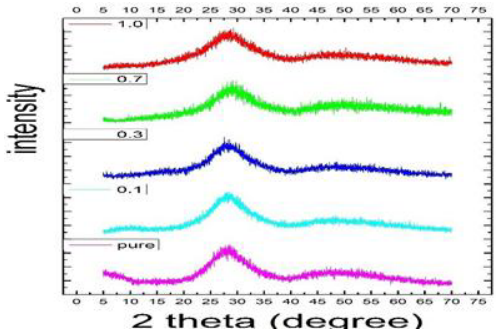

Figure1: X-ray diffraction pattern of Pr^{3+} doped TEBIB Glasses.

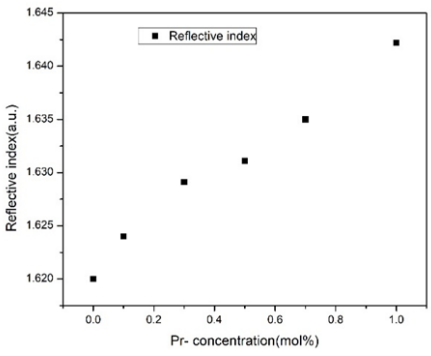

Figure 2: Reflective index v/s Pr- concentration (mol%) of Pr^{3+} doped TEBIB Glasses.

Table 2: Physical properties of Pr^{3+} doped TEBIB Glasses.

Properties	TEBIB	TEBIB0.1Pr	TEBIB0.3Pr	TEBIB0.5Pr	TEBIB0.7Pr	TEBIB1.0Pr
Reflective index(n)	1.6200	1.6240	1.6291	1.6311	1.6350	1.6422
Density(gm/cm^3)	3.10021	3.2410	3.2641	3.3320	3.3785	3.4413

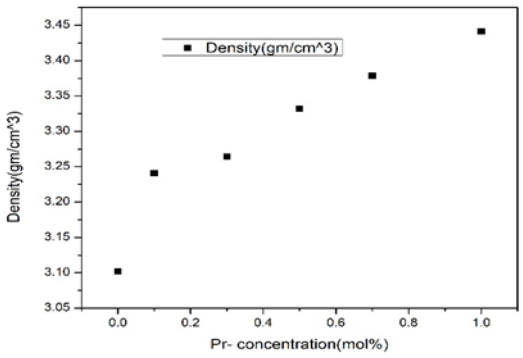

Figure 3: Density v/s Pr- concentration (mol%) of Pr^{3+} doped TEBIB Glasses.

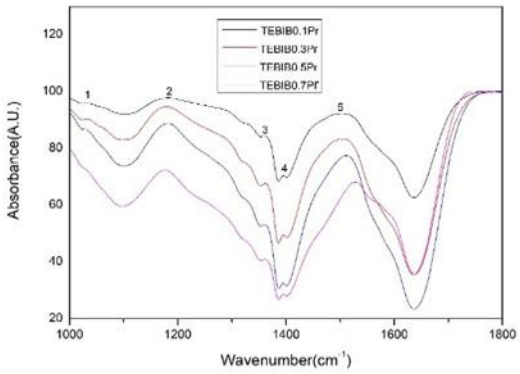

Figure 4: FTIR Spectra of Pr^{3+} doped TEBIB Glasses.

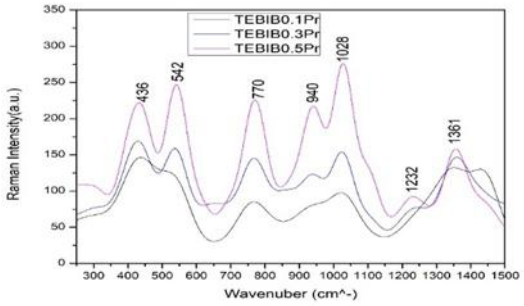

Figure 5: Raman Spectra of Pr^{3+} doped TEBIB Glasses.

Conclusion and Future Prospective

For a bismuth telluride borate glass sheet Pr_2O_3 with the composition of $20TeO_2$:(30-X), undoped and Pr^{3+}-doped Bi_2O_3:$50B_2O_3$:(X), use the usual melt quenching process to produce it (where X = 0, 0.1, 0.3, 0.5 and 0.7 mol%

vibration of Pr_2O_3-doped tellurium). The glass was characterized by FTIR spectroscopy. FTIR shows the symmetric stretching vibrations of Te-O and B-O stretching (BO_3) units. Although Raman scattering peaks appear around 446 cm^{-1}, 542 cm^{-1}, 770 cm^{-1}, 940 cm^{-1}, 1028 cm^{-1}, 1232 cm^{-1} and 1361 cm^{-1}, the FTIR signal usually appears at 1032 cm^{-1}, 1180 cm^{-1}, 1349 cm^{-1}, 1395 cm^{-1} and 1501 cm^{-1}. Both reflective index and density increases with increasing rare earth ion concentration.

References

1. Pisarska, M. Kowal, M. Kochanowicz, J. Zmojda, Optic Express 24 (2016) 2427 243.
2. Q. J. Chen Wenjie, Zhang, XY, Huang, G. P. My husband is tivthaiv. 513 (2012) 139-144.
3. Okamoto, K. Kasuga, I. Hara, Y. Kubota, Optic Express 17 (2009) 20227-20232.
4. E. A. Lalla, M. Aznar, M. Constantinidis, Polarized Raman Analysi ntawm (RE^{3+}) - Folded Florotellurite Glasses tiab Ceramics, Vibration Spectrum. 103 (2019) 102934.
5. Cantarero, Applications of Raman Scattering in Materials Science, Procedia Mater. education. 9 (2015) 113-122.

Effect of Ge Additive on the Morphological and Physical Properties of $Se_{100-x}Ge_x$ (x = 0, 1, 2, 4, 6, 10, 15 and 20) Chalcogenide System

Anjali[1,a], Balbir Singh Patial[2,b], Vaishnav Kiran[1,c] and Nagesh Thakur[2,d]

[1] *School of Basic and Applied Sciences, Himachal Pradesh Technical University, Hamirpur-177001, H.P., India.*
[2] *Department of Physics, Himachal Pradesh University Summer Hill Shimla-171005, H.P. India.*

[a] atshpu12@gmail.com
[b] bspatial@gmail.com
[c] vaishnav.rana5@gmail.com
[d] ntb668@yahoo.co.in

Abstract

Ge additive chalcogenide materials have become more prevalent in contemporary optoelectronics. The present study utilizes the melt-quenching process for preparing Se-Ge chalcogenide glasses. For the examined system, submicron structural and physical characteristics are examined and described. X-ray diffraction spectra show no characteristic peaks, this indicates that the glassy compositions under investigation are amorphous. A further confirmation of the amorphous nature is provided by SEM. The physical properties of the compositions under examination namely cross-linking density (X), average coordination number (<r>), lone-pair electrons (L), mean bond energy (<E>), constraints (Nc), fraction of floppy modes (f), cohesive-energy (CE), glass transition temperature (T_g), electro-negativity (χ) as well as heat of atomization (H_s) have been deduced in regard to the influence of Ge content. Cohesive-energy is computed using CBA, while mean bond energy is obtained by chemical-bond ordering approach. Shimakawa's relationship was utilized to theoretically compute band gap of the system under investigation. Average single-bond energy, electro-negativity and cohesive-energy were used to analyse the results. A relationship between the mean coordination number and a variety of inferred physical characteristics is established.

Keywords: XRD, SEM, Chalcogenide Glasses, Average Coordination Number, Band Gap, Cohesive-energy, Mean Bond Energy.
Received 29 January 2025; First Review 19 March 2025; Accepted 19 March 2025.

*** Address of correspondence**
Balbir Singh Patial
Department of Physics, Himachal Pradesh University Summer Hill Shimla-171005, H.P. India.

Email: bspatial@gmail.com

How to cite this article
Anjali, Balbir Singh Patial, Vaishnav Kiran and Nagesh Thakur, Effect of Ge Additive on the Morphological and Physical Properties of $Se_{100-x}Ge_x$ (x = 0, 1, 2, 4, 6, 10, 15 and 20) Chalcogenide System, J. Cond. Matt. 2025; 03 (01): 106-111.
Available from:
https://doi.org/10.61343/jcm.v3i01.95

Introduction

Glasses and other amorphous materials have a long history that predates nearly all human civilizations. These materials were utilised in pottery and as decoration supplies. Numerous attempts were undertaken at various times in time to explore the specific characteristics of these materials. On the basis of the absence of long-range order these materials were believed to be non-semiconductors [1]. Without the standardization of different techniques, the results obtained by different research groups happed to be quite divergent [2]. These factors prohibited the development and the proper understanding in this field. During fifteens and sixteen's this field again attracted the interest of researchers due to the groundbreaking work in the experimental sector [3]. Since then, this field has become the central field of research. This field is now acknowledged as being technologically sensitive. These materials have been found to have a number of remarkable characteristics, including switching, photoconductive, memory retention and semiconducting qualities [2-4]. Chalcogenide glasses have potential and current applications in infrared (IR) lasers, photonic crystals, transistors, optical memories, and IR transmitting optical fibres because of their thermal and optical properties, that depend on composition [5-6]. Chalcogenide materials are being developed for rewritable optical memory [7]. It is necessary to have precise understanding of these materials' optical constants across a broad spectrum in order to effectively use them in reflecting coatings and optical fibres. The electrical, electronic band and atomic structures of these material's influence optical characteristics [8]. Because of its commercial application and technological significance, Se-based glasses remain quite popular among

all chalcogenide system. These glasses are appealing because of their special ability to undergo reversible transformation, which has numerous device applications [9].

Even though Se is excellent for glass forming, it has drawbacks including a short lifespan and low sensitivity [10]. Alloying Se with impurity atoms like Te, Ge, Ga, and as may resolve these issues [11]. When Ge replace Se, Se_8 ring structure is broken, the chain fraction is marginally increased, but chain length decreased [12]. Since Ge improves stability, optical qualities, corrosion resistance, xerography, and the chemical durability of chalcogenide glassy semiconductors, we have chosen Ge to add in Se glasses [12]. Ge-doped glasses are emerged as a desirable material for basic studies of their structure and characteristics. Alterations in composition result in short-range order alterations, which are useful for modifying glassy materials' features to fulfil particular needs [13]. Additionally, assessing physical factors helps identify the system's greatest features and can more accurately predict a glass system's stability, which facilitates problem identification and resolution prior to experimentation.

This study examines the submicron structural characteristics and general physical characteristics of Ge doped $Se_{100-x}Ge_x$ (x = 0, 1, 2, 4, 6, 10, 15 and 20 at. wt.%) chalcogenide alloys prime using the melt-quench method. The amorphous nature of the composition under examination and its surface appearance is examined via the XRD and SEM methodology. A relationship between the mean coordination number and a variety of inferred physical characteristics is established.

Experimental Details

The process of melt quenching is utilised to prime bulk samples of $Se_{100-x}Ge_x$ (x = 0, 1, 2, 4, 6, 10, 15 and 20 at. wt.%). After being weighed based on their atomic percentages, at a vacuum of around ~ 2×10^{-5} mbar, 5N extremely pure materials (99.999%) are sealed in a quartz ampoule that is about 12 mm in diameter and 5 cm long. A furnace is used to elevate the temperature of the sealed ampoules to 900 °C at pace of 3-4 °C per minute. For 24 hours at maximum temperature, ampoules are rocked repeatedly to ensure a uniform melt. Rapid quenching is carried out in the ice-cooled water to avoid crystallisation. Then ingots of glassy materials have been removed by breaking the ampoules. A fine powder is made by grinding these ingots. Structural analysis is done at room temperature using the PANalytical X′Pert x-ray diffractometer source, which is equipped with a Ni filtered using Cu Kα (λ = 1.54056) radiation as X-Ray, to take the x-ray diffraction pattern of the examined samples at room temperature in the range 10°<2θ<90° at a scanning rate of 1°/min. Figure 1 shows XRD spectra of the $Se_{96}Ge_4$ chalcogenide alloy under investigation. The lack of identifiable, sharp peaks in the x-ray diffraction spectra indicates that the chalcogenide alloy under investigation is amorphous. For other samples, similar outcomes are realised. Surface morphology and amorphous nature of examined system is further analysed by SEM (QUANTA FEG 250) operating at accelerating voltage of 15 kV; which indicates good consistency with XRD outcome. The scanned images of the $Se_{96}Ge_4$ chalcogenide alloy are displayed in Figure 2. Amorphous character of primed chalcogenide alloy is indicated by SEM micrographs, which clearly illustrate phase separation in the scanned area of the material due to inhomogeneity in the sample. Other samples yield similar results.

Results and Discussion

Average Coordination Number and Constraints

The average coordination number was first used with binary alloys by Phillips and developed it to characterize characteristics of covalent chains forming glasses. The formula mentioned below is used to obtain <r> for the compound Se_{100-x} Ge_x (x = 0, 1, 2, 4, 6, 10, 15 and 20).

$$<r> = \frac{\alpha N_{Se} + \beta N_{Ge}}{\alpha + \beta} \qquad (1)$$

Where α, β, are respective at. wt. % of Se, Ge as well as N_{Se}, N_{Ge} denote their corresponding coordination numbers. Table 1 provides the <r> computed values. The <r> was found to be in the range of 2 <r> 2.04 (Table 1), indicating that <r> rises as Ge content rises. It demonstrates that as the Ge content rises, chains between the atoms are becoming more cross-linked.

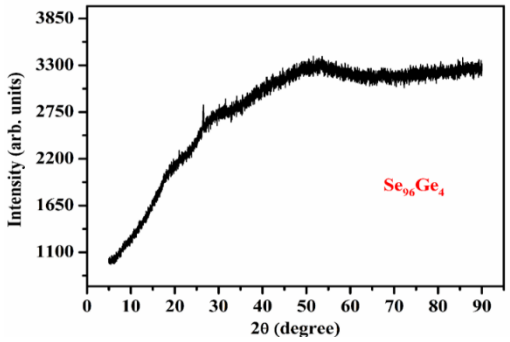

Figure 1: XRD patterns of $Se_{96}Ge_4$ Chalcogenide system.

Phillips, Thorpe along with Tanaka established topological limits 2.4 and 2.67, which are commonly recognised as mechanical as well as chemical thresholds, in context of constraint theories. Glasses of chalcogenides with <r> = 2.4 are under constrained or weakly connected, whereas those with <r> = 2.67 are over constrained or strongly

Table 1: Values of <*r*>, N_α, N_β, N_c, X and floppy modes (f) for amorphous $Se_{100-x}Ge_x$ (x = 0, 1,2,4,6,10,15 and 20 at. wt. %).

Composition	*<r>*	N_α	N_β	N_c	*f*	*X*
Se_{100}	2.00	1.00	1.00	2.00	0.333	0.00
$Se_{99}Ge_1$	2.02	1.01	1.04	2.05	0.316	0.05
$Se_{98}Ge_2$	2.04	1.02	1.08	2.10	0.300	0.10
$Se_{96}Ge_4$	2.08	1.04	1.16	2.20	0.266	0.20
$Se_{94}Ge_6$	2.12	1.06	1.24	2.30	0.233	0.30
$Se_{90}Ge_{10}$	2.20	1.10	1.40	2.50	0.166	0.50
$Se_{85}Ge_{15}$	2.30	1.15	1.60	2.75	0.083	0.75
$Se_{80}Ge_{20}$	2.40	1.20	1.80	3.00	0.000	1.00

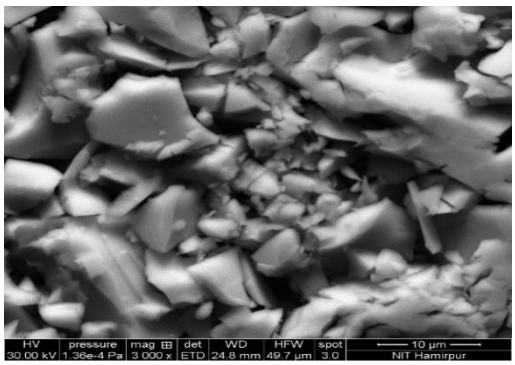

Figure 2: SEM Micrographs of $Se_{96}Ge_4$ chalcogenide alloy.

coupled [53]. The structural transforming a two-dimensional network into a three-dimensional one at the chemical threshold of <*r*> = 2.67. Stiffness percolation limit, for which <*r*> = 2.4 has been projected to be the greatest inclination for glass formation. There are two restrictions for mechanical constraints. Bond stretching constraints per atom are denoted by N_α = <*r*>/2 while Bond bending constraints per atom on a network are denoted by N_β = 2<*r*> - 3. Angular and radial stresses, respectively, cause N_β and N_α to emerge in covalently bonded glasses. Consequently, average of N_α and N_β equals the total number of mechanical constraints per atom (N_c), which is $N_c = N_\alpha + N_\beta$.

According to M. F. Thorpe [54], standard modes of vibration at zero frequency or "floppy modes" make up a finite proportion of uncoordinated networks, which can be computed using the following relationship:

$$f = 2 - \frac{5}{6}\langle r\rangle \qquad (2)$$

The density of cross-linking is determined using [57]:

$$X = N_c - 2 \qquad (3)$$

Table 1 lists determined outcomes for N_c, f along with X as well as plotted in Figure 3. Figure 3 yields the conclusion that value of N_c and X rise as Ge content rises. The ideal circumstance for glass production, as stated by Phillips & Thorpe [54], is when N_c equals degree of freedom N_c or $N_c = N_d = 3$. $N_c \rightarrow 3$ with Ge content increases shows that degree of freedom available to the atoms in network stabilizes number of constraints Nc in network. Additionally, the value of f –› 0 appears (Table 1). It shows a phase shift from floppy to rigid, and as a result the system becomes increasingly rigid; indicating a stronger propensity for glassmaking in the studied system.

Glass Forming Ability and Lone Pair Electrons

The valence band contains a single pair of electrons (L), which is a non-bonding pair of electrons. If there is a sufficient amount of L in the chalcogenide system, vitreous state is stable. Given that non-bonding electrons can establish chemical bonds, these bonds are naturally flexible [55]. Therefore, by eliminating strain tension from the system, lone-pair electron occurrence promotes the creation of glass. The following relation was put forth by Phillips [56–57] to calculate L in a semiconducting chalcogenide system:

$$L = V - \langle r\rangle \qquad (4)$$

where valance electrons are indicated by V. In order to assess the glass-forming ability of chalcogenide glasses, Zhenhua [56] proposed a straightforward criterion that states that L should be more than 2.6 for binary systems and greater than 1 for ternary systems. Table 2 lists the computed values of L and Figure 4 illustrates how they vary with the Ge additive. It illustrates how the Ge content causes L to decrease. The interaction between the lone pair electrons of the bridging Se atom and the Ge ion can be used to explain the decrease in L. L reduced as a result of this systemic interaction. Since values of L for the system under investigation are found to be more than three, the composition in question has a good propensity to form glass.

Deviation from Stoichiometry, Mean Bond Energy and Glass Transition Temperature

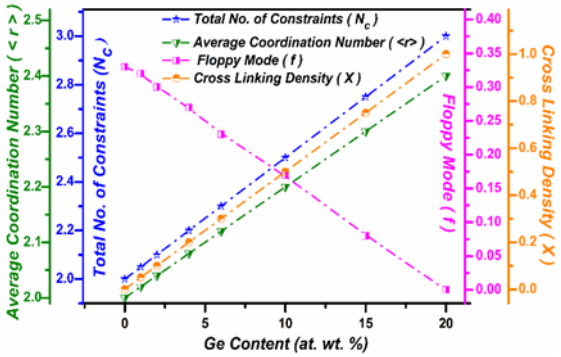

Figure 3: Values of average coordination number (<*r*>), bond bending constraints (N_α), bond stretching constraints(N_β), total number of constraints (N_c), cross-linking density (X) and floppy modes (f) for amorphous $Se_{100-x}Ge_x$ (x = 0, 1,2,4,6,10,15 and 20 at. wt. %) chalcogenide system.

R is a quantity that represents deviation from stoichiometry and is defined as ratio of chalcogen atoms covalent bonding assumptions to those of non-chalcogen atoms [56]. Only hetero-polar bonds can form at threshold, R = 1. If R > 1; composition is considered chalcogenide rich. If R < 1; the composition is deemed chalcogen deficient. The following relationship is used to determine R:

$$R = \frac{\alpha \times r_{Se}}{\beta \times r_{Ge}} \quad (5)$$

Plotting the calculated values of R in Figure 4 (Table 2) reveals that R >1 for the composition under investigation. Therefore, it seems that the system being studied is rich in chalcogen. Glassy system features are directly linked to overall and depend on bond energy, average coordination number, degree of cross linking and bond type. Using the correlation provided by Tichy, evaluated for composition under examination [57]:

$$\langle E \rangle = E_{cl} + E_{rm} \quad (6)$$

where E_{rm} represents contribution from weaker bonds that have maximised contribution from strong bonds and E_{cl} indicates overall participation to bond energy caused by strong hetero-polar bonds.

$$E_{cl} = P_r D_{hb} \quad (7)$$

P_r stands for degree of cross linking and D_{hb} for average energy of a hetero-polar bond. Table 2 summaries estimated values of <E> and shows that <E> rises as Ge is added. The system's bond energy increases when Ge substitutes Ge-Se heteropolar bonds (49.44 kcal/mol) for Se-Se homopolar bonds (44 kcal/mol) in the system under investigation [58].

A transition occurs at the glass transition temperature (T_g) and below T_g, a supercooled liquid turns into a glass. It follows that cohesive forces within material should be overcome in order to permit atomic movement and that their size is proportional to T_g. A lot of focus is placed on predicting T_g in chalcogenide glasses, which is correlated with <E>, which indicates both cohesive forces and material stiffness.

Tichy and Ticha have been linked to T_g with and the [60]. They provided following correlation between T_g and <E> and were regarded as covalent bond approach for chalcogenide systems:

$$T_g = 311[\langle E \rangle - 0.9] \quad (8)$$

Figure 4 shows rise in T_g with increase in Ge concentration and values of T_g derived from Tichy-Ticha are listed (Table 2). T_g increases when Ge substitutes Ge-Se heteropolar bonds (49.44 kcal/mol) for Se-Se homopolar bonds (44 kcal/mol) in system under investigation [58].

"Average Heat of Atomization, Average Single Bond Energy and Theoretical Band Gap"

Average heat of atomization ($\overline{H}_s$) is a metric that indicates relative bond strength of material. When all of the atoms in a chemical substance (either an element or a compound) are completely separated, it symbolizes a change in heat [56]. The average non-polar bond energy of the two atoms is related to the sum of the heat of formation (ΔH) and the average heats of atomization (H_s^A and H_s^B, respectively) for binary semiconductors made up of A and B atoms at standard pressure and temperature, according to Pauling [61]:

$$H_s(A-B) = \Delta H + \frac{1}{2}[H_s^A + H_s^B] \quad (9)$$

The square of the difference in the electro-negativity χ_A and χ_B of two atoms is associated with the ΔH term.

$$\Delta H \propto (\chi_A - \chi_B)^2 \quad (10)$$

For higher order semiconducting systems, this relation might be extended. $\overline{H}_s$ (kJ/mol) is a direct measure of cohesive-energy that may be represented as follows for a quaternary system $Se_\alpha Ge_\beta$:

$$\overline{H_S} = \frac{\alpha H_S^{Se} + \beta H_S^{Ge}}{\alpha+\beta} \quad (11)$$

Here H_s (Se) = 227 kJ/mol and H_s (Ge) = 377 kJ/mol [56,58,62]. Table 3 tabulates the obtained values of $\overline{H}_s$ and $\overline{H}_s$ /<r>. Figure 5 shows the change in $\overline{H}_s$ /<r> with Ge. The binding strength is shown by $\overline{H}_s$ /<r>. As the concentration of Ge increases, it is evident from Figure 5 and Table 3 that $\overline{H}_s$ /<r> decreases at the same time. The substitution of Ge-Se bonds (bond energies 49.44 kcal/mol) for Se-Se bonds (bond energies 44 kcal/mol) may be the cause of decrease in $\overline{H}_s$ /<r> [56,58].

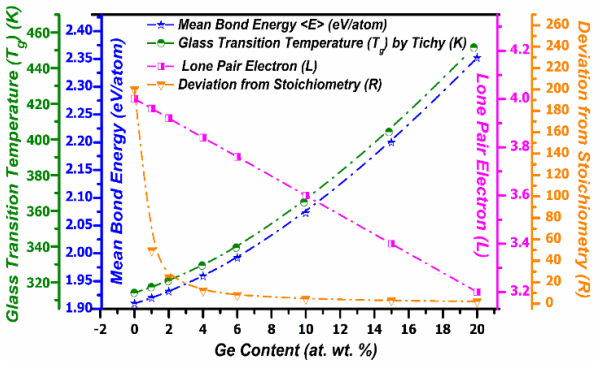

Figure 4: Variations of lone pair electron (L), R, <E> and T_g (K) for examined chalcogenide system.

Table 2: Values of *L*, *R*, <*E*> and T_g (K) for examined chalcogenide system.

Composition	*L=V-<r>*	*R*	*<E> eV/atom*	*T_g(K) by Tichy*
Se_{100}	4.00	200	1.91	314.02
$Se_{99}Ge_1$	3.96	49.5	1.92	317.16
$Se_{98}Ge_2$	3.92	24.5	1.93	320.77
$Se_{96}Ge_4$	3.84	12.0	1.96	329.32
$Se_{94}Ge_6$	3.76	7.83	1.99	339.33
$Se_{90}Ge_{10}$	3.60	4.50	2.07	364.75
$Se_{85}Ge_{15}$	3.40	2.83	2.20	404.19
$Se_{80}Ge_{20}$	3.20	2.00	2.35	451.47

Using Shimakawa correlation [14], the energy gap (E_g^{th}) for Se-Ge glassy composition is calculated theoretically and is as follows:

$$E_g^{th}(Se-Ge) = \alpha E_g(Se) + \beta E_g(Ge) \qquad (12)$$

where E_g (Se) = 1.95 eV and E_g (Ge) = 0.95 eV stand for the braced elements' energy gaps. The fluctuation of $\overline{H}_s$ /<*r*> with Ge content is shown in Figure 5. Ge addition is shown to reduce the energy gap in the studied Se-Ge system, which can be explained by a correlation between the energy gap and the system bond strength. With the addition of Ge, the energy gap (E_g^{th}) also reduces as $\overline{H}_s$ /<*r*> lowers. Moreover, the system's reducing E_g^{th} can be explained by the electro-negativity (χ) decreasing as Ge at. wt.% increases (Table 3). The anti-bonding band forms bottom of conduction band in a chalcogenide system, whereas lone pair of Se atoms forms top of valence band [63]. The lone pair energy decreases and the valence band shifts towards the energy gap when the electro-negativity of the Se atom (χ = 2.55) is substituted with that of the electronegative Ge atom (χ = 2.01) [64], which may result in a decrease in the energy band gap. With decreasing electro-negativity levels, Table 3 may make this clear.

Cohesive-energy and Electro-negativity

Cohesive-energy in a solid is defined as the energy needed to break every bond among its constituent atoms. Cohesive-energy is evaluated using chemical bond approach (CBA) [65]. The CBA model states that, unless the valence of the atoms is satisfied, hetero-polar bonds form more readily than homo-polar bonds and appears in a series of decreasing bond energies. Bond energies are also additive in nature. By summing the bond energies of each bond except in system under study, cohesive-energy is calculated as follows:

$$CE = \frac{\sum_i C_i D_i}{100} \qquad (13)$$

In this case, D_i represents energy of associated bonds, while C_i represents number predicted chemical bonds.

Table 3: Values of H_s/<*r*>, H_s), theoretical band gap (E_g^{th}), *CE* and χ for Se-Ge chalcogenide system.

Sample	*H_s*	*H_s/<r>*	*E_g^{th}*	*CE*	*χ*
Se_{100}	2.14	1.071	1.95	0.440	2.55
$Se_{99}Ge_1$	2.16	1.069	1.94	0.442	2.51
$Se_{98}Ge_2$	2.18	1.067	1.95	0.443	2.50
$Se_{96}Ge_4$	2.21	1.063	1.90	0.445	2.46
$Se_{94}Ge_6$	2.25	1.060	1.88	0.447	2.41
$Se_{90}Ge_{10}$	2.32	1.054	1.83	0.451	2.32
$Se_{85}Ge_{15}$	2.41	1.046	1.77	0.459	2.22
$Se_{80}Ge_{20}$	2.49	1.039	1.71	0.467	2.11

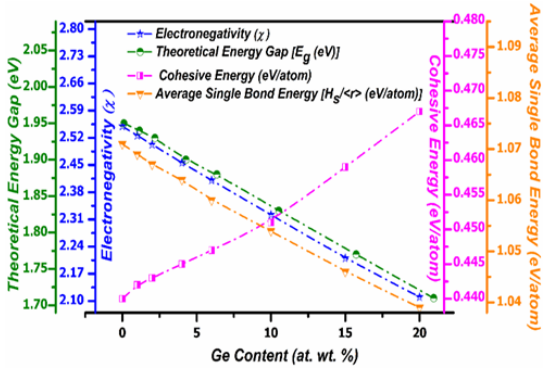

Figure 5: Variation of various physical parameters with Ge additive for Se-Ge chalcogenide system.

The examined composition's electro-negativity (χ) has been determined via Sanderson's technique [66].

The system's electro-negativity (χ) can be represented as the geometric mean of the electro-negativity of its component elements, in accordance with Sanderson's hypothesis [67]. The electro-negativity values for Se and Ge, respectively, are 2.55 and 2.01 on the Pauling scale [58]. Figure 5 (Table 3) illustrates how *CE* and χ change as Ge concentration rises. With content, it has been known that *CE* rises and χ declines [58, 61]. The decrease in energy gap can be explained by rise in *CE*. As a result, a fall in *CE* lowers the conduction band edge energy, which in turn lowers the band gap between bonding & anti-bonding orbitals. This results in a reduction of the optical energy gap [56].

Conclusions

This study examines the submicron structural characteristics and general physical characteristics of Ge-doped Se-Ge chalcogenide alloys prime through melt-quench method. X-ray diffraction pattern shows no characteristic peaks, this indicates that glassy compositions under investigation are amorphous. A further confirmation of the amorphous nature is provided by SEM. The inhomogeneity in the samples leads to phase separation in scanned area of SEM micrographs of material. Thus, SEM analysis is consistent with the XRD results. The impact of Ge content on the composition under investigation has been

investigated in theoretical predictions in relation to their physical characterisation using the following metrics: *f*, <*r*>, <*E*>, *X*, *L*, constraints (N_c), cohesive-energy (*CE*), electro-negativity (χ), *Hs* and T_g. Cohesive-energy is computed using CBA, while mean bond energy is obtained by chemical-bond ordering approach. Tichy-Ticha methods are used to estimate T_g. When Ge is added to the Se-Ge system, the <*r*>, N_c, *X*, <*E*>, *CE*, T_g and H_s are enhanced. However, it is discovered that the Ge content decreases *L*, *f*, *R*, χ and E_g^{th}. This is explained by the fact that as the Ge content increases, Se-Se homopolar bonds (44 kcal/mol) are replaced by Ge-Se heteropolar bonds (49.44 kcal/mol). Theoretically estimated T_g values utilising the Tichy-Ticha and Lankhorst techniques have been found to be congruent with experimental findings. Shimakawa's relationship was utilized to theoretically compute band gap of the system under investigation. Average single-bond energy, electro-negativity and cohesive-energy were used to analyse the results. A relationship between the mean coordination number and a variety of inferred physical characteristics is established.

References

1. M. Zemen. J. Non-Cryst. Solids, 4: 426, 1970.
2. A. H. Clark, Phys. Rev., 154: 750, 1967.
3. D. N. Payton and W. M. Visscher. Phys. Rev., 154: 802, 1967.
4. S. C. Moss and J. F. Graczyk. Phys. Rev. Lett., 23: 1167, 1969.
5. Sharma P and Katyal S C 2008 *Phil. Mag.* 88 2549.
6. Kumar K, Thakur N, Bhatt S S and Sharma P 2010 *Phil. Mag.* 90 3907.
7. Zhang X H, Guimond Y and Bellac Y 2003 *J. Non-Cryst.Solids* 519 326.
8. Shaaban E R 2008 *Phil. Mag.* 88 781.
9. Singh G, Sharma J, Thakur A, Goyal N, Saini G S S and Tripathi S K 2005 *J. Optoelectron. Adv. Mater.* 7 2069.
10. Anjali, Balbir Singh Patial and Nagesh Thakur Journal of Electronic Materials, 51 (2022) 1089-1096.
11. Anjali, Balbir Singh Patial, Surya Kant Tripathi and Nagesh Thakur Journal of Electronic Materials, 46 (2017) 1516-1524.
12. J. Sharma and S. Kumar. Journal of Non-Oxide Glasses, 1: 120-130, 2009.
13. Anjali, B. S. Patial and N. Thakur. Journal Of Asian Ceramic Societies, 8: 777-792, 2020.
14. Sharma N, Patial BS, Thakur N. Indian J Pure Appl Phys. 2018;56:128–135.
15. Thorpe MF. J Non Cryst Solids. 1983;57(3):355–370.
16. Phillips JC, Thorpe M., Solid State Commun. 985;53(8):699–702.
17. Saxena M, Kukreti AK, Gupta S, et al., Arch Appl Sci Res. 2012;4:994–1001.
18. Zhenhua L., J Non-Cryst Solids. 1991;127(3):298–305.
19. Ticha H, Tichy L, Rysava N, et al. J Non-Cryst Solid. 1985;74(1):37-46.
20. Tichy L, Ticha H, Mater Lett. 1994;21(3-4):313-319.
21. Pauling L. J Phys Chem. 1954;58(8):662–666.
22. Dahshan A, Aly KA. Philos Mag. 2008;88(3):361-372.
23. Sanderson RT., J Chem Educ. 1952;29(11):539-544.

Theoretical Study of Static and Dynamic Equation of State of Cerium and Ytterbium

Priyank Kumar[1,a], Rajesh C Malan[2,b], Kamaldeep G Bhatia[3,c], Nupur P Vora[4,d], Basant Kumar Das[5,e]

[1] *Department of Sciences & Humanities, Government Polytechnic, Dahod-389151, Gujarat, India.*
[2] *Department of Science, Government Engineering College, Valsad-396001, Gujarat, India.*
[3] *Department of Physics, L.J.I.E.T., L J University, Ahmedabad-382210, Gujarat, India.*
[4] *Department of Information Technology, Silver Oak University, Ahmedabad-382481, Gujarat, India.*
[5] *Department of Physics, COER University, Roorkee-247677, Uttrakhand, India.*

[a] pkumar@gtu.edu.in
[b] rcmgecv@gmail.com
[c] kamaldeep.bhatia1991@gmail.com
[d] nupurvora94@gmail.com
[e] drbkdas.iitd@gmail.com

Abstract

Theoretical study of the dynamic equation of state or shock Hugoniot plays a key role in describing behaviour of materials under simultaneous high temperature and high pressure that are very difficult to achieve in the experiments. Schock Hugoniot is locus of all possible states that arises due to a single shock from a given initial state, generally explained by thermodynamic variables like pressure, volume and internal energy or enthalpy. Anharmonicity aroused due to lattice ions and thermally excited electrons should be accounted properly at such high temperature and high pressure. In the present study, a conjunction scheme of a local form of the pseudopotential proposed by Krasko and Gruski (KG) and mean field potential (MFP) has been used to account anharmonic effects due to lattice vibrations. The anharmonicity due to thermally excited electrons has been included using Mermin functional. Static as well as dynamic equation of states along with temperature along principal Hugoniot of rare earth elements cerium and ytterbium have been studied theoretically. The conjunction scheme is found to be capable to account for anharmonicity at extreme environment such as high temperature and high pressure.

Keywords: Pseudopotential, Rare Earth Elements, Equation of State, Shock Hugoniot.
Received 29 January 2025; First Review 19 March 2025; Accepted 19 March 2025.

*** Address of correspondence**
Priyank Kumar
Department of Sciences & Humanities,
Government Polytechnic, Dahod-389151,
Gujarat, India.

Email: pkumar@gtu.edu.in

How to cite this article
Priyank Kumar, Rajesh C Malan, Kamaldeep G Bhatia, Nupur P Vora, Basant Kumar Das, Theoretical Study of Static and Dynamic Equation of State of Cerium and Ytterbium, J. Cond. Matt. 2025; 03 (01): 112-115.

Available from:
https://doi.org/10.61343/jcm.v3i01.100

Introduction

Equation of state (EOS) relates various state functions of materials like pressure, volume and temperature that is used to study thermodynamic behaviour of materials and modelling of interior of planets and stars [1].

To study behaviour of materials under simultaneous high temperature and high pressure produced due to shock wave, Dynamic equation of state or shock-Hugoniot is used which is fundamental relationship between pressure, volume and energy of a materials. Shock waves are sudden variations in pressure, density and internal energy of material that occur due to localised rapid release of energy [2]. Shock wave phenomenon has found its applications in shock welding and dynamic compaction of materials. Shock wave data are found useful not only in the measurement of densities of materials at high pressure but also in the study of terrestrial planets and the solid satellites [3]. These data can further be utilized to design systems like infantry helmets and ship hulls facades that are exposed to explosive or projectile loading [2]. Such facts lead to requirement of theoretical models that can be used to describe behaviour of transition and f-shell metals especially at high temperature and high pressure that are very difficult to achieve experimentally.

Due to complicated electronic and structural behaviour of

transition and f-shell metals, use of local pseudopotential for comprehensive study of their physical properties is very difficult to implement.

Though, the non-local and norm conserving pseudopotentials are found to be better but their mathematical complexity is a major hurdle in implementing them computationally for comprehensive studies of physical properties of materials. During, literature survey, we found that local pseudopotential has been used efficiently to explore properties of simple, transition and f-shell metals at extreme environment [4-8]. It is also important to note that limited efforts have been made to study physical properties of f-shell metals especially at extreme environment using pseudopotential theory [7-8].

Theory

The Helmholtz free energy at given volume (Ω) and temperature (T) is used to calculate thermodynamic properties of a material that is given by following equation [7]-

$$F(\Omega,T) = E_c(\Omega_0) + F_{ion}(\Omega,T) + F_{eg}(\Omega,T) \qquad (1)$$

Second order perturbation theory using pseudopotential due to Krasko and Gruski (KG) [9] has been used to find cold energy $E_c(\Omega_0)$. The pseudopotential used in the present study has following form in the q space [7,9].

$$V_{ion}(Q) = \left(\frac{8\pi Z}{\Omega Q^2}\right)\left(\frac{(2a-1)(Qr_c)^2-1}{[(Qr_c)^2+1]^2}\right) \qquad (2)$$

The pseudopotential has two adjustable parameters a and the core radius- r_c. Exchange and correlation function due to Hubbard [10] and Sham [11] has been used to screen the pseudopotential following equation has been used to calculate ionic contribution $F_{ion}(\Omega,T)$ to the Helmholtz free energy [7]

$$F_{ion}(\Omega,T) = -k_BT\left[\left(\frac{3}{2}\right)ln\left(\frac{mk_BT}{2\pi\hbar^2}\right) + ln\{v_f(\Omega,T)\}\right] \qquad (3)$$

Where $v_f(\Omega,T) = 4\pi\int exp\left[\frac{-g(r,\Omega)}{k_BT}\right]r^2dr$

Here, m is ionic mass and k_B is Boltzmann constant. The, mean field potential (MFP) as a function of cold energy- $E_c(\Omega_0)$ as suggested by Wang and Li [12] is given by

$$g(r,\Omega) = \frac{1}{2}[E_c(R_0+r) + E_c(R_0-r) - 2E_c(R_0)] + \left(\frac{\lambda}{2}\right)\left(\frac{r}{R_0}\right)[E_c(R_0+r) - E_c(R_0-r)] \qquad (4)$$

In equation 4, r defines deviation of lattice ion from its equilibrium position while R_0 is the lattice constant corresponding to equilibrium volume ($\Omega = \Omega_0$). The parameter λ has three possible integral values -1, 0 and +1 that correspond to three different choices of Gruneisen parameters due to Slater, Dugdale and MacDonald and Vashchenko and Zubarev respectively [12]. We have taken $\lambda = +1$ in the present study; because it reproduces good result of physical properties of different classes of metals [4-8]

We have calculated P-Ω relation at 300 K by following equation [13].

$$P = -\left[\frac{\partial F(\Omega,T)}{\partial\Omega}\right]_{T=300K} \qquad (5)$$

The internal energy or enthalpy is defined as [7, 12]

$$E_H(\Omega,T) = E_c(\Omega) + \xi(\Omega,T)k_BT \qquad (6)$$

With, $\xi(\Omega,T) = \frac{3}{2} + \left(\frac{\partial ln v_f(\Omega,T)}{\partial lnT}\right)_\Omega$

Further, Rankin-Hugoniot equations is used to calculate pressure-P_H and temperature-T_H along Hugoniot that is obtained from conservation laws of mass, momentum and energy [4-6],

$$(E_H - E_0) = \frac{1}{2}(P_H + P_0)(\Omega_0 - \Omega_H) \qquad (7)$$

Here, ρ, P and E represent density, pressure and enthalpy respectively. Suffix 0 and H represent quantities in the un-shocked and shocked region respectively.

Results and Discussion

On the line of many previous studies [4-8], the pseudopotential parameter a is kept equal to 3 to reduce number of adjustable parameters from two to one. The second pseudopotential parameter r_c has been fitted using zero pressure condition. The values of r_c for Ce and Yb are 0.569 a. u. and 0.572 a.u. respectively [7].

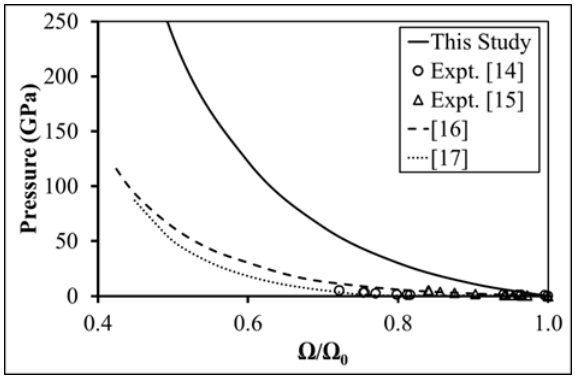

Figure 1: 300 K isotherm of Ce.

Equation of state of Ce and Yb at 300 K along with other experimental and theoretical results are shown in Fig.1 and Fig.2 respectively. Static EOS at 300 K of Ce and Yb are in reasonably good agreement with experimental and other theoretical results. At higher pressure results deviate from other reported experimental and theoretical results. Such variation may be due to the fact that the parameter λ involved in the equation 4 is kept equal to 1. Some studies [20-22] suggest that the parameter λ is temperature and

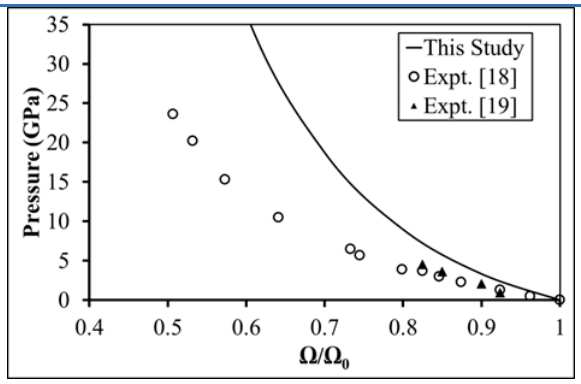

Figure 2: 300 K isotherm of Yb.

volume dependent. Therefore, results of EOS of Ce and Yb at 300 K can be improved by making temperature and volume dependent.

Static EOS is used to find shock Hugoniot and temperature along principal Hugoniot using iterative method [4-6]. The calculated shock wave pressure (P_H) of Ce as a function of reduced volume (Ω_H/Ω_0) and available experimental [23-24] as well as other theoretical results [16-17] are shown in Fig 3. Fig. 4 presents Shock Hugoniot of Yb along with experimental results [23].

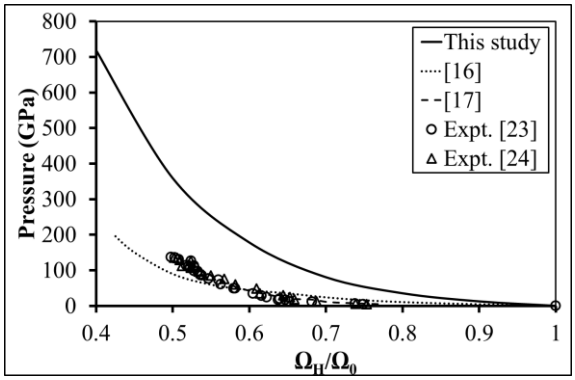

Figure 3: Shock Hugoniot of Ce.

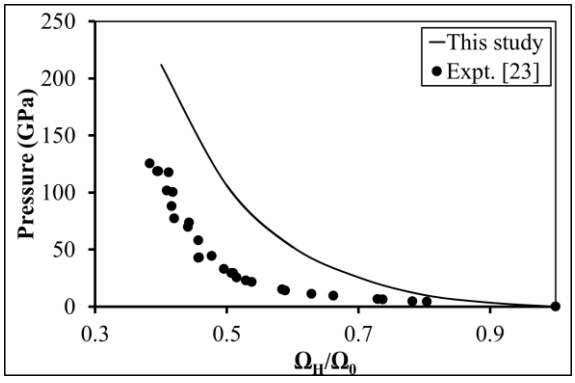

Figure 4: Shock Hugoniot of Yb.

Temperature along principal Hugoniot (T_H) of Ce and Yb as a function of reduced volume (Ω_H/Ω_0) are shown in Fig 5 and Fig. 6 respectively.

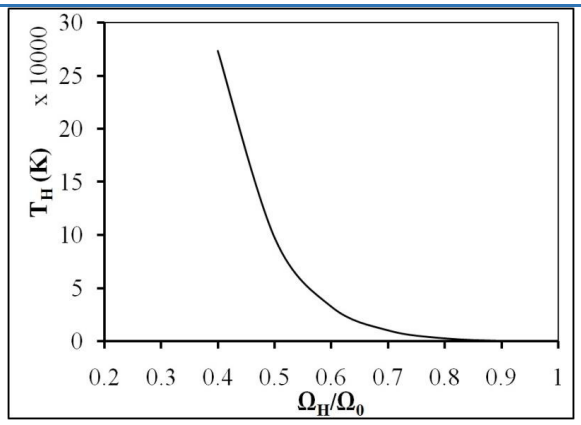

Figure 5: Temperature along principle Hugoniot of Ce.

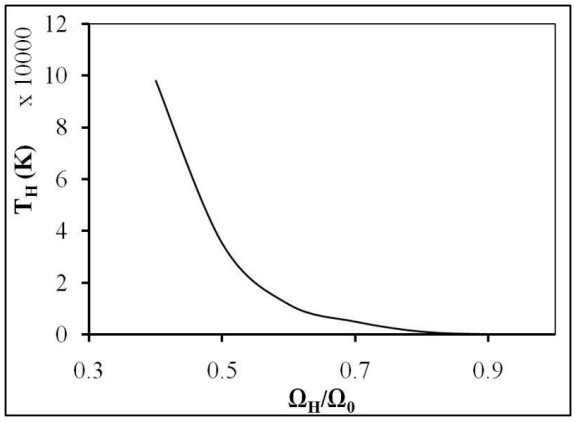

Figure 5: Temperature along principle Hugoniot of Yb.

We could not compare the results of temperature along principal Hugoniot with others because no experimental or theoretical study have been found in literature.

Conclusion

Local form of the KG pseudopotential in conjunction with MFP accounts the anharmonicity due to lattice vibrations and thermally excited electrons at high temperature. Presently used conjunction scheme does not require an additional Born-Mayer type of potential to accounts core-core repulsion and valency has also not been adjusted in the present study. Observed deviation in the theoretical results with experimental results especially at high temperature may have aroused because of the constant value of parameter $\boldsymbol{\lambda}$ which is appearing in the equation of $\mathbf{F_{ion}}$(see equation 3 and 4). The parameter $\boldsymbol{\lambda}$ depends on volume, temperature and material as suggested in some studies [20-21]. Thus, results can be improved by accounting anharmonicity properly at high temperature by making λ temperature and volume dependent [23] instead of using extra anharmonic contribution to the Helmholtz free energy as suggested in reference [25]. Thus, due to its computational simplicity and reliability, the present conjunction scheme of local pseudopotential and MFP can be used for theoretical study of thermodynamic properties of transition metals and f-shell metals.

References

1. A. Dewaele, M. Torrent, P. Loubeyre. and M. Mezouar, Phys. Rev. B 78 (2008) 104102.
2. F. R. Svingala, M. J. Hargather. and G. S. Settles, International Journal of Impact Engineering 50 (2012) 76.
3. T. J. Ahrens, eds. Asay J. R., and Shahinpoor M.,"High Pressure Shock Compression of Solids" (Springer, New York). (1993).
4. P. Kumar, N. K. Bhatt, P. R. Vyas and V. B. Gohel, Phase Transitions 90 (2017) 1167.
5. P. Kumar, N. K. Bhatt, P. R. Vyas, V. B. Gohel, Eur. Phys. J. B 89 (2016) 219.
6. P. Kumar, N. K. Bhatt, P. R. Vyas and V. B. Gohel HTHP 46 (2017) 167.
7. Kumar P., Bhatt N. K., Vyas P. R., Gohel V. B. (2017), Int. J. Thermophysics 38, 87.
8. P. Kumar, N. K. Bhatt, P. R. Vyas, V. B. Gohel, Int. J. Modern Phys. B 32 (2018) 1850065.
9. G. L. Krasko and Z. A. Gruskii, Zh ETF Pis. Red. 9 (1969) 596.
10. J. Hubbard, Proc. Roy. Soc. A 243 (1957) 336.
11. L. J. Sham, Proc. Roy. Soc. A 283 (1965) 33.
12. Y. Wang and L. Li, Phys. Rev. B 62 (2000) 196.
13. D. C. Wallace, "Thermodynamics of Crystals" (John Wiley and Sons Inc., New York). (1972).
14. J. S. Olsen, L. Gerward, U. Benedict and J. P. Itie, Physica B 133 (1985) 129.
15. W. H. Zachariasen and F. H. Ellinger, Acta Cryst. A33 (1977) 155.
16. N. K. Bhatt, P. R. Vyas, A. R. Jani and V. B. Gohel, Int. J.Modern Physics B 19 (2005) 999.
17. Y. Wang, Phys. Rev. B 61 (2000) R11863.
18. K. Takemura and K. Syassen, J. Phys. F: Met Phys. 15 (1985) 543.
19. S. U. Devi and A. K. Singh, Bull. Mater. Sci. 6 (1984) 395.
20. L. Burakovsky, C. W. Greef and D. L. Preston, Phys. Rev. B 67 (2003) 094107-1.
21. L. Burakovsky, L. Prestona and Y. Wang, Solid State Commun. 132 (2004) 151.
22. C. Bhattacharya, S. V. G. Menon, J. Appl. Phys. 105 (2009) 064907-1.
23. S. P. Marsh, LASL Shock Hugoniot Data S P University of California Press, Berkeley (1980).
24. W. J. Carter, J. N. Fritz, S. P. March and R. G. McQueen, J. Phys. Chem. Solids 36 (1975) 741.
25. C. Cazorla, D. Alfe and M. J. Gillan, Phys. Rev. B 85 (2012) 064113.

A DFT Approach to Structural, Electronic, and Thermodynamic Properties of Binary Rare-earth Nitrides REN (RE = Pr & Nd)

Suparn Kumar Barmase[1,a], Hansraj Dhadse[1,b], Purnima Singh[1,c], Shubha Dubey[2,d], and Jagdeesh Pataiya[3,e]

[1] *Department of Physics, Govt. Motilal Vigyan Mahavidyalaya, Bhopal – 462008, M.P., India.*
[2] *Department of Physics, Barkatullah University, Bhopal, 462026, M.P., India.*
[3] *Department of Physics, Dr. Bhimrao Ambedkar Government College, Amla, Betul, 460551, M.P., India.*

[a] suparn404880@gmail.com
[b] hrdhadse2050@gmail.com
[c] purnimasep@gmail.com
[d] shubha.dubey4@gmail.com
[e] jagdeesh8115@gmail.com

Abstract

In the present work, we apply density functional theory (DFT) with the PBE (Perdew–Burke–Ernzerhof) and WC (Wu–Cohen) exchange-correlation functionals using the generalized gradient approximation to investigate the structural, electronic, and thermodynamic properties of binary rare-earth nitrides REN (RE = Pr and Nd) compounds. Our computed structural parameters, such as equilibrium lattice constants, bond angles, and bond lengths, show excellent agreement with both experimental and previous theoretical results. The electronic properties of praseodymium and neodymium nitrides are examined through electronic band structure and density of states analyses. Additionally, we compute thermodynamic properties using the quasi-harmonic Debye model. This study provides a valuable basis for further experimental and theoretical exploration of the potential applications of these materials.

Keywords: Density of States; Structural Parameters; Metallicity; Rare-Earth.
Received 29 January 2025; First Review 10 February 2025; Accepted 20 March 2025.

*** Address of correspondence**
Suparn Kumar Barmase
Department of Physics, Govt. Motilal Vigyan Mahavidyalaya, Bhopal – 462008, M.P., India

Email: suparn404880@gmail.com

How to cite this article
Suparn Kumar Barmase, Hansraj Dhadse, Purnima Singh, Shubha Dubey, and Jagdeesh Pataiya, A DFT Approach to Structural, Electronic, and Thermodynamic Properties of Binary Rare-earth Nitrides REN (RE = Pr & Nd), J. Cond. Matt. 2025; 03 (01): 116-119.
Available from:
https://doi.org/10.61343/jcm.v3i01.103

Introduction

Rare-earth nitrides (RENs) exhibit an exceptional range of electrical and magnetic properties, making them highly versatile materials for advanced technological applications. Their unique characteristics arise from the interplay between their electronic structure and the localized nature of the 4f orbitals [1]. These materials demonstrate behaviours spanning metallic, semi metallic, and semiconducting regimes. NdN and PrN, in particular, stand out as remarkable magnetic narrow-gap semiconductors, ideally suited for devices requiring simultaneous magnetic and semiconducting functionalities. Beyond their potential in spintronics, NdN and PrN provide a valuable platform for exploring fundamental physical phenomena [2]. Their stable magnetic ordering and narrow electronic band gaps make them ideal for studying magneto-optical effects, magneto-transport phenomena, and the interplay between spin, charge, and lattice dynamics. These materials are also excellent candidates for both experimental and computational research into correlated electron systems. Computational techniques such as density functional theory (DFT) using Wien2k can offer detailed insights into their electronic, thermodynamic, and structural properties.

DFT studies have provided valuable insights into their lattice constants, bulk moduli, and cohesive energies, demonstrating good agreement with experimental data [3]. Investigations on NdN and PrN have revealed their stable magnetic ordering and magnetoresistance effects, further validating their potential for device applications [4]. Additionally, thermodynamic studies employing the quasi-harmonic Debye model have explored their heat capacity, thermal expansion, and Debye temperature variations under high-pressure and high-temperature conditions, highlighting their stability in extreme environments [5].

Recent advancements in experimental techniques such as high-resolution X-ray diffraction (XRD) and neutron scattering have significantly improved structural characterizations, while computational methodologies incorporating Hubbard U corrections and many-body perturbation theory (GW) calculations have enhanced the accuracy of electronic structure predictions [6]. These developments emphasize the importance of RENs in fundamental research and technological applications, particularly in the fields of high-performance electronics and spintronic devices.

Computational Details

Calculations are performed using the Wien2k software with the FP-LAPW method for DFT-based ground-state energy calculations [7]. The exchange-correlation potential is described by PBE-GGA, with an energy convergence parameter, $R_{MT}Kmax$, set to 7.0. The Gmax parameter is set to 12 $a.u.^{-1}$, and self-consistency is achieved when total energy stabilizes within 10^{-4} Ry. The Monkhorst-Pack method with 1000 k-points is used for Brillouin zone integration, and a cut-off energy of -6.0 Ry is applied to separate valence and core states, with a charge convergence threshold of 0.0001e. The Monkhorst-Pack method [8] is a systematic approach for generating k-points in the Brillouin zone of a crystal for numerical integration in electronic structure calculations, particularly in density functional theory (DFT).

Results & Discussion

The structural characterization of REN (RE = Pr and Nd) was executed by assigning the RE atoms to the Wyckoff position corresponding to the fractional coordinates (1/2, 0, 0) and the nitrogen atoms to the (0, 0, 0) position. The resultant optimized conventional unit cell, as depicted in Fig. 1, manifests a cubic crystal structure with the Fm-3m space group.

To ascertain the most energetically favourable configuration and magnetic ordering, total energy calculations were performed as a function of volume for both non-spin-polarized (NM) and ferromagnetic (FM) states. The energy in the NM state was consistently lower than that in the FM state across all volumes, thereby corroborating the thermodynamic stability of the NM configuration. Structural parameters, including lattice constant and bulk modulus, were derived using the Birch-Murnaghan equation of state. The optimized lattice constants, presented in Table 1, elucidate the most stable structural configuration for REN (RE = Pr and Nd). The results exhibit a commendable agreement with available theoretical values from alternative research groups, with the minor discrepancies ascribed to variances in computational methodologies employed.

Table 1: Optimized Structural parameters of REN (RE=Pr & Nd).

Parameters	PrN	NdN
a (Å)	4.9842	4.9541
V ($Å^3$)	208.8890	205.1310
B (GPa)	153.6173	149.4908
B′	4.5624	4.8269
E_0	-18595.272902	-19369.749887

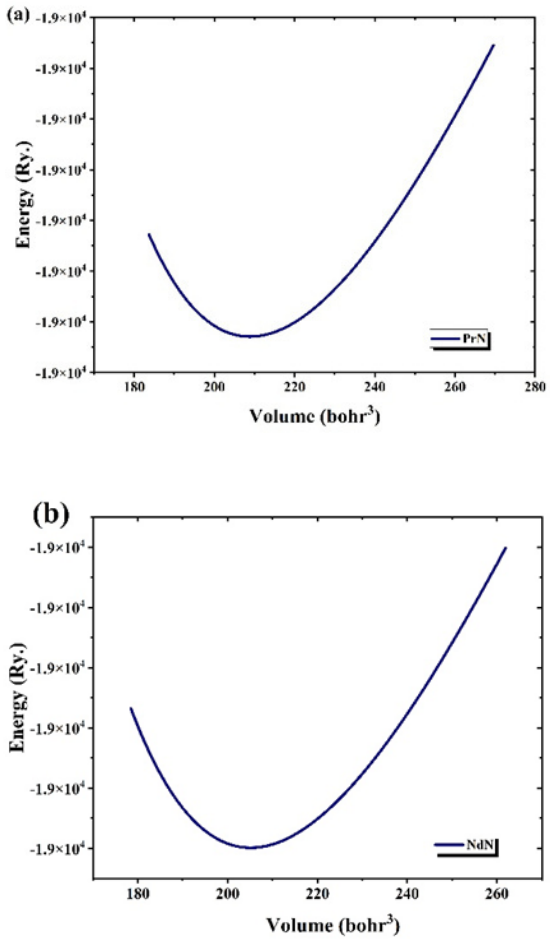

Figure 1: Energy versus Volume curve for REN (RE= Pr & Nd).

The figure 2 illustrates the Density of States (DOS) and electronic band structures for Praseodymium Nitride (PrN) and Neodymium Nitride (NdN), highlighting their electronic properties. The DOS plots, centered around the Fermi level (E_f=0), reveal sharp peaks near the Fermi level for both materials, indicative of a high density of electronic states. This suggests metallic behavior, as partially filled bands enable free electron movement [10]. For PrN, the DOS (panel a) shows pronounced features at both occupied and unoccupied energy levels, while the inset band structure (panel b) confirms the metallic nature through band crossings at the Fermi level along high-symmetry directions (W, L, Γ, X, and K). Similarly, the DOS for NdN (Figure 2c) also exhibits a sharp peak near the Fermi level, with its band structure (Figure 2d) showing comparable metallic behavior due to similar band crossings. Differences in band dispersion and DOS features between the two compounds

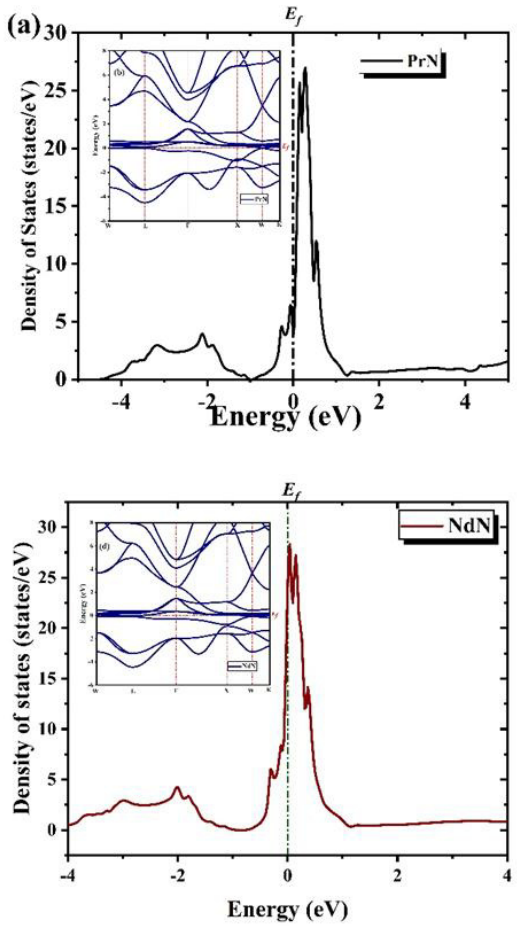

Figure 2: Total density of states TDOS and Band structure BS for REN (RE= Pr & Nd).

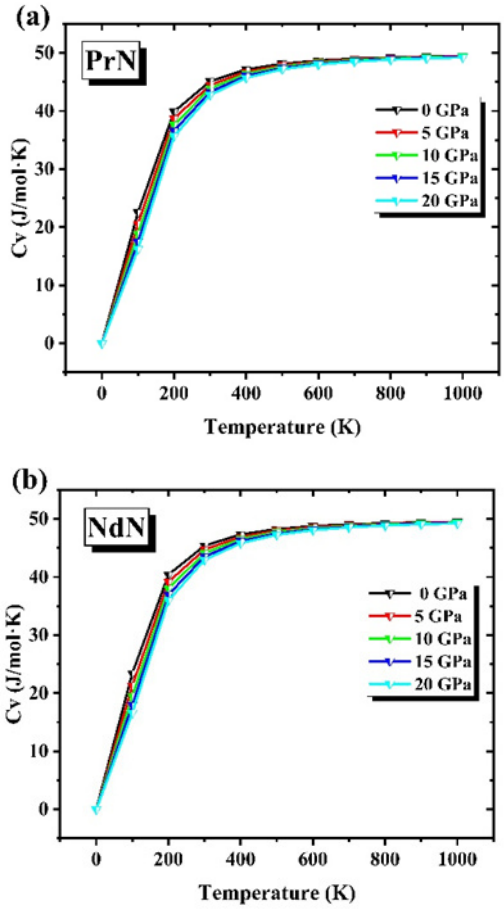

Figure 3: heat capacity at constant volume of REN (RE= Pr & Nd).

likely arise from variations in the electronic configurations and atomic interactions of Pr and Nd. These results emphasize the influence of localized f-electron states on the electronic structures of these nitrides, contributing to their characteristic peaks near the Fermi level. The calculated temperature dependent thermodynamic properties of REN's are calculated, including the variation of heat capacity at constant volume as a function of pressure range from 0 to 20 GPa within the temperature ranging from 0 to 1000 K, where the quasi-harmonic model remains valid [9]. The heat capacity at constant volume (C_v) for PrN and NdN exhibits (as shown in Figure 3) a typical temperature dependence, increasing sharply at low temperatures (<100K) due to phonon contributions and gradually saturating toward the Dulong-Petit limit (~50 J/mol·K) at higher temperatures (>300K).

The effect of pressure on C_v is minimal, with only slight variations observed as pressure increases from 0 to 20 GPa, indicating that phonon softening or stiffening effects are weak in both compounds. A comparison between PrN and NdN reveals similar overall trends, though NdN shows slightly lower C_v values at low temperatures, likely due to differences in phonon density of states arising from atomic mass variations. However, at higher temperatures, the C_v values for both compounds converge, reflecting dominant lattice contributions. This behaviour suggests that the thermodynamic properties of PrN and NdN are primarily governed by their photonic structure, with pressure exerting only a minor influence.

Conclusion and Future Prospective

We have conducted a detailed investigation into the structural, electronic, and thermodynamic properties of rare-earth nitrides REN (RE = Pr and Nd). Structural analysis reveals that REN exhibits non-magnetic behavior in the ground state, with the calculated equilibrium volume and lattice parameters provided. Electronic structure analysis shows that both REN compounds display metallic characteristics under the PBE-GGA exchange correlation. Additionally, high-temperature and high-pressure dependent thermodynamic parameter suggest that REN is a promising candidate for technological applications under extreme conditions.

References

1. P. Larson et al., Phys. Rev. B, 75, 4511 (2007).
2. T. A. Yamamoto et al., J. Alloys Compd., 376, 17 (2004).
3. M. G. Smith et al., J. Appl. Phys., 104, 093905

(2008).
4. S. R. Banerjee et al., J. Phys.: Condens. Matter, 21, 025501 (2009).
5. H. M. Wang et al., J. Phys. Chem. C, 124, 5436 (2020).
6. G. K. H. Madsen et al., J. Chem. Phys., 152, 7 (2020).
7. Blaha, P., Schwarz, K., Tran, F., Laskowski, R., Madsen, G. K. H., & Marks, L. D. Journal of Chemical Physics, 152(7), 2020.
8. H. J. Monkhorst and J. D. Pack, Phys. Rev. B 13, 5188 (1976).
9. Jain, E., Pagare, G., & Dubey, S. AIP Conference Proceedings, 2100, 2019.
10. Singh, D. J., & Nordström, L. Springer, Vol. 2, 2nd ed., (2006).

"Paper and Inks": Sustainable Sensing Through Development of Paper Platforms

Ayushi[1,a], Neha Agrawal[1,b], Niroj Kumar Sethy[2,c]

[1] *Human Factor Engineering and Military Ergonomics Division, DIPAS, DRDO, Timarpur, Delhi-110054, India.*
[2] *DDT Division, DIPAS, DRDO, Timarpur, Delhi-110054, India.*

[a] ayushi3068@gmail.com
[b] neha.dipas@gov.in
[c] niroj.dipas@gov.in

Abstract

The platform of biosensor plays a pivotal role in the efficacy of detection; therefore, the selection of an optimal material that meets all requisite criteria is essential. Paper as a platform for sensing application exhibit additive attributes over the other commercially available substrates as it might fulfils the 'REASSURED' benchmark introduced under WHO guidelines. The study entails the fabrication of an electrochemical biosensing platform using regular office paper with different GSM thickness (75, 85,120 and 140 GSM). The conductive inks, paper thickness, design pattern, hydrophobic layer and connection materials were iterated and optimized through multiple scans of cyclic voltammetry. A simplified design of three electrode system having reference and working electrode was optimized at a distance of around 1mm. The concentration and number of layers of conductive inks were optimized through conductivity measurements which lie between 1Ω to 4 Ω for reference electrode and 0.0005 MΩ to 0.025 MΩ for counter electrode. Working electrode was fabricated using two differently modified conductive CNTs ink where conductivity varied for PCNT as 0.06 kΩ to 0.1 kΩ while LCNT varied 0.014 kΩ to 1.33 KΩ. Beside this an ecofriendly volatile organic compound free hydrophobic reagents were also tested for fabricating the sensing region. The CV scans show stability of adsorbed conducting materials on the fabricated paper platform stating that the platform could be further evaluated for biosensing application.

Keywords: Paper platform, Carbon Nanotubes, ePADs, Electrochemical sensors, Cyclic Voltammetry.
Received 30 January 2025; First Review 21 February 2025; Accepted 19 March 2025.

*** Address of correspondence**
Dr. Neha Agrawal
Human Factor Engineering and Military Ergonomics Division, DIPAS, DRDO, Timarpur, Delhi-110054, India.

Email: neha.dipas@gov.in

How to cite this article
Ayushi, Neha Agrawal, Niroj Kumar Sethy, "Paper and Inks": Sustainable Sensing Through Development of Paper Platforms, J. Cond. Matt. 2025; 03 (01): 120-125.

Available from:
https://doi.org/10.61343/jcm.v3i01.110

Introduction

Biosensor platforms are designed with diverse architectures for the precise detection of biomolecules. These platforms are critical for advancing diagnostic accuracy, therefore optimal material selection is crucial for high sensitivity, specificity, and rapid response time. Paper has been widely used as a fascinating substrate for the development of biosensors as it offers the promising avenues for point of care diagnostics, aligning the 'REASSURED' criteria providing a current advancement in health monitoring. 'REASSURED' stands for Real-time connectivity, Ease of specimen collection, Affordable, Sensitive, Specific, User-friendly, Rapid and robust, Equipment free or simple Environmentally friendly, Deliverable to end-user [1]. Paper-based analytical biosensors provide portability, reliability, rapid detection, and a sustainable, eco-friendly approach for various detection methods, including electrochemical, optical, and fluorescence techniques, facilitating the identification of biomolecules such as bacteria, viruses, neurotransmitters, glucose, and proteins [2]. Numerous researches have reported the use of various paper types, including whatman filter paper, office paper, wax-printed paper, and chromatography paper, in the fabrication of paper-based analytical devices (PADs) [3]. Each type of paper exhibits distinct characteristics, specifically optimized and tailored for particular sensor functions. Electrochemical paper based analytic devices (ePADs) involves coupling of paper based biosensor with the use of electrochemical methods such as cyclic voltammetry [4]. In recent years, carbon-based nanomaterials, including carbon nanotubes, graphene, and graphite, have been recognized for their distinctive physical and chemical properties, such as biocompatibility, electrical conductivity, and high surface area, which are leveraged as critical components in the formulation of conductive inks

for the fabrication of paper-based sensors [5]. For instance, carbon nanotube inks can be dispersed in a solvent and printed onto paper substrates, facilitating the development of electrochemical sensors [6] Additionally, graphene-based inks exhibit exceptional conductivity and mechanical attributes, rendering them highly promising for similar applications [7].

The aim of this study is to develop a paper-based platform for sustainable sensing, utilizing standard office paper, which is subsequently printed with an inkjet printer to fabricate the electrode design. Carbon nanotube ink is employed for the working electrode. The fabricated electrode is characterized by assessing its conductivity and morphology. Furthermore, the electrode design is optimized based on variables such as paper type, hydrophobic barriers, and connection materials through cyclic voltammetry.

Materials and Method

Chemicals and apparatus

Potassium Ferrocyanide ($K_4[Fe(CN)_6]$), 6 amino caproic acid (AHA), polystyrene sulfonate (PSS), KCl (Potassium Chloride), Carbon nanotubes (CNTs), Milli-Q water (Millipore), Phosphate buffer solution (PBS) at pH 7.0, Mineral oil, Doms wax crayons, Silver paste, Office paper (JK excel Bond & Lotus Ivory Sheets) A4 75, 85, 120, 140 gm^{-2}, Apsara graphite 6B pencil. MS word software is used for the electrode design. Two probe multimeter is used for measuring ohmic resistance. Electrochemical experiments were performed using a *Emstat4S palm-sens potentiostat* and PS Trace 5.9 software was used for scanning. All experiments were conducted at room temperature.

Fabrication and testing of paper platform

For electrode fabrication, four types of A4 office paper with thicknesses of 75, 85, 120, and 140 g/m² were used, with two design patterns as mentioned in Table 1 and Figure 1. Pristine MWCNTs were modified via sonication, stirring, centrifugation, and drying using 1% PSS and lithium salt of 6-amino caproic acid (AHA), yielding PCNT (PSS-modified CNT) and LCNT (AHA-modified CNT) [11]. The electrodes were constructed by layering graphite for the counter electrode, silver paste for the reference electrode, and PCNT as well as LCNT conductive ink (50ul) for the working electrode. Hydrophobic barriers were added using wax crayon by coloring and heating while immersed and travelled through capillary driven force in mineral oil.

Electrochemical measurements

Cyclic voltammetry was conducted with an initial potential range of -1.6 V to +1.6 V. The analysis began with 5 cycles to assess potential etching, followed by an extended 25-cycle evaluation to ensure stability.

Table 1: Geometrical dimensions of the paper-based electrode employed for fabrication.

Dimension	Dimension 1	Dimension 2
Total length of electrode	60mm x 40mm	49.99mm x 13mm
Clipping Box	3mm x 3mm	4.99 mm x 3.5 mm
WE Diameter	3mm	3mm
Distance between RE and WE	4mm	1mm
Surface Area of CE	81.2 mm^2	40.5476 mm^2

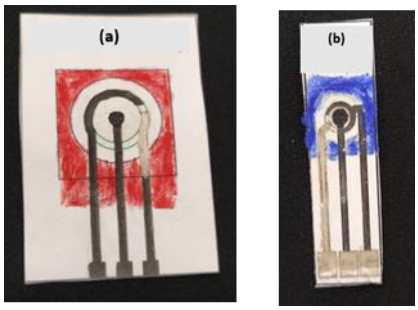

Figure 1: Paper electrodes were fabricated based on the specified dimensions, Dimension 1 (D1) and Dimension 2 (D2), as outlined in Table 1.

Each cycle was performed at a scan rate of 0.05 V/s with a step potential of 0.01 V. A 50 ul of 0.1M PBS solution served as the electrolyte for entire electrochemical reactions.

Results and Discussion

Investigation of modification of CNTs as conductive inks

For fabrication of paper electrodes investigation of interaction between platform and conductive inks is the primary step. The two biocompatible methods of CNTs modification, already explored for other applications are revisited over here to evaluate their conductivity henceforth utilized as conductive inks for ePADs [12-13]. The modification method of CNTs were optimized by varying various ratios and percentage of modifier (PSS and AHA).On basis of conductivity the most optimized concentration was chosen for further studies. We have restricted the use of modified CNTs as conductive inks only for working electrode to simplify the study with the purpose of understanding electrochemical interaction of ink with paper platform. The modified CNTs designated as LCNT for AHA salt modified CNTs and PCNT for PSS modified CNTs were chosen for the study. The reason behind the selection of such modifier was to deagglomerate pristine

CNTs in aqueous medium without usage of long chemical route and harsh chemicals. The two modifiers drew our attention due to their biocompatible nature, one being as FDA approved drug (AHA) while other as neuroactive agent (PSS). Both modifiers had ability to generate negative surface charge on being adsorbed through non covalent interaction keeping the carbon nanoform de-agglomerated and well dispersed in aqueous medium as well stated in earlier studies [14-16].

The morphological evidence of such modified CNTs were reported in our earlier work [17] which illustrated that the modified CNTs with AHA salt had been adsorbed on the surface of CNTs that had resulted in thickening of CNTs surface. Along with thickness of the wall, modified surface of CNTs were found rough and irregular in nature. This roughness and irregularity could be useful for ePADs fabrication as it could increase the electroactive area in contrast to unmodified CNTs or covalently modified CNTs which were often smoother compared to non-covalently modified surface.

Conductivity and Layer Optimization of Working, Counter and Reference electrodes on different papers type

The ohmic resistance of the conductive path is measured via two-point multimeter. The resistance measurements yielded crucial insights into the optimal deposition via concentration and number of depositing layers of conductive ink necessary to achieve sufficient conductivity on the electrodes. Moreover, for evaluating the reproducibility of the fabricated inks the electrical resistance of the electrode was tested so as to keep it similar among all designed electrodes. The average resistance value of counter, working and reference electrode is shown in figure 2 for the paper type of varied thickness. The graph indicates that LCNTs exhibit higher resistance than PCNTs, confirming PCNTs superior conductivity and higher current output potential for working electrodes as a conductive ink. The counter electrode was fabricated using a graphite layer via pencil friction due to its cost-effectiveness and simplicity, while the reference electrode utilized commercial silver paste, whose conductivity remained consistent across paper thicknesses ($p>0.05$, p value 0.2377). Although 75GSM paper showed significantly lower resistance ($p=0.003$) for the counter electrode which could be because of the easy penetration of graphite layers inside the pores in thinner paper, but later it was excluded due to fragility. Thicker papers exhibited no significant conductivity variation ($p>0.05$, p value 0.4105), leading to the selection of 85GSM for further studies.

The number of deposited layers significantly impacts the overall conductivity of the electrode. The ohmic resistance progressively decreased with the incremental addition of layers, until reaching a threshold where further layering no longer contributed to conductivity improvements. For all paper thicknesses, the counter electrode and working electrode were optimized with two layers of graphite and modified CNTs as conductive ink, respectively, while the reference electrode required only one layer of silver paste. After the deposition of the initial layer, a sufficient absorption time was allowed to ensure proper penetration of the material into the electrode substrate before applying subsequent layers.

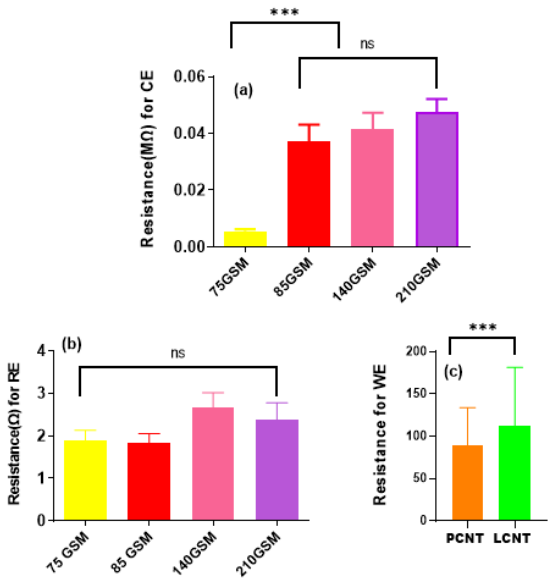

Figure 2: Resistance value across different thickness of office paper (75, 85, 140 and 210 GSM) (a) Resistance value for counter electrode (MΩ) (b) Resistance value for reference electrode (Ω) (c) Resistance value on 85GSM office paper for working electrode with different conductive ink [LCNT (kΩ) and PCNT(Ω)].

Optimization of Hydrophobic agent

To assess the impact of the hydrophobic barrier on the paper electrode, two sample electrodes were selected. In the first, wax crayon was applied, while in the second, the electrode was immersed in mineral oil until the hydrophobic region (demarcated by the orange line) was fully coated. The figure 3 clearly demonstrates that both methods are effective in confining the sample within the designated sample pad. So, a volatile organic free mineral oil shows to be effective in restricting the aqueous sample within the hydrophilic testing region. Mineral oil used stated its environment friendliness along with the ease of fabrication. For the wax deposition, the hydrophobic layer penetration was conducted through heating at a temperature of 121°C. Each paper type was optimized for heating on both sides for different durations according to its thickness factor, with the 75 GSM paper being treated for 5 minutes and the remaining types (85, 140, and 210 GSM) for 15 minutes

each. This variation in time could indicate that thinner papers require less time to absorb the wax, while thicker papers need extended heating to ensure complete integration of the hydrophobic barrier into the fibers.

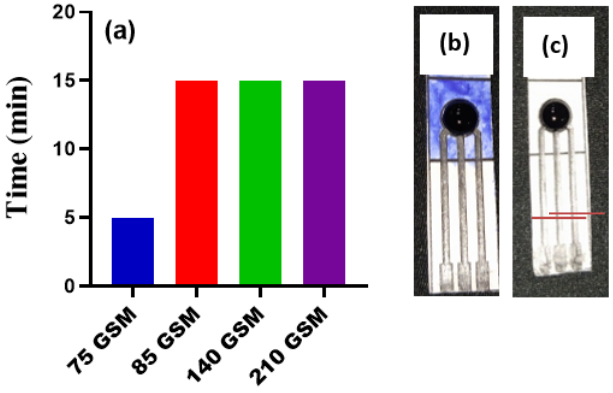

Figure 3: Optimized parameters (a) Time of heating required for different office paper for hydrophobic layer formation (b) Hydrophobic sample pad fabricated utilizing a wax-based crayon method (c) Hydrophobic sample pad fabricated utilizing a mineral oil method. Orange line indicated the mineral oil migration distance of 3.8 cm after immersion.

Electrochemical characterization of the fabricated electrodes

The paper electrodes were fabricated in two different dimensions along with two types of materials used for connections. The design aspect of electrode is an important factor for improving its efficiency. From the concept of electrochemistry and for the ease of fabrication an optimized design was selected through CV analysis as shown in figure 4. Here the two dimensions of electrode differing in certain aspects i.e. distance between reference and working electrode as well as counter surface area were compared. It was observed that an optimized design possessed lower current and selected for further study. Along with-it materials i.e. graphite and Ag paste were tested for connection where Ag always showed higher current compared to graphite but could cause overheating while working with biological buffers so graphite was used as optimized connection material.

To further evaluate the repeatability, reproducibility and lifetime of the electrodes the electrodes were evaluated for stability study through 25 cyclic scans on number of electrodes as shown in figure 5. The CV scans indicate the stability of the adsorbed materials on the engineered paper substrate, without any etching of the conductive ink. The electrochemical responses did not show any significant difference between number of electrodes scanned over a good period of time which showed its reproducibility along with a longer shelf life. This suggested that the platform is highly suitable for analytical feasibility related to biosensing and other electrochemical applications.

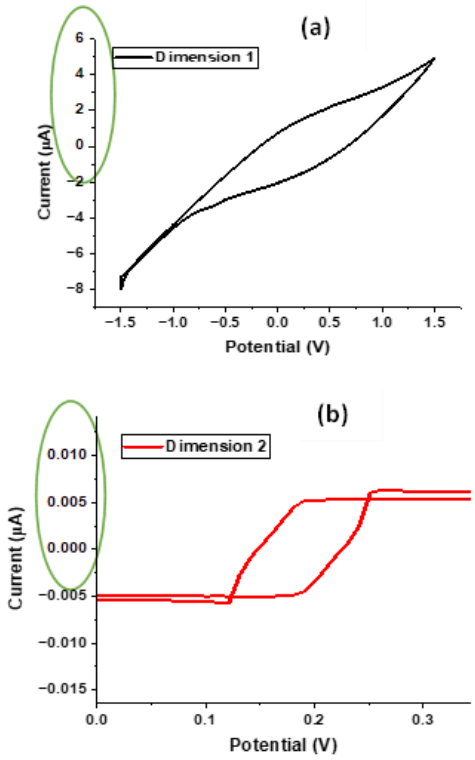

Figure 4: Electrochemical characterization of the electrode performed for (a) Dimension 1 (b) Dimension 2. The encircled region highlights a higher current response for Dimension 1 compared to Dimension 2.

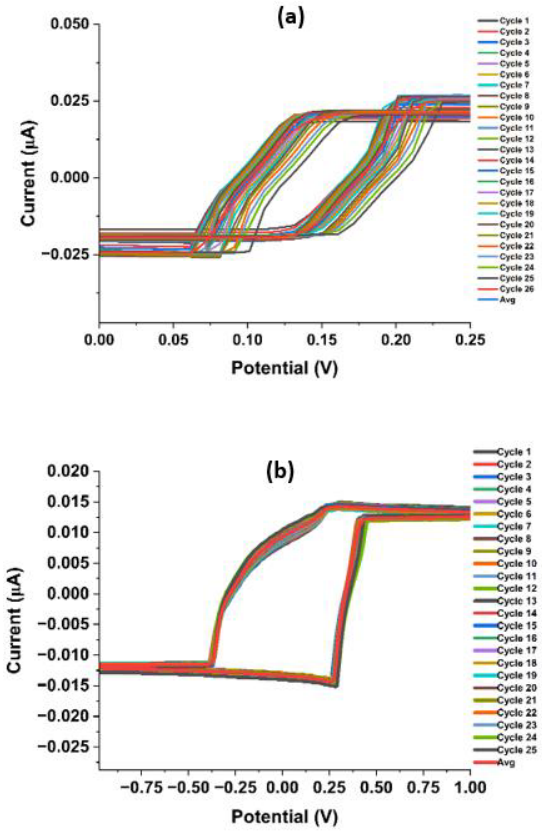

Figure 5: Stability of the conductive ink on 85 GSM, stability cycle (25 scans) for (a) LCNT on paper electrode (b) PCNT on paper electrode.

Conclusion and Future Prospective

The study had brought out optimization of different parameters to fabricate paper based electrochemical platform. The sustainability of the process to produce a final deliverable is the motivation and basis behind the work which is well achieved by using all environmentally friendly steps of fabrication. Two greener methods of modification of CNTs were successfully evaluated as conductive inks where PCNT showed 10 times higher conductivity to LCNTs attributing to its better ability of deagglomeration. The method of creating hydrophobic barrier was optimized with volatile-less oil and student wax crayon, additionally making the steps cost worthy and simple. The platform meets key REASSURED criteria, ensuring real-time connectivity (R) with a portable potentiostat, efficient sample collection (E) using 50 µL of non-invasive fluids, affordability (A) with cost-effective materials, user-friendliness (U), rapid analysis (R), and robustness, as the electrodes are disposable and recyclable. The selectivity and sensitivity (SS) of the paper platform for dopamine sensing with further improvisation in design will be investigated in the future work. The overall material selection had resulted in stable electrochemical response of the platforms showing its promising application not only in biosensing but also in varied other electrochemical processes.

References

1. K. J. Land, D. I. Boeras, X. S. Chen, A. R. Ramsay, and R. W. Peeling, *"REASSURED diagnostics to inform disease control strategies, strengthen health systems and improve patient outcomes,"* Nature Microbiology, vol. 4, no. 1, 2019, doi: 10.1038/s41564-018-0295-3.
2. S. R. Benjamin, F. de Lima, V. A. do Nascimento, G. M. de Andrade, and R. B. Oriá, *"Advancement in Paper-Based Electrochemical Biosensing and Emerging Diagnostic Methods,"* Biosensors, vol. 13, no. 7, 2023, doi: 10.3390/bios13070689.
3. A. E. Ferreira de Oliveira, A. César Pereira, and L. F. Ferreira, *"Fully handwritten electrodes on paper substrate using rollerball pen with silver nanoparticle ink, marker pen with carbon nanotube ink and graphite pencil,"* Analytical Methods, vol. 14, no. 19, 2022, doi: 10.1039/d2ay00373b.
4. G. Ebrahimi, P. S. Pakchin, A. Mota, H. Omidian, and Y. Omidi, *"Electrochemical microfluidic paper-based analytical devices for cancer biomarker detection: From 2D to 3D sensing systems,"* Talanta, vol. 257, 2023, doi: 10.1016/j.talanta.2023.124370.
5. A. M. Díez-Pascual, *"Carbon-based nanomaterials,"* International Journal of Molecular Sciences, vol. 22, no. 14, 2021, doi: 10.3390/ijms22147726.
6. J. R. Camargo et al., *"Development of conductive inks for electrochemical sensors and biosensors,"* Microchemical Journal, vol. 164, p. 105998, May 2021, doi: 10.1016/J.MICROC.2021.105998.
7. P. G. Karagiannidis et al., *"Microfluidization of Graphite and Formulation of Graphene-Based Conductive Inks,"* ACS Nano, vol. 11, no. 3, 2017, doi: 10.1021/acsnano.6b07735.
8. Y. Tian et al., *"Improved resistance stability of transparent conducting films prepared by PEDOT: PSS hybrid CNTs treated by a two-step method,"* Materials Research Express, vol. 6, no. 11, 2019, doi: 10.1088/2053-1591/ab46ea.
9. Y. Tian et al., *"High-performance transparent pedot: Pss/cnt films for oleds,"* Nanomaterials, vol. 11, no. 8, 2021, doi: 10.3390/nano11082067.
10. S. V. Mamykin, I. B. Mamontova, T. S. Lunko, O. S. Kondratenko, and V. R. Romanyuk, *"Fabrication and conductivity of thin PEDOT: PSS-CNT composite films,"* Semiconductor Physics, Quantum Electronics and Optoelectronics, vol. 24, no. 2, 2021, doi: 10.15407/spqeo24.02.148.
11. T. Xue et al., *"Multiwalled Carbon Nanotube-N-Doped Graphene/Poly(3,4-ethylenedioxythiophene):Poly(styrenesulfonate) Nanohybrid for Electrochemical Application in Intelligent Sensors and Supercapacitors,"* ACS Omega, vol. 5, no. 44, 2020, doi: 10.1021/acsomega.0c02224.
12. H. U. Rehman et al., *"Stretchable, strong and self-healing hydrogel by oxidized CNT-polymer composite,"* Composites Part A: Applied Science and Manufacturing, vol. 90, pp. 250–260, Nov. 2016, doi: 10.1016/J.COMPOSITESA.2016.07.014.
13. X. He, J. Shi, Y. Hao, L. Wang, X. Qin, and J. Yu, *"PEDOT:PSS/CNT composites based ultra-stretchable thermoelectrics and their application as strain sensors,"* Composites Communications, vol. 27, p. 100822, Oct. 2021, doi: 10.1016/J.COCO.2021.100822.
14. N. Agrawal, D. Bhagel, P. Mishra, D. Prasad, and E. Kohli, *"Post-synthetic modification of graphene quantum dots bestows enhanced biosensing and antibiofilm ability: efficiency facet,"* RSC Advances, vol. 12, no. 20, 2022, doi: 10.1039/d2ra00494a.
15. C. Hassam and D. A. Lewis, *"Dispersion of single and multiwalled nanotubes with poly(sodium styrene sulfonate) - Effect of pH and ionic strength on dispersion stability,"* Australian Journal of Chemistry, vol. 67, no. 1, 2014, doi: 10.1071/CH13350.

16. S. E. Moya, A. Ilie, J. S. Bendall, J. L. Hernandez-Lopez, J. Ruiz-García, and W. T. S. Huck, *"Assembly of polyelectrolytes on CNTs by Van der Waals interactions and fabrication of LBL polyelectrolyte/CNT composites,"* Macromolecular Chemistry and Physics, vol. 208, no. 6, 2007, doi: 10.1002/macp.200600530.
17. N. Agrawal, S. Gaur, K. V. Mani, and R. Arora, *"Carbon Nanotubes/Polyurethane Foam for Noise Passivation at 4000 Hz,"* ACS Applied Nano Materials, vol. 7, no. 1, 2024, doi: 10.1021/acsanm.3c03866.

Mössbauer Spectroscopic Study of Sub – Surface Samples of the DND#28 Well of the Jaisalmer Basin Located in Western Rajasthan, India

Hemant Dhaka[a], and Samay Singh Meena[b]

Department of Physics, Jai Narain Vyas University, Jodhpur, Rajasthan, India.

[a] hdhaka810@gmail.com
[b] ssmeenaphy12@gmail.com

Abstract

The Jaisalmer Basin is a pericratonic basin located on the northwest slope of the Jaisalmer Mari foundation arch that deepens southwest. With a dip angle of 30 to 50, the basin is late Paleozoic-Mesozoic and is made up of Permian rocks that unconformably rest on Proterozoic foundation. The sedimentary samples of the Pariwar Formation from the Danewala well DND#28 in the Jaisalmer Basin were the subject of the current Mössbauer spectroscopic investigation. The primary iron-bearing minerals include siderite, pyrite, and Fe^{3+} and Fe^{2+} in clay. When humic organic matter is present, the presence of Fe^{3+} in clay is more favourable, and siderite indicates that the source rocks are not as mature.

Keywords: Basin, Clay, Mineralogy, Mössbauer, Sediments.
Received 30 January 2025; First Review 14 February 2025; Accepted 19 March 2025.

*** Address of correspondence**
Hemant Dhaka
Department of Physics, Jai Narain Vyas University, Jodhpur, Rajasthan, India.

Email: hdhaka810@gmail.com

How to cite this article
Hemant Dhaka, and Samay Singh Meena, Mössbauer Spectroscopic Study of Sub – Surface Samples of the DND#28 Well of the Jaisalmer Basin Located in Western Rajasthan, India, J. Cond. Matt. 2025; 03 (01): 126-128.

Available from:
https://doi.org/10.61343/jcm.v3i01.119

Introduction

The source rocks are thought to be the sediments that contain organic stuff. The only substance used to generate hydrocarbons is these source rocks. The maturity and quality of a basin's source rocks have a substantial impact on its hydrocarbon potential and accumulation pattern. One important factor in the characterisation of source rocks is the degree of diagenesis of the inorganic minerals. ^{57}Fe Mössbauer spectroscopy may be used to analyze Iron-containing minerals, including pyrite, carbonates, clay minerals, and oxides that are found in the inorganic materials associated with organic rich sediments [1-2].

Siderite is form diagenetic and redox condition during deposition as early diagenesis, shortly after sediment deposition, through the interaction of iron-rich pore waters and carbonate ions and also the reduction of iron oxides and hydroxides can lead to the formation of siderite and anoxic environments, where the lack of oxygen prevents the oxidation of iron and allows the formation of iron carbonate minerals. Reducing conditions, such as those found in sediments with high levels of organic matter, can also favour the formation of siderite [3-6]. The presence of siderite, calcite, and dolomite suggests a shallow marine to lacustrine depositional environment [7].

Mössbauer spectroscopy study also compared with other analyse technologies like SEM-EDS and XRD. SEM-EDS provides elemental analysis, including iron, but does not offer information on the iron oxidation state or coordination environment other hand Mössbauer spectroscopy provides detailed information on the iron-bearing phases [8-9]. And XRD cannot directly determine the iron oxidation state, whereas Mössbauer spectroscopy can provide information on the iron oxidation state and coordination environment. [10]. The current study used ^{57}Fe Mössbauer spectroscopy to examine The Lower Cretaceous sedimentary sequence of well DND#28, dug in the Danewala structure of the Jaisalmer basin, contains sedimentary materials from the Pariwar formation at different depths. Mössbauer spectroscopy is a valuable tool for identifying iron-bearing minerals [11-13].

The method has been applied to coal, oil shale, and rocks that are sources of petroleum to investigate the iron's chemical composition. The studies give helpful information regarding the use of fossil fuels. This method is often used to study geological samples, encompassing every kind of

sediment. The state of sedimentary iron metal oxidation is a well-known indication of the oxidation reduction condition of sedimentation [14-18].

In order to better We have restricted our investigation to Cretaceous sediments in order to comprehend the relative distribution of iron-bearing minerals with depths and ascertain whether the presence or lack of these minerals is correlated with the environment of deposition, which in turn determines the rate of sedimentation, a critical parameter in assessing the quality of organic matter for hydrocarbon prospecting in a basin. The presence of organic-rich shales and the mineralogical evidence for anoxic conditions suggest a high potential for source rock formation.

Method

In a sample holder (25 mm in diameter), finely ground sediment samples were sandwiched between two paper discs to form Mössbauer absorbers.

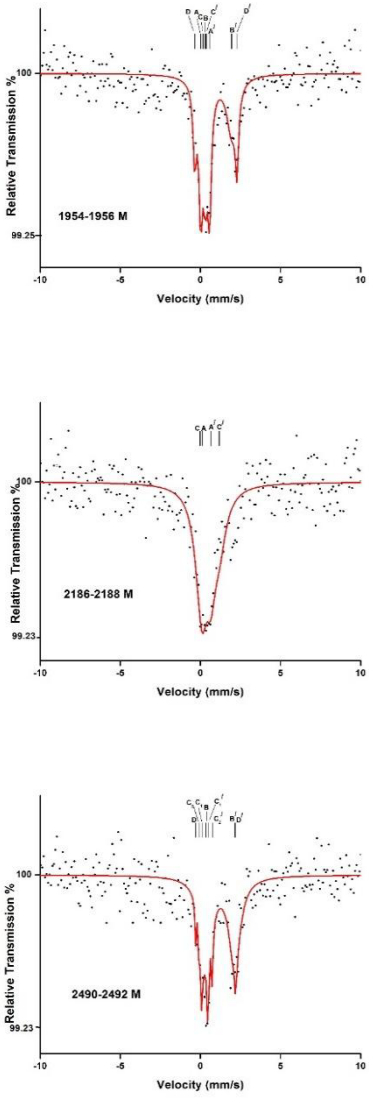

Figure 1: Mössbauer spectra of the samples at room temperature

Table 1: Mössbauer parameters of the samples of Pariwar formation of well DND#28

Depth	Peaks	IS (mm/s)	QS (mm/s)	LW	RA	X^2	Assignment
1954-1956 M	AA/	0.29	0.55	0.24	27.7	1.61	Pyrite
	BB/	1.11	1.92	0.76	45.1		Siderite
	DD/	0.96	2.63	0.24	19		Fe^{2+} in clay
	CC/	0.31	0.09	0.24	8.2		Fe^{3+} in clay
2186-2188 M	AA/	0.34	0.66	0.73	49	1.26	Pyrite
	CC/	0.58	1.19	1.06	51		Fe^{3+} in clay
2228-2230 M	CC/	0.55	0.34	0.78	61.6	1.17	Fe^{3+} in clay
	NN/	0.04	0.41	0.92	38.4		Non identify
2370-2372 M	C_1C_1/	0.18	0.77	0.61	38.2	1.14	Fe^{3+} in clay
	C_2C_2/	0.32	0.27	0.67	61.8		Fe^{3+} in clay
2490-2492 M	BB/	1.24	1.78	0.84	81.2	1.12	Siderite
	C_1C_1/	0.29	0.37	0.07	8		Fe^{3+} in clay
	C_2C_2/	0.39	0.81	0.07	6.9		Fe^{3+} in clay
	DD/	0.95	2.52	0.07	3.9		Fe^{2+} in clay

The thickness of the absorbers remained constant. Using a typical constant acceleration spectrometer, Mössbauer spectra were recorded at room temperature (300K) using a 10 mCi source in a Pd-matrix. The experimental setup's specifics are comparable to those previously described by Nigam et al. [19]. A 25 µm thick α-iron foil spectrum's centroid has been used to report the isomer shift (IS). A computer program created by Meerwall was used to suit each spectrum [20].

Discussion

The Danewala structure from the Jaisalmer basin is where the well DND#28 is situated. ^{57}Fe Mössbauer spectroscopy was used to analyse sedimentary samples from the Pariwar Formation at different depths in the upper Cretaceous succession. Figure shows the typical Mössbauer spectra of well DND#28 that were taken at ambient temperature. AA/

attributes pyrite, BB/ attributes siderite, CC/ attributes Fe^{3+} in clay, DD/ attributes Fe^{2+} in clay, and NN/ attributes an unidentified peak. The depth at which the sample is obtained is shown in the graphic itself.

Conclusion and Future Prospective

All of the samples used in this investigation have a noticeable amount of Fe^{3+} in clay, Presence of Fe^{3+} in clay is more favorable when the humic type of organic matter is present and presence of siderite shows the poor maturity of source rocks. The presence of siderite, calcite, and dolomite suggests a shallow marine to lacustrine depositional environment. So the rock is immature and in future they will be matured as compression of hydrocarbon prospects. The presence of organic-rich shales and the mineralogical evidence for anoxic conditions suggest a high potential for source rock formation.

References

1. G M Bancroft, *"Mössbauer Spectroscopy: An Introduction for Inorganic Chemists and Geochemists"*, McGraw-Hill. 1973.
2. S Mørup, J Franck, *"Mössbauer spectroscopy study of the chemical state of iron in Danish Mesozoic sediments"*, Fuel, 64: 528–538,1985.
3. Curtis, C. D., *"Geochemistry of diagenesis in sediments. In A. Parker & B. W. Sellwood (Eds.)"*, Sediment diagenesis,15–34,1983.
4. Canfield, D. E., *"Reactive iron in marine sediments"*, Geochimica et Cosmochimica Acta, 53: 619–632, 1989.
5. Berner, R. A., *"A new geochemical classification of sedimentary environments"*, Journal of Sedimentary Petrology, 51: 359–365,1981.
6. Froelich, P. N., *"Early oxidation of organic matter in pelagic sediments of the eastern equatorial Atlantic: suboxic diagenesis"*, Geochimica et Cosmochimica Acta, 43: 1075–1090, 1979.
7. Tucker, M. E., *"Sedimentary petrology: An introduction to the origin of sedimentary rocks"*, Wiley-Blackwell, 2001.
8. Reed, S. J. B., *"Electron microprobe analysis"*, Cambridge University Press, 1993.
9. Hawthorne, F. C., *"Mössbauer spectroscopy. In F. C. Hawthorne (Ed.), Spectroscopic methods in mineralogy and geology"*, Mineralogical Society of America: 255–274, 1988.
10. Coey, J. M. D., *"Mössbauer spectroscopy of iron in clay minerals. In J. E. Firth (Ed.), Clay minerals: Their structure, properties, and uses"*, Royal Society of Chemistry: 191–206,1984.
11. S Ram, *"Distribution of iron in siderite in sub-surface sediments of Jaisalmer Basin (India) using Mössbauer spectroscopy"*, Fuel, 77: 1507–1512,1998.
12. B Bhatia, *"Mössbauer spectroscopic study of sediments collected from test wells drilled in the Bikaner-Nagaur Basin"*, Fuel, 98: 140–148,2012.
13. R P Tripathi, *"Fe Mössbauer spectroscopy study of organic rich sediments (source rocks) from test well CT-1, Chinnewala structure of Jaisalmer basin, India"*, Geosciences Frontiers, XXX: 1–6,2015.
14. S S Meena, *"Mössbauer Spectroscopic Study of the Sedimentary Samples Collected from Barmer Hill Formation of Northern Barmer Basin, Western Rajasthan (India)"*, IJIRET, 5: 1558–1560,2016.
15. S S Meena, *"Fe Mössbauer Spectroscopic Study of Sedimentary Samples from Goru Formation in Well MNW-1 of Jaisalmer Basin, Rajasthan, India"*, Journal of Pure and Applied Science & Technology, 7: 18–26,2017.
16. R Pandey R, A S Maurya, *"Hydrocarbon Uncertainty Based on Facies Analysis: Middle Jurassic Sequence (Jaisalmer Formation), Jaisalmer Basin, Rajasthan"*, Journal Geological Society of India, 95:301−307,2020.
17. M Bohra, *"Mössbauer spectroscopy study of Samples from Cambay Shale Formation, Cambay Basin, in context of Shale Oil"*, Journal Geological Society of India, 96: 603−608, 2020.
18. S Ram, *"Estimation of Environment of Sedimentary Deposition in Parh Formation of Tertiary Sediments of Jaisalmer Basin, Rajasthan, India"*, Applied Ecology and Environmental Sciences, 10: 802−805,2022.
19. A N Nigam, R P Tripathi, H S Singh, R S Gambhir and N G Lukose, *"Mössbauer studies on Ghotaru Well No.1 of Jaisalmer Basin"*, Fuel, 68:209–212,1989.
20. E V Meerwall, *"A least-squares spectral curve fitting routine for strongly overlapping Lorentzians or Gaussians"*, Computer Physics Communications, 9: 117–128,1975.

Applications of Rare Earth Metal Ion-Embedded Nano Ferrites in Dye Removal from Water

Ashvini V Meshram[1,a], Indrani B Das Sarma[2,b] and Kishor M Hatzade[3,c]

[1] *Department of Chemistry, M. B. Patel College, Deori, Maharashtra, India.*
[2] *Department of applied science and humanities, Jhulelal Institute of Technology, Nagpur, Maharashtra, India.*
[3] *Department of Chemistry, Dhote Bnadhu Science College, Gondia, Maharshtra, India*

[a] ashvinim20@gmail.com
[b] dassarmaindrani@gmail.com
[c] kishorhatzade@gmail.com

Abstract

Nano-ferrites are proved to be a powerful and commendable material nowadays for removal of hazardous pollutants from waste water. Incorporation of rare earth metal ions into these metal ferrites alters the characters of specific metal nano-ferrites. In this study, Lanthanum doped (x=0,0.1,0.3,0.5) cobalt ferrites ($CoLa_xFe_{2-x}O4$) were prepared via sol-gel synthesis. Synthesized doped nano-ferrites were characterized through FTIR, XRD (26.74 nm, 7.66 nm, 39.57 nm and 2.12 nm), SEM-EDX and SEM techniques. The impact of incorporation of lanthanum ions on adsorption efficiency of different nano-ferrites material was checked to the adsorption of methylene blue dye and Rhodamine B dye and the results were compared.

Keywords: Lanthanum Doped Nano-Ferrites; Characterization; Adsorption; Dye Removal Efficiency; Methylene Blue.
Received 31 January 2025; First Review 10 March 2025; Accepted 19 March 2025.

*** Address of correspondence**
Ashvini V Meshram
Department of Chemistry, M. B. Patel College, Deori, Maharashtra, India.

Email: ashvinim20@gmail.com

How to cite this article
Ashvini V Meshram, Indrani B Das Sarma and Kishor M Hatzade, Applications of Rare Earth Metal Ion-Embedded Nano Ferrites in Dye Removal from Water, India, J. Cond. Matt. 2025; 03 (01): 129-132.

Available from:
https://doi.org/10.61343/jcm.v3i01.133

Introduction

Water body contamination is one of the main issues with environmental degradation that exists today. Because of the presence of multiple contaminations less than 1% of the total water is fit for human consumption [1]. Unusual industrial and population growth led to environmental problems, which prompted scientists to look for cutting-edge materials to adapt to the new environment [2]. Adsorptive removal involves physically removing of pollutant molecules by filtering them after they have been adsorbed on the particle surface. Pollutants that are exposed to light causing electron-hole generation on the particle surface, which initiates electron transfer processes that lead to chemical deterioration through photocatalytic degradation [3].

The most frequent waste that the textile and printing industries discharge into water bodies is dyes. Due to their complicated aromatic structure and resistance to heat, light, and chemicals, these colours biodegrade extremely slowly [4]. These dyes can penetrate the food chain and cause a variety of deadly diseases in humans by way of other living species. They can also produce a large number of secondary products through a sequence of photochemical and physiochemical reactions. Therefore, it is crucial to remove these dangerous pigments from water [5].

Adsorbent materials such as clay, zeolite, metal oxides, activated carbon, and carbon allotropes are frequently utilised in the removal of dyes. Although clay, activated carbon, and metal oxide-based adsorbents have strong adsorption efficiency, their usage is limited by a number of drawbacks, such as the production of sludge, high regeneration costs, the high cost of activated carbon, and the leaching effect's ability to remove metal oxides [6]. Methylene blue (MB) is a substance with a wide range of uses. It is used in the photo-reducible dyes used in galvanic cells in industry, as oxygen detectors in vacuum-packed food items, as an electrochromic material in windows, sun roofs, and rear-view mirrors, as well as staining, bacteriology, and microscopy in medicine. However, when consumed by people, it results in a number of health issues. Because of this, dyes shouldn't be released into natural sources or effluents unless they have first undergone partial or complete elimination procedures [7].

Method

The reagents used in 1:2 ratios to produce the cobalt ferrite through sol-gel synthesis. $Fe(NO_3)_3.9H_2O$, $Co(NO_3)_2.6H_2O$ and Urea were dissolved in 30 mL of deionized water. Three other compositions also were prepared using $La(NO_3)_3.6H_2O$ to produce samples with the formula $CoLa_xFe_{2-x}O_4$, with x values of 0.1, 0.3 and 0.5. In order to obtain the products, the precursors in solution were heated to 85 °C for 3 h under magnetic stirring until a gel was achieved. Subsequently, the gel was dried at microwave oven on 900 volt for 6 minutes, then it was crushed in Morton-piston for 12 hours then it was transferred to an alumina crucible and treated in a muffle furnace at 300 °C for 20 h to ensure the complete decomposition of organics. Finally, the characterization of the black powder was carried out. Crystalline structures of the samples were characterized in an X-ray diffractometer (XRD, Philips, X'pert MPD) equipped with a CuKα source with step size 0.02° and a 2θ range of 10-90 degree. ICSD data banks were used for the identification of the resulting crystalline phases. The shape and morphology of the particles were analysed using scanning electron microscopy (SEM). Fourier transform infrared (FT-IR) spectrum is recorded on Perkin Elmer 2000 FT-IR spectrometer in KBr pellets. EDX is done to confirm the chemical composition of the ferrites. Adsorption of methylene blue dye and Rhodamin B dye is studied by dissolving 0.01 g of ferrites and stir it for 30 minutes. The stock solution of 1 ppm was prepared and 25 Ml was taken for the adsorption study. The adsorption is taken at two different Ph acidic and basic which is adjusted using (0.1 mol/L) HCL and NaOH. The absorbance was recorded for the interval of the 5 minutes on SHIMADZU UV Spectrophotometer, UV-1800.

Discussion

Characterization: In this study, different techniques (FTIR, XRD, EDX-SEM and SEM) were used to characterised the prepared lanthanum doped cobalt ferrites. The FTIR spectrum of synthesised ferrites within the wavelength range 400 to 4000 cm^{-1} is shown in figure 1. In the spectrum, the absorption peaks at 525 cm^{-1} and 446 could be ascribed to stretching vibration of metal-oxygen bond (Fe-O) at octahedral and tetrahedral sites, respectively. These two peaks suggest the formation of spinel ferrite-type oxide [8]. The absorption peak at 1036 cm^{-1} could be attributed to NO_3-group [9]. But this peak is not observed in case on $CoLa_{0.3}Fe_{1.7}O_4$. This indicates the structural changes at the x=0.3 doped ferrite. The observed peak at 2350 cm^{-1} is assigned to the C-H vibration.

Figure 2 displays the XRD patterns of doped ferrites samples made using the sol-gel method. Indexed as (220), (311), (222), (400), (422), (511), (440), (533) and (622)

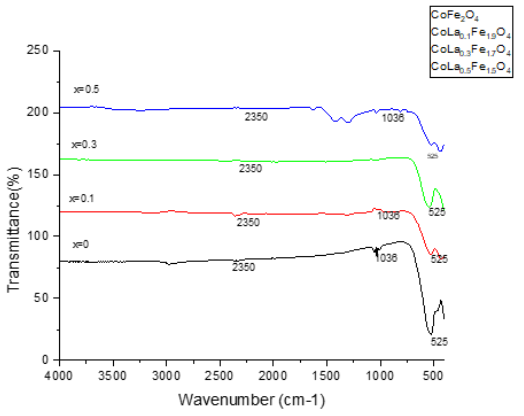

Figure 1: FTIR Spectrum of $CoLa_xFe_{2-x}O_4$ (x=0, 0.1, 0.3, 0.5).

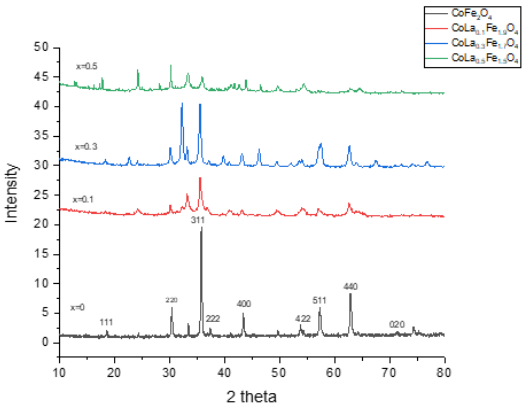

Figure 2: XRD Pattern obtained for $CoLa_xFe_{2-x}O_4$ (x=0.1, 0.3, 0.5).

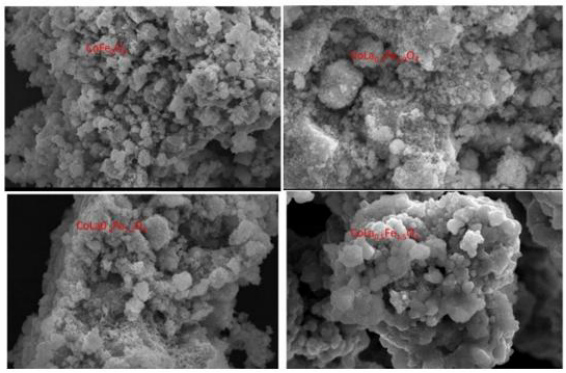

Figure 3: SEM images of $CoLa_xFe_{2-x}O_4$ (x=0, 0.1, 0.3, 0.5).

planes, the well-defined peaks that have been detected correspond to a single phase with cubic spinel. The broadening of the peaks is due to nano size of the crystalline particles. The size is calculated using Debey-Sherrer formula and is found that 26.74 nm, 7.66 nm, 39.57 nm and 2.12 nm for $CoLa_xFe_{2-x}O_4$ from x=0, 0.1, 0.3 and x=0.5 respectively. The extra peaks found at for the x =0.3 dopes ferrites. This also indicates the change in the structure of this doped ferrites.

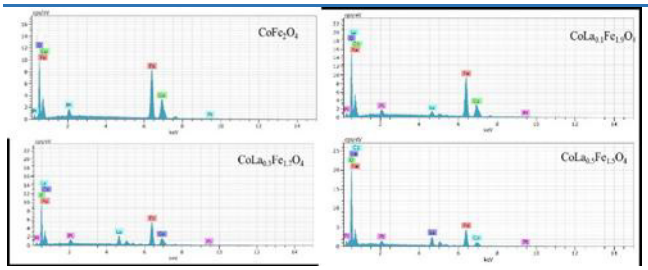

Figure 4: EDX of $CoLa_xFe_{2-x}O_4$ (x=0, 0.1, 0.3, 0.5).

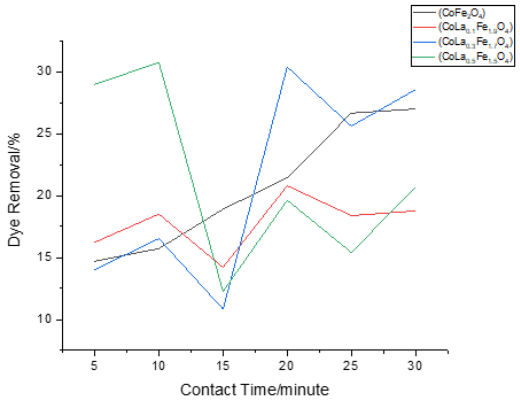

Figure 5: Effect of contact on MB removal percentage (Acidic medium).

Scanning electron microscopy (SEM) wad used to investigate the surface morphology of the synthesised ferrites, as shown in figure 3. As can be seen from the SEM image, the surface of ferrites consists of large grains which are surrounded by small particles. It is observed from the images that for cobalt ferrite x =0.3 doped ferrite the particle is well dispersed but in case of x =0.1 and 0.5 observed the cluster.

The SEM-EDX is shown in the figure 4, this elemental analysis shows the presence of the elements Co, La and Fe. The increased concentration was seen as the increase in height of peaks of Lanthanum from 0.1 to 0.3.

Effect of contact time for MB dye: Figure 5 shows the effect of contact time on the removal percentage of methylene blue. In this experiment, the contact time was changed and the removal percentage increases with time. It is observed that maximum efficiency reached the 30% for $CoLa_{0.3}Fe_{1.7}O_4$. It has been found that with increase in doping percentage of lanthanum contact time of for the adsorption required less in acidic medium. In the basic medium, $CoFe_2O_4$ adsorbed good as compared to the lanthanum doped cobalt ferrites.

Effect of contact time for Rhodamine B dye: Figure 7 shows as the contact time increases the dye removal capacity in acidic medium. The dye removal percentages increase from $CoFe_2O_4$ to $CoLa_xFe_{2-x}O_4$ as the concentration of lanthanum

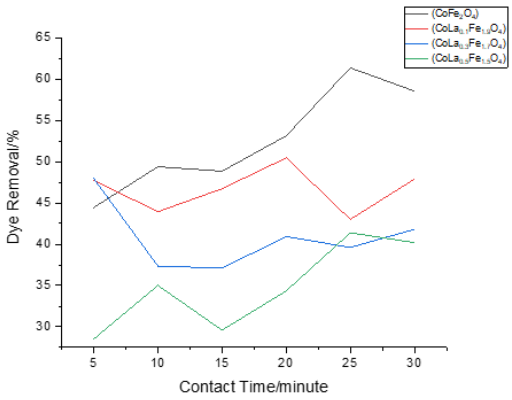

Figure 6: Effect of contact on MB removal percentage (Basic medium).

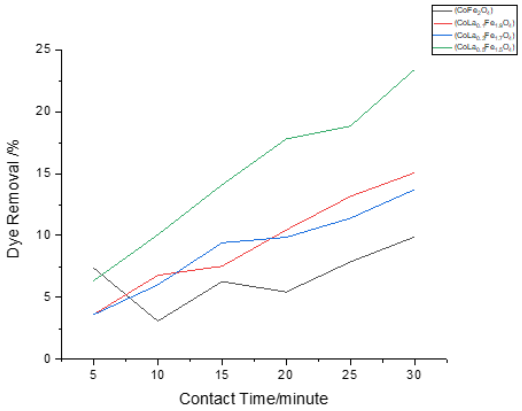

Figure 7: Effect of contact on Rhodamine B removal percentage (Acidic medium).

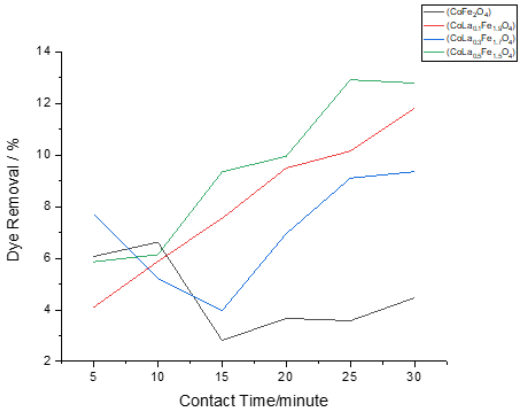

Figure 8: Effect of contact on Rhodamine B removal percentage (Basic medium).

increases. The maximum efficiency is 23.39% for $CoLa_{0.5}Fe_{1.5}O_4$.

Figure 8 shows the dye removal % in basic medium. It is observed that with increase in contact time % removal increases. Also, with increase in the doping concentration % removal increased.

Conclusion and Future Prospective

In summary, the ferrites $CoLa_xFe_{2-x}O_4$ where x=0, 0.1, 0.3, 0.5 synthesised successfully. Dye removal efficacy increases with increase in contact time and increase with lanthanum doping in case of Rhodamine B dye in acidic and basic medium with maximum efficiency reached to 23.29 %. in case of methylene blue dye with increase in contact time dye removal % increase but the maximum efficiency is found for $CoLa_{0.3}Fe_{1.7}O_4$. This is due to the structural changes found in this ferrite. Comparing the acidic and basic medium dye removal %, in methylene blue dye in acidic medium removal is less as compared to basic one. In case of Rhodamine B dye, in acidic medium the dye removal % is more as compared to the basic medium.

This result can be used to waste water treatment release from industries. The water may be acidic or basic depending upon the which type of industry, so the both acidic and basic medium results are helpful form the purification of water.

References

1. Mariosi, Fabricio Ravanello et al, *"Lanthanum-doped spinel cobalt ferrite ($CoFe_2O_4$) nanoparticles for environmental applications",* Ceramics International 46.3 (2020): 2772-2779.
2. Keerthana, S. P. et al, *"Synthesis of pure and lanthanum-doped barium ferrite nanoparticles for efficient removal of toxic pollutants",* Journal of Hazardous Materials 424 (2022): 127604.
3. Singh, Somendra, Yogendra Yadawa, and Amit Ranjan, *"Enhanced adsorption of methylene blue by mixed-phase bismuth ferrite prepared by non-aqueous sol-gel route"*, Journal of Environmental Chemical Engineering 11.1 (2023): 109229.
4. Chahar, Deepika et al, *"Visible light induced photocatalytic degradation of methylene blue dye by using Mg doped Co-Zn nanoferrites"*, Materials Research Bulletin 162 (2023): 112205.
5. Haider, Sajjad et al, *"Visible light active Cu-doped iron oxide for photocatalytic treatment of methylene blue"*, Ceramics International 48.6 (2022): 7605-7612.
6. Abbasi, Muhammad Ali et al, *"Congo red removal by lanthanum-doped bismuth ferrite nanostructures"*, Journal of Physics and Chemistry of Solids 170 (2022): 110964.
7. Cabrera, A. F. et al, *"Degradation of methylene blue dye under dark and visible light conditions in presence of hybrid composites of nanostructured $MgFe_2O_4$ ferrites and oxygenated organic compounds"*, Journal of Environmental Chemical Engineering 8.5 (2020): 104274.
8. Kumar L., Kumar P., Kar M.J. Alloy. Compounds, 2013, 551:72.
9. Konicki, Wojciech, et al, *"Equilibrium and kinetic studies on acid dye Acid Red 88 adsorption by magnetic $ZnFe_2O_4$ spinel ferrite nanoparticles"*, Journal of colloid and interface science 398 (2013): 152-160.
10. Zhao, Xiruo, et al, *"Synthesis and characterization of gadolinium doped cobalt ferrite nanoparticles with enhanced adsorption capability for Congo Red",* Chemical Engineering Journal 250 (2014): 164-174.
11. Keerthana, S. P., et al, *"Pure and Ce-doped spinel $CuFe_2O_4$ photocatalysts for efficient rhodamine B degradation"*, Environmental Research 200 (2021): 111528.
12. Juna, Byung-Moon, et al, "Accelerated photocatalytic degradation of rhodamine B over carbonate-rich lanthanum-substituted zinc spinel ferrite assembled reduced graphene oxide by ultraviolet (UV)-activated persulfate",
13. Abdo, M. A., Reem Al-Wafi, and M. S. AlHammad, *"Highly efficient visible light driven photocatalytic activity of rare earth cerium doped zinc-manganese ferrite: Rhodamine B degradation and stability assessment"*, Ceramics International 49.17 (2023): 29245-29258.
14. Samoila, Petrisor, et al, *"Boosting catalytic wet-peroxide-oxidation performances of cobalt ferrite by doping with lanthanides for organic pollutants degradation"*, Journal of Environmental Chemical Engineering 9.1 (2021): 104961.
15. Jamaludin, N., et al, *"Photocatalytic degradation of rhodamine B dye under visible light using cerium-cobalt co-doped bismuth ferrite nanoparticles"*, Journal of Physics: Conference Series. Vol. 2432. No. 1. IOP Publishing, 2023.
16. Pardhi, Khushboo T., et al, *"Ionizing Radiation Induced Structural Modification in Nanoferrites"*, (2024).

Solitons in Discrete Waveguides

Ramesh Kumar[1,3,a], U. Singh[1,2], A. K. Nagar[1] and O. P. Swami[1]

[1] *Department of Physics, Govt Dungar college, Bikaner, 334001, Rajasthan, India.*
[2] *Department of Physics, SRRM Govt College, Jhujhunu, 333001, Rajasthan, India.*
[3] *Department of Physics, SNDB Govt PG College, Nohar, Hanumangarh, 335523, Rajasthan, India.*

[a] rphysics52@gmail.com

Abstract

We analyse soliton stability in discrete waveguides, revealing the impact of waveguide parameters and nonlinearity. Our analysis reveals the impact of waveguide parameters and nonlinearity on soliton stability, identifying design guidelines for stable propagation.

Keywords: Soliton Stability, Discrete Waveguides, Nonlinearity, Design Guidelines.
Received 28 January 2025; First Review 17 March 2025; Accepted 24 March 2025.

*** Address of correspondence**
Ramesh Kumar
Department of Physics, SNDB Govt PG College, Nohar, Hanumangarh, 335523, Rajasthan, India.

Email: rphysics52@gmail.com

How to cite this article
Ramesh Kumar, U. Singh, A. K. Nagar and O. P. Swami, Solitons in Discrete Waveguides, India, J. Cond. Matt. 2025; 03 (01): 133-134.

Available from:
https://doi.org/10.61343/jcm.v3i01.79

Introduction

Solitons are stable, localized waves that resist dispersion. In discrete waveguides, nonlinearity and coupling effects enable soliton formation with distinct characteristics compared to continuous media [1]. Discrete solitons have been observed in various physical systems, including optical waveguide lattices, Bose-Einstein condensates, and DNA molecules [2,3]. This study explores the behaviors of onsite and intersite discrete solitons, relevant for photonics applications.

Theoretical Background

Discrete solitons in waveguide lattices follow the discrete nonlinear Schrödinger equation:

$$i\frac{dA_n}{dz} + \eta A_n + \beta(A_{n+1} + A_{n-1}) + \gamma|A_n|^2 A_n = 0$$

where A_n the wave amplitude at site n, β is the coupling coefficient, and γ denotes nonlinearity. The linear terms $\beta(A_{n+1} + A_{n-1})$ describe tunneling (or diffraction) of the wave between adjacent lattice sites. The nonlinear term $\gamma|A_n|^2 A_n$ accounts for self-phase modulation, which can lead to localized solutions (solitons). This equation captures the interplay between diffraction, coupling, and nonlinearity, leading to solitonic behavior [4,5].

Types of Solitons

1. Onsite Solitons

Onsite solitons are localized at a single lattice site, meaning their energy or amplitude is concentrated at a particular point in the discrete lattice. These solitons typically emerge in discrete nonlinear Schrödinger equations (DNLS) and other nonlinear lattice models.

Key Characteristics of Onsite Solitons

Strong Localization: The wave function is sharply peaked at one site.

High Stability: Due to their strong localization, onsite solitons are often more stable compared to intersite solitons.

Discreteness Effect: Unlike continuous solitons, onsite solitons experience lattice discreteness, which prevents them from dispersing.

2. Intersite Solitons

Intersite solitons are cantered between two adjacent lattice sites, meaning they are not localized at a single site but rather spread across two or more sites.

Key Characteristics of Intersite Solitons

Weaker Localization: The energy is distributed over multiple sites, usually peaking between two adjacent sites.

Lower Stability Compared to Onsite Solitons: Since their energy is less confined, intersite solitons can be more susceptible to perturbations.

Existence in Various Nonlinear Lattices: Found in photonic lattices, Bose-Einstein condensates, and discrete waveguide arrays.

Methodology

Using numerical simulations, we explored soliton behavior by varying β and γ values, initializing with single-site (onsite) and dual-site (intersite) excitations.

Results

Onsite solitons remained confined and stable, with minimal energy leakage [6]. Intersite solitons required higher coupling for stability and showed sensitivity to small perturbations. Figure 1(a) and (b) shows Onsite and Intersite Soliton Profiles illustrates the distinct spatial distributions of both soliton types. Onsite solitons exhibit strong localization, whereas intersite solitons spread across multiple lattice sites due to coupling effects.

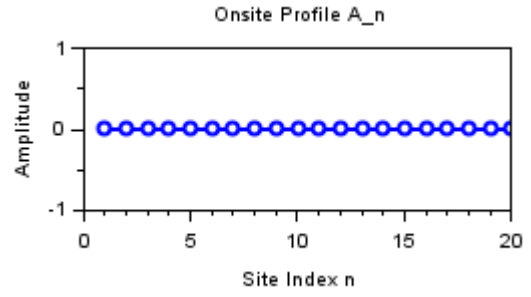

Figure 1(a): Onsite soliton profile.

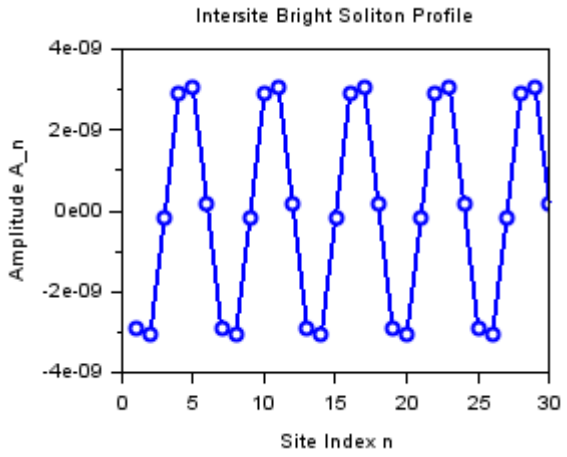

Figure 1(b): Intersite Soliton Profiles

For onsite Profile

Parameters

η =1, β = 0.5, γ = 0.2, n = 20

Intersite Bright Soliton Profile

Parameters

η = -1, β = 1, γ = 0.5, n = 30

Conclusion

Onsite solitons demonstrate greater stability and resilience to parameter variations than intersite solitons. These findings offer insights into discrete solitons potential for robust light localization in photonic applications.

References

1. Christodoulides, D. N., Lederer, F., & Silberberg, Y. (2003), "*Discretizing light in waveguide lattices",* Nature, 424(6950), 817-823.
2. Fleischer, J. W., Segev, M., Efremidis, N. K., & Christodoulides, D. N. (2003), *"Observation of two-dimensional discrete solitons in optically induced photonic lattices"*, Nature, 422(6928), 147-150.
3. Kumar, R., Singh, U., Swami, O., Suthar, G., & Nagar, A. (2024), *"Existence and Stability of Discrete Intersite Bright Solitons in Bose Einstein condensates in parabolic trapped optical lattices"*. AIP Conference Proceeding, 3149 (1), 1-5.
4. Kevrekidis, P. G., Bishop, A. R., & Weinstein, M. I. (2001), *"Modulational instability in discrete nonlinear Schrödinger systems"*, Physica D: Nonlinear Phenomena, 142(1-2), 87-100.
5. Lederer, F., Stegeman, G. I., Christodoulides, D. N., et al. (2008), *"Discrete solitons in optics"*, Physics Reports, 463(1-3), 1-126.
6. Kivshar, Y. S., & Agrawal, G. P. (2003), *"Optical Solitons"*, Academic Press.

Study of the transport characteristics in LCMO (Perovskite manganite)-rGO nanocomposite System at various temperature for Resistive Switching (RS) Application

Tinku Kumar[1,a], Ashok Kumar Jha[1], Sumita Singh[1] and Shankar Kumar[2]

[1] *Department of Physics, Patna University, Patna, Bihar, India.*
[2] *Department of Physics, Patna Science College, Patna University, Patna, Bihar, India.*

[a] tinkujaymatadi@gmail.com

Abstract

Intensive studies of resistive switching mechanisms in oxide systems have been studied extensively due to its great potential prospect in non-volatile memory applications. Several materials are well-explored for the Resistive Switching (RS) phenomenon as binary oxides, polymers, perovskites, chalcogenides and even 2-D materials. The investigation for the best material offering RS behaviour is still going on some magnetite like ($Pa_{0.7}Ca_{0.3}MnO_3La_{0.7}Sr_{0.3}MnO_3$) also depicts the RS behaviour and their performance are limited by the random. Oxygen vacancies perform a vital role in initiating the resistive switching (RS) phenomenon in oxide-based systems. The random oxygen vacancies can be limited by two methods (1) by doping and (2) by forming nanocomposite. Interest has grown in understanding to perovskite material. Among the several oxide materials, oxygen vacancies are introduced in oxide-based systems using the synthesis method itself. So, lanthanum calcium manganites ($La_{0.3}Ca_{0.7}MnO_3$) are taken as active materials due to their fascinating physical and electrical properties and study its RS effects, the small amount of reduced graphene oxide(rGO) in it.

Keywords: Perovskites, Manganites.
Received 28 January 2025; First Review 11 February 2025; Accepted 24 March 2025.

*** Address of correspondence**
Tinku Kumar
Department of Physics, Patna University, Patna, Bihar, India.

Email: tinkujaymatadi@gmail.com

How to cite this article
Tinku Kumar, Ashok Kumar Jha, Sumita Singh and Shankar Kumar, Study of the transport characteristics in LCMO (Perovskite manganite)-rGO nanocomposite System at various temperature for Resistive Switching (RS) Application, India, J. Cond. Matt. 2025; 03 (01): 135-138.
Available from:
https://doi.org/10.61343/jcm.v3i01.81

Introduction

Resistive switching (RS) mechanism in oxide system has been studied extensively due to its prospect in non-volatile memory application [1-5]. Several materials have been well explored for the RS phenomenon like, binary oxides, chalcogenides, polymers, perovskites and even 2-dimensional materials [6-9]. The quest for the best materials offering RS behavior is still going on. The manganites like ($Pa_{0.7}Ca_{0.3}MnO_3$, $La_{0.7}Sr_{0.3}MnO_3$) also depicts the RS behavior, but their performances are limited by the random oxygen vacancies [10-11]. In oxides-based system oxygen vacancies play an important role to initiate the RS phenomenon [12-15]. The introduction of oxygen vacancies into an oxides material may increase the probability of better RS behavior. The oxygen vacancies can be controlled by two approaches by doping or by making nanocomposite. Since nanocomposite approach is better and easier process than the doping and also has an advantage in terms of cost, processability, integrability and flexibility in the standard process [16-19]. Among several oxides materials, perovskite system has the advantages, that oxygen vacancies can be easily induced into the system by synthesis process itself. So, we have chosen a Lanthanum calcium manganites ($La_{0.7}Ca_{0.3}MnO_3$) as an active material because its shows fascinating physical and electrical properties and introducing small amount of reduced graphene oxide (rGO) as a nano-fillers in it to study the RS effects of it [20-22]. In this paper, we have studied the transport properties in LCMO (perovskite manganite)-rGO nanocomposite system at different temperature for RS application.

Experimental setup

$La_{0.7}Ca_{0.3}MnO_3$ (LCMO) polycrystalline sample was prepared using standard solid-state route. The LCMO powder is mixed with reduced graphene oxide (rGO) to make (1-x)LCMO.(x)rGO nanocomposite samples with varying the value of x from 0.001 to 0.005. X-ray diffraction (XRD), Field effect scanning electron microscope (FESEM), Raman spectroscopy, X-ray photoelectron spectroscopy (XPS), Transmission electron microscopy (TEM) measurements are performed to see the structural

properties of the samples. Keithley source meter was used to measure I(Current)-V(Voltage) characteristic of all the composite samples using two probe methods. The low temperature measurements were done in the liquid Nitrogen atmosphere using Keithley source meter interfaced with cryogenic probe station.

Results and Discussion

The structural properties of (1-x) LCMO. (x)rGO nanocomposite samples were analyzed by X-ray diffractometer and Raman spectroscopy. The Fig 1(a) and 1(b) shows the XRD pattern and Raman spectra of the nanocomposite samples respectively. The XRD pattern of LCMO shows the presence of secondary phase. As XRD did not detect the small concentration of rGO in the nanocomposite, Raman spectra show the presence of rGO in the nanocomposite with the Raman shift corresponding to D- and G-band at 1352 cm^{-1} and 1583 cm^{-1} respectively.

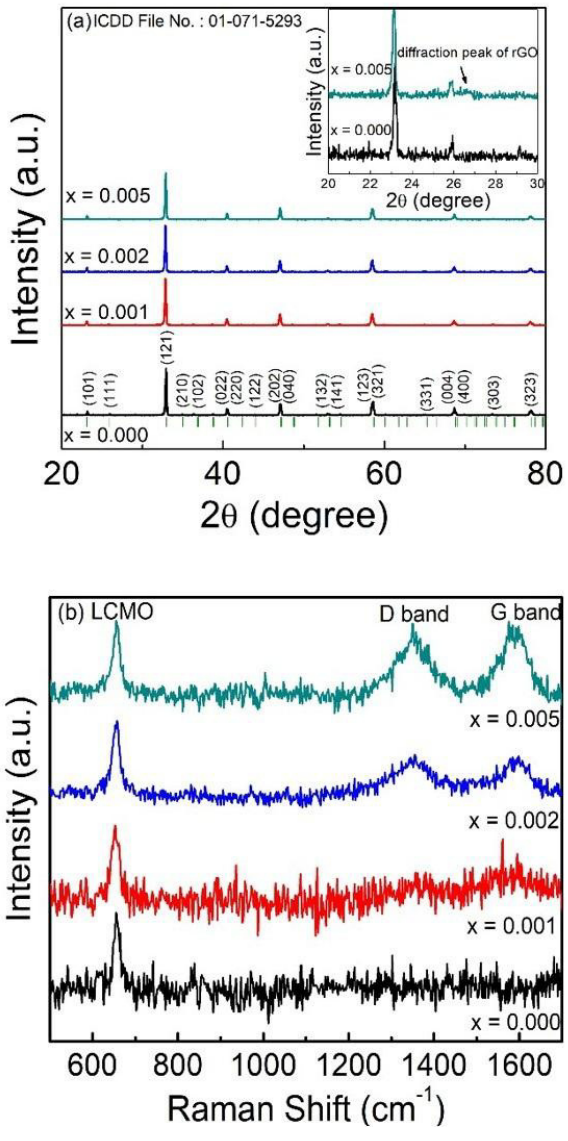

Figure 1: XRD pattern of (1-x)$La_{0.7}Ca_{0.3}MnO_3$.(x)rGO nanocomposite samples [23].

The RS behavior of the samples was study from the I vs V measurement done at room temperature. The I vs V measurement of the LCMO sample is shown in the Fig.2. The I vs V curve is observed after applying a voltage in the forward direction i.e, -3V to 3V. On reversing the direction of voltage, the current follows the same path and hence depicts the Ohmic nature. This exhibits that the LCMO sample does not show any hysteresis.

The I vs V measurement of the sample is shown in Fig.2(a-c). The compliance current is set to 200 mA before starting the experiment to avoid any breakdown. In the given sample, the forming is observed at 10.4 V. Once the sample is activated by electroforming, the I vs V measurement is performed. A pinched hysteresis I vs V loop is observed and is the fingerprint of a memristor.

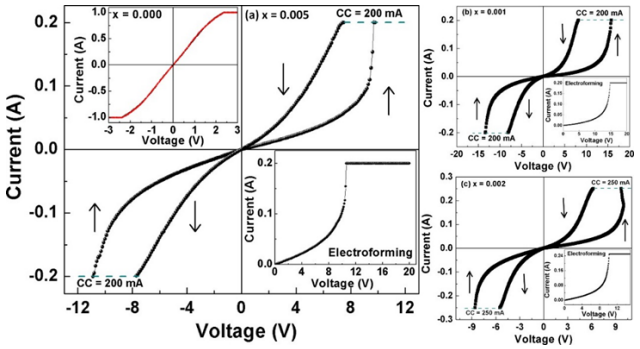

Figure 2: (a) I vs V measurement for (1-x) $La_{0.7}Ca_{0.3}MnO_3$.(x)rGO nanocomposite sample with x=0.005. (b) I vs V measurement of first cycle of x=0.001 and **(c)** x=0.002 [23].

As the voltage is increased the non-linear nature of current is observed and further increase in the voltage leads to a sudden change in the current at 9.8 V (V_{set}). The system changes its states from high resistance state to low resistance state. This is known as the SET process. Further, on application of negative voltage, the samples change its state of resistance from low resistance state to high resistance state at -9.4 V (V_{reset}) through the RESET process. The linear I vsV curve for x = 0.001 and 0.002 are shown in Fig. 2(b) and (c) respectively. It shows the forming process of both the samples. The process is repeated for performing the I vs V measurements of the other samples also. From the I vs V curves of all the samples under study, the steep increase in current region as SET state is observed and becomes more steeper for x = 0.005 as compared with the other samples. This suggests that the numbers of oxygen vacancies are lesser in the small concentration of x sample and hence it is not enough to make the filament type-conducting path within the samples. The steep increase in the current with increasing voltage for x = 0.005 may be due to the increase in the oxygen vacancies in the sample. Increase in oxygen vacancies allows formation of conducting path and it is the reason for the change of resistance state of the samples.

The plot of resistivity vs. temperature plot show that with the increase in rGO concentration, there is a shift in the metal to insulator transition temperature towards the low temperature range. This is shown in the Fig 3. The decrease in metal to insulator transition may be due to the creation of strain in the sample and hence a change in Mn-O-Mn angle.

To observe the effect of temperature in the RS behavior of the LCMO-rGO samples, the I vs V curve has been studied at different temperature, varying from 100 K to 250 K (Fig 4 a-b). The loss in the hysteretic nature was observed at lower temperature region (< 200 K). Further, as the temperature increases a decrease in the operating voltages are observed and are shown in Fig. 4(c).

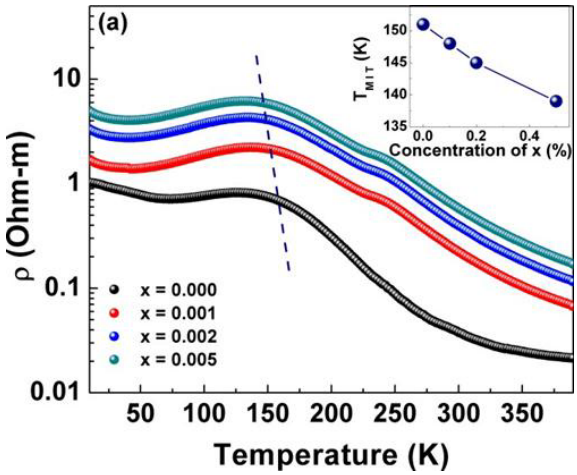

Figure 3: Resistivity vs. Temperature plot of (1-x) $La_{0.7}Ca_{0.3}MnO_3$.(x)rGO samples. The dashed line represents the metal-insulator transition temperature [23].

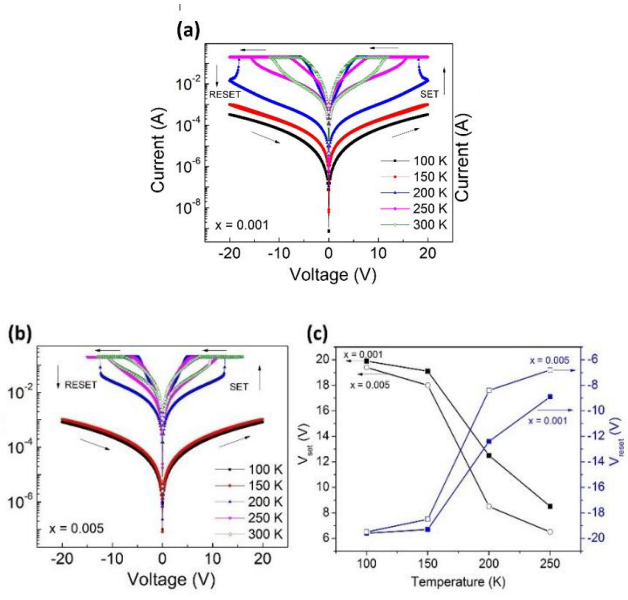

Figure 4: Temperature dependent I-V curve of (1-x) $La_{0.7}Ca_{0.3}MnO_3$.(x)rGO in semilogarithmic scale for **(a)** x=0.001 and **(b)** x = 0.005 varying from 100 K to 300 K. **(c)** Variation of operating voltages V_{set} and V_{reset} as a function of temperature [23].

Conclusion

The presence of both the phases in the nanocomposite is confirmed by structural characterization using XRD and Raman spectra of (1-x)$La_{0.7}Ca_{0.3}MnO_3$.(x)rGO. The I vs V curve of LCMO shows linear nature and retrace its path when the voltage is swept in the opposite direction, however, the nanocomposite sample with x = 0.005 shows the hysteresis in the I vsV curve and can be attributed to the resistive switching behavior. The material under study shows pinched off I vs V nature, which may be due to the memristor-type behavior. The RS behavior in the nanocomposite has been explained using conducting filament model and may be attributed to the creation of oxygen vacancy in the nanocomposite. The resistivity vs. temperature plot suggests that the metal insulator transition temperature decreases with the increase in the concentration of rGO in the sample. This may be attributed to the decrease in the concentration of oxygen and due to change of the Mn-O-Mn angles. The transport mechanism behind the I vs V curve gives better fit for space charge limited conduction in the linear variation of the current for the low bias region ($I \propto V$), exhibits quadratic dependence ($I \propto V^2$) for the intermediate voltage region (Child's law region) and steep increase in current region for the high bias region. The temperature dependent I-V nature suggests that the sample losses its hysteresis nature with the decrease in temperature. In addition, there is decrease in the V_{set} and V_{reset} is observed with increasing temperature.

Acknowledgement

Authors would like acknowledge the Minor Research Project funding by Patna University vide letter number S. No. 001/R&DC/RP/PU/Sanction Date. 26.08.2023 to Dr Ashok Kumar Jha, Assistant Professor, Department of Physics, Patna University for project entitled "A study of half Heusler, alloys for thermoelectric energy harvesting using density functional theory".

References

1. Y. Deng et al., Pesticide Biochemistry and Physiology 195, 105529 (2023). https://doi.org/10.1016/j.pestbp.2023.105529.
2. K. Kumari et al., Materials Research Bulletin 139, 111195 (2021).
3. S. K. Hong et al., IEEE Electron Device Lett. 31, 10051007 (2010).
4. C. He, Z. Shi et al., ACS Nano. 6, 42144221 (2012).
5. C.-Y. Liu et al., Nanoscale Res. Lett. 8, 156 (2013).
6. S. Seo, M. J. Lee et al., Appl. Phys. Lett., 85, 5655-5657 (2004).

7. B. J. Chol, D. S. Jeong et al., J. Appl. Phys. 98, 033715 (2005).
8. K. Park et al., Nanotechnology 27, 125203 (2016).
9. C. Y. Lin et al., J. App. Phys. 102, 094101 (2007).
10. W. W. Zhuang et al., Tech. Dig. Int. Electron Devices Meet. 193, (2002).
11. A. Odagawa et al., Phys. Rev. B 70, 224403 (2004).
12. Y. B. Nian et al., Phys. Rev. Lett. 98, 146403 (2007).
13. Z. Guo et al., J. Alloy. Compd. 580, 148 (2013).
14. J. Zhang et al., Appl. Phys. A, 123, 10 (2017).
15. R. Zhang et al., Adv. elec. materials. 5, 1800833 (2014).
16. R. M. Mutiso et al., Appl. Phys. Lett. 103, 223302 (2013).
17. W. T. Kim et al., Appl. Phys. Lett. 96, 253301 (2010).
18. T. Tan et al., J. Alloys Compds, 610, 388 (2014).
19. S. Jou et al., Surf. Coat. Technol, 231, 311 (2012).
20. D. Rubi et al., Appl. Phys. Lett., 103, 163506 (2013).
21. M. Quintero et al., Phys. Rev. Lett., 98, 116601 (2007).
22. M. B. salamon et al., Rev. Mod. Phys. 73, 583 (2001).
23. K. Kumari, PhD thesis entitled, *"Charge transport studies of Pervoskite and 2d material oxide composite system"*, IIT Patna (2022). Url: http://hdl.handle.net/10603/463993.